

# Desiccation and Consolidation in Centrifuge Cake Oil Sands Tailings

By

Oswaldo Hurtado  
B.Eng., Carleton University, 2018

A thesis submitted to the Faculty of Graduate and Postdoctoral Affairs in partial fulfillment of the requirements for the degree of

Master of Applied Science

In

Environmental Engineering

Department of Civil and Environmental Engineering  
Carleton University

Ottawa-Carleton Institute of Civil and Environmental Engineering  
Ottawa, Ontario

©2018, Hurtado Oswaldo

## Abstract

Among the technologies available to the oil sands mining industry for processing Mature Fine Tailings (FFT) and improve deposits for reclamation, centrifuge treatment technology has had some success at larger scales. Optimization of centrifuge cake deposition requires knowledge of the various post-deposition dewatering mechanisms and their interactions. In order to study coupled evaporation-consolidation behavior of centrifuged tailings in some detail, a multilayer "dry box" deposition test was performed.

Two thick (0.5m) and three thin (0.35m) layers of centrifuge oil sands tailings were deposited in a 0.7m by 1m "dry box", a steel reinforced Plexiglas box, and allowed to dry and consolidate while measuring gravimetric water content, total suction, osmotic suction, and drainage history. In addition, core samples analysis of each layer, a vane shear test, and the analysis of crack development were used to further assess their dewatering behavior. The influence of cracking on evaporation appears to be minimal, though this might be due to the aspect ratio of the drying box experiment. While evaporation rates remained near the potential rate for most of the tests, an eventual decline in evaporation rate appears to arise from high osmotic suctions generated by propagation of dissolved mass to the surface. In terms of dewatering optimization, results suggest that thin-lift deposition is somewhat more advantageous than thick-lift deposition, registering evaporation as the most influential water removal mechanism. However, these observations need to be evaluated by extending the results using numerical modeling and comparing them to field trials.

## Dedication

To my loving parents, who made my dreams come true.

## Acknowledgements

Firstly, I would like to express my deepest appreciation to my supervisor Paul H. Simms, who guided me throughout the duration of my master's degree. Thank you very much for giving me the opportunity of being part of this project, and for having so much patience while I was still trying to figure things out.

I would also like to appreciate the staff of the Department of Civil and Environmental Engineering at Carleton University, without their constant assistance, this experiment would have crashed to its demise.

In addition, I am also grateful to my fellow students, Muhammad, Chris, Manuel, Hissan, Etienne, Shabnam, Juan, and John, for giving me the advice and support I needed to finalize this project.

Also, I would like to give special thanks to Priscilla, Meagan, Rebecca, Michael, and Carol, whose help kept me sane for the last two years.

Finally, to my friend Liza, thank you for showing me the way.

Financial support provided by the Natural Science and Engineering Research Council of Canada (NSERC) and the Canada's Oil Sands Innovation Alliance (COSIA) is deeply appreciated.

# Table of Contents

Abstract .....	I
Dedication .....	II
Acknowledgements .....	III
Table of Contents .....	IV
List of Figures .....	VIII
List of Abbreviations .....	XIII
1 Introduction .....	1
1.1 Problem statement .....	1
1.2 Objectives and scope of work .....	2
1.3 Thesis outline .....	3
1.4 Novelty of the thesis .....	3
2 Literature Review .....	4
2.1 Oil sands tailings .....	4
2.1.1 Oil Sands characteristics .....	5
2.1.2 Bitumen extraction process .....	6
2.1.3 Tailings disposal method .....	7
2.1.4 Challenges associated with FFT .....	8
2.1.5 Tailings regulations .....	8
2.1.6 Tailings dewatering technologies .....	9
2.1.6.1 Filtered tailings .....	9
2.1.6.2 In-line flocculation .....	9
2.1.6.3 Electrical .....	10
2.1.6.4 Centrifuge tailings .....	10
2.2 Consolidation .....	11
2.2.1 Consolidation and sedimentation .....	11
2.2.1.1 One dimensional consolidation theory .....	11
2.2.1.2 Two dimensional consolidation theory .....	14
2.2.1.3 Three dimensional consolidation theory .....	14
2.2.2 Piece-wise linear formulations and extension to UNSATCON solution .....	15
2.2.3 Constitutive relationship .....	15
2.3 Desiccation .....	19

2.3.1	Definition .....	19
2.3.2	Evaporation.....	19
2.3.3	Pore water salinity effects .....	22
2.3.4	Crack formation.....	23
2.3.5	Desiccation in different types of tailings .....	23
2.4	Theory of unsaturated soils .....	26
2.4.1	Soil suction .....	26
2.4.1.1	Matric suction .....	28
2.4.1.2	Osmotic suction.....	28
2.4.2	Measurement of soil suction .....	29
2.4.2.1	Matric suction measurements .....	30
2.4.2.1.1	Air-entry porous ceramics.....	30
2.4.2.1.2	Tensiometers.....	31
2.4.2.1.3	Axis translation technique .....	32
2.4.2.2	Osmotic suction measurements.....	35
2.4.2.2.1	Squeezing technique.....	35
2.4.2.2.2	Saturation technique .....	36
2.4.2.3	Total suction measurements.....	37
2.4.2.3.1	Chilled-mirror psychrometer.....	37
2.4.3	Water storage and permeability .....	39
2.4.3.1	Soil-water characteristic curve.....	39
2.4.3.1.1	Measurement of the SWCC.....	41
2.4.3.1.2	SWCC equations .....	43
2.4.3.2	Shrinkage curve .....	45
2.4.3.3	Unsaturated hydraulic conductivity .....	46
2.4.3.3.1	Hydraulic conductivity function models .....	46
3	Methods and Materials.....	49
3.1	Oil sands tailings characteristics .....	49
3.2	Dry box experiment set up .....	52
3.3	Evaporation.....	59
3.4	Sampling schedule and Monitoring .....	62
3.5	Property analyses.....	63
3.5.1	Solid content .....	63

3.5.2	Water content .....	63
3.5.3	Total organic content .....	64
3.5.4	Unit weight.....	64
3.5.5	Void ratio .....	65
3.5.6	Atterberg limits determination .....	65
3.6	Determination of SWCC .....	66
4	Results.....	67
4.1	Thick-lift dry box test.....	67
4.1.1	First Layer deposition .....	67
4.1.1.1	Surface samples.....	76
4.1.1.2	Core sample analysis .....	78
4.1.2	Second layer deposition .....	81
4.1.2.1	Surface samples.....	90
4.1.2.2	Core sample analysis .....	91
4.1.2.3	Un-drained shear strength.....	94
4.2	Thick-lift overall results .....	96
4.3	Thin-lift dry box test.....	108
4.3.1	First layer deposition .....	108
4.3.1.1	Surface samples.....	115
4.3.1.2	Core sample analysis .....	117
4.3.2	Second layer deposition .....	119
4.3.2.1	Surface samples.....	128
4.3.2.2	Core sample analysis .....	129
4.3.3	Third layer deposition.....	131
4.3.3.1	Surface samples.....	141
4.3.3.2	Core sample analysis .....	143
4.4	Thin-lift overall results.....	146
5	Discussion of results .....	161
5.1	Thin vs. Thick-lift tests.....	161
5.2	SWCC and shrinkage curves inferred from the dry box experiments.....	165
5.3	Centrifuge tailings vs. different type of tailings.....	171
6	Conclusions .....	175
7	Recommendations.....	176

References .....	177
Appendices.....	185
Appendix A: Thick-lift – First layer.....	185
Appendix B: Thick-lift – Second layer .....	186
Appendix C: Thick-lift – UNSATCON simulation .....	188
Appendix D: Thin-lift – First layer .....	191
Appendix E: Thin-lift – Second layer .....	192
Appendix F: Thin-lift – Third layer .....	194
Appendix G: Tailings characterization analysis .....	196

## List of Figures

Figure 1: Oil sands deposits in Alberta (Audet, Pinno, & Thiffault, 2014). .....	5
Figure 2: Generalized scheme of Clark Hot Water Extraction Process (Chalaturnyk et al., 2004; Jeeravipoolvarn, 2010). .....	7
Figure 3: Compressibility of Mature Fine Tailings (Jeeravipoolvarn, 2010). .....	17
Figure 4: Hydraulic conductivity of Mature Fine Tailings (Jeeravipoolvarn, 2010). .....	18
Figure 5: Stages of evaporation (Wilson, Fredlund, & Barbour, 1994). .....	20
Figure 6: Crack volume and measured cumulative evaporation in first layer of gold tailings (Simms, et al., 2017). .....	24
Figure 7: Relative evaporation and crack volume in thickened oil sands tailings (Simms, et al., 2017). .....	24
Figure 8: Blow-up of layer 1 evaporation and crack volume in polymer-amended MFT (Simms, et al., 2017). .....	25
Figure 9: A schematic of a tensiometer model, T5x from UMS GmbH, Germany (2009). .....	31
Figure 10: Use of the axis translation technique to avoid metastable states. (a) atmospheric conditions. (b) axis translation technique (Marinho, Take, & Tarantino, 2008) .....	33
Figure 11: Axis translation equipment (Tarantino & Romero, 2009; from Power, 2005) .....	34
Figure 12: Osmotic suction versus electrical conductivity for pore water containing mixtures of dissolved salts (USDA Agricultural Handbook No. 60, 1950). .....	36
Figure 13: Schematic diagram of chilled-mirror WP4 Water PotentialMeter (Fredlund et al., 2012; after Leong et al., 2003). .....	38
Figure 14: SWCC desorption branch with associated parameters (Fredlund et al., 2012). .....	39
Figure 15: Relationship of initial stress to hysteresis loop of SWCC (Fredlund et al., 2012, from Fredlund, 2003). .....	40
Figure 16: Gravimetric water content SWCC's measured on oil sands tailings (SFR=0.1) (Fredlund, Houston, & Caicedo, 2013). .....	42
Figure 17: Shrinkage curve with its relationship to the Atterberg Limit classification properties (Fredlund, Stone, Stianson, & Sedgwick, 2011). .....	45
Figure 18: Particle size distributions of centrifuge cake from hydrometer and sieve analysis with depth (Mizani, 2016) .....	50
Figure 19: Oil sands tailings delivery. ....	51
Figure 20: Drum mixer (Model No DLM150VGD, Mixer Direct) .....	51
Figure 21: Dry box set up. ....	52
Figure 22: Specific calibrations for raw MFT and polymer-amended MFT (modified from Witteman, 2013) .....	53
Figure 23: Comparison of calculated VWC and VWC obtained by Decagon 5TE sensors (Daliri, 2013) .....	53
Figure 24: Schematic of sensor locations in dry box (Daliri, 2013). .....	54
Figure 25: Decagon 5TE sensor (Decagon, 2016). .....	54
Figure 26: T5 tensiometer (UMS, 2009). .....	55
Figure 27: (a) Ultrasonic distance sensors, (b) load cells, and (c) tipping bucket rain gauge. ....	57
Figure 28: Ultrasonic distance sensor (Senix, 2017) .....	57
Figure 29: RH/Temperature Easy Log sensor (OMEGA, 2018) .....	57

Figure 30: Crack measurement geometry (Innocent-Bemard, 2013).....	58
Figure 31: Crack measurement techniques.....	58
Figure 32: Evaporation test used to calculate wind function.....	61
Figure 33: Crack sampling locations (Innocent-Bemard, 2013). .....	62
Figure 34: Air drying of tailings samples .....	65
Figure 35: (a) "Fredlund" SWCC device, and (b) non-contact displacement sensor .....	66
Figure 36: Temperature, RH and dewpoint profiles above the tailings - First layer .....	68
Figure 37: Actual and potential evaporation - First layer .....	69
Figure 38: Gravimetric water content - First layer .....	69
Figure 39: Average void ratio - First layer .....	70
Figure 40: Average degree of saturation - First layer .....	71
Figure 41: Shrinkage curve - First layer .....	72
Figure 42: Crack development - First layer .....	72
Figure 43: Surface cracks solid content - First layer .....	73
Figure 44: Surface cracks total suction - First layer .....	74
Figure 45: Volumetric water content at various heights - First layer .....	74
Figure 46: Drainage - First layer .....	75
Figure 47: Matric suction at various heights - First layer.....	76
Figure 48: Surface sample total and osmotic suction - First layer.....	77
Figure 49: Crack progression - First layer .....	77
Figure 50: Core sample, top (left hand-side) to bottom (right hand-side) - First layer .....	78
Figure 51: Core sample gravimetric water content profile - First Layer.....	79
Figure 52: UNSATCON prediction - First layer .....	80
Figure 53: Core sample suction profile - First layer .....	80
Figure 54: Temperature, RH and dewpoint profiles above the tailings - Second layer.....	81
Figure 55: Actual and potential evaporation - Second layer.....	82
Figure 56: Gravimetric water content - Second layer.....	82
Figure 57: Average void ratio - Second layer.....	83
Figure 58: Shrinkage curve - Second layer .....	84
Figure 59: Crack development- Second Layer .....	85
Figure 60: Surface cracks solid content - Second Layer.....	85
Figure 61: Surface cracks total suction - Second layer.....	86
Figure 62: Volumetric water content at various heights top layer –Second layer.....	87
Figure 63: Volumetric water content at various heights bottom layer - Second layer .....	87
Figure 64: Cumulative drainage - Second layer .....	88
Figure 65: Matric suction at various heights top layer - Second layer .....	89
Figure 66: Matric suction at the bottom of bottom layer - Second layer.....	89
Figure 67: Surface sample total and osmotic suction - Second layer .....	90
Figure 68: Crack progression - Second layer .....	91
Figure 69: Core sample: (a) top section (top at left hand-side) and (b) bottom section (top at left hand-side) - Second layer .....	92
Figure 70. Core sample gravimetric water content profile - Second layer .....	92
Figure 71: UNSATCON prediction - Second layer .....	93
Figure 72. Core sample suction profile - Second layer .....	94

Figure 73: Tailings top view after vane shear test- Second layer .....	94
Figure 74: Un-drained shear strength profile - Second layer .....	95
Figure 75: Overall temperature profile - Thick-lift test.....	96
Figure 76: Temperature profiles upon completion of each layer - Thick-lift test .....	97
Figure 77: Temperature profiles progression of (a) first layer deposition, and (b) second layer deposition - Thick-lift test.....	98
Figure 78: Volumetric water content profiles progression of (a) first layer deposition, and (b) second layer deposition.....	99
Figure 79: Temperature, RH and dewpoint profiles above the tailings - Thick-lift test .....	99
Figure 80: Actual and potential evaporation - Thick-lift test .....	100
Figure 81: Gravimetric water content - Thick-lift test .....	101
Figure 82: Crack development - Thick-lift test .....	101
Figure 83: Surface sample solid contents - Thick-lift test .....	102
Figure 84: Surface cracks total suction - Thick-lift test.....	103
Figure 85: Volumetric water content at various heights - Thick-lift test.....	103
Figure 86: Drainage - Thick-lift test.....	104
Figure 87: Matric suction at various heights - Thick-lift test.....	105
Figure 88: Surface sample total and osmotic suction - Thick-lift test .....	106
Figure 89: Dry box weight variation - Thick-lift test .....	106
Figure 90: Solid content comparison - Thick-lift test.....	107
Figure 91: Actual and potential evaporation - First layer .....	108
Figure 92: Gravimetric water content - First layer .....	109
Figure 93: Average void ratio - First layer .....	109
Figure 94: Average degree of saturation - First layer .....	110
Figure 95: Shrinkage curve - First layer .....	111
Figure 96: Crack development - First Layer.....	111
Figure 97: Surface cracks solid content - First Layer.....	112
Figure 98: Surface cracks total suction - First layer .....	112
Figure 99: Volumetric water content at various heights - First layer .....	113
Figure 100: Drainage - First layer .....	114
Figure 101: Matric suction at various heights - First layer .....	115
Figure 102: Surface sample total and osmotic suction - First layer.....	116
Figure 103: Crack progression - First layer .....	117
Figure 104: Tailings top view after extraction- First layer .....	118
Figure 105: (a) Core sample bottom section and (b) core sample top section, both: top (right hand-side) to bottom (left hand-side) - First layer .....	118
Figure 106: Core sample gravimetric water content profile - First Layer .....	118
Figure 107: Core sample suction profile - First layer .....	119
Figure 108: Actual and potential evaporation - Second layer.....	120
Figure 109: Gravimetric water content - Second layer .....	120
Figure 110: Average void ratio - Second layer.....	121
Figure 111: Average degree of saturation - Second layer.....	121
Figure 112: Shrinkage curve - Second layer .....	122
Figure 113: Crack development- Second layer.....	122

Figure 114: Surface cracks solid content - Second layer.....	123
Figure 115: Surface cracks total suction - Second layer.....	124
Figure 116: Volumetric water content top layer–Second layer .....	125
Figure 117: Volumetric water content bottom layer - First layer .....	125
Figure 118: Cumulative drainage - Second layer .....	126
Figure 119: Matric suction top layer - Second layer .....	127
Figure 120: Matric suction bottom layer - Second layer.....	127
Figure 121: Surface sample total and osmotic suction - Second layer .....	128
Figure 122: Crack progression - Second layer .....	129
Figure 123: Tailings top view after extraction- Second layer .....	129
Figure 124: Core sample from top (right hand-side) to bottom (left hand-side) - Second layer	130
Figure 125: Core sample gravimetric water content profile - Second layer .....	130
Figure 126: Core sample suction profile - Second layer .....	131
Figure 127: Actual and potential evaporation - Third layer .....	132
Figure 128: Gravimetric water content - Third layer .....	132
Figure 129: Average void ratio - Third layer .....	133
Figure 130: Average degree of saturation - Third layer .....	133
Figure 131: Shrinkage curve - Third layer.....	134
Figure 132: Crack development- Third Layer .....	135
Figure 133: Surface cracks solid content - Third layer .....	135
Figure 134: Surface cracks total suction (a) regular figure and (b) low suction range detail - Third layer .....	136
Figure 135: Volumetric water content at various heights top layer –Third layer .....	137
Figure 136: Volumetric water content middle layer –Third layer .....	138
Figure 137: Volumetric water content at various heights bottom layer - Third layer .....	138
Figure 138: Cumulative drainage - Third layer .....	139
Figure 139: Matric suction at various heights top layer - Third layer.....	140
Figure 140: Matric suction middle layer - Third layer.....	140
Figure 141: Matric suction at various heights bottom layer - Third layer .....	141
Figure 142: Surface sample total and osmotic suction - Third layer .....	142
Figure 143. Crack progression -Third layer.....	143
Figure 144: Tailings top view after extraction- Third layer .....	144
Figure 145: Core sample from top (right hand-side) to bottom (left hand-side) - Third layer ...	144
Figure 146: Core sample gravimetric water content profile - Third Layer.....	145
Figure 147: Core sample suction profile - Third layer.....	145
Figure 148: Overall temperature profile - Thin-lift test .....	146
Figure 149: Temperature profiles upon completion of each layer - Thin-lift test .....	147
Figure 150: Temperature profiles progression of (a) first layer deposition, (b) second layer deposition, and (c) third layer deposition - Thin-lift test .....	149
Figure 151: Volumetric water content profiles progression of (a) first layer deposition, (b) second layer deposition, and (c) third layer deposition - Thin-lift test.....	150
Figure 152: Temperature, RH and dewpoint profiles above the tailings - Thin-lift test.....	151
Figure 153: Actual and potential evaporation - Thin-lift test.....	152
Figure 154: Gravimetric water content - Thin-lift test.....	153

Figure 155: Crack development - Thin-lift test.....	153
Figure 156: Surface sample solid contents - Thin-lift test.....	154
Figure 157: Surface cracks total suction (a) regular figure and (b) low suction range detail - Thin-lift test.....	155
Figure 158: Volumetric water content at various heights - Thin-lift test .....	156
Figure 159: Drainage - Thin-lift test .....	157
Figure 160: Matric suction at various heights - Thin-lift test .....	157
Figure 161: Surface sample total and osmotic suction (a) regular figure and (b) low suction range detail (b) - Thin-lift test.....	159
Figure 162: Dry box weight variation - Thin-lift test.....	160
Figure 163: Solid content comparison - Thin-lift test .....	160
Figure 164: Comparison weight variation in thick and thin-lift tests .....	161
Figure 165: Cumulative potential evaporation for thick and thin-lift dry box experiments.....	162
Figure 166: Comparison weight variation in relation to the cumulative potential evaporation for thick and thin-lift dry box experiments .....	162
Figure 167: Comparison between (a) average, (b) maximum crack depth, and (c) exposed surface area in the second layer of both thick and thin-lift tests.....	164
Figure 168: Shrinkage curve all tests .....	165
Figure 169: SWCC for centrifuge oil sands tailings in terms of GWC.....	166
Figure 170: SWCC for centrifuge oil sands tailings in terms of degree of saturation.....	166
Figure 171: SWCC for centrifuge oil sands tailings in terms of void ratio.....	167
Figure 172: SWCC in terms of GWC and total suction from surface samples from the first layer of the thick-lift test, compared with those of the SWCC .....	168
Figure 173: Water content and total suction measurements of surface samples and matric suction tensiometer data from the thick-lift test, compared with those of the SWCC.....	169
Figure 174: SWCC in terms of GWC and total suction from surface samples.....	169
Figure 175: SWCC in terms of GWC and total suction from all core samples.....	170
Figure 176: Crack progression comparison between the second layer of centrifuge oil sands tailings and polymer-amended MFT .....	171
Figure 177: Crack volumes comparison between (a) thickened oil sands tailings, (b) polymer-amended MFT, and (c) centrifuge oil sands tailings .....	173
Figure 178: Comparison between evaporation behavior and surface suction development of the tailings surface, for all layers .....	174
Figure 179: Overall results obtained from UNSATCON for the first layer deposition using CASE I parameters (thick-lift test).....	188
Figure 180: Overall results obtained from UNSATCON for the second layer deposition using CASE I parameters (thick-lift test) .....	189
Figure 181: Overall results obtained from UNSATCON for the first layer deposition using CASE II parameters (thick-lift test).....	190
Figure 182: Overall results obtained from UNSATCON for the second layer deposition using CASE II parameters (thick-lift test) .....	190

## List of Abbreviations

AE – Actual evaporation

AER – Alberta Energy Regulator

AEV – Air-entry value

AFD – Atmospheric fine drying

COSIA – Canada’s oil sands innovation alliance

EC – Electrical conductivity

FFL – Fluid fine tailings

GWC – Gravimetric water content

LL – Liquid limit

MFT – Mature fine tailings

PE – Potential evaporation

PL – Plastic limit

RH – Relative humidity

TRO – Tailings reductions operations

SWCC – Soil water characteristic curve

VWC – Volumetric water content

XRD – X-ray diffraction analysis

# 1 Introduction

## 1.1 Problem statement

The waste stream from the bitumen extraction process, in Northern Alberta, Canada, produces a low solid content slurry called oil sands tailings. Oil sands tailings comprise a range of solid particle sizes: the coarse particles (sands) settling out following deposition, and the fines fraction left behind with solids content of 8%. After several years, fine tailings will typically settle out to a solids concentration of about 35%. At this point these tailings are termed Fluid Fine Tailings (FFT), and are in a very soft state with little strength (<1kPa un-drained shear strength), and are much wetter than their liquid limit (~180% compared to 50%). FFT typically manifests slow or negligible dewatering due to the poor consolidation properties as well as the build-up of pre-consolidation pressure due to thixotropic re-alignment of particles (Scott, Jeeravipoolvarn, Kabwe, Wilson, & Sorta, 2013).

Recent regulations now mandate that all oil sands tailings reach a “ready to reclaim status” 10 years after the end of operations of a particular mine (Alberta Energy Regulator, 2016). This is understood by many that the tailings require sufficient strength to be incorporated into dry landform reclamation, requiring water contents probably on the order of their plastic limit. The oil sands industry has investigated several techniques at pilot and commercial demonstration scales, to improve the rate of Fluid Fine Tailings dewatering. Technologies that have had some success at larger scales include in-tank thickening, centrifugation, and in-line flocculation, all of which are combined with some sort of deposition control to maximize post-deposition dewatering. Variants on in-line flocculation using anionic polymers and controlled lift deposition, termed Atmospheric Fines Drying (AFD) and Tailings Reductions Operations (TRO), have been employed at Shell and Suncor operations (Matthews et al., 2011; Wells et al., 2011; Dunmola et al., 2013; Caldwell et al., 2014), while after years of development by Syncrude and Shell, centrifuge technology is now considered to be commercially ready with a \$1.9 billion full scale centrifuge plant in progress and partially operational since 2005 (COSIA, 2015).

Mechanisms contributing to post-deposition dewatering include evaporation, self-weight consolidation, and freeze-thaw consolidation. While thin layer deposition maximizes the contribution of evaporation and freeze-thaw to dewatering, it may minimize the contribution of consolidation. Properly assessing the contribution of each mechanism to dewatering is important to optimize this technology, and minimize required footprints of tailings disposal areas. The work presented in this paper focuses on quantifying the rate of evaporation from centrifuge MFT deposits, particularly tracking the influence of cracking on the evaporation rate. The movement of salts may also affect the evaporation rate. Both phenomena have been shown to affect evaporation from hard rock and finer grained tailings (Fujiyasu et al. 2000; Fisseha et al. 2010). With respect to oil sand tailings, Innocent–Bernard (2013) showed that cracking is intimately linked with evaporation from Fluid Fine Tailings treated in a thickener; evaporation rates were shown to cycle from the potential rate down to a residual value as surface crust dried out, cracks subsequently formed, cracks dried out, and new cracks subsequently formed. By contrast, Daliri et al. (2016, 2013) and Simms et al. (2017) showed that cracking in thickened gold tailings did not measurably affect the

evaporative behavior. In all cases, however, evaporation at the surface at some point became limited by mass transport to the surface and salt formation.

The present study examines the evaporative behavior of centrifuge cake oil sands tailings, using a multilayer deposition in a “drying box”, 0.7 by 1.0m in plant. The outcomes of the test are compared to other drying box simulations of different tailings (Simms et al. 2017; Rozina et al. 2015). This work complements another ongoing work on evaluating the suitability of desiccation-consolidation numerical models to assist deposition design (Qi, Simms, & Vanapalli, 2017)

## 1.2 Objectives and scope of work

The objectives of this project are to:

1. Evaluate the dewatering behavior from centrifuge oil sands tailings, while measuring the cracks' and mass transport's influence on the evaporation rate.
2. Assess the effects of layer deposition thickness on the evaporation rate.
3. Compile sufficient experimental data to assist on the development of desiccation-consolidation numerical models used on tailings dewatering applications.

In order to achieve these objectives, the following experimental work was performed:

1. Centrifuge tailings characterization tests including Atterberg limits, grain size distribution, water chemistry, and XRD analysis.
2. Two tailings deposition simulations on a thick (0.5m) and thin (0.35m) multilayer dry box deposition setups in order to study their evaporation rate in relation to crack development on the surface and salt precipitation.
3. Extraction of core samples upon each layer completion in order to examine the influence of dewatering along the tailings height, with respect of gravimetric water content, total suction, osmotic suction, and drainage history.
4. Measurement of the soil-water characteristic curve (SWCC) and shrinkage curve using axis translation and dewpoint hygrometer instruments.
5. A comparison of experimental data with the numerical model UNSATCON in order to better interpret certain results.

### 1.3 Thesis outline

The outline of this thesis is presented below:

Chapter Two: Literature Review – This section consists of a brief description of the oil sands tailings and the industry behind them. In addition, it includes a review on the theory of unsaturated soils relevant to this topic.

Chapter Three: Methods and Materials – This section describes the materials and procedures used on this experiment, as well as some of the analytical work behind the findings.

Chapter Four: Results – This section provides a detailed description of all the results obtained from both tests.

Chapter Five: Discussion of Results – This section includes an analysis of the tests findings. In addition, comparisons between these experimental results and other kinds of tailings dewatering behaviors is discussed. Finally, the possibility of extrapolating the results in the field is considered.

Chapter Six: Conclusions - This section summarizes of the most significant findings of the project.

Chapter Seven: Recommendations - A summary of recommendations for future similar or related work.

### 1.4 Novelty of the thesis

This is the first publically reported study on multilayer deposition of oil sands tailings centrifuge cake.

## 2 Literature Review

This section reviews some background information on the oil sands industry. In addition, it presents the general management approach and technologies used when dealing with the environmental problems associated with the oil sands extraction in Alberta.

### 2.1 Oil sands tailings

The Alberta oil sands refers to the vast mineral deposits of crude oil contained in sands and carbonate sedimentary formations in northern Alberta. This type of crude oil, known as bitumen, is almost entirely located in only three areas in Alberta: Athabasca, Peace River, and Cold Lake (Figure 1). Of these regions, the Athabasca deposits are the largest and only ones to be shallow enough to allow surface mining techniques. Alberta holds over 170 billion proven barrels of bitumen economically available for extraction with current technologies (Government of Alberta, 2016). As a result, it has been transformed into one of the world-leading energy suppliers. However, the large volume of tailings generated by the bitumen extraction process, already forecasted to reach 2 billion m<sup>3</sup> by 2034 (Houlihan & Haneef, 2008), must be properly managed.

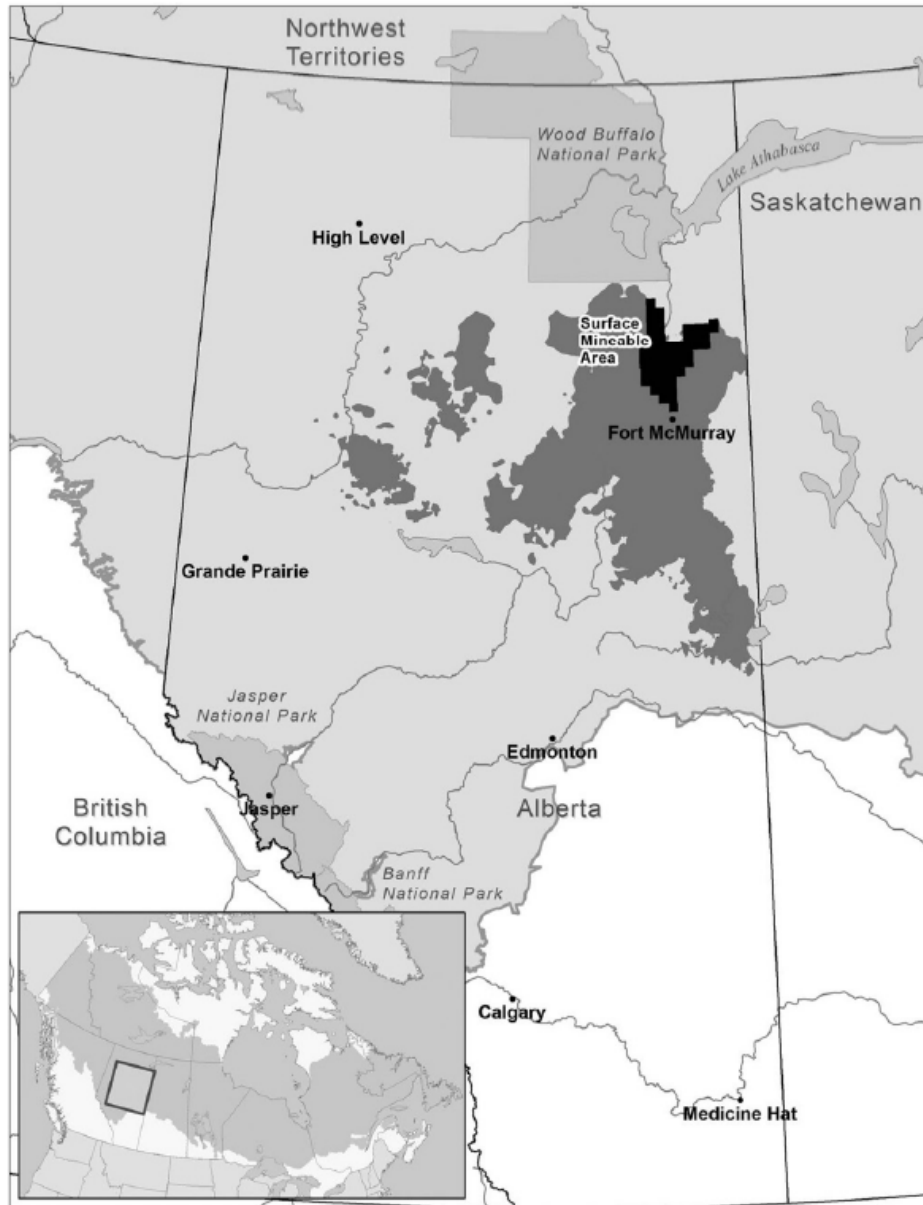


Figure 1: Oil sands deposits in Alberta (Audet, Pinno, & Thiffault, 2014).

### 2.1.1 Oil Sands characteristics

Usually formed by the association of uncemented quartzose sands and finer grained lithologies (Jeeravipoolvarn, 2010), the oil sands deposits are mainly contained within the lower Cretaceous McMurray formation (McLaws, 1980). The sand grains are coated by a 10nm film of water below a bitumen film (Zhu, 2013). Originally deposited 100 million years ago, these sand were spread by an ancient inland sea, eventually becoming saturated with oil (Jeeravipoolvarn, 2010). Currently in Fort McMurray, however, the formation is composed of bitumen (12% in average of total mass), water (3-6%) sands, silts

and clays minerals (84-86%) (Chalaturnyk, Don Scott, & Özüm, 2002) Usually, the deposits are overlain by a 50 to 200m layer of overburden made of rock, soil, vegetation, and muskeg of varying depths (NRCan, 2013), while the deposit themselves may be up to 150m thick.

### 2.1.2 Bitumen extraction process

Initially proposed by Professor Karl Clark, the Clark Hot Water Extraction Process (CHWE) is the most successful method of separating the bitumen, which exists between the voids of water-wet sand structures, from the oil sands through a combination of hot water, steam and sodium hydroxide (NaOH) (Jeeravipoolvarn, 2010; Chalaturnyk et al., 2002). Fine clay particles are found in the water film surrounding the sand particles or as discontinuous thin beddings.

The CHWE process of extraction (Figure 2) can be divided in three stages: conditioning, primary extraction, and final extraction (Moussavi, 2013). On the first stage, NaOH is added in conjunction with hot water (80-85°C) to facilitate the separation of the sand particles and bitumen. The sodium hydroxide is added with the intent of increasing the pH to 8.0-8.5 and reducing the surface and interfacial tensions. These steps, in turn, are conducive to the degradation of the oil sands ore structure. Concurrently, however, they lead to the dispersion of the clay particles in the water, conferring the resulting tailings effluent with poor dewatering characteristics (Boratynec et al., 1998; Chalaturnyk et al., 2002). On the second stage, the slurry is transported to the separation vessels where bitumen is disassociated and recovered on top of the vessel by means of flotation, while the coarse soil grains settle at the bottom. The un-floated part of the stream composed of a mixture of bitumen, sand, clay and water in the middle is referred to as middlings slurry. The settled sand component accumulated at the bottom by action of a rake also located at the bottom of the vessel becomes part of the tailings stream. On the third stage, further bitumen recovery is achieved from the middling slurry by discharging it into a scavenging cell where additional air is injected. The resulting 2-4% bitumen recovered within the created bitumen froth is then added back to the separation vessels (Oil Sands Discovery Centre, 2009) . Finally, the fine and coarse mineral streams are combined, which by the addition of water, a pumpable tailings stream is formed (Boratynec, 2003).

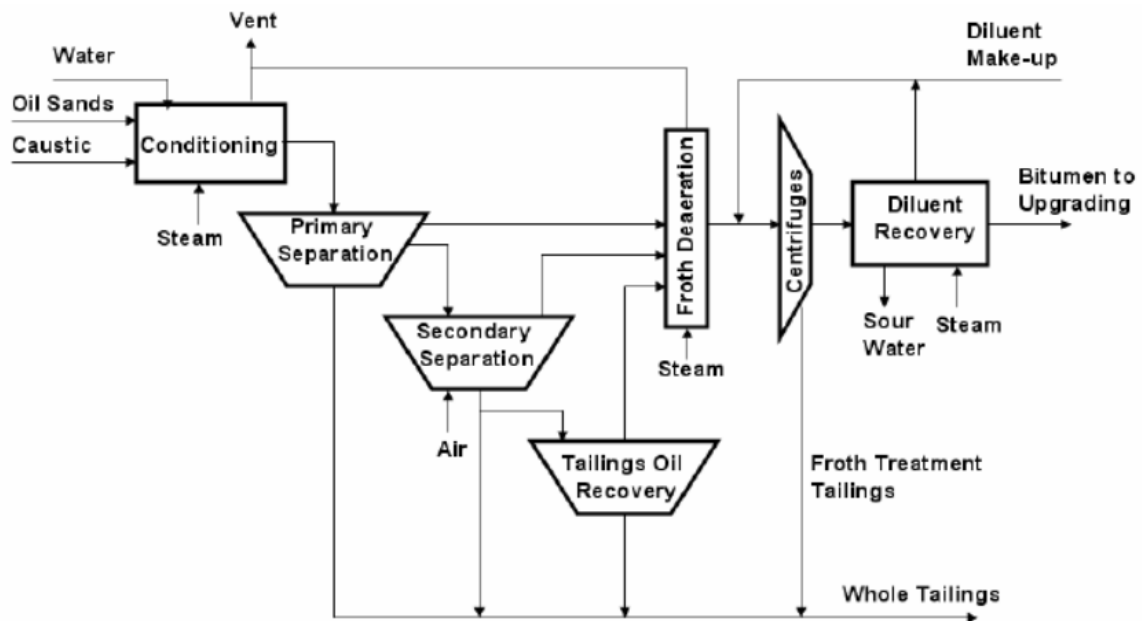


Figure 2: Generalized scheme of Clark Hot Water Extraction Process (Chalaturnyk et al., 2004; Jeeravipoolvarn, 2010).

### 2.1.3 Tailings disposal method

The resulting tailings slurry is characterized by having very poor consolidation properties, while been composed of 10-30% fines, residual bitumen and approximately three times more water than the oil extracted (Xu, Dabros, & Kan., 2008). This slurry, now referred to as whole tailings, is hydraulically transported and discharged into surface (out-of-pit) or in-pit storage ponds (Moussavi, 2013). Following deposition, the tailings coarse fraction will settle, forming a beach, while the fine fraction, which contains the residual bitumen, will flow into the pond at approximately 8% solid content. As time progresses, water at the top of the pond will disassociate from the rest of the tailings, allowing it to be pumped back to the extraction facility. Settling rates slow down once tailings reach a solid content of around 15-20%, slowly increasing to a solid content of 30% after a few years, at which point no further settlement takes place. At this stage, the resulting slurry is referred to as Mature Fine Tailings (MFT) or Fluid Fine Tailings (FFT). The poor consolidation behavior of FFT is credited to low hydraulic conductivity and the development of pre-consolidation pressure due to thixotropy.

As a result of this process, large amounts of water end up permanently trapped in the pond, which in conjunction with a zero discharge policy for the tailings operations, results in a massive accumulation of Fluid Fine Tailings over time. This, in turn, represents a great challenge for the industry (Birn & Khanna, 2010).

#### 2.1.4 Challenges associated with FFT

After reaching a solid content of ~30%, any further FFT dewatering becomes problematic. The addition of NaOH during the extraction process facilitates the bitumen extraction by inducing negative surface charges and promoting dispersion. However, in turn, it also reduces much of the tailings sedimentation and consolidation potential, ensuring large accumulations of MFT over time. In addition, issues associated with the tailings water management also arise. Increasing ion concentrations due to the constant recycling the water associated with the bitumen extraction process and the tailings pond, increase the risk of scaling of piping and equipment while reducing the efficiency of the extraction process (Beier & Segó, 2008). Finally, there are concerns associated with the tailings released water which could potentially influence the ecosystem.

#### 2.1.5 Tailings regulations

As a result of these challenges, in 2009, Directive 074, (now superseded by Directive 085) was introduced. With it, the Energy Resource Conservation Board (ERCB), from Alberta, aimed to decrease the increasing tailings fluid volume in the province by creating a trafficable surface which would lead to the reclamation of the tailings deposits within a few years after deposition. In this context, a trafficable surface was defined as having a minimum un-drained shear strength of 10kPa. In addition, as a requirement, an un-drained shear strength of 5kPa had to be achieved within a year after deposition, and 10kPa after five.

However, due to the inability of the industry to meet these criteria at a reasonable cost, Directive 074 was repealed in March 2015, and the Tailings Management Framework for Mineable Athabasca Oil Sands (TMF) was released. The main objective became the regulation of volumes and the minimization of risks associated with fluid tailings buildups. As a result, the TMF focused on decreasing tailings accumulated volume through proper tailings life-cycle management. In addition, the TMF required all fluid tailings to reach a "ready to reclaim status" within ten years from the end of the mine life. "Ready to reclaim" is interpreted by some (McKenna, 2017) to imply that the tailings can be used to support a landform of similar topography to the pre-existing boreal forest. This would imply an un-drained shear strength of at least 20kPa, to prevent deep seated slope stability failures. In FFT, this would necessitate a solids content greater than 70%.

Finally, as recently as October 2017, the Alberta government introduced the updated version of Directive 085. Originally introduced in July 2016, it focus on new application and performance reporting requirements by applying an outcomes- and risk-based approach that holds operators accountable in the process. In this policy, management plans are associated with the implementation of the TMF, which in conjunction with Directive 085, focuses on the measurement of tailings overall volume as a performance criteria for tailings fluid volume reduction (Alberta Energy Regulator, Directive 085, 2017).

To implement these regulations, the industry has initiated research in a number of dewatering technologies which could be implemented at large scales. More information about these technologies can be found below.

### 2.1.6 Tailings dewatering technologies

Large amounts of time and effort have been invested in researching several dewatering technologies that could potentially be used by the industry to address the aforementioned issues. However, high operational cost, skilled labor shortage, long time commitment, low energy efficiency, low bitumen extraction, inconsistency due to tailings variability, difficulty to remove supernatant liquid, detrimental effects on water quality, and low pumping efficiency have been cited as the main reasons why most efforts have only achieved limited success (BGC Engineering, 2010). Some of the technologies available are:

#### 2.1.6.1 Filtered tailings

This technology consists of mechanically dewatering the tailings through filtration. This is done either by pressure or vacuum forces. Typical plant configurations vary from drums, horizontally or vertically stacked plates, and horizontal belts. The unsaturated tailings resulting from this process are later transported, spread, and compacted into a stable tailings pile (dry stack) in a disposal area. Most applications of the technology have been unsuccessful, as the formation of a layer of fines particles on top of the coarse particle generated porous filter cake would blind the filtration process. In addition, as observed by Xu et al. (2008), while the filtration of untreated tailings with ~4.3% fines content is possible, great volumes of oil sands tailings with over 8% fines content would be impractical. In general, in Kasperski's (1992) view, the technology was not able to produce a feasible economic filtration process which can be acceptable to the industry.

#### 2.1.6.2 In-line flocculation

In this technology, water decoupling is promoted by the addition of polymer solutions while tailings are still in the transfer pipeline in order to dredge them prior to their deposition into cells. After flocculation, two depositional techniques are available. Thin-lift deposition can be used where the flocculated mixture is released into a gently sloping beach in thin layers at a solid content of 30-35% (Kolstad, et al., 2012). Initially caused by flocculation, substantial dewatering occurs as a result, enhancing the tailings permeability and water-release properties. Over time, however, the main mechanisms driving the dewatering process becomes evaporation, settlement, seepage, and freeze-thaw. In the past, Suncor implemented this technology as part of its tailings reduction operations (Wells, Revington, & Omotoso, 2011) at a commercial-scale. Shell's Atmospheric Fines Drying (AFD) has also been implemented at their Muskeg River Mine location (COSIA, 2015).

On the other hand, deep (>10m depth) deposition, as another alternative, relies mostly on self-weight consolidation. In this case, effective dewatering and strength development is aided through the use of decant structures and perimeter ditching as water is released to the surface (Beier, Wilson, Dunmola, & Segó, 2013). Between 2012 and 2013, Syncrude piloted this technique, referred to as "accelerated dewatering", which next phase currently encompasses its implementation on a commercial-scale (COSIA, 2015).

#### 2.1.6.3 Electrical

As one of the most recent technologies developed to treat oil sand tailings, this method is based on the application of a AC or DC current which directs negatively charged particles (clay) to a positive electrode, therefore achieving dewatering through accelerated sedimentation. However, high energy costs, corrosion issues, difficulty in removing supernatant liquid, and general unfamiliarity with the technology currently constrain its implementation.

#### 2.1.6.4 Centrifuge tailings

Once the MFT is dredged from the tailings pond, diluted, and mixed with a polyacrylamide flocculant, water separation is achieved by subjecting the tailings to forces many times the force of gravity, resulting in a tailings stream at a solid content as high as 60% (Devenny, 2010). At that density, the cake has to be treated as a solid, allowing it to be conveyed or trucked to the disposal site. The main advantages of the technology include an instantaneous water release and a "ready to reclaim" status cake. However, high capital and operational cost has precluded its implementation in the past.

After years of previous pilot-scale and commercial-scale development by Syncrude and Shell, the technology is now considered to be commercially ready, with a \$1.9 billion full scale centrifuge plant in progress and partially operational since 2005. At full capacity, it is expected to include 18 centrifuges and to be operational year-round (COSIA, 2015).

In general, however, current feasibility problems have led to the conclusion that a combination of current technologies should yield the best results when dewatering tailings. For more detailed information about this subject, an in-depth review of 34 existing oil sands fine tailings treatment technologies was published by BGC Engineering Inc. (2010).

## 2.2 Consolidation

This section examines the theory of consolidation developed until today, In addition, it presents the forms of compressibility and permeability constitutive relationships required for tailing modeling.

### 2.2.1 Consolidation and sedimentation

Consolidation is a time-dependent process by which soil decreases in volume while gaining effective stress through the dissipation of excess pore water pressure. Sedimentation, on the other hand, is considered a prior stage of settlement, when effective stress does not exist. The exact point at which the sedimentation process becomes a consolidation process is not completely agreed upon. As shown by Imai (1981), the corresponding void ratio at which the effective stress starts to occur is dependent on the initial void ratio. As a result, it has been suggested that countless compression curves exist corresponding to very low effective stresses. As pointed out by Carrier et al. (1983), however, in practice the initial void ratio does not significantly affect tailings storage capacity calculations as the depth of a pond imply that 90% or greater of the tailings will develop higher effective stresses than the effective stress region of indeterminate compression. In general, the end of sedimentation and the start of consolidation are usually arbitrarily chosen (Jeeravipoolvarn, 2010).

#### 2.2.1.1 One dimensional consolidation theory

In the context of geotechnical engineering, in 1925, Karl Terzaghi proposed the classical one dimensional small-strain consolidation theory to calculate the settlement of soils. This theory is based on the following assumptions (Qiu, 2000):

- Fully saturated soil.
- Both pore water and the soil particles are incompressible.
- Darcy's law is valid.
- The strains of the soil skeleton are governed by a linear time-dependent relationship between the void ratios and the effective stress.
- Quasi-static theory; strains, stress increments and velocities are small.
- Homogeneous soil.
- Load increments do not influence compressibility and permeability of the soil, which remain constant during consolidation (Gibson, England, & Hussey, 1967).

The mathematical expression is as follows:

$$c_v \frac{\partial^2 u}{\partial z^2} = \frac{\partial u}{\partial t} \quad [2.2.1]$$

where,  $c_v$  is the coefficient of consolidation,  $u$  is the excess pore pressure,  $t$  is the time and  $z$  is the vertical dimension.

Even though this theory is very successful in predicting consolidation in normal geotechnical work, it is not appropriate for soft materials such as oil sands tailings. Compressibility and hydraulic conductivity of tailings are highly non-linear leading to large settlement of the material when it is subjected to stress increments by continuous deposition (Jeeravipoolvarn, 2010).

As a result of these problems, a non-linear finite strain consolidation theory would be more appropriate. In this context, in 1967, Gibson, England and Hussey proposed a robust one dimensional finite strain consolidation theory incorporating additional theoretical formulations. This theory is often used in applications associated with self-weight consolidation, including tailings pond size, strength implications, and pore water pressure in slurries (Rozina, Mizani, Malek, Sanchez, & Simms, 2015). In addition, Been (1980) reported that, by setting the effective stress to zero, the theory of hindered sedimentation (Kynch, 1952) can be derived from the finite strain consolidation theory.

The governing equation in terms of void ratio is as follows (Gibson, England, & Hussey, 1967):

$$\pm \left( \frac{\rho_s}{\rho_f} - 1 \right) \frac{d}{de} \left[ \frac{k(e)}{(1+e)} \right] \frac{\partial e}{\partial z} + \frac{\partial}{\partial z} \left[ \frac{k(e)}{\rho_f(1+e)} \frac{d\sigma'}{de} \frac{\partial e}{\partial z} \right] + \frac{\partial e}{\partial t} = 0 \quad [2.2.2]$$

where,  $\rho_s$  is solids density,  $\rho_f$  is fluids density,  $e$  is the voids ratio,  $k$  is hydraulic conductivity,  $\sigma'$  is effective stress,  $t$  is the time and  $z$  is a reduced or material coordinate.

This theory assumes that Darcy's law is valid and that the soil skeleton has no time-dependent effect.

When characterizing a flow mathematically, the Eulerian method considers the rates of flux and soil movement with respect to the fixed plane of reference while the Lagrangian's approach focuses on the molecules of a mass element while analyzing its motion and distortion over time. Since, in a finite strain

consolidation problem, the thickness of the soil sample changes over time, the boundary is always moving, turning the position of the upper boundary into a time-dependent variable. The Lagrangian's approach overcomes this problem as the material spatial coordinate is already in its exact position, as in the equation above. However, the Eulerian's approach which uses a fixed spatial coordinate on an element which is assumed not to distort, is more appropriate in a small strain scenario (Jeeravipoolvarn, 2010).

Another formulation of this theory, in terms of pore water pressure, was proposed by Lee (1979) using the convective coordinate. However, it has been characterized as being more difficult to program due to changes of settlement during consolidation (Jeeravipoolvarn, 2010). This formulation is expressed as follows:

$$-\frac{\partial}{\partial x} \left[ \frac{k(1+e)}{\rho_f} \frac{d\sigma'}{de} \frac{\partial n}{\partial x} \right] - \left\{ (G_s - 1) \frac{d[k(1-n)^2]}{dn} - \frac{\partial q}{\partial n} \frac{d}{dn} \left[ \frac{k}{\rho_f} (1-n) \right] \right\} \frac{\partial n}{\partial x} + \frac{k}{\rho_f} \frac{\partial^2 q}{\partial x^2} (1-n) = \frac{\partial n}{\partial t} \quad [2.2.3]$$

where,  $n$  is the porosity,  $q$  is the applied stress, and  $x$  is the convective vertical coordinate.

A third formulation of this theory, developed by Somogyi in 1980, based on Koppula's (1970) rearrangement of continuity and fluid flow relationships, presents the expression in terms of excess pore water pressure. This formulation is expressed as:

$$\frac{\partial}{\partial z} \left[ \frac{k(e)}{\gamma_w(1+e)} \right] \frac{\partial u}{\partial z} + \frac{k(e)}{\gamma_w(1+e)} \frac{\partial^2 u}{\partial z^2} + \frac{de}{d\sigma'} \frac{\partial u}{\partial t} - \frac{de}{d\sigma'} \left[ (G_s - 1) \gamma_w \frac{\partial(\Delta Z)}{dt} \right] = 0 \quad [2.2.4]$$

All formulations stated remain theoretically identical even though each one will require different initial and boundary conditions to solve. Consequently, each formulation is to be utilized on a case by case basis (Jeeravipoolvarn, 2010).

In 1984, Bromwell estimated that the finite strain consolidation theory predicted a smaller influence of height on time of consolidation in comparison to the classical consolidation theory. Moreover, Schiffman (1984) reported it to predict slower dissipations of excess pore water pressure. However, the one dimensional consolidation theories above were found to be satisfactory when making predictions on containment ponds of depth lesser than the width and length, as the fluid flow and settlement are primarily vertical. As a result, one dimensional consolidation assumptions remain valid (Jeeravipoolvarn, 2010).

### 2.2.1.2 Two dimensional consolidation theory

In 1982, Bromwell Engineering Inc. proposed a two dimensional finite strain consolidation theory called pseudo two dimensional finite strain consolidation analysis. This theory, in Somogyi's view (1984), is associated with an idealized model where soil particles are unable to move in the vertical direction but the pore fluid is, in addition to the horizontal direction. It does not include multidimensional constitutive relations and failure criteria. In addition, this theory hinders lateral particle movement modeling (Jeeravipoolvarn, 2010). Building upon these models however, Huerta and Rodriguez (1992) proposed a pseudo bi-dimensional extension in order to model the influence of vertical drains. This theory presents a governing equation which is expressed as follows:

$$\frac{\partial}{\partial z} \left[ -\frac{k_z}{\gamma_w(1+e)} \frac{\partial u}{\partial z} \right] + (1+e) \frac{\partial}{\partial x} \left[ -\frac{k_x}{\gamma_w} \frac{\partial u}{\partial x} \right] + \frac{de}{d\sigma'} \left[ \gamma_b \frac{\partial \sigma_b}{\partial t} - \frac{\partial u}{\partial t} \right] = 0 \quad [2.2.5]$$

where,  $x$  is the horizontal coordinate,  $k_x$  is the horizontal hydraulic conductivity and  $k_z$  is the vertical hydraulic conductivity.

As a result of their studies, they were able to show that the drain influence is more relevant during the first stages of consolidation because of the large pore pressure gradients that they induce in proximity to the drains. In 1984, Bromwell argued that only when side drainages' width to height ratio was on the order to 5 or less, the two dimensional effects would become significant. Finally, the two dimensional sedimentation and consolidation analysis performed by Burger et al. (2004) in various shapes of a thickener used mainly for dewatering of slurries, described a faster growth of sediment for cone shape compared to cylindrical shape containments. Most notably, during the analysis, the volumetric solids concentration was assumed to be constant across each horizontal cross section. However, their method of analysis diverge from the ones of Somogyi et al. (1984) and Huerta and Rodriguez (1992) as their approaches do not consider the horizontal pore water flow.

### 2.2.1.3 Three dimensional consolidation theory

Even though three dimensional consolidation models have been developed in the past, such as the one proposed by Biot in 1955, and as described by Bromwell (1984), two dimensional effects become significant at impoundment's width to height ratios of the order of five or less (associating with side drainages), inadequate constitutive relationships, time, and numerical difficulties remain the main reasons why two and three dimensional modeling is rarely used in the industry. In practice, most tailings storage facilities present ratios of much higher magnitude. As a result, these models are rarely used to solve problems associated with consolidation (Ding, Wang, & McLeod, 2010).

Based on either one, two, and three dimensional consolidation theories, several numerical models have been developed around the world. Some of the most prominent models were: FSCON 1-I and FSCON 2-I (Cargill & Schiffman, 1980), 1D CONDESO (Yao & Znidarcic, 1997), CONSOL 2D (Jakubick, McKenna, & Robertson, 2003), CCI (Fox & Baxter, 1997), and 3D CONDESO (Coffin, 2010).

## 2.2.2 Piece-wise linear formulations and extension to UNSATCON solution

From the various solutions developed to solve large strain consolidation problems in saturated soils, CS2 offers one of the most accurate alternatives (Daliri, Simms, & Sivathayalan, 2016). In 1997, Fox and Berles developed CS2, a versatile one dimensional large strain consolidation model with; a piece-linear finite-difference formulation, an Eulerian coordinate system, and fixed data points specified constitutive relationships. This model was designed to operate while accounting for large strain, self-weight, the relative velocity of fluid and solid phases, and variable hydraulic conductivity and compressibility. In addition, its dimensionless approach allows it to yield solutions independent of the initial height of the compressible layer and the absolute magnitude of the hydraulic conductivity of the soil. The formulation of CS2 was extended to unsaturated conditions by Qi, Simms, and Vanapalli (2017), which is the basis for the UNSATCON model used later in the thesis.

## 2.2.3 Constitutive relationship

Two important relationships are used to solve finite strain consolidation equations: the void ratio-effective stress, known as compressibility, and the void ratio-hydraulic conductivity relationships. These relations are employed to reduce the number of unknowns and solve for void ratios when analyzing the finite strain consolidation governing equations. Conventional and current approaches used to obtain a finite strain solution combine the use of experimental data based continuous functions in association with numerical methods. In addition, interpolation of experimental data points is often utilized to construct these relationships (Jeeravipoolvarn, 2010). Mathematical formulas often used when modeling consolidation include Equations [2.2.6] and [2.2.7] by Somogyi (1980), Equations [2.2.8] and [2.2.9] by Carrier et al. (1983), and Equations [2.2.10] and [2.2.11] by Bartholomeeusen et al (2002).

$$e = A\sigma'^B \quad [2.2.6]$$

$$k = Ce^D \quad [2.2.7]$$

$$e = A(\sigma' + B)^C \quad [2.2.8]$$

$$k = \frac{E e^F}{(1 + e)} \quad [2.2.9]$$

$$e = A \ln \sigma' + B \quad [2.2.10]$$

$$e = C \ln k + D \quad [2.2.11]$$

where parameters  $A, B, C, D, E$  and  $F$  are laboratory determined parameters.

Different functions describe different finite strain model behaviors, which alternation is used to approximate the constitutive relationships as close to the real soil behavior as possible while conferring mathematical flexibility to the solution. In addition, Carrier et al. (1983) showed that it is also possible to obtain finite strain consolidation parameters by constructing empirical correlations based on Atterberg limits, specifically by correlating data between liquidity index and effective stresses (Jeeravipoolvarn, 2010). Similarly, in 1984, Carrier and Beckman described compressibility and hydraulic conductivity with respect to their liquid limit and plastic limit for deposited slurries. Equations based on these correlations in combination with compressibility, were able to yield finite strain consolidation parameters. At the time, the empirical correlations developed by Carrier et al. (1983) were used only for the preliminary design of tailings impoundments and to estimate the time of consolidation by finite strain consolidation theory. However, Nagaraj et al. (1994) conclusion of constant engineering properties at the liquid limit, regardless of type of soil, led to the reliable estimation of tailings consolidation behavior by means of index properties correlation (Morris, Lockington, & Apelt, 2000).

The void ratio-effective stress relationship have been found to be crucial during consolidation analysis. However, the pre-consolidation behavior shown by oil sands fine tailings casts doubt on the reliability of a power law function. As a result, Jeeravipoolvarn (2010) proposed the use of a Weibull function instead, as it is able to describe pre-consolidation behavior while better estimating the coefficient of determination in comparison to the power law function. This equation is expressed as (Jeeravipoolvarn, 2010):

$$e = A - B \exp(-E \sigma'^F) \quad [2.2.12]$$

where,  $A, B, E,$  and  $F$  are curved fitted parameters.

In practice, previously carried out consolidation tests at different eras of tailings consolidation studies are the source of most compressibility and hydraulic conductivity parameters. Consequently, the correct comprehension of consolidation behavior is based on the reliability and quality of the test performed by using similar types of tailings in the impoundment (Siddiqua & Ahmed, 2014).

Finally, as wide as the range of mathematical formulas and empirical parameters is available in the literature, detailed consolidation analysis of soft soil should only be performed based on direct measurements as well as an appropriate mathematical form of the constitutive relationships decided based on the experimental data. This translates to taking into account all the range of void ratios that the material would be subject to in the field (Jeeravipoolvarn, 2010).

For Mature Fine Tailings, the void ratio-effective stress and the void ratio-hydraulic conductivity relationships are presented in Figure 3 and Figure 4.

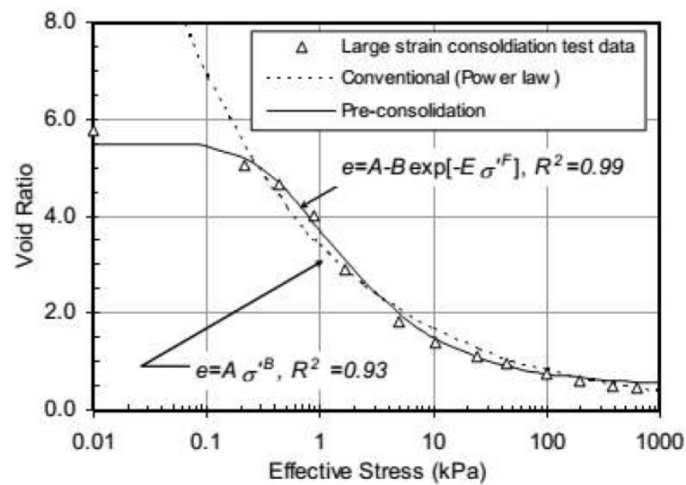


Figure 3: Compressibility of Mature Fine Tailings (Jeeravipoolvarn, 2010).

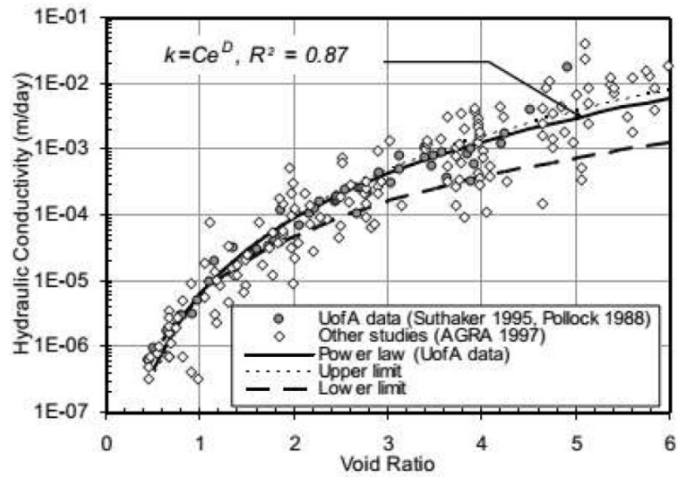


Figure 4: Hydraulic conductivity of Mature Fine Tailings (Jeeravipoolvarn, 2010).

## 2.3 Desiccation

Tailings desiccation is one of mechanisms most often used when assisting the stabilization and reclamation of tailings impoundments. As a result, this section focuses on the examination of the theory of evaporation, the effects of crack development, and salt precipitation.

### 2.3.1 Definition

In Robinsky's (1999) view, desiccation, or the process of extreme drying, is the natural mechanism by which tailings surface consolidation is further increased. In return, desiccation can potentially yield the necessary tailings strength required for reclamation purposes. Potentially driven by both surface evaporation and liquid infiltration into the underlying tailings layers, this mechanism is composed of the evaporation process, shrinkage, and crack formation (Simms et al., 2009; Qiu, 2000).

### 2.3.2 Evaporation

In this context, evaporation is the process by which water is transferred from the bare soil into the gas phase (Lal & Shukla, 2004). This process, as observed by Wilson et al. (1997), is driven by the vapor pressure and temperature differential between the soil surface and its surrounding atmosphere. Classically divided in three stages (Figure 5), tailings evaporation mimic the classic evaporation behavior in soils (Simms, Dunmola, & Fisseha, 2009). These stages are summarized below (Wilson, Fredlund, & Barbour, 1994):

- Stage I: The soil is at or close to saturation. The evaporation rate (actual rate of evaporation) closely resembles the potential evaporation.
- Stage II: Due to limitations with the conductive properties of the soil, the flow of water to the surface becomes insufficient and the maintenance of the maximum potential rate of evaporation is no longer possible. The rate of evaporation decreases.
- Stage III: The flow of liquid water to the drying front is interrupted as the liquid-water phase becomes discontinuous. Further migration of water molecules takes place through vapor diffusion (Hillel, 1980)

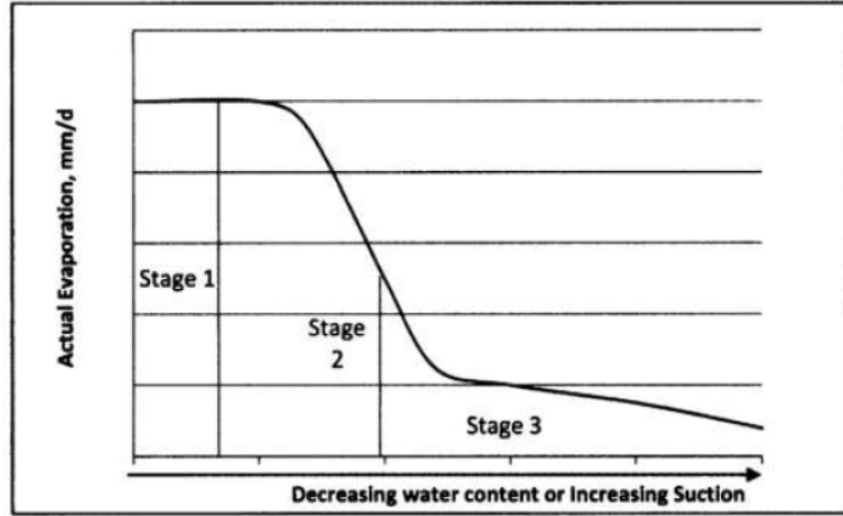


Figure 5: Stages of evaporation (Wilson, Fredlund, & Barbour, 1994).

Potential evaporation is the maximum possible amount of water that can be emitted from the soil based on the environmental conditions, surface characteristics, and assuming unlimited amounts of water available for evaporation (Simms, et al., 2017). Through the years, a number of methods have been developed in order to estimate the actual and potential evaporation from soils or mine tailings. For example, the Class A Pan evaporation method, consisting on the measurement of the water loss and temperature fluctuations in a customized pan over a 24 hour interval, has been used to measure the potential evaporation from tailings storage facilities (Fujiyasu et al., 2000; Newson & Fahey, 2003). Similarly, the Bowen ratio method, consisting on the data analysis of the air temperature and relative humidity measurements at different heights above the evaporating surface, has been used to determine the evaporation rates from a freshwater tailings evaporation pond (Fujiyasu, Fahey, & Newson, 2000) and from saline tailings storage (Newson & Fahey, 2003).

However, in this experiment, the Penman-Monteith equation, which relates temperature, relative humidity, wind speed, and radiation, was used for all potential evaporation analysis (Allen, 1996):

$$P_E = \frac{1}{\lambda} \frac{\Delta(R_n - G) + \rho_a C_a [(v_s - v_a)/r_a]}{\Delta + \gamma(a + r_s/r_a)} \quad [2.3.1]$$

where,  $\lambda$  is the latent heat of evaporation, [MJ/kg];  $\Delta$  is the slope of the vapor pressure-temperature relationship, [kPa/°C];  $\gamma$  is the psychrometric constant, [kPa/°C];  $R_n$  is the net short- and long-wave radiation that depends on the albedo, [MJ/m<sup>2</sup>d];  $G$  is the flux of heat into the soil away from the soil surface, [MJ/m<sup>2</sup>d];  $\rho_a$  is density of air, [kg/m<sup>3</sup>];  $C_a$  is specific heat of air, [MJ/kg°C];  $v_s$  and  $v_a$  are the vapor

pressures at the soil surface and in the air, [kPa]; and  $r_s$  and  $r_a$  are soil surface and aerodynamic resistance factors, respectively.

Actual evaporation, on the other hand, is defined as "the quantity of water that could be emitted from an unsaturated soil per unit surface area and unit time under current atmospheric conditions" (Int'l Glossary of Hydrology WMO, 1974). As a result, actual evaporation is usually just a fraction of the potential evaporation estimated from a pure water surface under the same atmospheric conditions (Wilson, Fredlund, & Barbour, 1994).

In the laboratory, actual evaporation can be estimated by the monitoring of weight variations of the soil over specific time intervals, while accounting for, or suppressing, drainage.

During stage I, while the soil is still saturated, the actual evaporation is almost equivalent to the potential evaporation until the beginning of stage II. On stage II, the actual evaporation rate becomes depended on the climatic parameters and soil characteristics, such as unsaturated vapor conductivity (Wilson, Fredlund, & Barbour, 1994). As a result, stage II evaporation and seepage modeling becomes possible by the use of conventional unsaturated flow models, assuming proper tailings characterization (Simms et al., 2007, 2009). For this purpose, as implemented by Wilson et al., (1994, 1997), the PdV approach is frequently used. This approach consist on relating the decrease on soil evaporation to the decrease in the differential in vapor pressures between the atmosphere and the soil surface; which coincidentally is related to the total suction on the soil surface at equilibrium. By linking this relationship to the Penman-Monteith equation, it is possible to describe the evaporation rate in terms of the surface suction as follows (Philips and Vries, 1957; Wilson et al., 1997):

$$\frac{A_E}{P_E} = \frac{e^{\frac{-\psi W}{RT}} - R_{Ha}}{1 - R_{Ha}} \quad [2.3.2]$$

where,  $R_H$  is the relative humidity;  $\psi$  is the total suction, [kPa];  $W$  is the molecular weight of water, [kg/mol];  $R$  is the universal gas constant;  $T$  is the temperature;  $A_E$  is the actual evaporation; and  $R_{Ha}$  is the relative humidity of the air above the evaporation surface.

When dealing with suction values below  $\sim 3000$  kPa, the  $A_E/P_E$  component approximates 1. However, often enough, models employing the PdV/Wilson approach may not be able to anticipate the correct timing or the correct decrease rate of the evaporation (Bittelli, et al., 2008). As a result, empirical equations describing soil resistance are often used to account for this early decrease in evaporation. The most widely used was proposed by van de Griend and Owe (1994):

$$r_s = 10e^{a(\theta_{ref}-\theta_{top})} \quad [2.3.3]$$

where,  $r_s$  is the soil resistance;  $\theta_{ref}$  is the water content at an arbitrary reference point, above which evaporation proceeds at the potential rate,  $\theta_{top}$  is the actual water content at the same reference depth, and  $a$  is a soil-dependent parameter.

Once the soil reaches its residual water content at stage III, the evaporation rate becomes comparatively constant and a new equilibrium between the water supply and evaporation is achieved. At this stage, all liquid water flow is minimal and all flow occurs exclusively through water vapor diffusion (Wilson et al., 1994; Hillel, 1998).

An important phenomenon sometimes encountered when studying evaporative drying in porous media is declining stage I evaporation. This phenomenon, measured and described by Lehmann et al. (2008) and Shahraneeni et al. (2012), is observed for high rates of potential evaporation when "patchy" water concentrations at the surface caused by water menisci surface retreat into individual pores. On the other hand, for low rates of potential evaporation, three-dimensional vapor transport from the aforementioned patches is able to successfully prolong initial potential evaporation rates.

### 2.3.3 Pore water salinity effects

One important phenomena that can influence evaporation from soils and tailings is salinity. As evaporation progresses, dissolved mass contained in the water precipitates in the top layer, resulting in the formation of a salt crust. This concentration of dissolved mass in the evaporating surface has been shown to hinder evaporation by at least three mechanisms: osmotic suction, physical effects of salt precipitation, and change in albedo. Osmotic suction negatively influences the evaporation rate through its influence in the soil's total suction as dissolved mass accumulates in the evaporation front on top of the soil. These salts, in turn, may further affect evaporation by diminishing the soil's porosity and permeability or by forming a crust. Finally, resulting high levels of shortwave reflectivity from the crust may appreciably reduce the net amount of radiation reaching the soil's surface (Simms, et al., 2017). In fact, up to 90% of the actual evaporation has been reported to be reduced due to salinity (Fujiyasu & Fahey, 2000; Fujimaki et al., 2006; Shimojima et al., 1996).

#### 2.3.4 Crack formation

Another factor that can potentially affect the evaporation rate is cracking. In the past, this by-product of shrinkage has been shown to be associated with an evaporation rate higher than what it would be expected based on one dimensional analysis (Fujiyasu, Fahey, & Newson, 2000).

Once formed, cracks allow further escape of water by functioning as channels for water flow during evaporation (Vogel, Hoffmann, Leopold, & Roth, 2005). This can be especially significant when evaporation from the surface is constrained due to the presence of a salt crust. In fact, as observed by Adams and Ritchie (1974), evaporation occurs almost exclusively through the crack-exposed wetter surface on clayey soils. Further, through the use of anemometers placed inside cracks, evaporation rates have been observed to be higher than potential evaporation rates measured at the surface caused by the acceleration of wind speeds within the cracks (Adams & Hanks, 1964; Adams & Ritchie, 1974; Weisbrod et al., 2005, 2011). In fact, at least temporarily, and depending on the crack depth and moisture content, actual evaporation rates measured from cracks have been estimated to approximate the potential evaporation measured with anemometers (Adams & Hanks, 1964).

#### 2.3.5 Desiccation in different types of tailings

With the objective of studying the effects of cracks and salinity during tailings evaporation, Daliri (2013) deposited gold tailings into a drying experiment similar to this one at a gravimetric water content of 40%. Here, instead of classic evaporation behavior, declining stage I evaporation was observed (Figure 6). However, crack development did not had a distinguishable effect on evaporation, phenomenon attributed to the relative drying of the tailings in relation to their depth, and possibly the offsetting effect of salt precipitation at the surface.

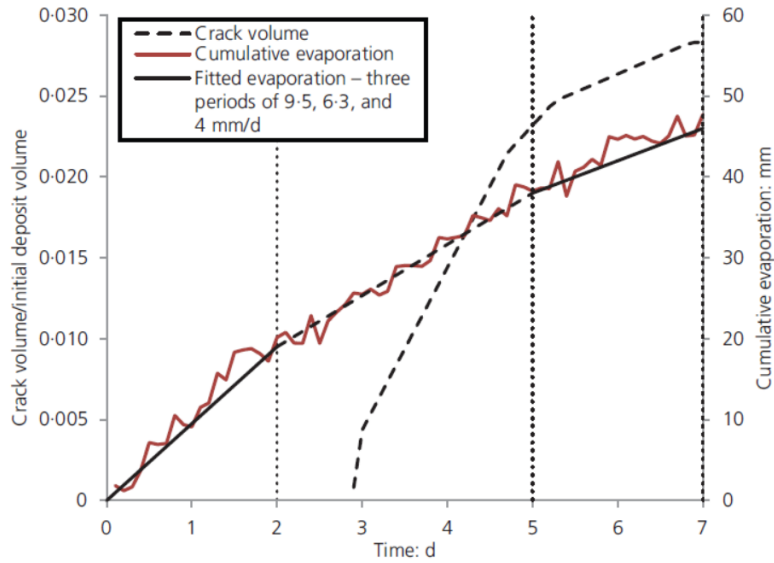


Figure 6: Crack volume and measured cumulative evaporation in first layer of gold tailings (Simms, et al., 2017).

In the case of thickened oil sands tailings deposited at a gravimetric water content of 100%, studied by Innocent-Bernard (2013), where drying was non-uniform with depth and shallow cracks developed, crack volumes developed coincidentally with the  $A_E/P_E > 1$  (Figure 7).

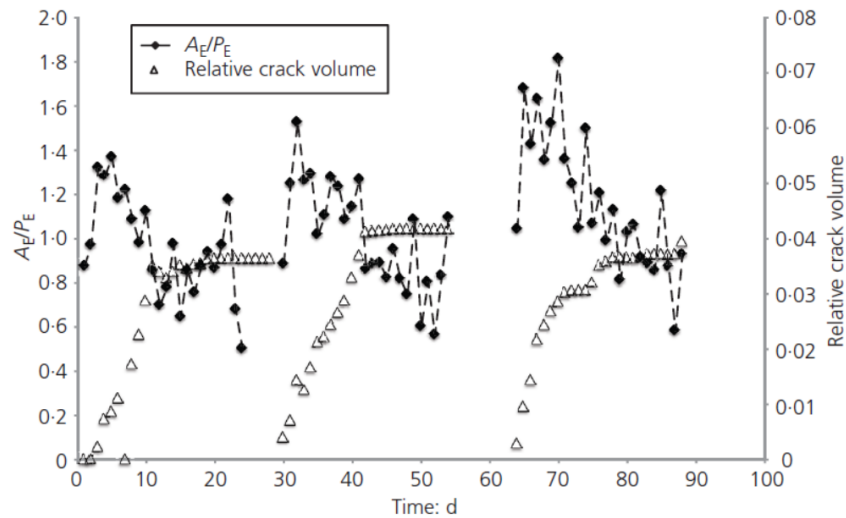


Figure 7: Relative evaporation and crack volume in thickened oil sands tailings (Simms, et al., 2017).

In this case, the evaporative behavior is explained by the uneven drying process with depth undergone by the tailings and the temporary contribution of cracks to  $A_E$ . The fast dewatering behavior lead to high

mass precipitation in the surface level, which in turn, lead to high suction levels. In addition, softer material exposed by crack development further temporarily increased the  $A_E$  past the  $P_E$  until the top 1cm total suction value of 3MPa was reached. At this point surface dewatering and suction increments finally leveled off, signaling the beginning of stage II. Further contribution of stage I evaporation was still observed past this point, however, at least until crack development stopped.

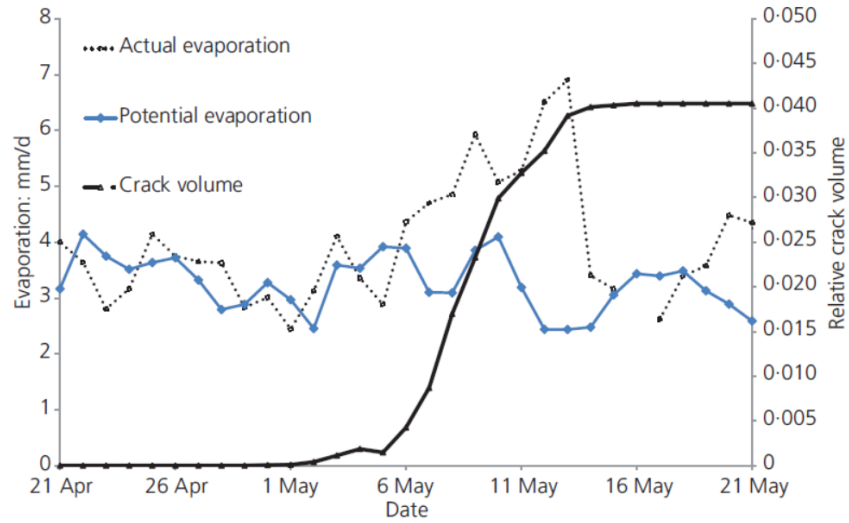


Figure 8: Blow-up of layer 1 evaporation and crack volume in polymer-amended MFT (Simms, et al., 2017).

In 2013, Rozina studied oil sands Mature Fine Tailings treated with high-molecular weight anionic polymer evaporation behavior at a gravimetric water content of 180%. These tailings also presented  $A_E > P_E$  during crack development. However, as can be seen from Figure 8,  $A_E/P_E$  increased or remained steady until the end of crack development, at which point it decreased to, and eventually, fell below (Stage II) the  $P_E$ . This development, in turn, coincided with the measurement of suctions above 3MPa, similar to the thickened oil sands tailings case. In addition, in this experiment, more uniform drying relative to depth (as opposed to the thickened oil sands tailings) as well as relatively small contribution of osmotic suction to total suction characterized the experience.

## 2.4 Theory of unsaturated soils

As oil sands tailings go through the desiccation process, they become unsaturated. As a result, the understanding of the mechanics of unsaturated soils is essential for their analysis. This section examines the mechanics of unsaturated soils, including soil suction, methods of suction measurement, the soil water characteristics curve (SWCC), and unsaturated permeability.

### 2.4.1 Soil suction

Soils in an unsaturated state are described by their void spaces being only partially filled with water, which in turn translates into them having negative pore water pressures (or suction). In this context, soil suction is defined as the energy required to remove a unit weight of water from the soil. According to Richards (1965), this suction, or free energy of the soil-water, can be related to the adjacent partial vapor pressure. This formulation is described by the following expression (Fredlund, Rahardjo, & Fredlund, 2012):

$$\psi = -\frac{RT_K}{v_{w0}w_v} \ln\left(\frac{\bar{u}_v}{\bar{u}_{v0}}\right) \quad [2.4.1]$$

where,  $\psi$  is soil suction or total suction, [kPa];  $R$  is the universal (molar) gas constant, [i.e., 8.3 J/(mol K)];  $T_K$  is absolute temperature, [K];  $v_{w0}$  is specific volume of water, [m<sup>3</sup>/kg];  $w_v$  is molecular mass of water vapor, [i.e., 18.016 kg/kmol];  $\bar{u}_v$  is partial pressure of pore water vapor, [kPa]; and  $\bar{u}_{v0}$  is the saturation pressure of water vapor over a flat surface of pure water at the same temperature, [kPa].

For analysis purposes, the suction's reference state in the equation above is the vapor pressure above the flat surface of pure water (i.e., water with no salts or impurities). The relative vapor pressure in the air contiguous to the water,  $\bar{u}_v/\bar{u}_{v0}$ , is referred to as relative humidity (Fredlund, Rahardjo, & Fredlund, 2012).

For most geotechnical engineering problems, soil suction is referred to as "total suction", recognizing matric suction and osmotic suction as its two main components. These components are defined as (Aitchison & Richards, 1965):

- Total Suction: The equivalent suction identical in measurement with the partial pressure of the water vapor in equilibrium with the soil-water, relative to the partial pressure of water vapor in equilibrium with free pure water.

- Matric Suction: The equivalent suction identical in measurement with the partial pressure of the water vapor in equilibrium with the soil-water, relative to the partial pressure of water vapor in equilibrium with a solution identical in composition with the soil-water.
- Osmotic Suction: The equivalent suction identical in measurement with the partial pressure of the water vapor in equilibrium with a solution identical in composition with the soil-water, relative to the partial pressure of water vapor in equilibrium with free pure water.

In addition, these components, in turn, mathematically relate to each other as follows:

$$\psi = (u_a - u_w) + \pi \quad [2.4.2]$$

where,  $(u_a - u_w)$  is the matric suction, [kPa];  $u_a$  is the pore-air pressure, [kPa];  $u_w$  is pore-water pressure, [kPa]; and  $\pi$  is the osmotic suction, [kPa].

In practice, soil suction influences the soil's engineering behavior by influencing its geotechnical characteristics. Suction greatly influences the coefficient of permeability (Fredlund & Rahardjo, 1993), while shear strength is associated with matric suction (Escario & Saez 1986; Vanapalli et al., 1996). Consequently, proper understanding of this phenomenon is necessary for geotechnical applications such as the design and management of landfills and mine tailings disposal facilities (Newson & Fahey, 2003; Simms et al. 2007; Fisseha et al. 2010).

#### 2.4.1.1 Matric suction

Matric suction is best described in terms of capillary forces. It is possible to consider the rise in soil-water above the water table through the soil pores as being analogous to capillary tubes being filled with water having negative pressure with respect to the air pressure (generally atmospheric; i.e.,  $u_a = 0$ ). In this context, the partial pressure directly associated to the resulting meniscus formed in the capillary tube would be less than the partial pressure associated to water vapor directly above a flat surface of the same water. In other words, the relative humidity in the soil would decrease as a result of the curved water surface associated to the capillary phenomenon. Based on this analysis, it is possible to conclude that the water vapor pressure (relative humidity) decreases in relation to the decrease in the water's radius of curvature, making it inversely proportional to the difference between the air and water pressures across the surface ( $u_a - u_w$ ). Therefore, matric suction contributes to the reduction in relative humidity, which turns it into a component of total suction (Fredlund, Rahardjo, & Fredlund, 2012). Matric suction can be expressed as (Fredlund & Rahardjo, 1993):

$$\text{Matric suction} = (u_a - u_w) \quad [2.4.3]$$

where,  $u_a$  is the pore-air pressure, [kPa];  $u_w$  is pore-water pressure, [kPa].

#### 2.4.1.2 Osmotic suction

Known as the solute component of free energy, osmotic suction is associated with the decrease in relative humidity caused with the presence of dissolved salts in the pore water of the soil. This decrease in relative humidity is caused by the fact that water vapor pressure above a flat surface of solvent (i.e., salt solution) is lower than the one above a flat surface of pure water. Consequently, the relative humidity decreases with increasing dissolved salt concentration in the pore water of the soil (Fredlund, Rahardjo, & Fredlund, 2012). As ionic concentrations in pore water are associated with osmotic suction, there are many formulations capable of relating it to electrical conductivity, such as the following (United States Department of Agriculture, 1954):

$$\pi = 0.36 \times EC \times 101.35 \quad [2.4.4]$$

where,  $EC$  is electrical conductivity, [mS/cm].

In general, a significant fraction of the total suction may be linked to osmotic suction in very dry soil.

## 2.4.2 Measurement of soil suction

Soil suction can be measured either in a direct or indirect manner. The direct approach focuses on the measurement of the moisture equilibrium condition of the soil while the indirect approach attempts to manage the matric suction in terms of the negative pore water pressure in the soil. Commonly used measuring devices for soil suction can be found in Table 1.

Table 1: Devices for measuring soil suction and its components (Fredlund, Rahardjo, & Fredlund, 2012).

Name of Device	Suction Component Measured	Range, kPa	Comments
Psychrometers	Total	100 <sup>a</sup> to ~8000	Constant-temperature environment required
Filter Paper	Total	Entire range	May measure matric suction when in good contact with moist soil
Tensiometers	Negative pore water pressures or matric suction when pore-air pressure is atmospheric	0-90	Difficulties with cavitation and air diffusion through ceramic cup
Null-type pressure plate (axis translation)	Matric	0-1500	Range of measurement is a function of the air-entry value of ceramic disk
Thermal conductivity sensors	Matric	10 to ~1500	Indirect measurement using variable-pore-size ceramic sensor
Pore fluid squeezer	Osmotic	Entire range	Used in conjunction with psychrometer or electrical conductivity measurement

<sup>a</sup> Controlled temperature environment to  $\pm 0.001^\circ\text{C}$

#### 2.4.2.1 Matric suction measurements

Matric suction, which is the difference between the pore-air and pore water pressures, is directly quantified through the measurement of negative pore water pressure. In regular circumstances, the pore-air pressure component of matric suction is atmospheric. As a disadvantage of this approach, direct measurements of the pore water pressure constrain the method's working range to very low suctions or require raising the air pressure to be able to measure high suction values. Indirect methods, on the other hand, utilize some other variable than the negative pore water pressure through the use of a specifically designed ceramic material (Fredlund, Rahardjo, & Fredlund, 2012).

Among the options for matric suction measurement available, the concept of measuring a pressure differential across a high air-entry porous ceramic is utilized by both hydraulic tensiometers (or pressure transducers) and the axis translation technique (Marinho, Take, & Tarantino, 2008).

##### 2.4.2.1.1 Air-entry porous ceramics

High-air-entry ceramic disks are characterized for being made of ceramic materials such as sintered kaolin, while having small pores of relatively uniform size allowing them to work as a separator or membrane between air and water. This process occurs once their saturation with water has been achieved, which hinders the movement of free air passing through the disk. The ceramic's capacity to resist the flow of free air is associated to the surface tension of the contractile skin. The difference between the air pressure and the water pressure surrounding the contractile skin is equal to the matric suction, which maximum increment maintained by the ceramic is referred to as the air-entry value  $(u_a - u_w)_d$ . This air-entry value is described by using Kelvin's capillary equation (Fredlund, Rahardjo, & Fredlund, 2012):

$$(u_a - u_w)_d = \frac{2T_s}{R_s} \quad [2.4.5]$$

where,  $(u_a - u_w)_d$  is the air-entry value of the high-air-entry disk, [kPa];  $T_s$  is the surface tension of the contractile skin or the air-water interface; and  $R_s$  is the radius of curvature of the contractile skin or the radius of the maximum pore size, [m].

#### 2.4.2.1.2 Tensiometers

Tensiometers are devices used for the direct measurement of negative pore water pressures. As observed in Figure 9, they are made of the combination of a high-air-entry, porous ceramic cup connected to a pressure measuring device through a small-bore tube filled with de-aired water. Appropriate connection between the high-air-entry ceramic and the soil is essential. Once the device is set up, the soil and the measuring system will eventually reach equilibrium at which point the water within the tensiometer and the pore water in the soil will have the same negative pressure. The pore-air pressure is almost always atmospheric (i.e.,  $u_a =$  zero gauge pressure), as such the measured negative pore water pressure is equal to matric suction of the soil. The measured matric suction should not surpass the air-entry value of the ceramic cup. In fact, for most cases, due to the possibility of cavitation of the water in the tensiometer, the measurable pore water pressure is limited to approximately negative 90kPa. However, some tensiometers, such as T5 tensiometers, are specifically designed to make reliable measurements of up to 200kPa (UMS, 2009). Successful measurements when using tensiometers, nevertheless, will depend in proper saturation and pre-conditioning of the water contained within the porous cup and the reservoir of the device (Marinho, Take, & Tarantino, 2008). Osmotic suction, on the other hand, cannot be measured using tensiometers, as soluble salts are able to freely cross the tensiometer's ceramic cup (Fredlund, Rahardjo, & Fredlund, 2012).

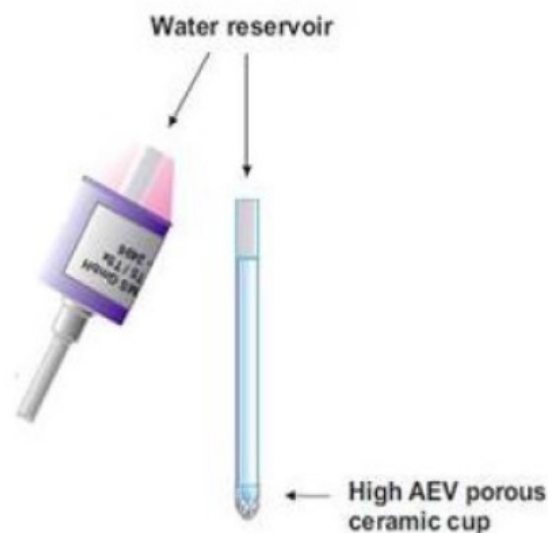


Figure 9: A schematic of a tensiometer model, T5x from UMS GmbH, Germany (2009).

#### 2.4.2.1.2.1 Cavitation nuclei phenomenon

Cavitation is said to occur when vapor bubbles are formed within the liquid due to the decrease of the fluid pressure of the liquid below its vapor pressure (Marinho, Take, & Tarantino, 2008). In Gibbs' (1948) perspective, from the thermodynamic point of view, the water is said to be 'metastable', or to put it differently, water is unstable in the liquid form due to the presence of gas bubbles, referred to as cavitation nuclei. Consequently, if any amount of gas is pre-existing in the liquid phase, the gas phase will rapidly separate in the liquid phase prompted by the water being under tension (Delage, Romero, & Tarantino, 2008), once the absolute pressure of the water drops below its saturation pressure.

#### 2.4.2.1.3 Axis translation technique

This technique, initially proposed by Hilf (1956), is used for laboratory measurements of negative pore water pressures of either undisturbed or compacted soil samples. Originally introduced to circumvent the problems associated with cavitation, this technique translates the origin of reference for the pore water pressure from standard atmospheric conditions to the final air pressure in the chamber. Figure 10 shows the principle associated with this method. The equipment used to measure matric suction (shown in Figure 11a), is conventionally called a null pressure plate apparatus.

The axis translation technique enables the measurement (or control) of the pore water pressure in an unsaturated soil by the usage of a ceramic disk with fines pores (referred to as the high air-entry disk) which acts as an interface between the air and water phases. This method works by placing the soil on top of a high-air entry saturated disk (while ensuring good contact) in a closed pressure chamber, which immediately drives the water in the tube (Figure 11b) into tension. As the water in the tube tends to go into tension, the air pressure of the chamber counters it, eventually reaching an equilibrium condition (i.e. attains null condition). The resulting pressure differential between the air pressure in the chamber and the measured water at equilibrium is taken to be as the matric suction ( $u_a - u_w$ ). The matric suction can be considered equal to the negative pore water pressure if the air pressure is atmospheric (i.e.,  $u_a =$  zero gauge pressure).

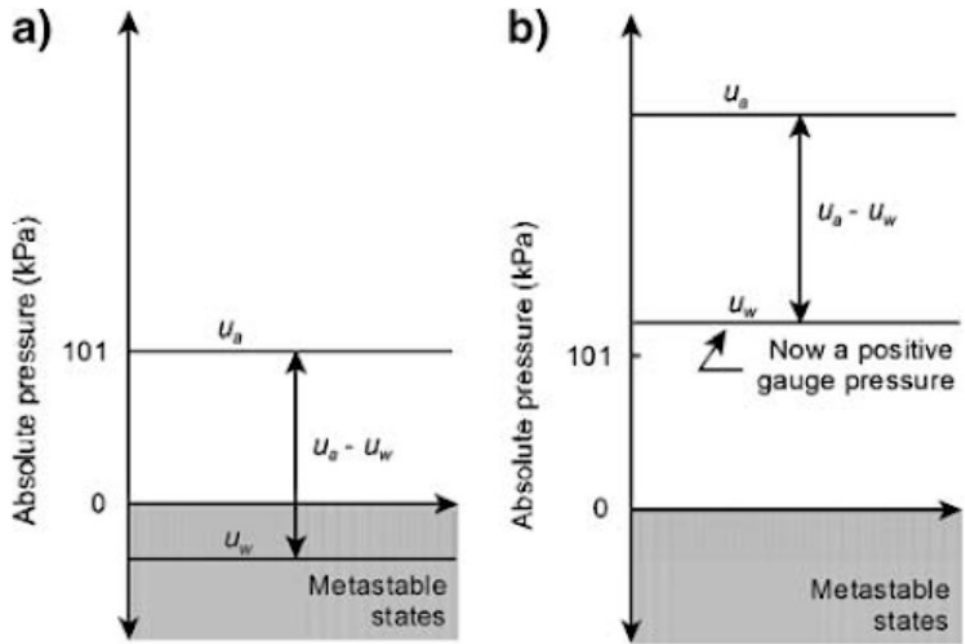


Figure 10: Use of the axis translation technique to avoid metastable states. (a) atmospheric conditions. (b) axis translation technique (Marinho, Take, & Tarantino, 2008)

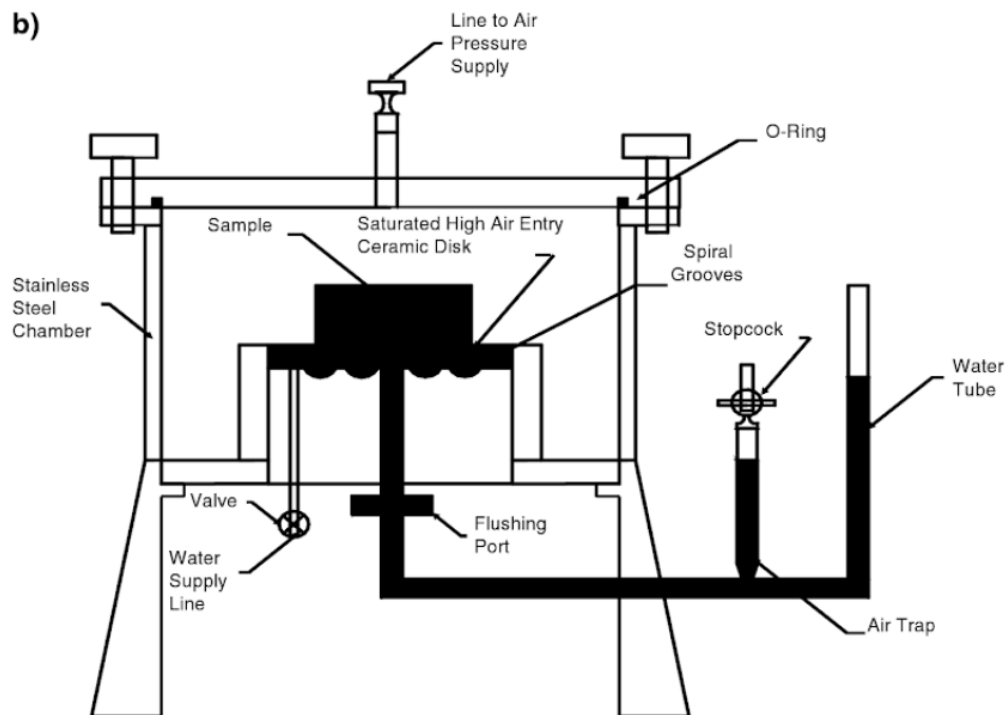


Figure 11: Axis translation equipment (Tarantino & Romero, 2009; from Power, 2005)

It is important that all measurement using this device are performed below the air-entry value stipulated by the manufacturer; otherwise, free air may cross the disk, rendering all measurements unreliable. Measurements of up to 1500kPa can be performed using this technique (Rahardjo & Leong, 2006).

The advantage of the axis translation technique lies on the fact that by translating the origin of reference of the pore water pressure from standard atmospheric condition to the final air pressure in the chamber, the water pressure in the measuring systems does not become highly negative. As a result, cavitation is prevented (Fredlund, Rahardjo, & Fredlund, 2012).

#### 2.4.2.2 Osmotic suction measurements

Based on the association of osmotic suction and the amount of dissolved salts in the free pore water, it is possible to measure osmotic suction from the electrical conductivity of the soil. The saturation extraction technique and the squeezing technique are based on this indirect method of measurement.

##### 2.4.2.2.1 Squeezing technique

This technique is based on the measurement of the electrical conductivity of the small amount of pore water extracted from the soil. Firstly, the pore water in the soil is extracted using a heavy-walled cylinder and piston squeezer. By isolating the electrical conductivity of the sample's free pore water; subsequently, it is possible to estimate the total concentration of dissolved salts. Finally, after the electrical conductivity is measured, a calibration curve can be used to associate it with osmotic suction. Figure 12 illustrates the calibration relationship which applies to most salts commonly encountered in soils (Fredlund, Rahardjo, & Fredlund, 2012). Limitations with this method involve its application to drier soils.

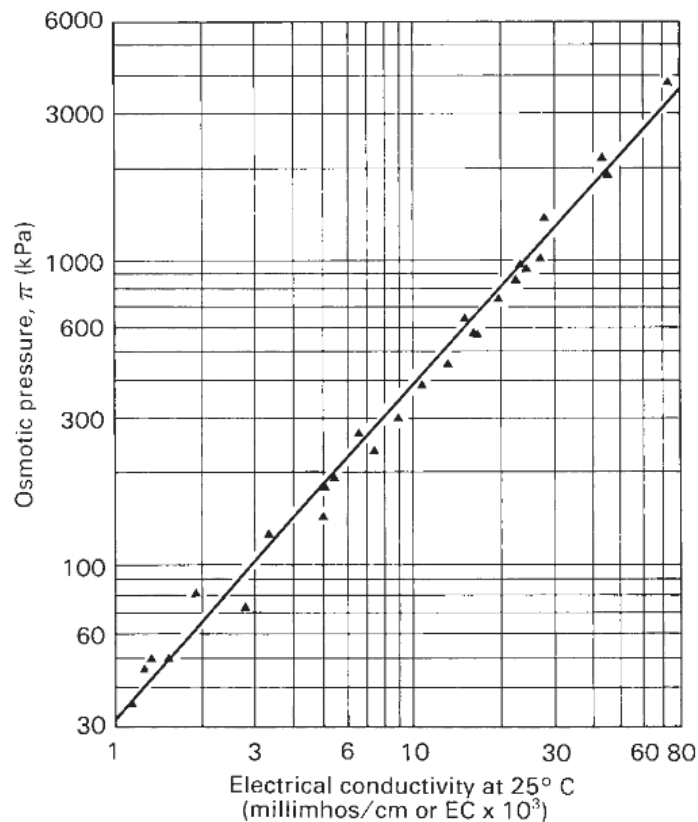


Figure 12: Osmotic suction versus electrical conductivity for pore water containing mixtures of dissolved salts (USDA Agricultural Handbook No. 60, 1950).

#### 2.4.2.2.2 Saturation technique

This method involves the addition of de-ionized or distilled water to the soil, which by mixing or centrifuging both components, it is possible to disassociate the pore water. Subsequently, the electrical conductivity of the effluent or supernatant is recorded and extrapolated to the corresponding osmotic suction linked to the original water content (United States Department of Agriculture, 1954). Even though this procedure is simple, the relationship between dilution and electrical conductivity may lead to inaccurate results (Krahn & Fredlund, 1972). As per equation, the osmotic suction is estimated by the equation [2.4.4].

It is important to point out that during the evaporation process of the soil, some amounts of salt are left behind, close to the evaporation front, leading to an increment in the concentration of salt in the pore water of the soil in that area. As a result, the osmotic component of suction increases near the evaporation surface. This phenomenon is known as "shut off" and can greatly decrease the evaporation rate of water of the soil. As such, a decrease in the evaporation rate is often related to a significant increase in the soil's osmotic suction (Fredlund, Rahardjo, & Fredlund, 2012).

### 2.4.2.3 Total suction measurements

In the field, environmental changes, such as evaporation or moisture infiltration, are the main drivers of pore water pressure variations in the soil. However, the matric component of soil suction appear to be the most influenced by the soil mass change. As a result, most changes in the soil suction can be considered to be quite representative by the change in matric suction. From the geotechnical engineering point of view, total suction measurements, in turn, can sometimes be used to represent changes in matric suction. This simplification is mainly true in the high-suction range when temperature fluctuations are small (Fredlund, Rahardjo, & Fredlund, 2012).

In practice, the free energy of the soil (i.e., total suction) is quantified by estimating either the relative humidity in the soil or by measuring the vapor pressure in the direct vicinity of the soil-water. For the case of total suction measurement, the direct approach focuses in measuring the relative humidity in the soil using a device called psychrometer, while it can also be indirectly approximated using the filter paper method (Fredlund, Rahardjo, & Fredlund, 2012).

#### 2.4.2.3.1 Chilled-mirror psychrometer

Psychrometers are used to quantify the total suction in the soil by measuring the relative humidity in the soil's air phase or the environment directly adjacent to the soil surface. This is done by measuring the difference in temperature between a non-evaporating surface (i.e., dry bulb) and an evaporating surface (i.e., wet bulb). This difference in surface temperatures, in turn, is associated with relative humidity.

In the case of a chilled-mirror psychrometer, a dewpoint measurement is performed under isothermal conditions in the confinements of a sealed container. Firstly introduced by Gee et al. (1992), and eventually commercialized by Decagon Co., the technique can be used for measuring suction in the range from 3 000 to 300 000kPa. Currently called the WP4-T, a schematic of the chilled-mirror Water PotentiaMeter can be seen in Figure 13.

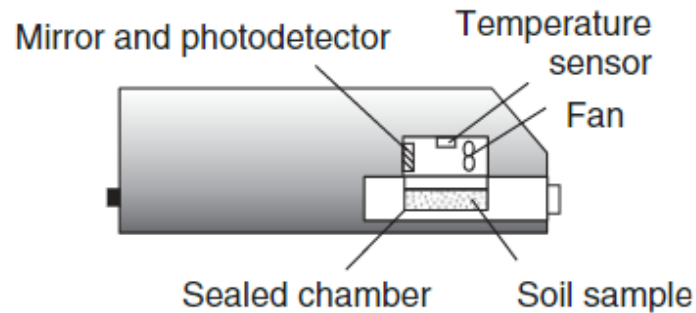


Figure 13: Schematic diagram of chilled-mirror WP4 Water Potential Meter (Fredlund et al., 2012; after Leong et al., 2003).

As can be observed from the figure above, the device consists of a sealed chamber with a fan, a mirror, a photo-electric cell, and an infrared thermometer. When operating the WP4-T, firstly, a plastic container of a diameter of 40mm is used to place the soil sample on top of a tray before introducing it inside the chamber. Once the chamber is closed, a fan-aided thermodynamic equilibrium is reached inside the chamber between the sample and its environment. A cooling system is used to minimize temperature increments on the surface of the mirror to the dewpoint temperature, eventually achieving condensation on the mirror. Immediately after, a photoelectric cell which was monitoring the mirror, ensures the dewpoint temperature measurement by a thermocouple at the first signs of condensation. Finally, an infrared thermometer measures the chamber's temperature, which is assumed to be the same as the soil specimen. Both the vapor pressure above the sample and the saturated vapor pressure, which are at the same temperature, are computed using the dewpoint and specimen temperatures, respectively. Kelvin's equation is used to calculate the soil's total suction (Fredlund, Rahardjo, & Fredlund, 2012).

Temperature control is essential when using the WP4-T due to the fundamental characterization of humidity in terms of temperature at which vapor condenses. Consequently, the differences in temperature between the sample and the dewpoint should be minimized. Further, prior to operation, the sample's temperature and the device's should be as close as possible; otherwise, long equilibration times and inaccurate results may occur (Leong, Tripathy, & Rahardjo, 2003).

The WP4-T is one of the most reliable tools used to measure total suction currently available. Its reliability of measurements of total suction of up to 300 000kPa, makes it especially useful when studying saturated soil's behavior in the residual soil suction range (Fredlund, Rahardjo, & Fredlund, 2012). However, in-situ measurements are not appropriate for the device due to the non-isothermal conditions in the field (Fredlund & Rahardjo, 1993).

### 2.4.3 Water storage and permeability

When dealing with engineering challenges associated with converting the oil sands tailings into a material with sufficient strength for reclamation purposes, proper consideration has to be taken due to their considerable volume change as suction is increased during their drying process. Questions associated with thickness deposition and drying behavior, which are usually addressed through soil-atmospheric modeling software, require saturated-unsaturated soil properties estimated from measured water content and soil suction relationships (i.e., the soil-water characteristic curve). As a result, adequate numerical modeling requires proper estimation of the soil property functions (Fredlund, Stone, Stianson, & Sedgwick, 2011).

#### 2.4.3.1 Soil-water characteristic curve

The soil-water characteristic curve (SWCC) defines the relation between the mass (and/or volume) of water in the soil and the energy state of the water phase (soil suction). As a result, it is the main source of soil information required for the analysis of seepage, shear strength, volume change, and air flow problems involving unsaturated soils (Fredlund, 1997; Fredlund M. D., 2000). In fact, both the permeability function and the water storage are associated with the SWCC. Consequently, the SWCC has become the most significant piece of information involving unsaturated soils (Fredlund, Rahardjo, & Fredlund, 2012). A typical SWCC is shown in Figure 14.

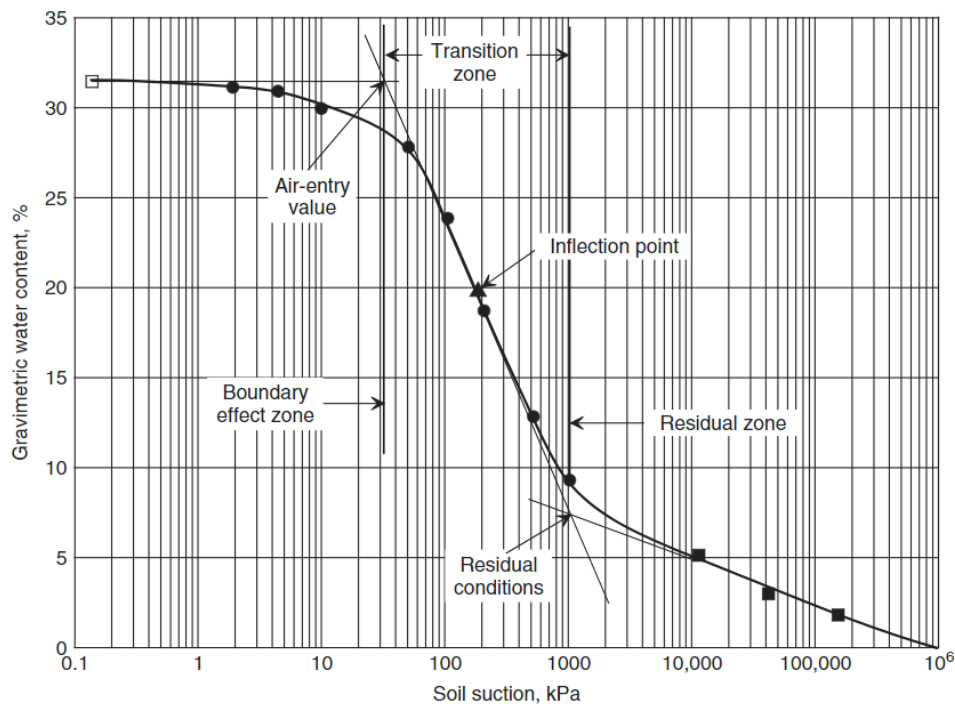


Figure 14: SWCC desorption branch with associated parameters (Fredlund et al., 2012).

The slope of the volumetric water content and the soil suction relationship defines the water storage. The air-entry value and the residual value for suction and water content are considered key transition points subdividing the saturation stages that the soil goes through during desaturation. Vanapalli et al. (1996) further described these three stages as:

- Boundary effect stage: In this stage the soil is fully saturated, while all the water menisci are continuous. This stage ends at the air-entry value.
- Transition stage: As the soil desaturates, the air starts entering the largest pores in the soil while the water content decreases significantly and suction increases. The water menisci area directly adjacent to the soil is no longer continuous, and is ever decreasing.
- Residual stage unsaturation: Starts when large increments in suction are associated only to small variations in water content. At the beginning of this stage, the water content is referred to as residual water content.

The grain size distribution of the soil governs the air-entry value, the residual water content, and the slope of the transition zone to some extent. As a result, sands have been reported to have much lower air-entry values than clays. On the other hand, in clays, the SWCC slope at high suctions ( $>1$  MPa) is related to their mineralogy and correlates with the plasticity index (Marinho F. A., 2005).

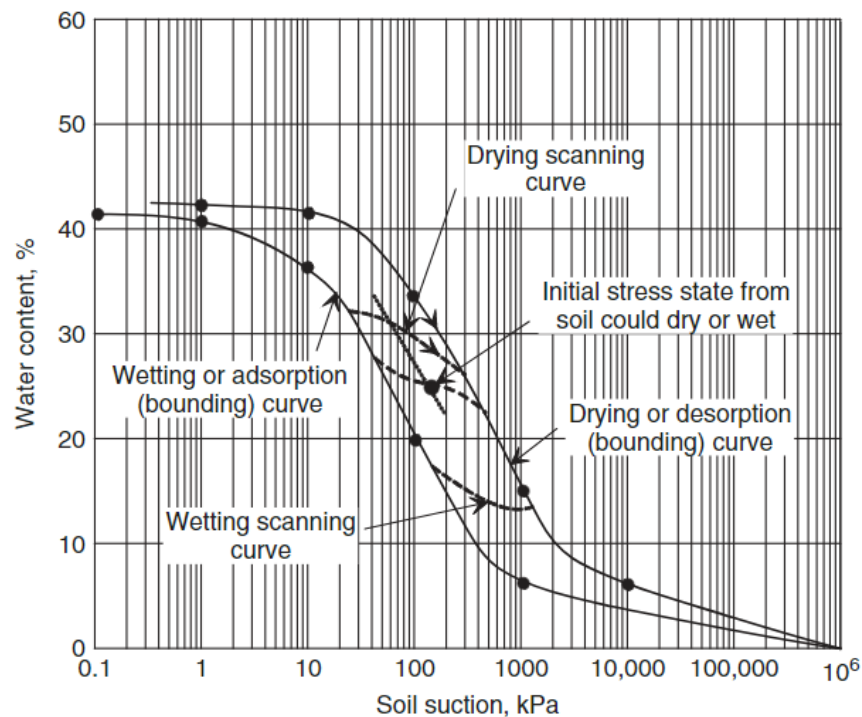


Figure 15: Relationship of initial stress to hysteresis loop of SWCC (Fredlund et al., 2012, from Fredlund, 2003).

As shown in Figure 15, during drying and wetting processes, the SWCC displays hysteresis, or different suctions for the same water content upon the soil's wetting or drying history. However, the desorption curve in the figure may not be located at the end point of adsorption due to air entrapment in the soil (Fredlund & Xing, 1994).

Even though identification of the air-entry value can be assisted by the changes in slope along the SWCC, the slope itself is dependent on how the amount of water in the soil is quantified. As soil suction is increased, different air-entry values associated to different suction values emerge, depending on how the amount of water is defined (Fredlund, Stone, Stianson, & Sedgwick, 2011). Special significance can be conferred to different variables used to designate the amount of water; however, proper interpretations have to be applied depending of the stage of the analysis (Fredlund, Wilson, & Fredlund, 2002). These variables are (Fredlund, Stone, Stianson, & Sedgwick, 2011):

- Gravimetric water content
- Volumetric water content (calculated using the instantaneous total volume)
- Volumetric water content (calculated using water volume referenced to original total volume)
- Degree of saturation

All amount of water designation above would yield similar geotechnical information if the soil did not undergo large volume changes as suction is increased; however, in the case of oil sands tailings, appropriate curves have to be plotted when evaluating soil property functions associated with numerical simulations. The instantaneous volumetric water content designation is used when calculating water storage, and degree of saturation is exceptionally linked to the development of a proper unsaturated permeability function for the soil (Fredlund, Stone, Stianson, & Sedgwick, 2011).

However, Fredlund (1967) showed that proper interpretation of unsaturated soil behavior associated with high volume changes require conventional SWCC measurements in conjunction with shrinkage curve information.

#### 2.4.3.1.1 Measurement of the SWCC

The measurement of the SWCC entails the direct or indirect measurement of the water content over the suction range. Volumetric water content and degree of saturation data are associated, and consequently, require gravimetric water content information, and often void ratio information. In addition, when dealing with suction measurements on soils, volume change information is recommended (Fredlund & Rahardjo, 1993; Fredlund M. D., 2000; Fredlund, 2006). This is especially true when other parameters are required, such as the air-entry value at saturation or the shrinkage limit. In the case of oil sands, in fact, due to their high volume variation during desaturation, the air-entry value is very difficult to estimate. The SWCC for oil sands tailings obtained by Fredlund et al., (2011) can be observed in Figure 16.

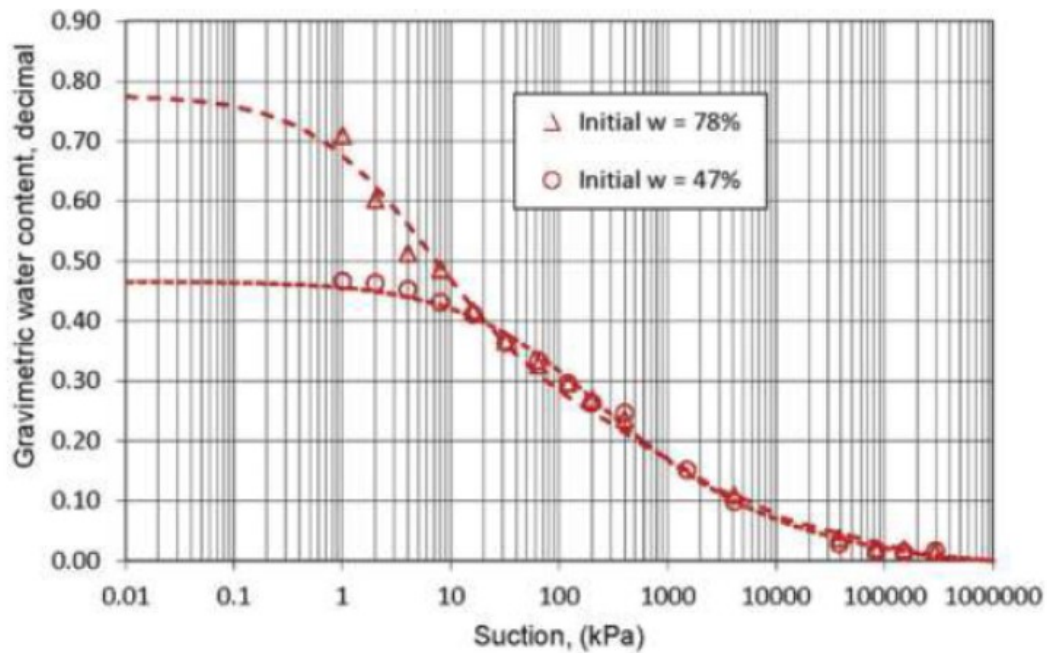


Figure 16: Gravimetric water content SWCC's measured on oil sands tailings (SFR=0.1) (Fredlund, Houston, & Caicedo, 2013).

The SWCC is determined through incremental measurements of soil suction in relation to its water content after equilibrium is achieved. However, not all methods of suction measurement are able to provide a complete range of data for all the suction range. As a result, a combination of measuring methods can be used for measuring the overall suction range for a specific type of soil. A summary of the direct and indirect methods used for suction measurements can be found in Table 2.

Table 2: Summary of suction measurements methods (Fredlund et al., 2012, adapted from Pan et al., 2010).

			Technique (Method)	Suction (kPa)	range	Equilibrium time
Direct measurement	suction	Matric	Axis translation technique Pressure transducer	0-1500		Hours minutes
Indirect measurement	suction	Osmotic	Pore-squeezing technique	0-15000		Days
Indirect measurement	suction	Total	Chilled-mirror hydrometer	150-300000		10 minutes
			Non-contact filter paper	all		7-14 days

The SWCC can also be estimated through the use of empirical equations that fit the experimental SWCC data of any soil under consideration.

#### 2.4.3.1.2 SWCC equations

Among all the equations available in the literature, the SWCC models proposed by Fredlund and Xing (1994) and van Genuchten (1980) are the ones that give more flexibility to the equation to best-fit the measured data (Leong & Rahardjo, 1997). In Ganuchten's (1980) case, a three parametric SWCC model was proposed as follows:

$$W_W = W_{rvg} + (W_s - W_{rvg}) \left[ \frac{1}{1 + [a\psi]^n]^m} \right] \quad [2.4.6]$$

where,  $W_W$  is gravimetric water content at a particular matric suction,  $W_{rvg}$  is residual gravimetric water content,  $W_s$  is saturated gravimetric water content,  $\psi$  is matric suction, and  $a$ ,  $n$ ,  $m$  are fitting parameters.

On the other hand, Fredlund and Xing (1994) proposed an analytical based model applicable for matric suction from 0 to 1 000 000kPa:

$$\theta = C(\psi) \frac{\theta_s}{\{\ln\{e + (\frac{\psi}{a})^n\}\}^m} \quad [2.4.7]$$

where,  $e$  is the natural number,  $a$  is an approximate value of air-entry value,  $\theta_s$  is saturated volumetric water content (porosity),  $m$ , and  $n$  are fitting parameters,  $\psi$  is matric suction, and  $C(\psi)$  is the correction factor.

The correction factor can be expressed mathematically as:

$$C(\psi) = 1 - \frac{\ln\{1 + \frac{\psi}{C_r}\}}{\ln\{1 + \frac{1000000}{C_r}\}} \quad [2.4.8]$$

where,  $C_r$  is the suction value corresponding to the residential water content.

As observed by Leong and Rahardjo (1997), in this case,  $C(\psi)$  can be assumed to be equal to unity without having a major impact to the initial section of the SWCC, which has the advantage of reducing the amount of parameters in the equation.

### 2.4.3.2 Shrinkage curve

The shrinkage curve plays an important role in the interpretation of the SWCC. It describes the relationship between the instantaneous void ratio and gravimetric water content in soils (Zhang, Wilson, & Fredlund, 2017), starting from initial high water content conditions to completely dry conditions.

In the case of clay soils, the point at which the desaturation process begins is in close proximity to the plastic limit. As a result, the air-entry value and its plastic limit can be correlated. In addition, the point at which any further drying does not result in any change in overall volume can be referred to as the true "shrinkage limit", which its associated gravimetric water content in turn is commonly associated with residual soil conditions (Fredlund, Stone, Stianson, & Sedgwick, 2011).

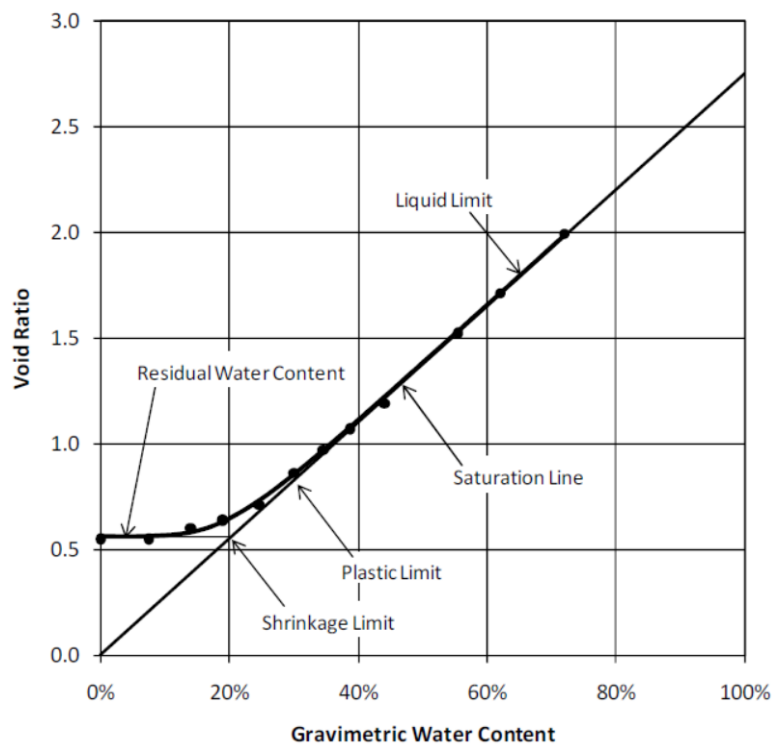


Figure 17: Shrinkage curve with its relationship to the Atterberg Limit classification properties (Fredlund, Stone, Stianson, & Sedgwick, 2011).

### 2.4.3.3 Unsaturated hydraulic conductivity

Water flow in a porous medium is governed by the hydraulic conductivity. As a result, its determination is essential when analyzing steady-state and transient flow problems. In general, during flow analysis, hydraulic conductivity is assumed to be constant in saturated soils; however, hydraulic conductivity can vary significantly when analyzing unsaturated soils, turning it into a mathematical formula (Fredlund, Rahardjo, & Fredlund, 2012).

In an unsaturated soil, permeability is dependent on both the water content and the void ratio in the soil, or in other words, it is dependent on soil suction (Fredlund, Xing, & Huang, 1994). In this context, permeability, or the hydraulic conductivity function, can be expressed in terms of relative permeability as follows:

$$k_r(\psi) = \frac{K(\psi)}{k_s} \quad [2.4.9]$$

where,  $k_r(\psi)$  is the relative permeability;  $K(\psi)$  is the permeability at a given suction, [m/d]; and  $k_s$  is the saturated permeability, [m/d].

Normally, due to the time-consuming nature and high cost of measuring the permeability function in the laboratory, it is usually estimated through the use of theoretical models associated with the SWCC. Through the years, many estimation models have been proposed to estimate the permeability function based on the SWCC; however, no unified model that can be used on all types of soils has been presented (Mualem, 1986).

#### 2.4.3.3.1 Hydraulic conductivity function models

Empirical models associate experimental data measurements and the saturated hydraulic conductivity that are best fitted. As the equations are related to suction or the volumetric water content, known SWCC parameters can be employed to determine the unsaturated hydraulic conductivity function (Leong & Rahardjo, 1997). A brief summary of some empirical models can be found in Table 3.

Table 3: Empirical models used to determine unsaturated hydraulic conductivity.

Model	Reference
$k = a\psi + b$	Richards(1931)
$k_r = \exp(-\alpha\psi)$	Gardner (1958)
$k = \frac{k_s}{a\psi^n} + 1$	
$k = k_s \text{ for } \psi \leq \psi_{AEV}$	Brooks & Corey (1964)
$k_r = \left(\frac{\psi}{\psi_{AEV}}\right)^{-n} \text{ for } \psi > \psi_{AEV}$	

In contrast, statistical (theoretical) models are derived of the combination of the SWCC data and a flow equation, resulting in an equation able to estimate the permeability function. More explicitly, models are constructed based on the SWCC and a relative permeability equation (Rahimi, Rahardjo, & Leong, 2015). Statistical models provide more flexibility than empirical models.

Statistical models are further subdivided in macroscopic and microscopic models, basing their differentiation on their assumptions about the soil's pore size distribution and their interpretation of the SWCC (Fredlund, 2006; Mualem, 1986). Some statistical models can be found in Table 4.

Table 4: Statistical models based on the SWCC and saturated hydraulic conductivity (Ebrahimi et al., 2004, as cited by Fredlund, 2006).

Models	References for SWCC			
	van Genuchten (1980)	Fredlund & Xing (1994)	Brooks & Corey (1964)	Campbell (1974)
Childs & Collis-George (1950)	-	$k_r = \frac{\int_{\psi}^{\psi_r} \frac{\theta(y) - \theta(\psi)}{y^2} \theta'(y) dy}{\int_{\psi_{AEV}}^{\psi_r} \frac{\theta(y) - \theta_s}{y^2} \theta'(y) dy}$	-	$k_r = \left(\frac{\psi}{\psi_{AEV}}\right)^{-2\left(\frac{2}{b}\right)}$
Burdine (1953)	$k_r(\psi) = \frac{1 - (\alpha\psi)^{n-2}[1 + (\alpha\psi)^n]^{-m}}{[1 + (\alpha\psi)^n]^{2n}}$ $m = 1 - \frac{2}{n}$	-	$k_r(\psi) = (\alpha\psi)^{-2+3\lambda}$	-
Mualem (1976)	$k_r(\psi) = \frac{\{1 + (\alpha\psi)^{n-1}[1 + (\alpha\psi)^n]\}^2}{[1 + (\alpha\psi)^n]^{1/2}}$ $m = 1 - \frac{1}{n}$	-	-	-

where,  $k$  is the unsaturated coefficient of permeability,  $k_s$  is the saturated permeability coefficient,  $k_r$  is the relative permeability,  $\alpha$  and  $\lambda$  are fitting parameters, and  $y$  is a dummy variable.

### 3 Methods and Materials

This section describes the experimental features of these tests, including oil sands tailings characteristics, set up, equipment used, and analytical methods involved in the calculations.

#### 3.1 Oil sands tailings characteristics

As a way to construct a baseline conducive of a proper analysis of the tailings dewatering behavior, a series of characterization tests were performed on the centrifuge tailings once they arrived to the laboratory. Centrifuged tailings were obtained from a pilot plant in Fort McMurray in 3 batches. An initial shipment of one 205L drum full of oil sand thickened tailings was initially received in October 2014, a shipment of eight 208L drums was received in April 2015, and a final 1000L bin was received in 2017 (See Figure 19).

Testing procedures were first performed by Mizani (2016) on the drums associated with the first and second batches of tailings. Samples extracted from these drums, corresponding to core samples #1, #2 and #3, respectively, were profiled with depth. The resulting geotechnical properties and particles size distribution (PSD) of the tailings are shown in Table 5 and Figure 18, respectively.

Table 5: Centrifuge cake sample identification and geotechnical properties (Mizani, 2016)

Sample ID	Date sample received	Sampling Procedure	Bottom (cm)	Top (cm)	Solid content (%)	PL	LL	Yield stress from stress growth (Pa)	Date tested
1	22/Oct/14	Core #1	0	6	46.63	-	-	-	
2	22/Oct/14	Core #1	6	12	46.18			-	
3	22/Oct/14	Core #1	12	18	46.19	35.8	68.9	-	
4	22/Oct/14	Core #1	18	24	45.26			1410	12/Nov/14
5	22/Oct/14	Core #1	24	32	45.17	36.2	68.9		
6	22/Oct/14	Core #1	69	79	44.73	-	-	857	12/Nov/14
7	22/Oct/14	Core #1	79	89	39.21	41.7	105.0	704	12/Nov/14
8	22/Oct/14	Core #2	12	21	45.17	37.6	84.5	1950	19/Feb/15
9	21/Apr/15	Core #3	0	12	57.54	-	-	2460	15/May/15
10	21/Apr/15	Core #3	12	24	60.60	-	-	1650	15/May/15

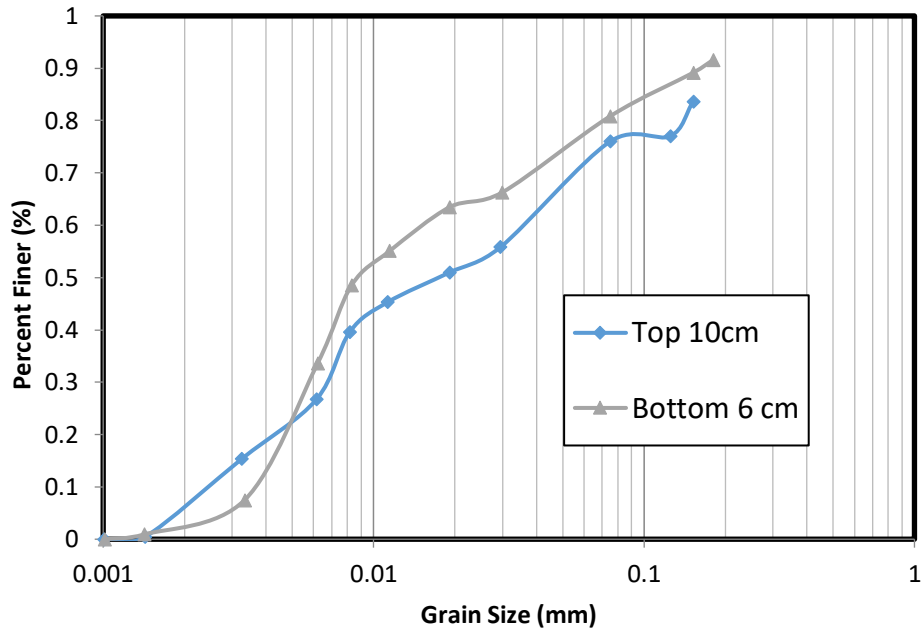


Figure 18: Particle size distributions of centrifuge cake from hydrometer and sieve analysis with depth (Mizani, 2016)

In addition, in order to further characterize the tailings, cake samples were submitted for analysis of pore-water chemistry and mineralogical composition. These results can be found in Appendix G.

Due to tailings settlement and consolidation, prior to deposition, bleed water was removed from the barrels before re-mixing it with the tailings using a drum mixer (Figure 20) in order to recover their initial solid content concentrations.

The solids content (geotechnical water content) of the re-mixed barrels ranged from 50% to 53% (100% to 90%). The centrifuge cake tailings had a LL and PL of 70% and 35%. Yield stress measured in a stress growth rheometer on a sample on the as-received tailings was 1.3kPa. The second batch of centrifuge cake tailings had a LL and PL of 65% and 39%.



Figure 19: Oil sands tailings delivery.



Figure 20: Drum mixer (Model No DLM150VGD, Mixer Direct)

### 3.2 Dry box experiment set up

A metal framed Plexiglas box was prepared with a base of 69.7cm x 63cm and a height of 100cm, similar to the experiment performed by Rozina et al. (2015), described in Simms et al. (2017) and Daliri et al. (2016), and shown in Figure 21.



Figure 21: Dry box set up

The box was designed with multiple ports at 16 cm height intervals, as shown in Figure 24, for Decagon 5TE sensors (Figure 25) and tensiometers (Model T5 from UMS).

Decagon 5TE sensors measure volumetric water content, temperature and bulk electrical conductivity. Volumetric water content is determined by the use of an in-probe oscillator running at 70MHZ which measures the dielectric permittivity of the soil, and relates it to the volumetric water content through the Topp equation. Electrical conductivity is measured separately by the screws on the sensor's surface while a thermistor in thermal contact with the sensor measures temperature. For the purpose of this experiment, factory calibrations were applied to all volumetric water content measurements. However, previous calibration experiments using gold tailings (Daliri, 2013) and thickened oil sands tailings (Innocent-Bernard, 2013) revealed low variation between the calibrated and measured data. Calibration results of Decagon T5E sensors for polymer-amended MFT and gold tailings can be found in Figure 22 and Figure 23, respectively.

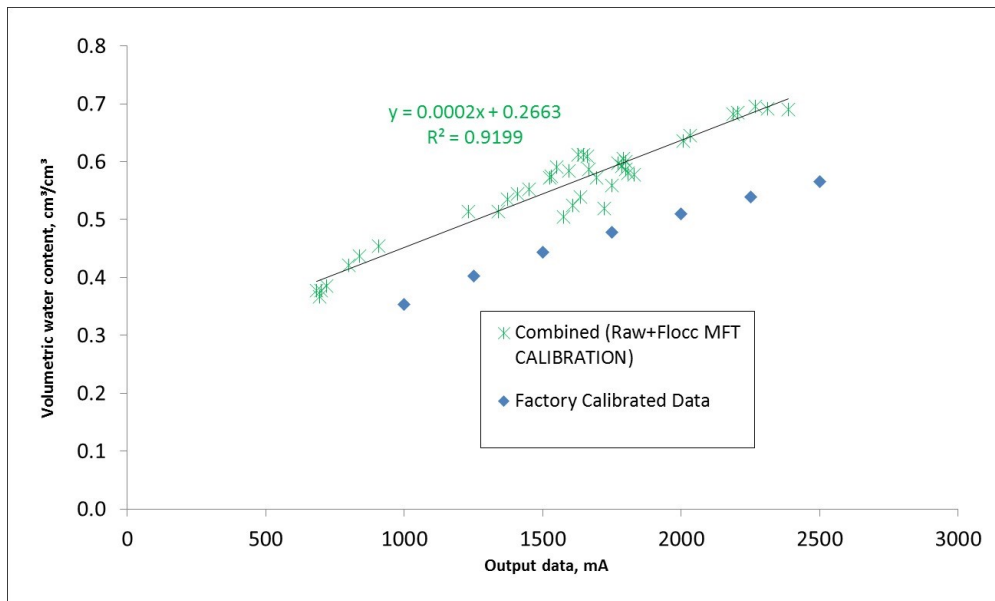


Figure 22: Specific calibrations for raw MFT and polymer-amended MFT (modified from Witteman, 2013)

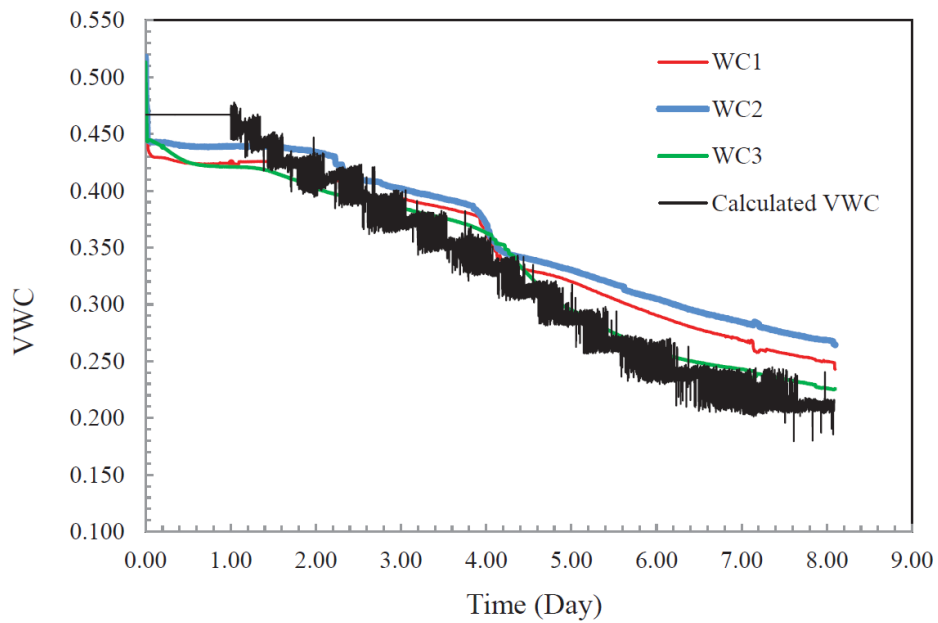


Figure 23: Comparison of calculated VWC and VWC obtained by Decagon 5TE sensors (Daliri, 2013)

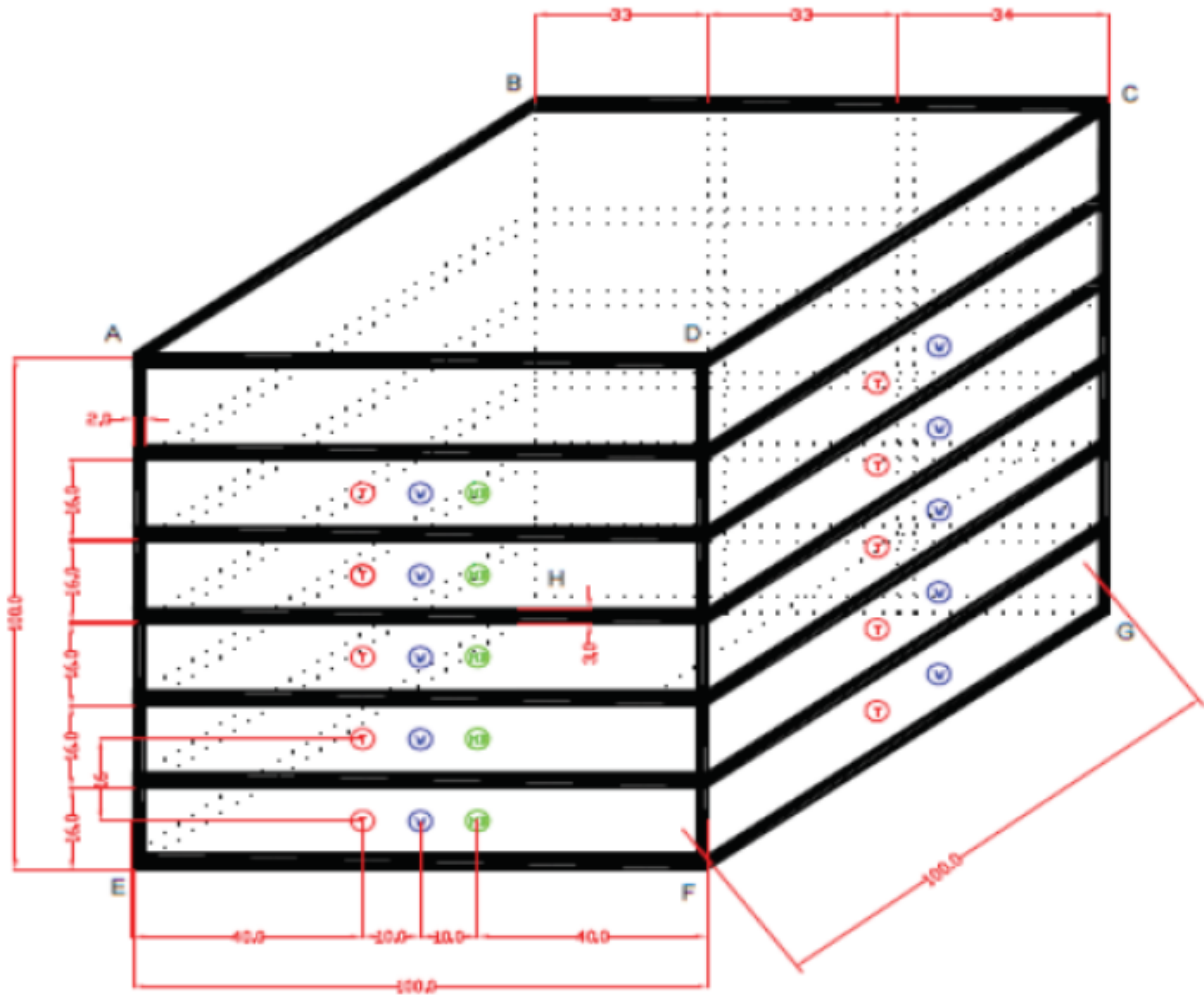


Figure 24: Schematic of sensor locations in dry box (Daliri, 2013).



Figure 25: Decagon 5TE sensor (Decagon, 2016).

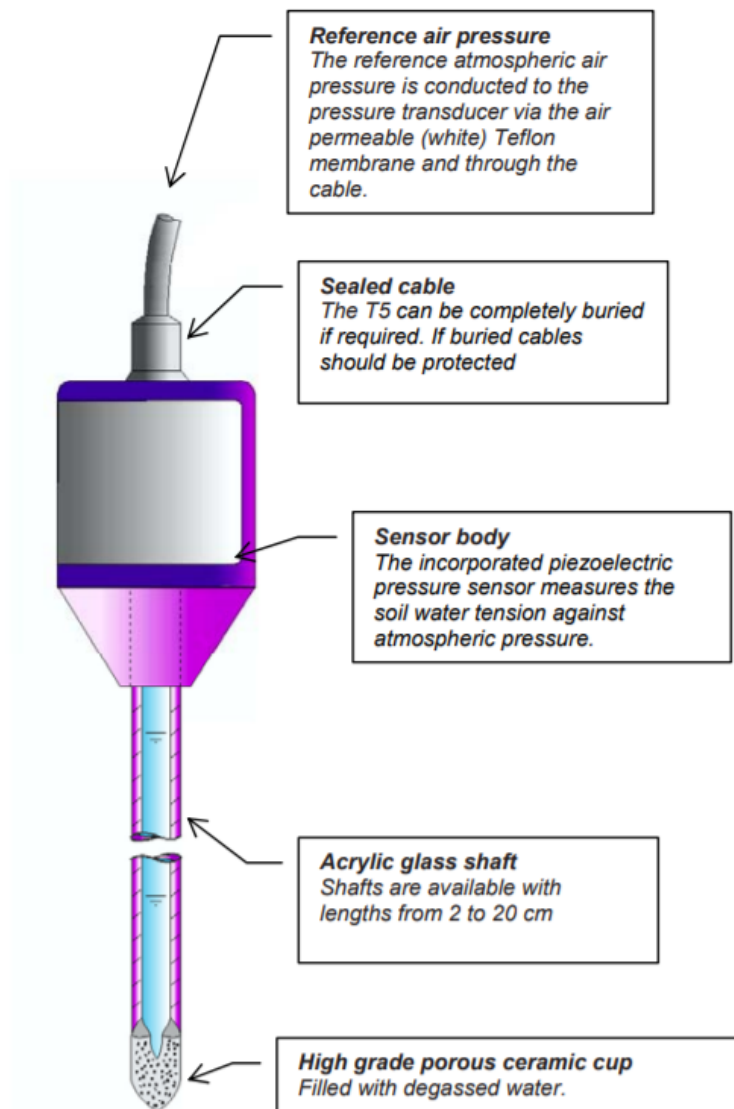
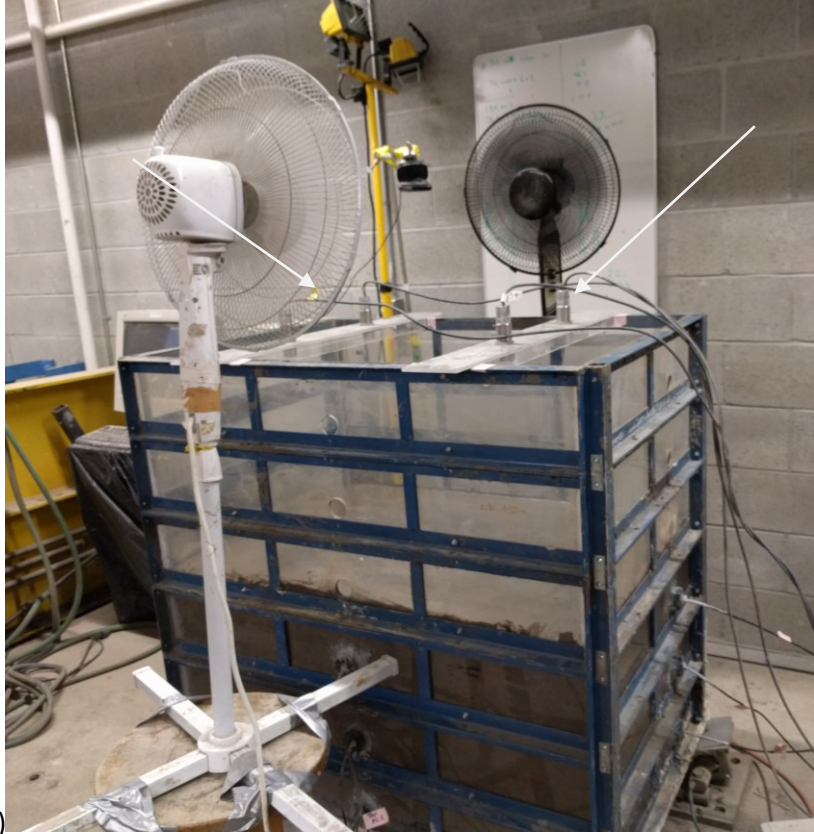
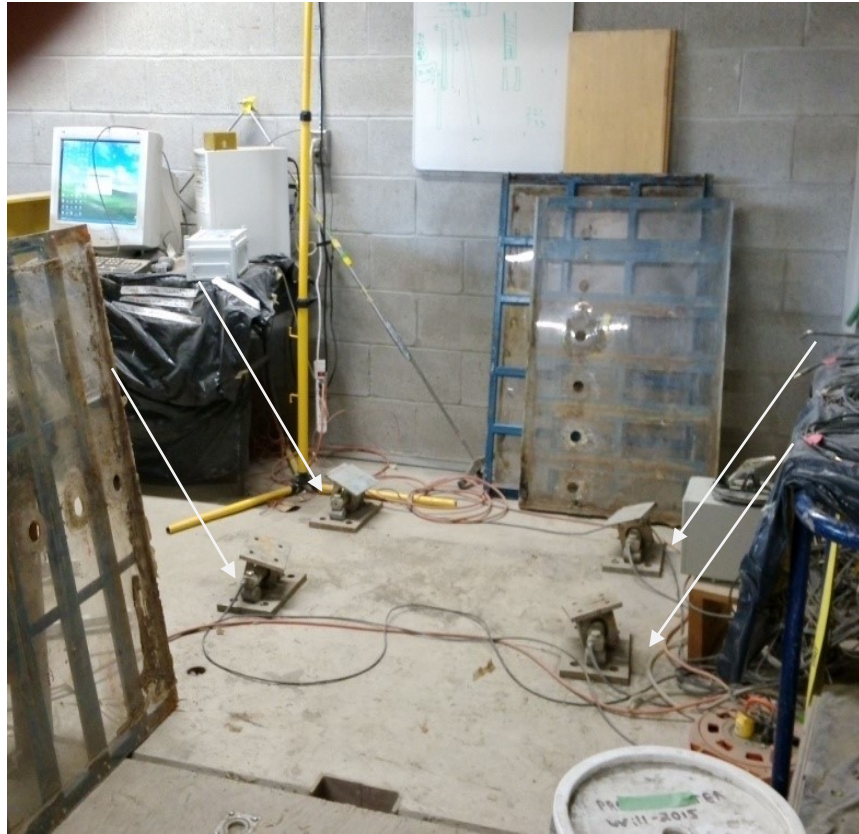


Figure 26: T5 tensiometer (UMS, 2009).

Prior to deposition, all tensiometers, which possess a measuring range of 85 to negative 100kPa with an accuracy of +0.5kPa, were pre-treated to ensure accurate suction measurements. During this process, the T5 sensor water reservoir and shaft was filled with de-aired distilled water while the tip was saturated with it for 30 minutes, all within the confines of a vacuum chamber. Both components, subsequently, were subject to consecutive 15-20 minute cycles of vacuum while in between cycles, a syringe was used to manually remove air bubbles from them. Once all discernable air bubbles were removed from the tensiometers, their reading responses were tested at different heights in a water column.



(a)



(b)



(c)

Figure 27: (a) Ultrasonic distance sensors, (b) load cells, and (c) tipping bucket rain gauge.

As shown in Figure 27, four ultrasonic distance sensors (Senix Model TSPC-30S1-232) were suspended from the top of the box to measure vertical displacement of the tailings. These sensors, which have a factory resolution of 0.1mm and a maximum range of 4.3m, were calibrated correlating their readings to known heights. The box sat on four balanced load cells to record its weight. Drainage was recorded through an orifice at the bottom of the box which lead to a valve and to a tipping bucket rain gauge located below the dry box.



Figure 28: Ultrasonic distance sensor (Senix, 2017)



Figure 29: RH/Temperature Easy Log sensor (OMEGA, 2018)

Geotextile was placed at the bottom of the box directly underneath the tailings, to prevent loss of solids through the drainage port. Four RH/Temperature sensors (Easy Log Model OM-EL-USB-2-LCD, Figure 29) were placed on the surface of the tailings, two on the beams at the top of the box, and once cracking occurred, one inside one of the cracks.

A webcam was suspended over the tailings to guide crack morphology measurement. Using the webcam pictures as a reference, crack depth, width, and length were recorded at 5cm intervals or less along each crack by hand with calipers, as represented in Figure 30 and Figure 31.

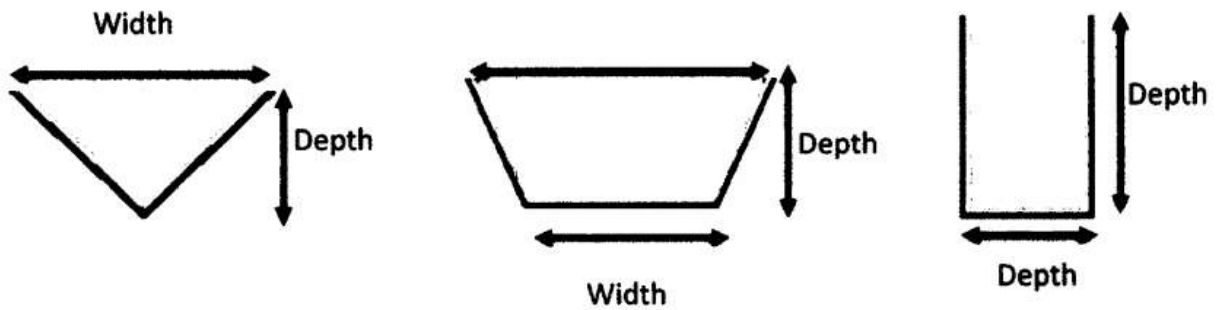


Figure 30: Crack measurement geometry (Innocent-Bernard, 2013).



Figure 31: Crack measurement techniques.

### 3.3 Evaporation

Actual evaporation was calculated from changes in weight of the dry box, subtracting water lost to drainage. Potential evaporation was estimated using recorded RH and temperature values and the Penman-Monteith equation:

$$P_E = \frac{\Delta(R_n - G) + \frac{\rho_a C_p (e_s - e_a)}{r_a}}{\Delta + \gamma \left( a + \frac{r_s}{r_a} \right)} \quad [3.3.1]$$

where,  $P_E$  is potential evaporation, [mm/d];  $R_n$  is net radiation, [ $\text{MJm}^2/\text{d}$ ];  $G$  is soil heat flux, [ $\text{MJm}^2/\text{d}$ ];  $\gamma$  is psychrometric constant, [ $\text{kPa}/^\circ\text{C}$ ];  $\Delta$  is the slope of saturation vapor curve, [ $\text{kPa}/^\circ\text{C}$ ];  $e_s$  is the mean saturation pressure, [ $\text{kPa}$ ];  $e_a$  is the actual vapor pressure from relative humidity, [ $\text{kPa}$ ];  $e_s - e_a$  is saturation vapor pressure deficit, [ $\text{kPa}$ ];  $r_s$  is soil surface resistance, [ $\text{s}/\text{m}$ ];  $r_a$  is bulk surface aerodynamic resistance to water vapor, [ $\text{s}/\text{m}$ ];  $\rho_a$  is density of air, [ $\text{kg}/\text{m}^3$ ]. and  $C_p$  is specific heat of air, [ $1.013 \times 10^{-3} \text{ MJ}/\text{kg}^\circ\text{C}$ ].

This experiment was performed indoors, therefore nullifying the radiation component of the equation. In addition, by assuming short crops as a simplification for a bare soil, equation [3.3.1] was further reduced to:

$$P_E = \frac{0.408\Delta(R_n - G) + \gamma \frac{900}{T + 273} u_2 (e_s - e_a)}{\Delta + \gamma(1 + 0.43u_2)} \quad [3.3.2]$$

where,  $u_2$  is wind speed, [ $\text{m}/\text{s}$ ];  $R_n$  is net radiation, [ $\text{MJm}^2/\text{d}$ ];  $T$  is temperature, [ $^\circ\text{C}$ ];  $\gamma$  is equal to  $0.665 \times 10^{-3} P$ ; and  $P$  is atmospheric pressure, [ $\text{kPa}$ ].

It is also possible to derive:

$$\Delta = \frac{4098(0.6108e^{\frac{17.27T}{T+273.3}})}{(T + 273.3)^2} \quad [3.3.3]$$

where,  $T$  is mean air temperature, [ $^\circ\text{C}$ ].

$$e_s = \frac{e^o(T_{max}) + e^o(T_{min})}{2} \quad [3.3.4]$$

where:

$$e^o(T_i) = 0.6108e^{\left(\frac{17.27T}{T+273.3}\right)} \quad [3.3.5]$$

$$e_a = \frac{\frac{e^o(T_{max})RH_{max}}{100} + \frac{e^o(T_{min})RH_{min}}{100}}{2} \quad [3.3.6]$$

$$G = C_s \frac{T_i - T_{i-1}}{\Delta t} \Delta z \quad [3.3.7]$$

where,  $C_s$  is soil heat capacity, [MJ/m<sup>3</sup>d];  $T_i$  is mean air temperature at time  $i$ , [°C];  $T_{i-1}$  is mean air temperature at time  $i-1$ , [°C];  $\Delta t$  is length of time interval, [d]; and  $\Delta z$  is effective soil depth, [m].



Figure 32: Evaporation test used to calculate wind function

The wind function in the Penman–Monteith equation was determined from back-calculation from measurements of evaporation in the dry box, filled to various heights with water (Figure 32). The evaporation was recorded over 3-4 days each time at ~65 and ~35 cm heights in conjunction with two Easy Log sensors on top of the dry box and the wind contribution generated by fans positioned at two ends of the drying box. The wind function, once calculated, was used in correlation with each specific layer's height to account for wind dynamics within the dry box. Results can be found in Table 6.

Table 6: Wind speed measurements

Initial Height (cm)	Water Level	Date	Air Velocity (m/s)			
			Top 1	Top 2	Top 1	Top 2
66.14	High	2017-05-06	7.16	7.09		
		2017-05-07	12.70	12.27	12.16	11.41
		2017-05-08	16.23	14.62		
		2017-05-09	12.55	11.66		
34.13	Low	2017-05-11	6.61	6.44		
		2017-05-12	7.30	6.53	7.02	6.34
		2017-05-13	5.67	5.57		

### 3.4 Sampling schedule and Monitoring

Surface samples were taken on a daily basis from the top 1cm tailings surface and also from the middle of the cracks to measure water content, total suction using a dewpoint hydrometer (WP4-T from Decagon), and osmotic suction (using the saturation technique). Surface samples varied between 1-5mm in thickness in order to fit into a sample container with a 40mm diameter used by the WP4-T hydrometer. Water content was measured from these samples afterwards, total organic content measurements followed. Osmotic suction samples were aimed to weight 5g each. In addition, edge of cracks and bottom of cracks samples were taken every three days. A schematic describing the location where the samples were taken can be found in Figure 33. The following link provides a time lapse of crack development in the thin-lift dry box: "<https://paulsimms0.wixsite.com/tailings-carleton>".

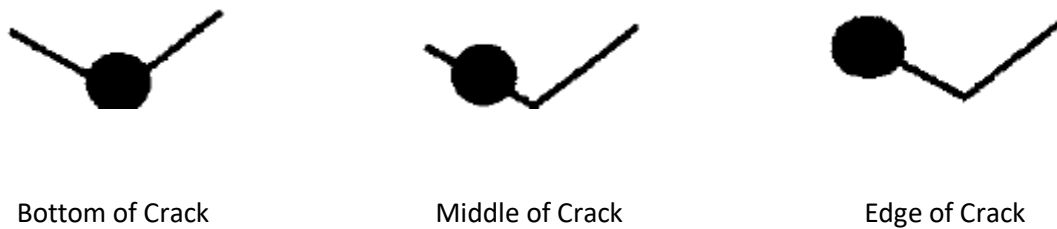


Figure 33: Crack sampling locations (Innocent-Bernard, 2013).

Crack volume measurements were taken on a daily basis, Ultrasonic distance sensor and load cells data was recorded every minute, tensiometer data and Decagon 5TE sensors data every five minutes, Easy Log USB sensors data every thirty minutes, and the webcam recorded an image every hour.

Finally, core sample profiles were extracted upon completion of each layer in order to further study their desiccation profile history.

### 3.5 Property analyses

During this study, a number of laboratory analyses were performed on the tailings samples in order to characterize them as time progressed. In the oil sands industry context, these properties are:

#### 3.5.1 Solid content

Defined as the ratio between the mass of all solids, including bitumen and other minerals, and the total mass, in the laboratory, the solid content is calculated by drying a sample in the oven for a period of 24 hours at 105°C. Then, the following mathematical expression can be used:

$$\text{Solid content} = \frac{M_s}{M_t} \times 100 \quad [3.5.1]$$

where,  $M_s$  is the mass of solids, and  $M_t$  is the total mass.

#### 3.5.2 Water content

Similarly, the water content is defined as the ratio between the mass of water and the total mass, as expressed by the expression:

$$\text{Water content} = \frac{M_w}{M_t} \times 100 \quad [3.5.2]$$

where,  $M_w$  is the mass of water, and  $M_t$  is the total mass.

In addition, the water content can also be expressed in relation to the total mass of solids, in which case is referred to as the gravimetric water content:

$$\text{Gravimetric water content} = \frac{M_w}{M_s} \times 100 \quad [3.5.3]$$

where,  $M_w$  is the mass of water, and  $M_s$  is the mass of solids.

Similarly to the solid content, both properties are determined by placing samples in an oven for a period of 24 hours at 105°C.

### 3.5.3 Total organic content

Similar to the method employed by Innocent-Bernard (2013), total organic content is determined by combusting samples, previously dried in an oven for a period of 24 hours at 105°C, at 500°C for 4 hours. This property is calculated as:

$$\text{Total organic content} = \frac{(\text{Dried weight} - \text{Ash weight})}{(\text{Total weight of sample})} \times 100 \quad [3.5.4]$$

where, *dried weight* is weight of sample after being dried at 105°C, and *ash weight* is weight of sample after being dried at 500°C.

### 3.5.4 Unit weight

This property is defined as the weight per unit volume of a material and it can be calculated as:

$$\gamma_m = \frac{G + Se}{1 + e} \gamma_w \quad [3.5.5]$$

where,  $\gamma_m$  is bulk unit weight,  $G$  is specific gravity,  $e$  is void ratio, and  $\gamma_w$  is unit weight of water.

### 3.5.5 Void ratio

The void ratio is defined as the ratio between the volume of voids to volume of soil particles. This is mathematically expressed as:

$$e = \frac{V_v}{V_s} \quad [3.5.6]$$

where,  $V_v$  is the volume of voids (air and water),  $V_s$  is the volume of solids.

In a saturated soil, all voids are filled with water; however, in the case of unsaturated soils, voids are either filled with air or water.

### 3.5.6 Atterberg limits determination

A fall-cone apparatus with a 30° cone was used to determine the LL and PL following the standard cone penetrometer test. With this objective, the specimen preparation procedure started by air-drying the tailings until the water content was low enough to ensure complete measurement of the water content-penetration depth relationship, as shown in Figure 34. Subsequently, a series of fall-cone penetration tests (3.6cm initial sample height) were carried out with specimens of increasing water content achieved through their mixing with distilled water. Finally, the LL and PL were calculated through the determination of the water content corresponding to the displacement penetration of 20 and 2 mm depth in the semi-log penetration-water content curve.



Figure 34: Air drying of tailings samples

### 3.6 Determination of SWCC

As part of the characterization analysis of the oil sands tailings, the entire range of the SWCC was measured. Through the use of the axis translation technique, the centrifuge tailings were placed on a modified "Fredlund" SWCC device (GCTS Testing Systems) for matric suction values less than 500kPa, while drier samples were analyzed using a WP4-T hydrometer for total suction measurements. Between each stage in the axis-translation test, weight variations were recorded using a scale, vertical variations were estimated using a non-contact ultrasonic displacement sensor, cracks volumes were estimated by hand, using calipers, and checked using a camera over the sample. Total suction measurements were performed on air-dried small tailings samples (<100g), followed by water content measurements on the oven. Some of the equipment used can be seen in Figure 35.

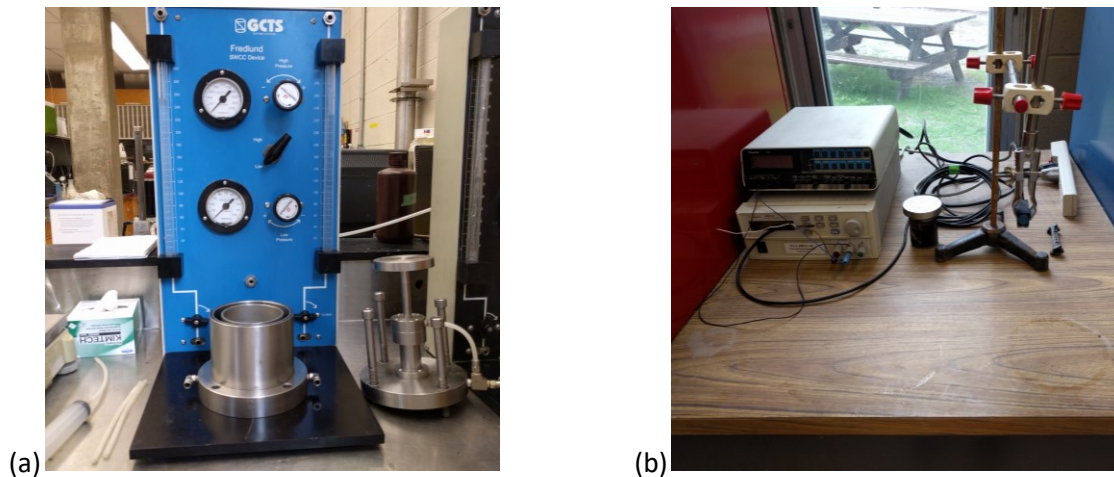


Figure 35: (a) "Fredlund" SWCC device, and (b) non-contact displacement sensor

## 4 Results

This section focuses on the thick (2016) and thin-lift (2017) dry box tests results and interpretation. In addition, a comparison between both deposition tests is included.

### 4.1 Thick-lift dry box test

After the mixing of the tailings, the material was deposited into the dry box using plastic buckets each having ~7kg of material, until a layer of 50cm was achieved. In addition, a slump test and a solid content test were performed every 10 buckets for quality control purposes. The first layer, deposited the 13<sup>th</sup> of June, started with an initial average GWC of 89% (53% solids), while the second layer, deposited the 2<sup>nd</sup> of September, started with an initial average GWC of 65% (61% solids). Each deposition lasted two and a half and two hours, respectively. A time lapse of one of the deposition processes is provided at the following link: "<https://paulsimms0.wixsite.com/tailings-carleton>". Additional details concerning the deposition can be found in Appendix A and B.

#### 4.1.1 First Layer deposition

Figure 36 shows the temperature, RH and dewpoint profiles recorded by the Easy log sensors located above the tailings. Overall, RH varied from 35 to 65%, an increasing trend also observed in the dewpoint values. These results are expected as the summer season settles during that time of the year. Temperature, on the other hand, stayed steady for most of the test, varying between 20 to 30°C.

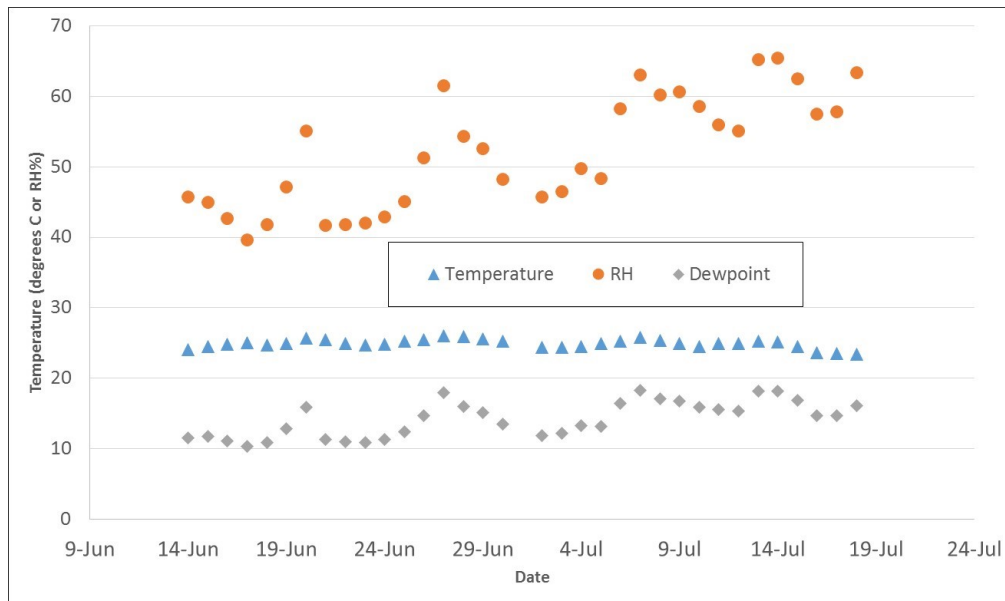


Figure 36: Temperature, RH and dewpoint profiles above the tailings - First layer

Daily evaporation was calculated based on the weight variation of the dry box provided by the load cell data and the drainage recordings from the tipping bucket at noon. As can be seen in Figure 37, the actual evaporation was approximately equal to the potential evaporation for most the test. However, towards the end, actual evaporation declined below the potential evaporation.

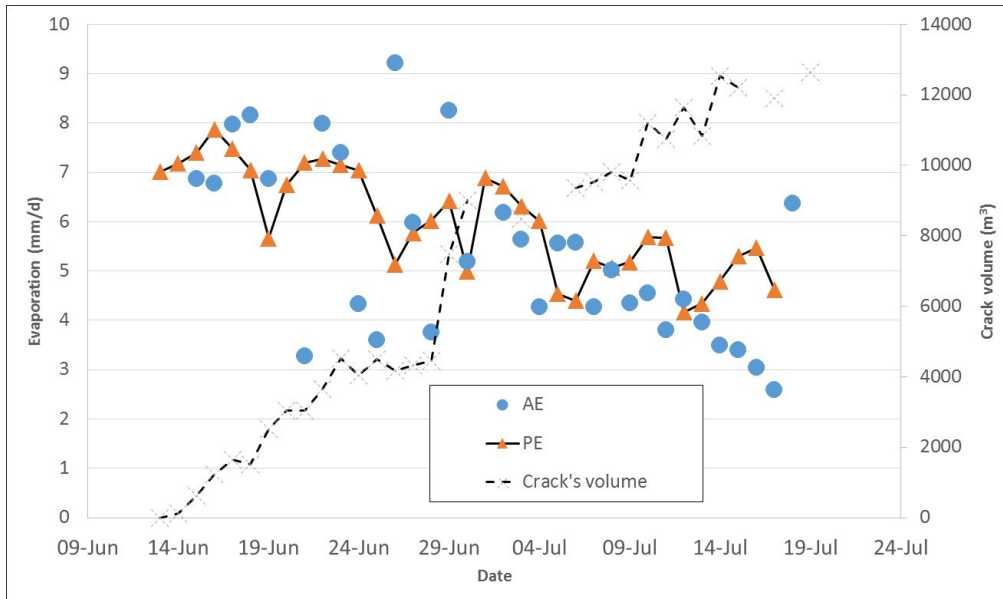


Figure 37: Actual and potential evaporation - First layer

The average GWC of the dry box was calculated in association with the dry box weight data and drainage measurements, and steadily decreased throughout the experiment, as seen in Figure 38. In comparison to the overall layer; however, the tailings surface samples leveled off, reaching almost a constant value by the end of June.

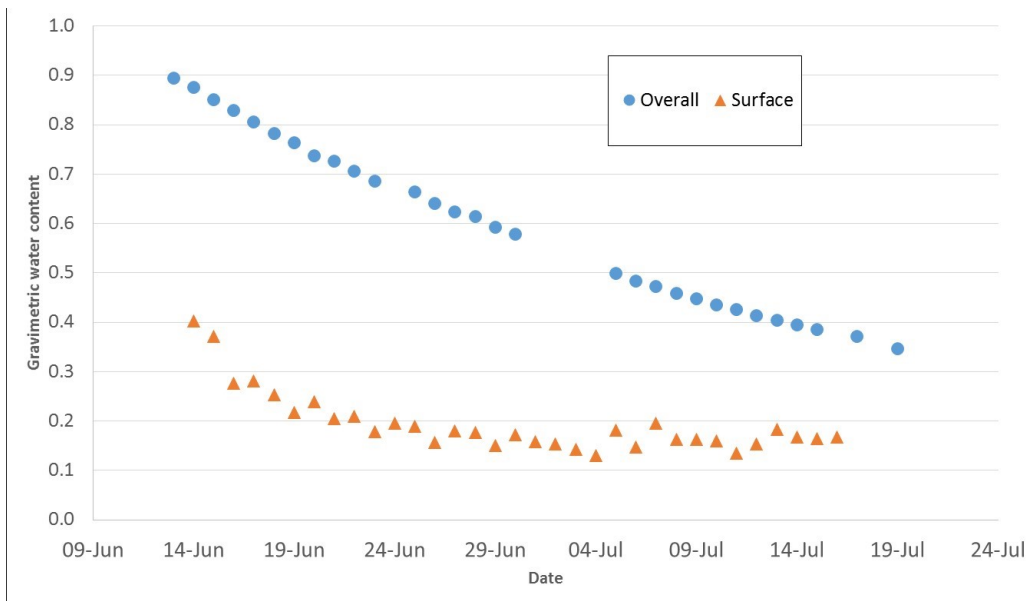


Figure 38: Gravimetric water content - First layer

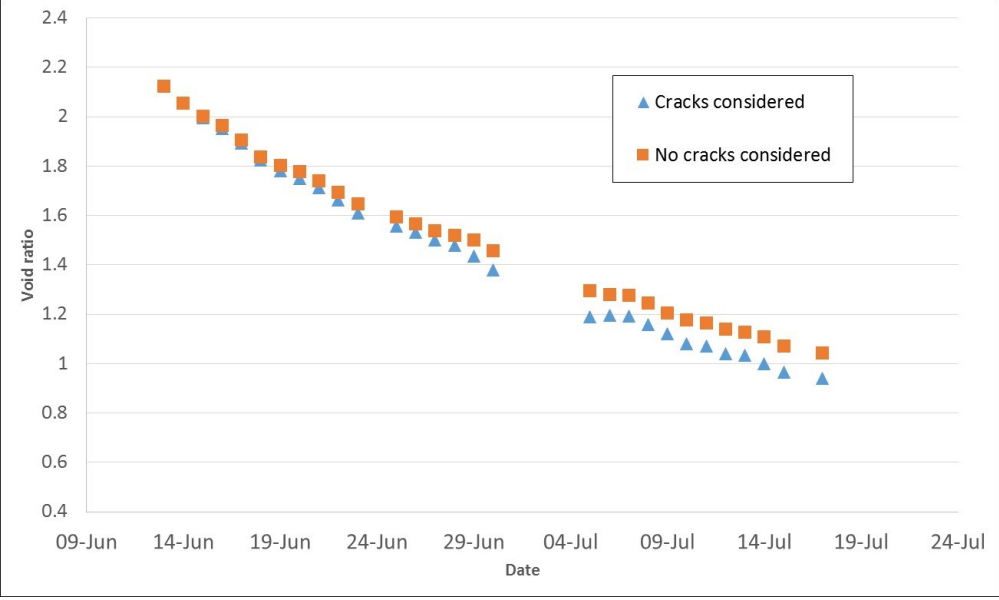


Figure 39: Average void ratio - First layer

The void ratio was calculated based on the senix distance sensors readings as well as the crack volume measurements and its progression can be found in Figure 39. As expected, void ratio values did not present a considerable difference when taking into consideration crack volumes, however, as the cracks grew in size, the variation on readings did as well.

Figure 40 shows the variation in average degree of saturation.

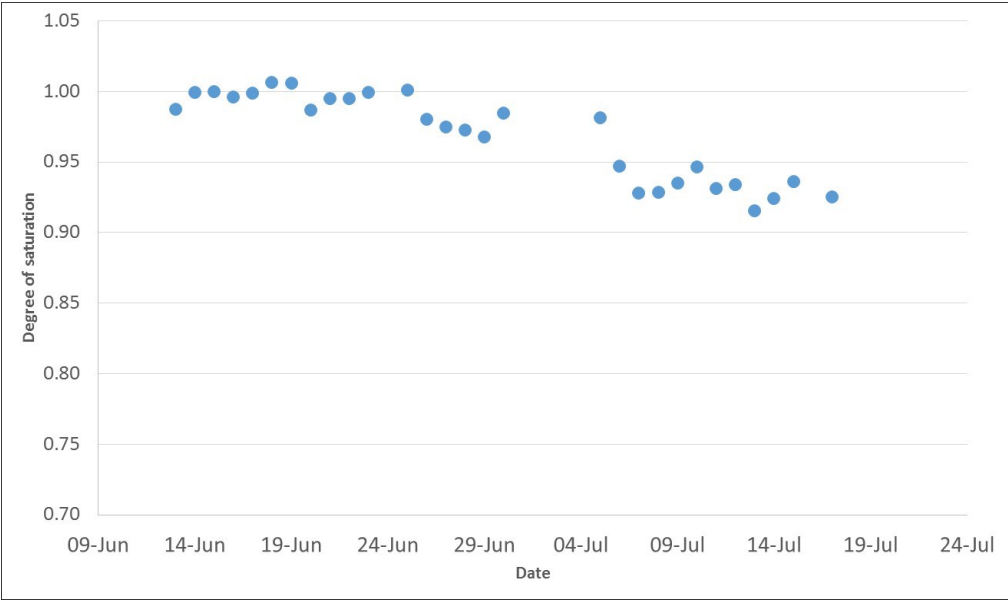


Figure 40: Average degree of saturation - First layer

In addition, void ratio (considering cracks) was plotted with the average GWC of the layer to generate an apparent shrinkage curve, shown in Figure 41. This layer was approaching but did not reach the shrinkage limit before the next layer was placed.

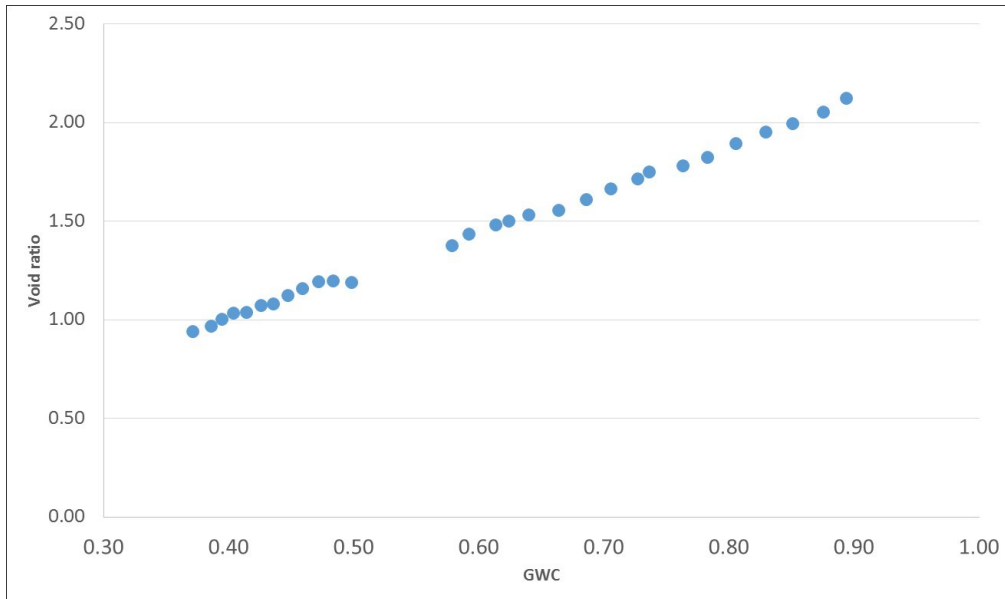


Figure 41: Shrinkage curve - First layer

Crack development, shown in Figure 42, suggests an uninterrupted linear progression throughout the first layer of the experiment.

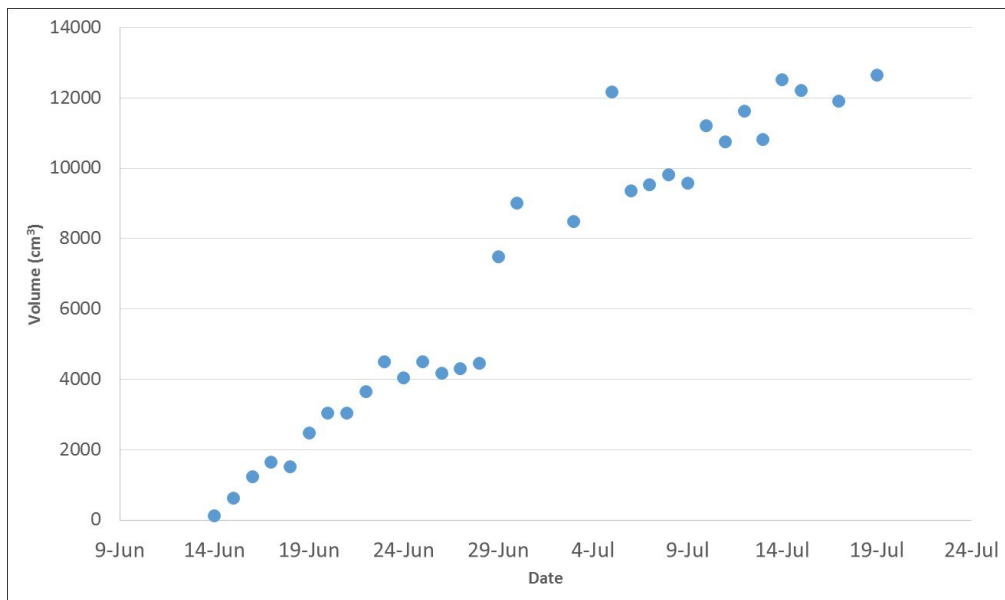


Figure 42: Crack development - First layer

Figure 43 presents the solid content progression over time from samples taken at various locations on the top of the tailings.

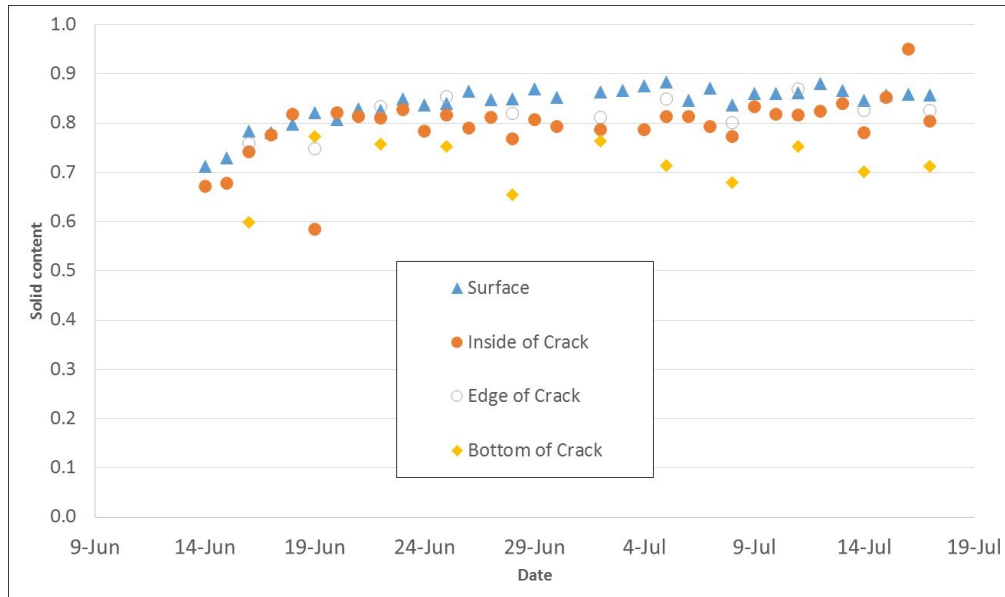


Figure 43: Surface cracks solid content - First layer

Samples taken from the top 1cm of the surface of the tailings, middle of crack, edge of crack, and bottom of crack, as described in chapter 3, were analyzed for total suction using the WP4-T dewpoint hydrometer. As observed from the results, in Figure 44, the suction values remained the highest at the surface, constantly increasing as the layer dried up. Similarly, suction values at the edge of the cracks showed a sharp increase in suction, in some instances even surpassing the surface values. However, the measurements taken from the bottom of the cracks were always the lowest, as they corresponded to the recently surfaced underlying material.

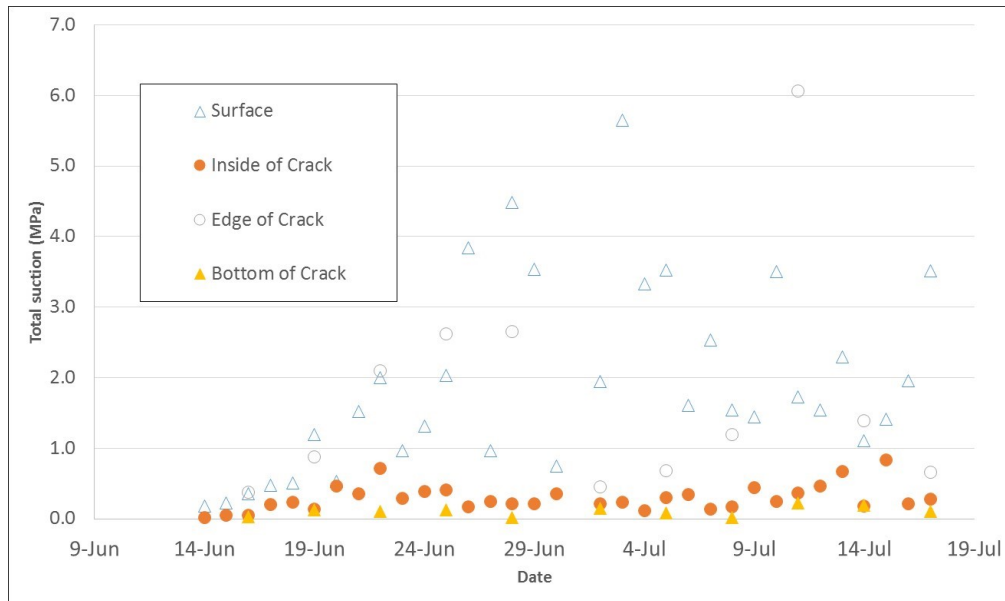


Figure 44: Surface cracks total suction - First layer

The volumetric water content readings suggest an initial sharp decrease in the moisture content at the bottom of the layer due to consolidation, which is also evident in the drainage data at the beginning of the experiment (Figure 45 and Figure 46). At later times, desiccation became the dominant mechanism for water removal, as reflected by the decrease in VWC higher in the tailings.

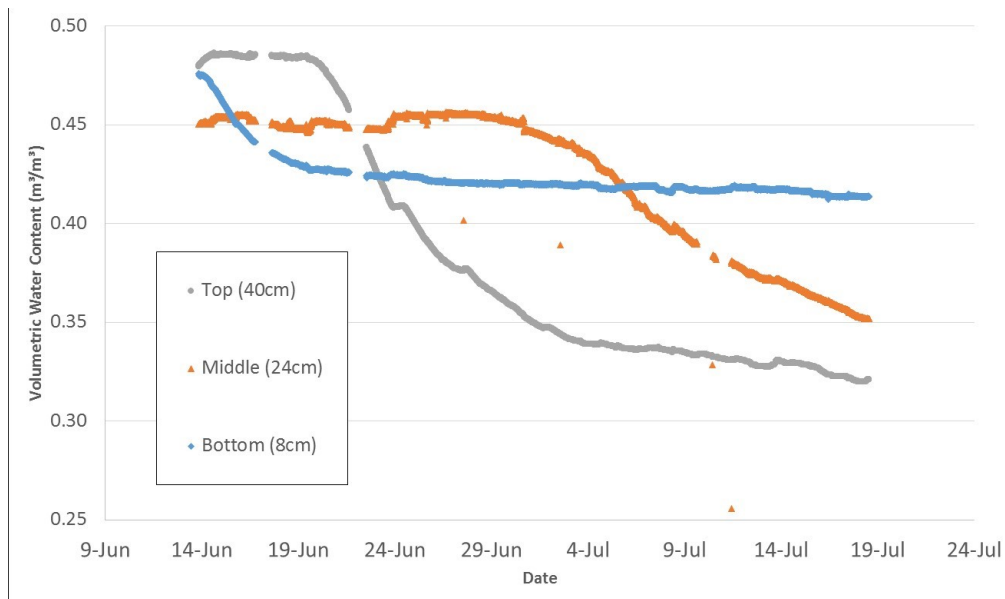


Figure 45: Volumetric water content at various heights - First layer

Figure 46 shows the drainage recorded throughout the test.

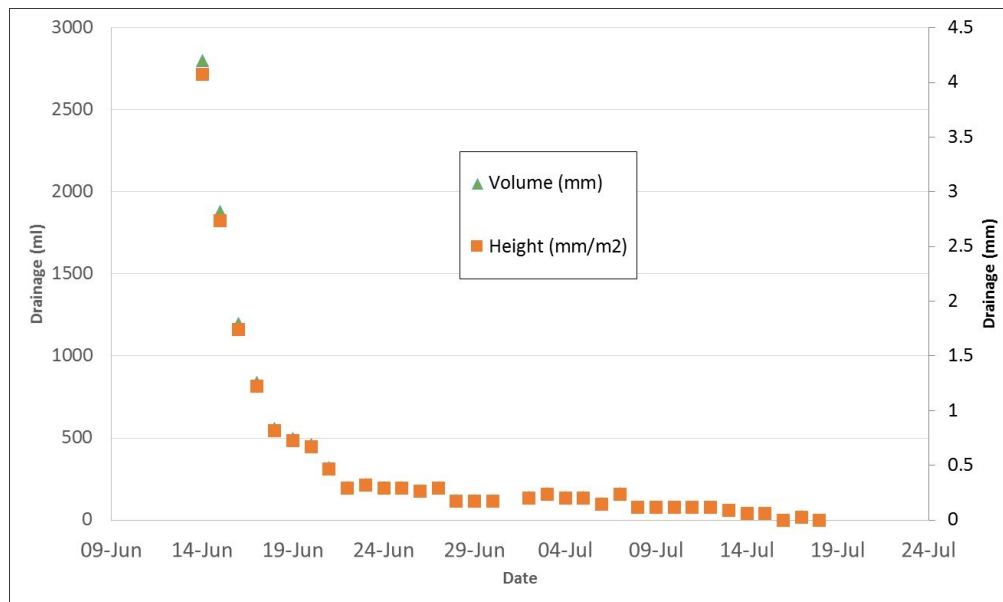


Figure 46: Drainage - First layer

Matric suction measurements were obtained from the tensiometers located along the height of the dry box. The top and middle levels of the layer recorded a high increment in matric suction within the first 3 weeks of the experiment, reaching 105kPa for the top tensiometer, and 60kPa for the middle one (Figure 47). On the other hand, matric suction levels were recorded as very low for most of the experiment at the bottom level until the very end. This information in conjunction with the sharp decline of VWC data at the beginning of the experiment (observed in Figure 45) further supports the consolidation hypothesis as being the main driver of water removal at the bottom of the tailings.

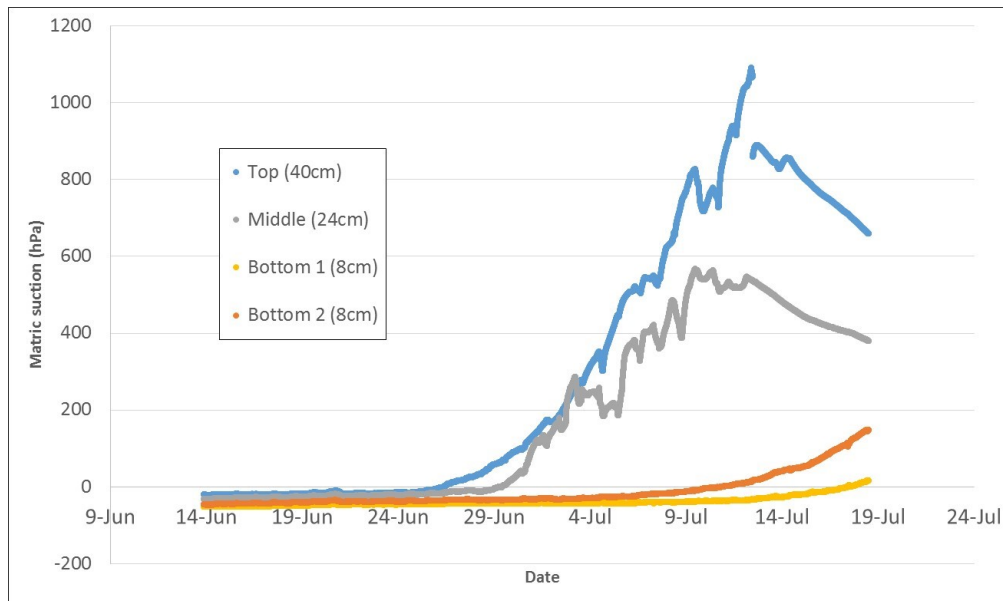


Figure 47: Matric suction at various heights - First layer

#### 4.1.1.1 Surface samples

Figure 48, shows osmotic and total suction values measured from surface grab samples. Two notable observations are that i) osmotic suction formed the largest component of total suction, similar to observations made by Innocent-Bernard et al. (2014) in thickened oil sands tailings, and ii) both total and osmotic suction reached a maximum value about July 3<sup>rd</sup> or 4<sup>th</sup>, thereupon decreasing to a more or less constant value (~3MPa). This correlates with the leveling off of surface gravimetric water content and the end of oscillating actual evaporation. This decrease in osmotic suction is possibly due to a backdiffusion effect when the evaporation rate from the surface decreased. From previous studies on oil sands tailings (Simms et al., 2017; Rozina et al., 2015), surface evaporation is expected to decrease when total suction in the grab samples reaches 5MPa. However, the overall evaporation rate did not decrease below the potential ratio until some days later. Another possibility is that the limit in osmotic suction signifies that the solubility limit was reached. This conclusion is further backed up by visual inspection of the tailing's surface, shown in Figure 49, which shows the formation of white precipitate on the surface after June 20<sup>th</sup>.

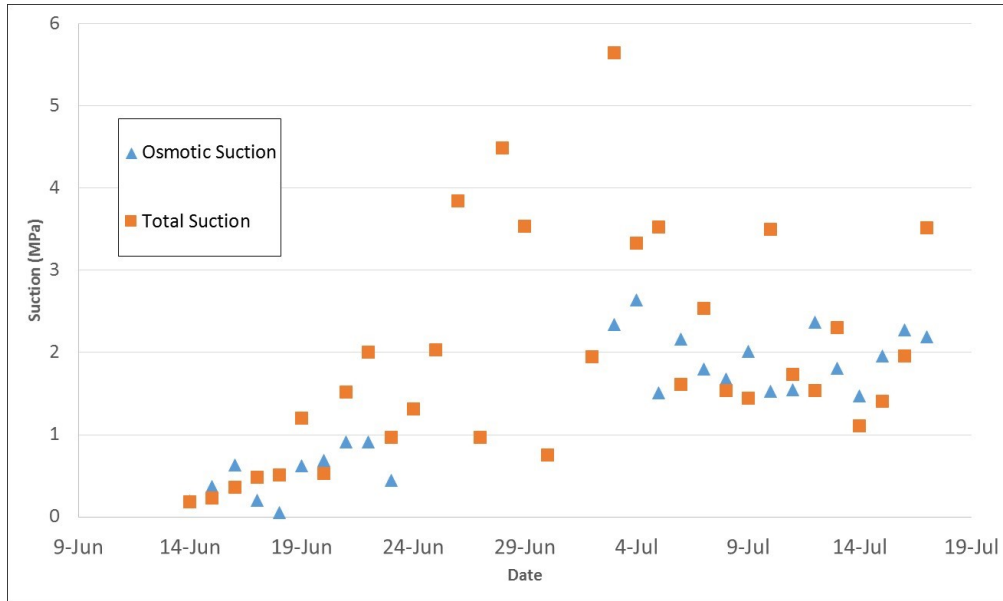


Figure 48: Surface sample total and osmotic suction - First layer

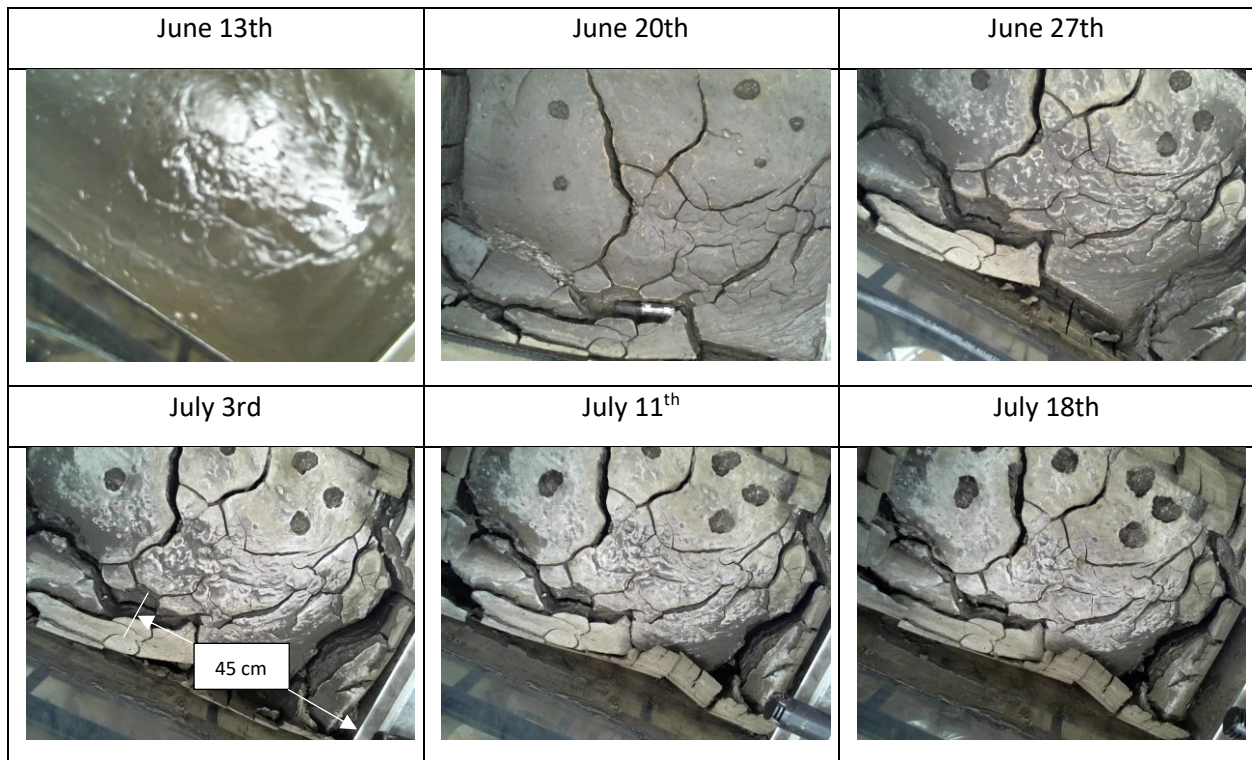


Figure 49: Crack progression - First layer

#### 4.1.1.2 Core sample analysis

Upon completion of the first layer, a core sample was extracted in order to further study the desiccation history of the layer along its height (Figure 50). The sample is numbered from top to bottom.



Figure 50: Core sample, top (left hand-side) to bottom (right hand-side) - First layer

As expected, the GWC was the lowest close to the surface, gradually increasing in the downward direction (Figure 51). A decrease in the GWC after the 16 height interval may indicate combined influence of consolidation and desiccation, whereas the very bottom of the core appears to have mostly been influenced by consolidation.

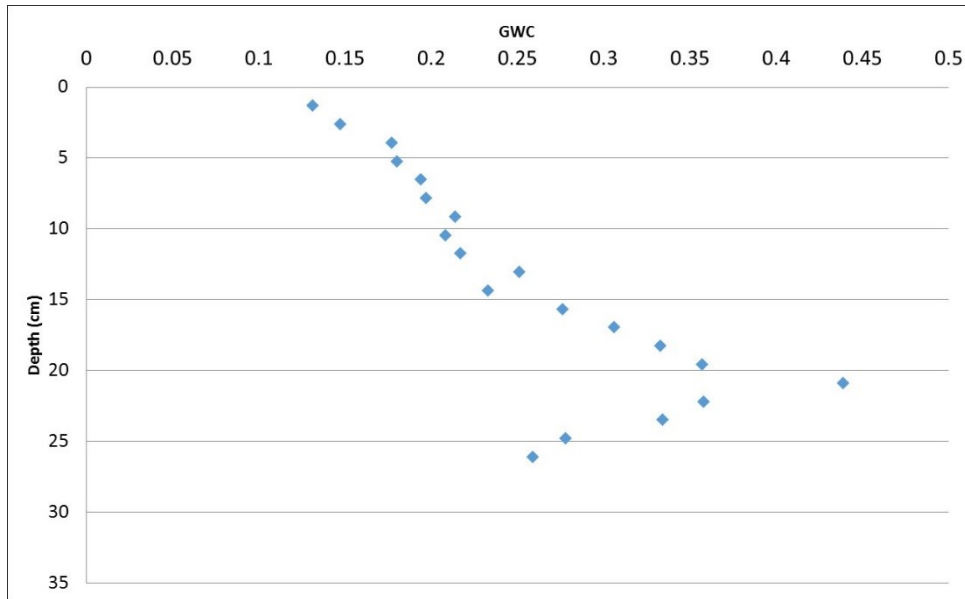


Figure 51: Core sample gravimetric water content profile - First Layer

The relative amount of consolidation and desiccation was also assessed using the UNSATCON software, using input parameters associated with polymer-ameded MFT, similar to the ones used by Rozina et al. (2015). In this context, the resulting UNSATCON predictions (Figure 52) showed a similar pattern in terms of the gravimetric water content profile, although showing a somewhat more wetter profile than in the experimental data (Figure 51). This divergence between the figures may be explained by a large difference in the compressibility parameters between the tailings or a large variation in the degree of consolidation. However, in terms of shape, the model predictions were found to be satisfactory, as it further confirms the consolidation effects from dewatering at the bottom of the layer.

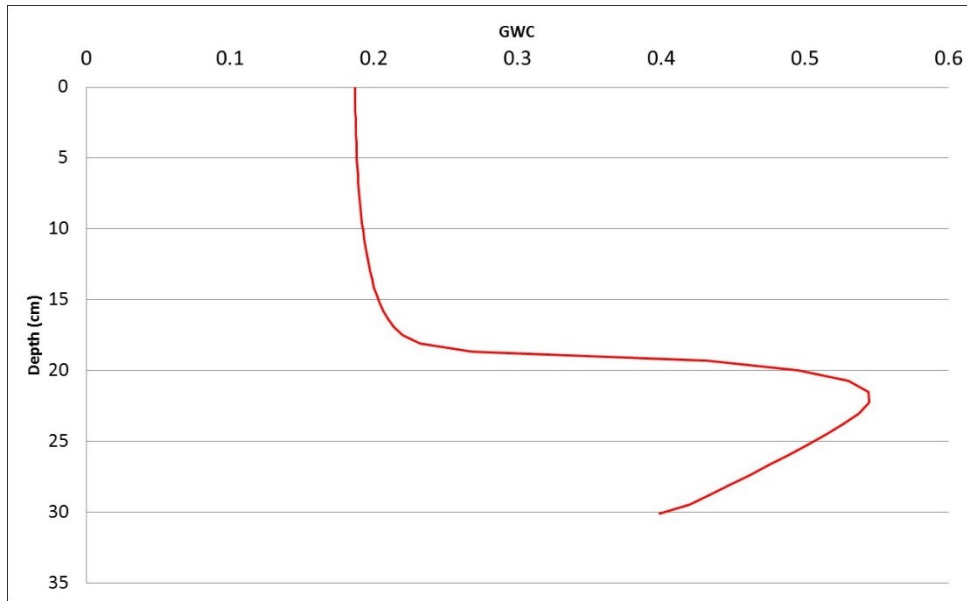


Figure 52: UNSATCON prediction - First layer

High levels of total and matric suction at the surface level were reported, both decreasing dramatically with depth (Figure 53). High proportions of osmotic suction compared to total suction, also seen in the surface samples, illustrate the transport of dissolved mass to the surface of the tailings and its role in reducing evaporation.

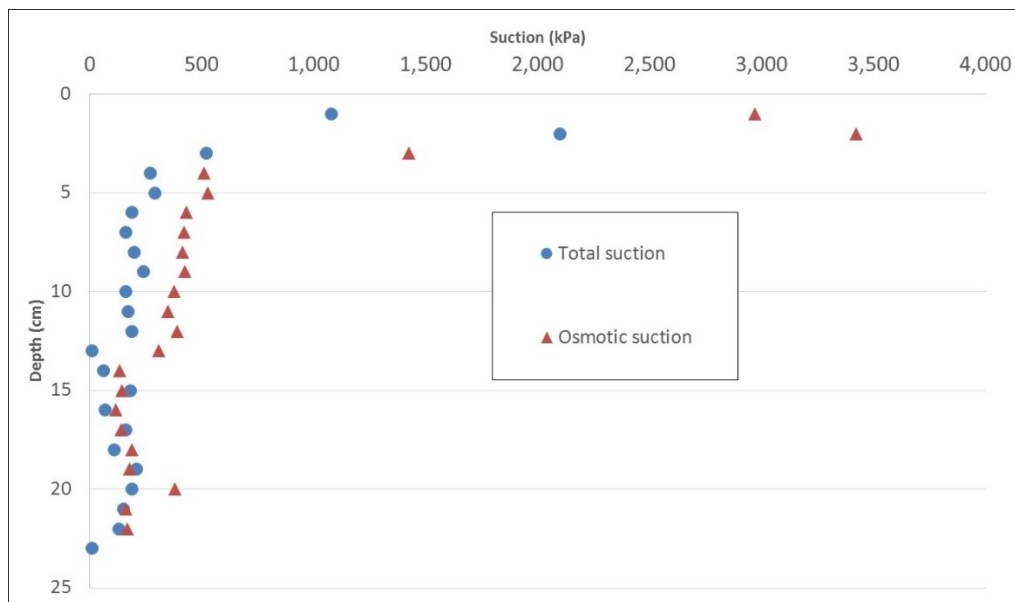


Figure 53: Core sample suction profile - First layer

#### 4.1.2 Second layer deposition

After the first layer reached an average GWC of 35%, (74% solids), the second layer (50% solids) was added. Following the same re-mixing process used for the first layer, the new tailing material was deposited on top of the first layer. After the end of the two-hour deposition process, the total height of the tailings was 80.4 cm, of course some of the added tailings flowed to existing cracks and some consolidation would occur during the two hours of deposition.

Figure 54 shows the temperature, RH and dewpoint profiles recorded after deposition. Consistent with the previous layer, temperatures stayed between 20 to 30°C, on a decreasing pattern. RH and dewpoint values followed this pattern as well. These results were also expected, as environmental conditions shifted to the fall season.

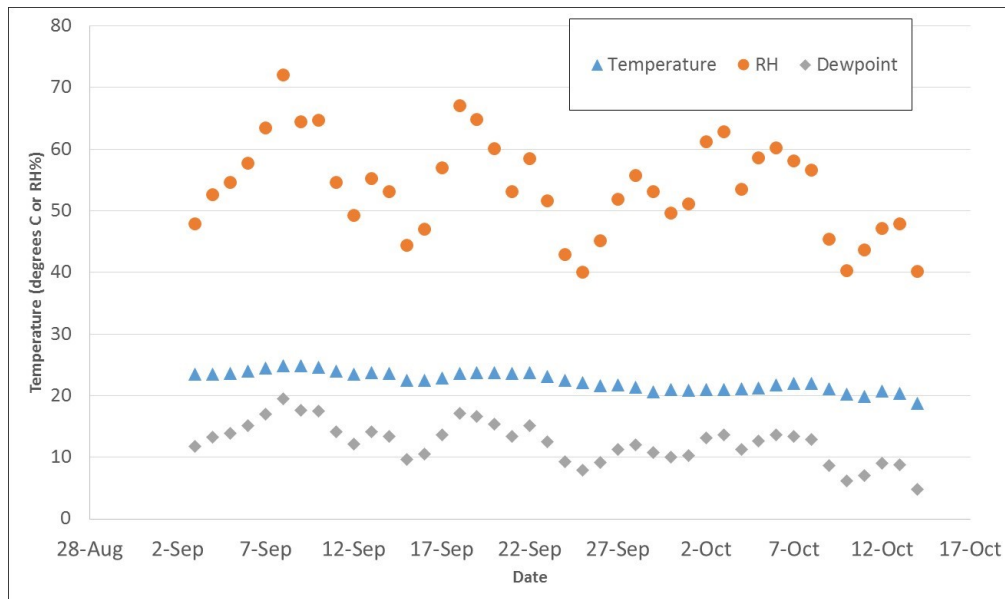


Figure 54: Temperature, RH and dewpoint profiles above the tailings - Second layer

A few weeks into the experiment, there was a malfunction with the scale which resulted in the loss of some of the data of the experiment. However, based on the available information, the actual evaporation rate was found to oscillate between 2.5 and 6mm/d, as can be seen in Figure 55. The available evaporation data suggests that  $A_E$  began to decrease below  $P_E$  around Sept 30<sup>th</sup>.

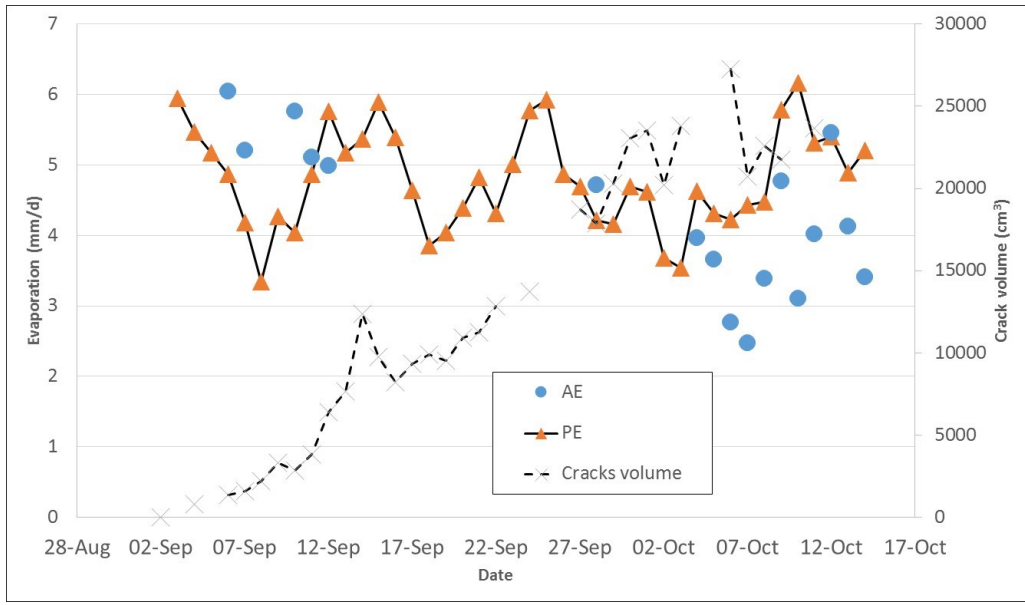


Figure 55: Actual and potential evaporation - Second layer

Similar to the experience in the first layer, the GWC at the surface (top 1cm) also presented a sharp decline in its moisture content, before leveling off to around 12%, in contrast to the slow decline in moisture content of the overall dry box (Figure 56).

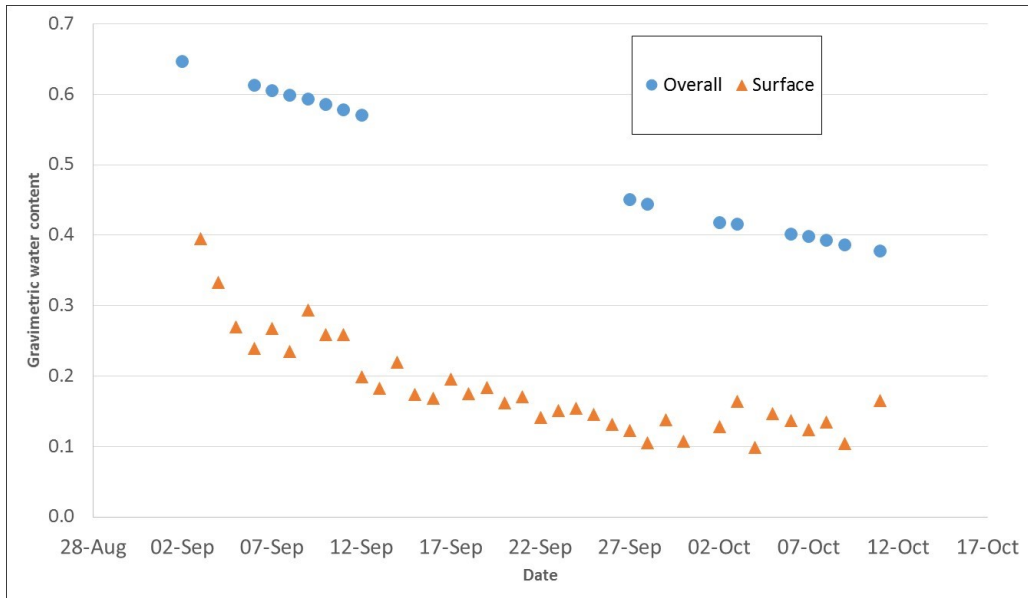


Figure 56: Gravimetric water content - Second layer

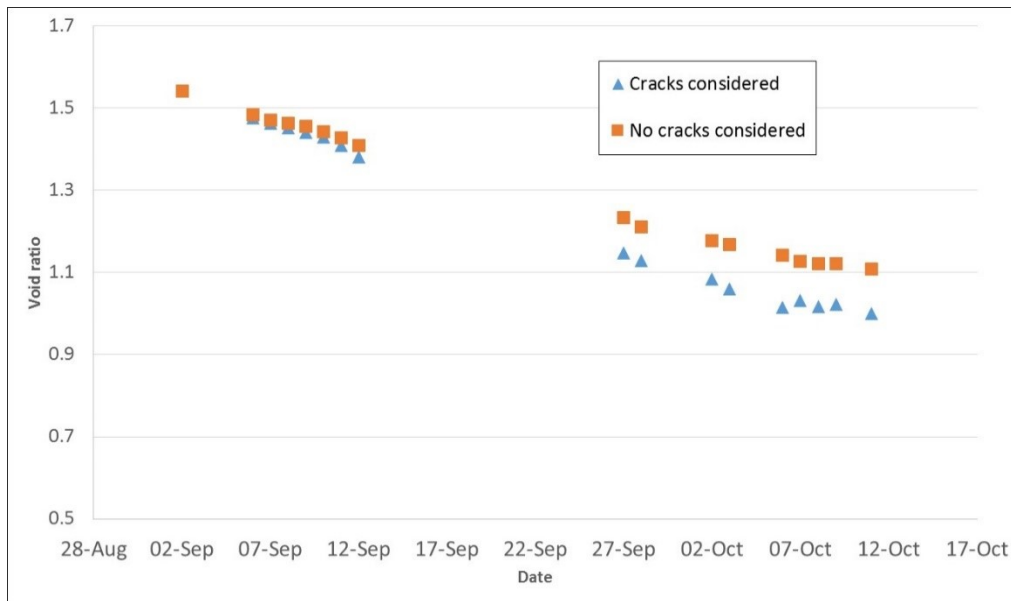


Figure 57: Average void ratio - Second layer

Based on the vertical displacement of the material, and the weight change over time, void ratio was calculated with and without considering cracks in Figure 57. Here again, the difference between the measurements was observed to increase as the cracks grew in size.

In the same fashion as the previous experiment, a shrinking curve was constructed in association with the evaporation data, drainage, and tailings volume variations, as seen in Figure 58. In this case, as well, the shrinkage limit was not reached.

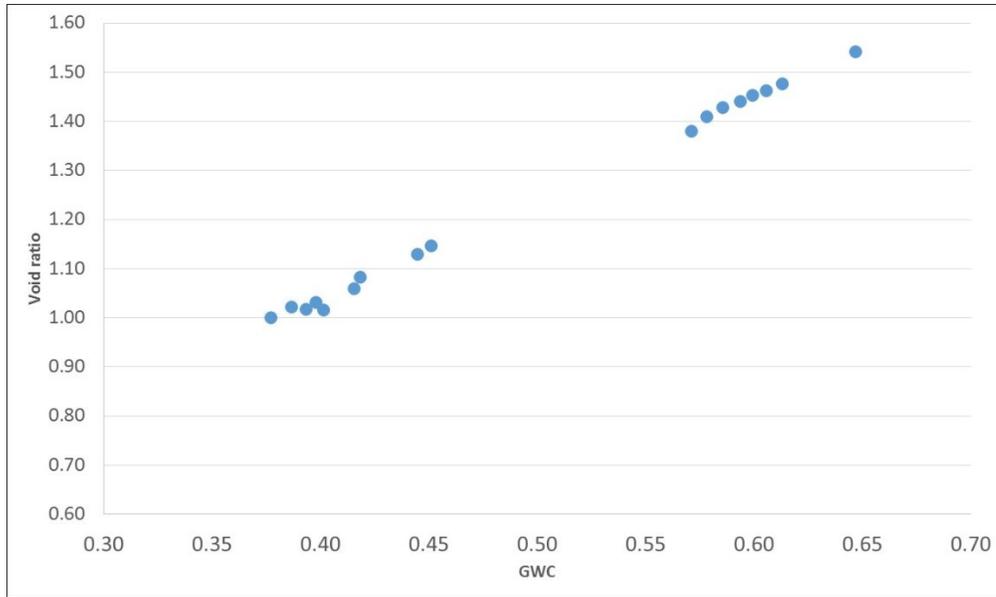


Figure 58: Shrinkage curve - Second layer

Consistent with the first layer deposition, a linear progression in the crack development at the surface level of the second layer was observed (Figure 59).

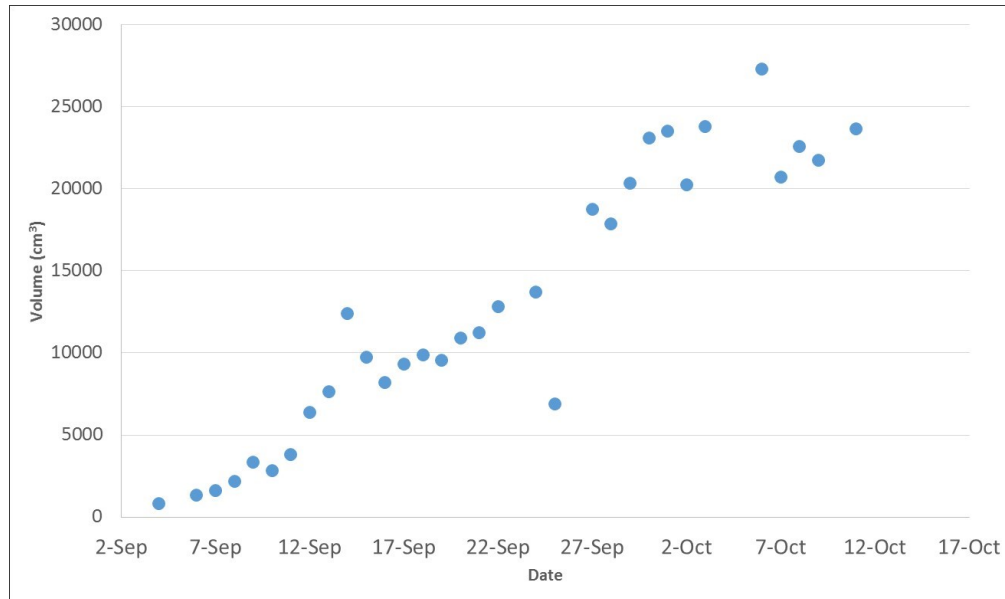


Figure 59: Crack development- Second Layer

Surface samples taken from various locations at the top of the tailings (Figure 60) suggested a similar desiccation process with the crack's geometry in relation as the previous deposition.

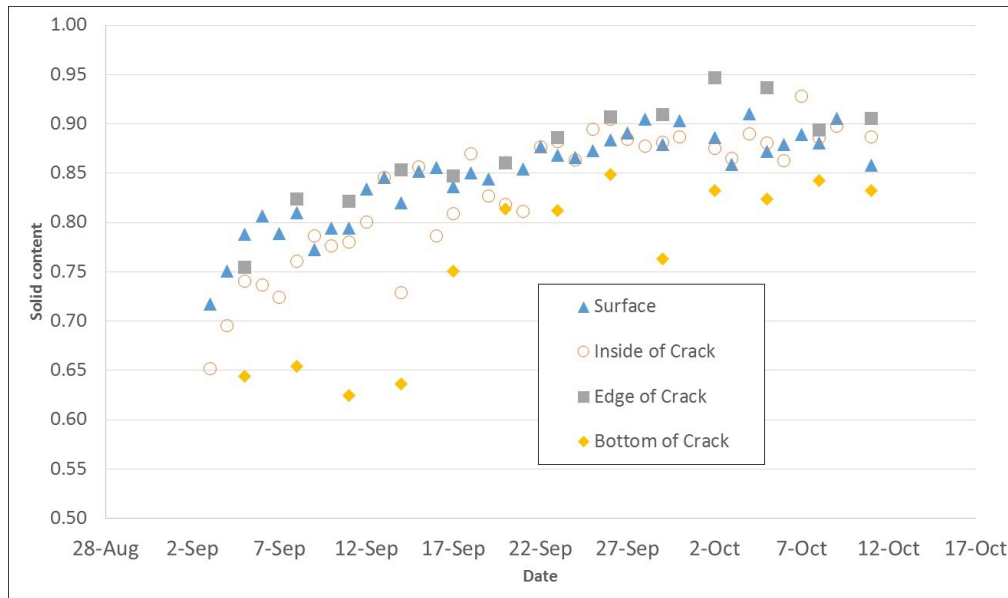


Figure 60: Surface cracks solid content - Second Layer

As expected, suction measurements taken from the top 1cm of the surface of the tailings as well as various location around the geometry of the cracks revealed a similar pattern in relation to the previous layer, being the surface and edge of crack measurements comparatively much higher than the ones taken within the cracks (Figure 61).

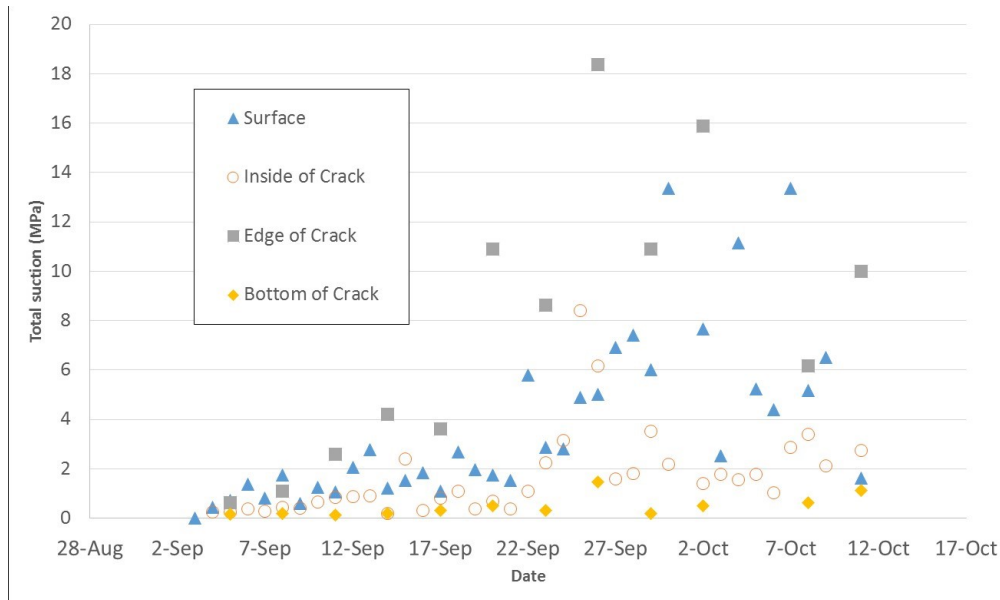


Figure 61: Surface cracks total suction - Second layer

The VWC at the bottom of the second layer was very quickly reduced, indeed, the lowest sensor in the second layer (Figure 62) was already registering a water content almost as low (0.42) as the post-consolidation water content recorded near the bottom of the first layer (Figure 45), by the time deposition was completed. This can be explained at least partially by the adsorption of water into the underlying layer, as evidenced by the increase in moisture content near the top of the underlying layer (Figure 63).

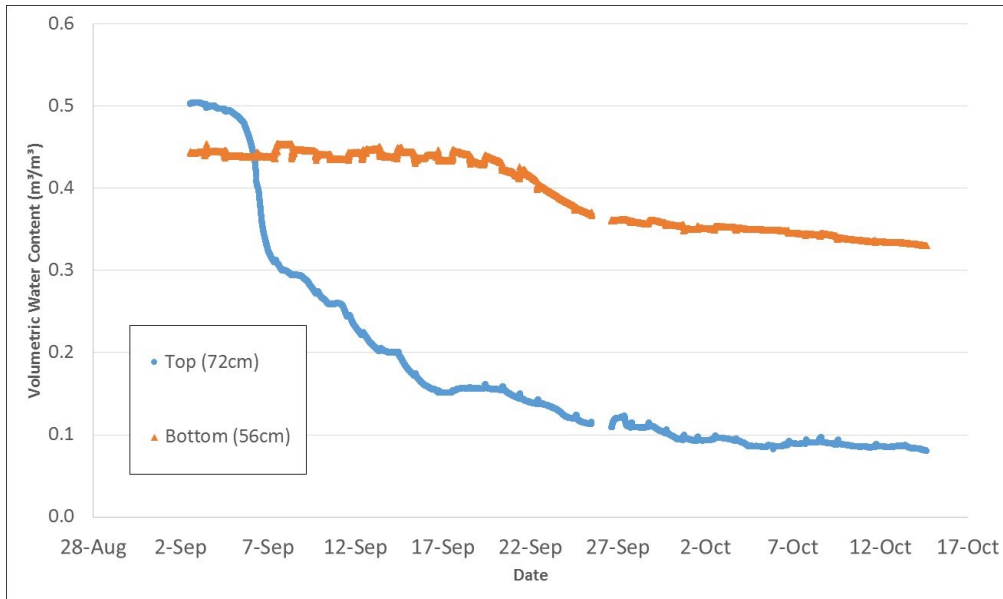


Figure 62: Volumetric water content at various heights top layer –Second layer

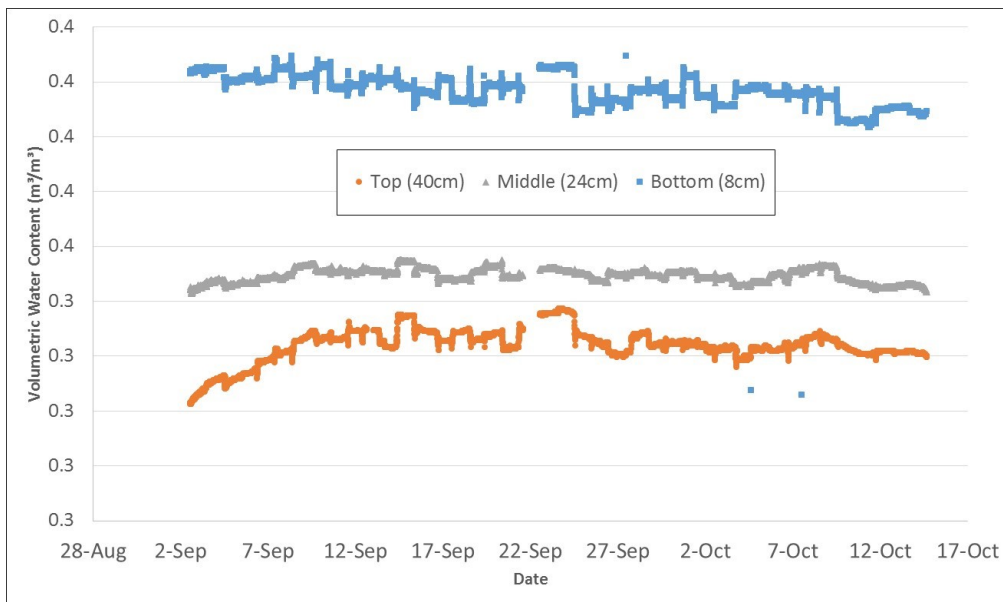


Figure 63: Volumetric water content at various heights bottom layer - Second layer

Figure 64 shows the cumulative drainage recorded by the tipping bucket below the dry box.

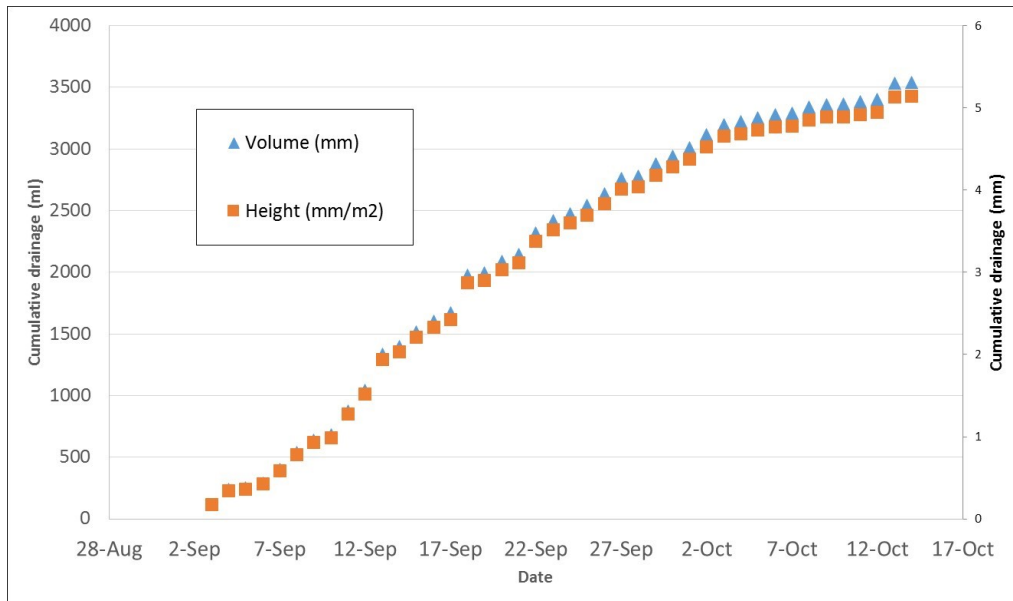


Figure 64: Cumulative drainage - Second layer

Figure 62 also shows a more rapid rate of drying at the surface of the top layer. This is also reflected in the matric suction development, shown in Figure 65, where suction values as high as 210kPa were reached before cavitation of the sensor, well over the ones recorded during the first layer experience. This is attributed to the combined effects of both evaporation and infiltration into the first layer.

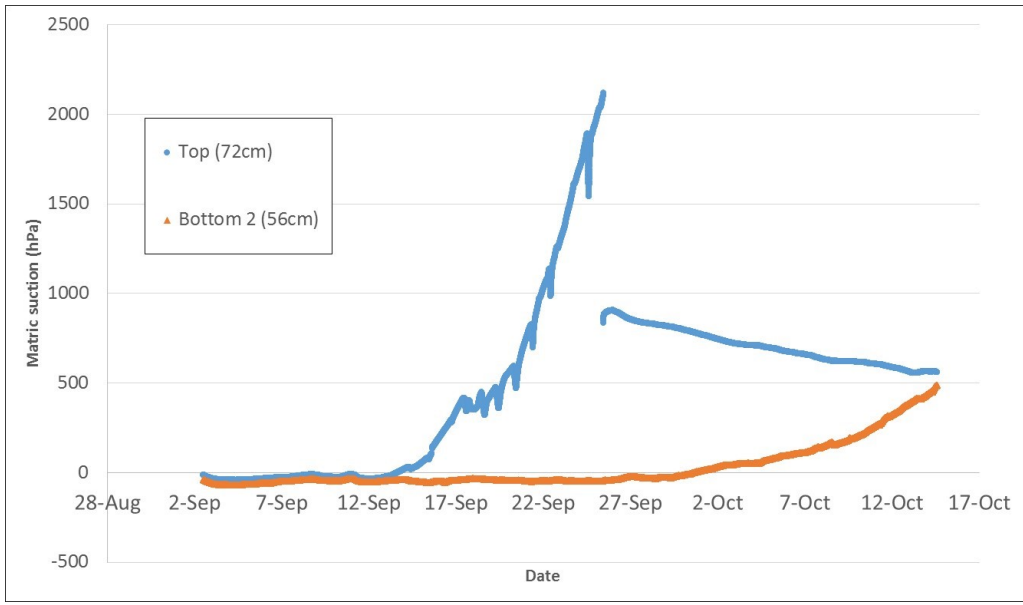


Figure 65: Matric suction at various heights top layer - Second layer

In order to minimize interference with the logger, only one of the tensiometers located at the lowest height in the bottom layer was used after the second layer deposition. Measurements from this sensor can be found in Figure 66.

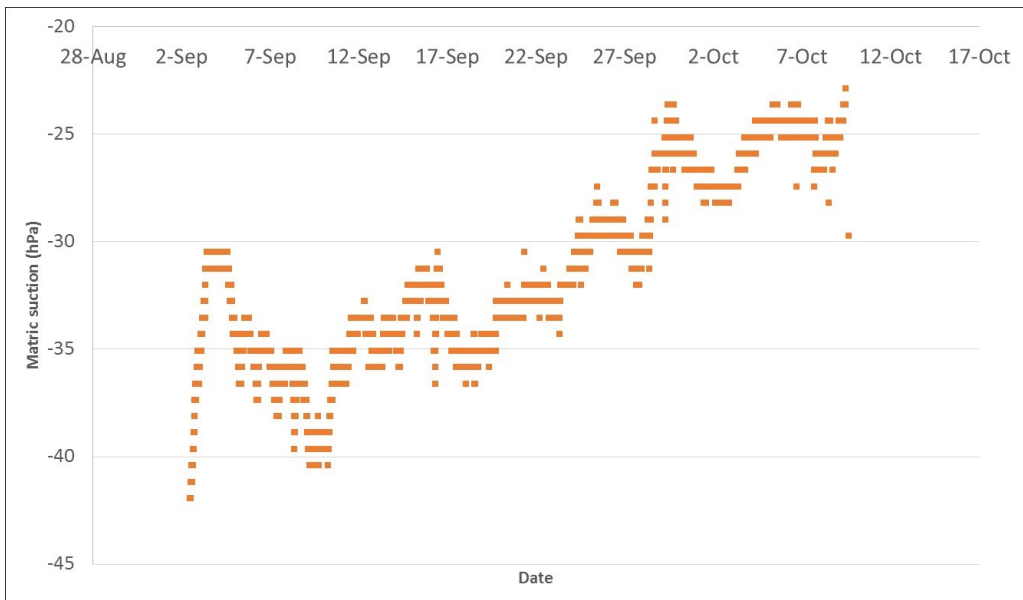


Figure 66: Matric suction at the bottom of bottom layer - Second layer

#### 4.1.2.1 Surface samples

Figure 67 describes a slow but constant increment in both the total and osmotic suction values of the tailings, similar to the previous layer, which reached a maximum value around October 1<sup>st</sup>. This corresponds to the decrease in actual evaporation below potential evaporation for the overall dry box.

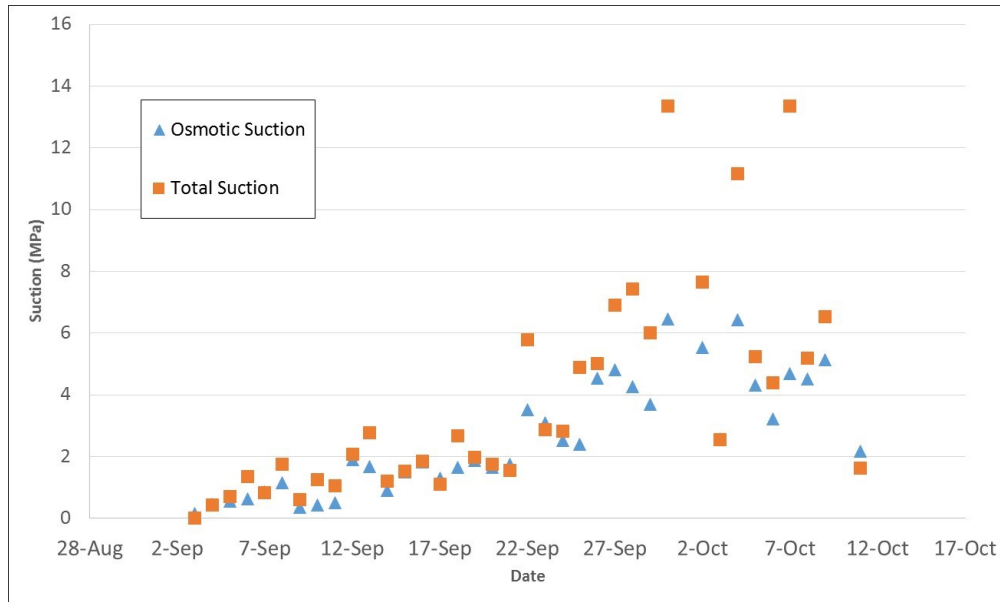


Figure 67: Surface sample total and osmotic suction - Second layer

As in the previous layer, some formation of white precipitate can be observed in the tailing's surface (Figure 68).

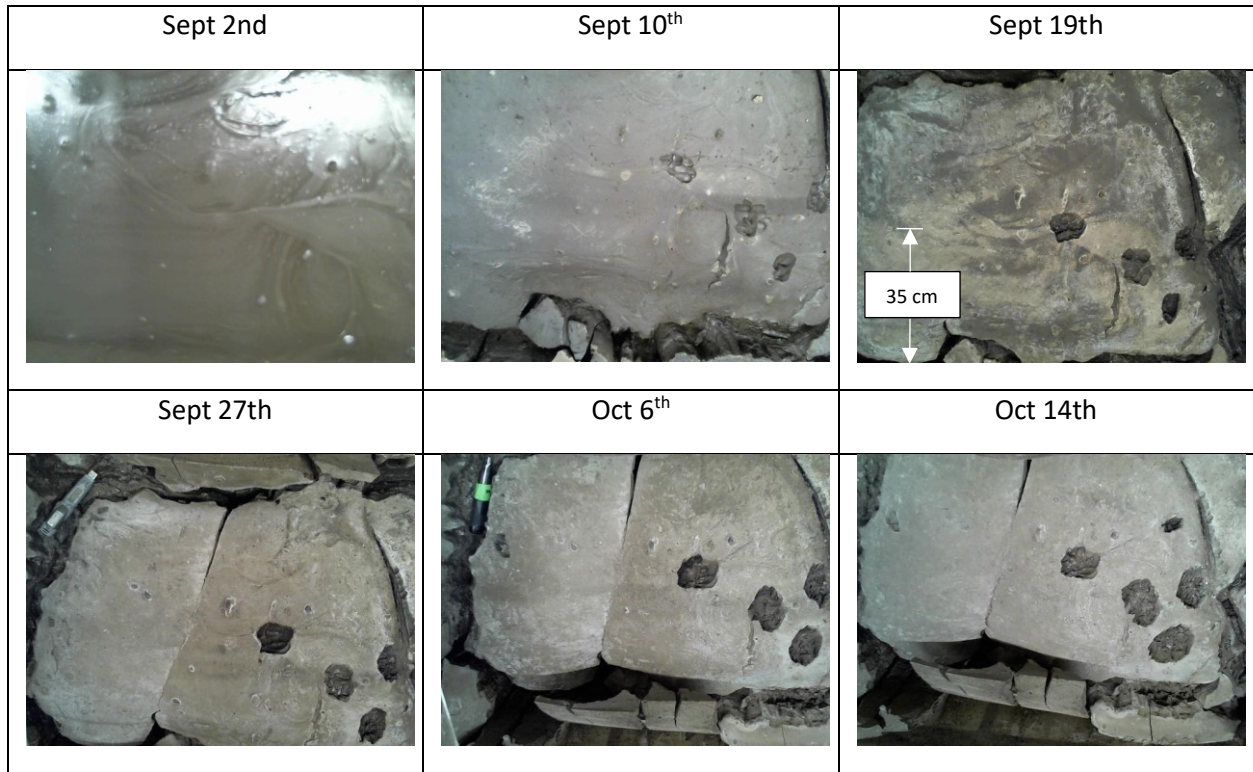


Figure 68: Crack progression - Second layer

#### 4.1.2.2 Core sample analysis

In the same fashion as the first layer, a core sample was extracted once an average solids content of 73% was reached. The sample was divided in 31 height intervals (Figure 69).





Figure 69: Core sample: (a) top section (top at left hand-side) and (b) bottom section (top at left hand-side) - Second layer

As can be seen in Figure 70, the lowest GWC value was measured at the surface of the second layer, from where the moisture content increased with depth. As with the first layer, the second layer showed a decrease in GWC towards the layer interface. Here consolidation was enhanced somewhat through absorption of water from the underlying layer.

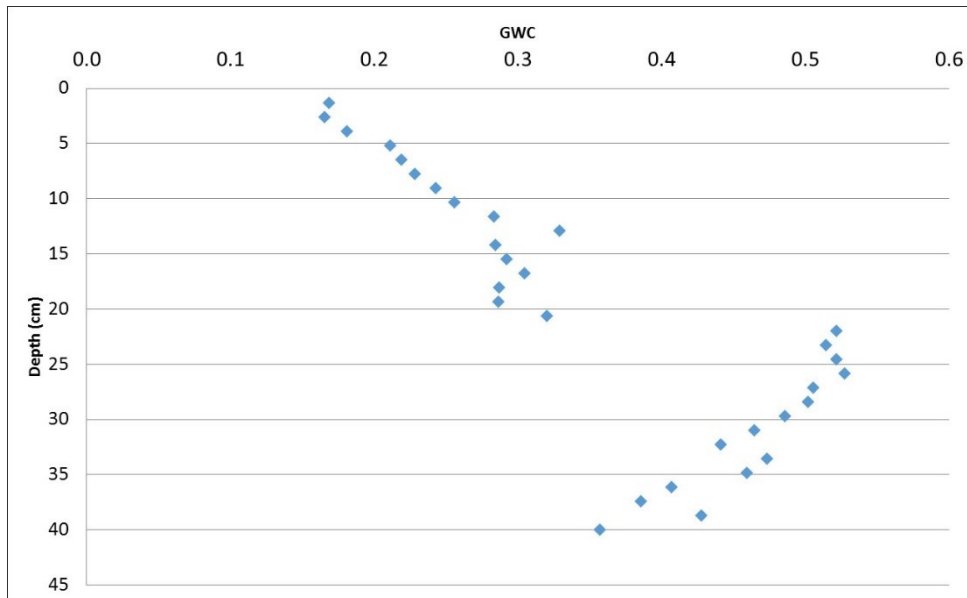


Figure 70. Core sample gravimetric water content profile - Second layer

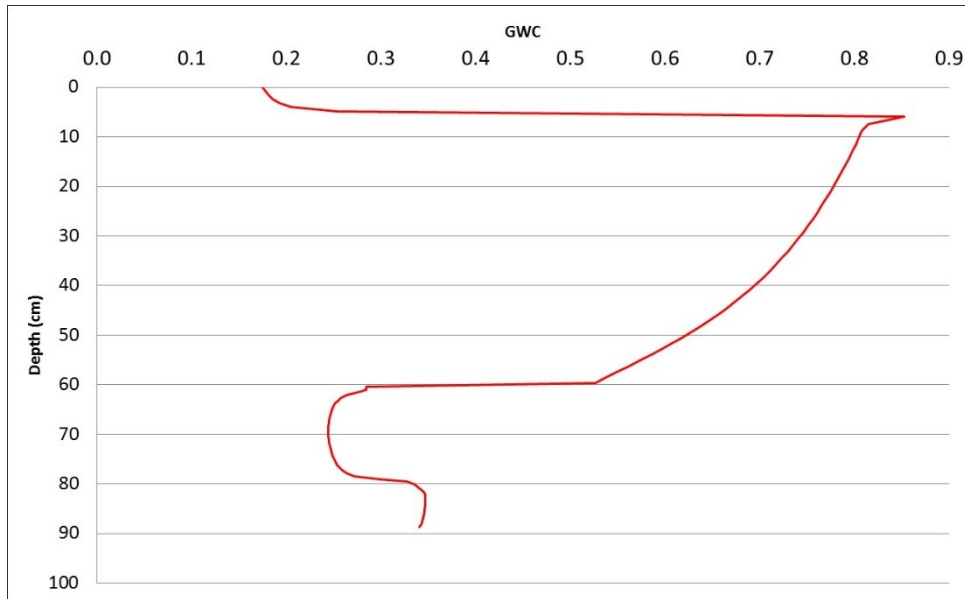


Figure 71: UNSATCON prediction - Second layer

In this case, the UNSATCON predictions further diverged from the measured data. This is both due to the lack of calibration of model parameters, and also to uncertainty as the correct depth of the core data, as the core broke into two during extraction. However, somewhat similar patterns of dewatering can still be observed from the model profile.

As expected, suction was the highest at the surface. In addition, consistent with the first layer as well, the high levels of osmotic suction relative to total suction imply high levels of solute transport along the height of the tailings (Figure 72). The generally higher values of osmotic suction compared to total suction imply that substantial precipitated mass was dissolved during dilution of the individual samples for EC measurements. Therefore, a considerable accumulation of precipitate mass is indicated near the surface.

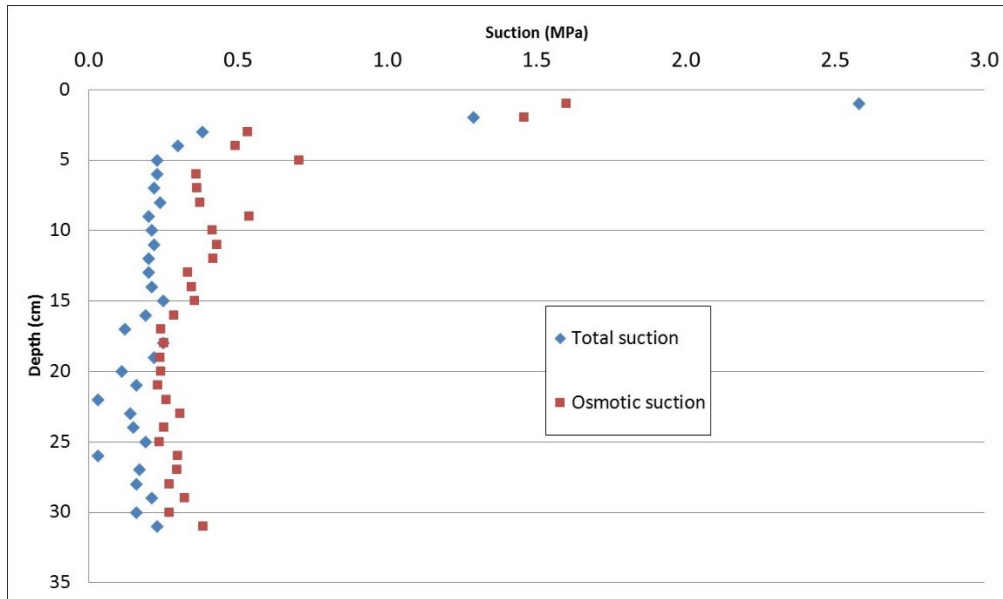


Figure 72. Core sample suction profile - Second layer

#### 4.1.2.3 Un-drained shear strength

A vane shear test was performed in close proximity to the core sample removal location, which extraction point was localized just to the left of the vane shear test location, as can be seen in Figure 73. Results of this test can be found in Figure 74.



Figure 73: Tailings top view after vane shear test- Second layer

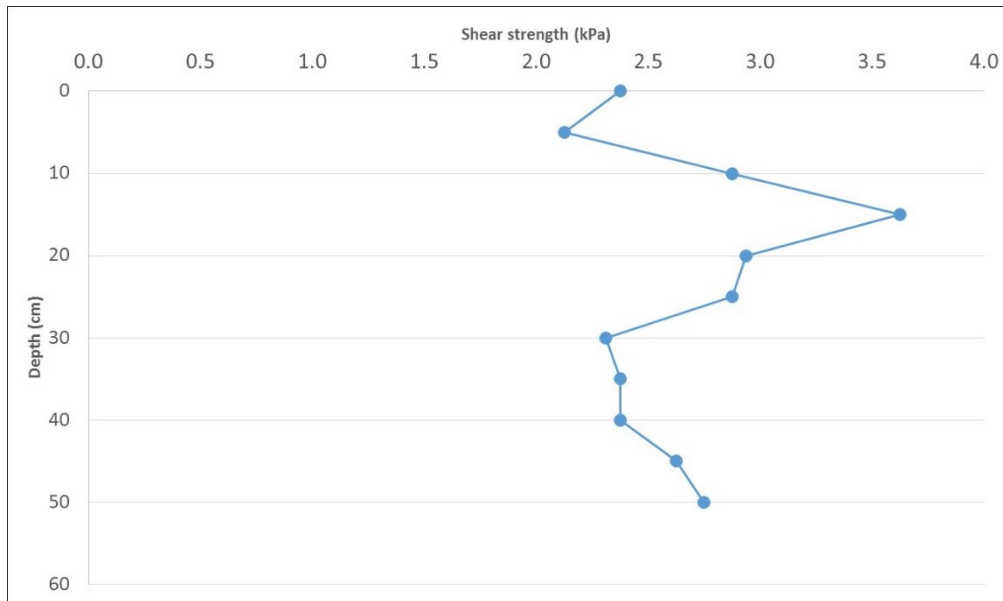


Figure 74: Un-drained shear strength profile - Second layer

## 4.2 Thick-lift overall results

This section provides a compilation of the results of both layers of the thick-lift dry box test.

Figure 75 shows temperature measurements obtained from the moisture content sensors located along the height of the dry box and from an Easy Log USB sensor located above the tailings. During the desiccation of the first layer, temperatures remained the highest at the bottom of the tailings, decreasing with elevation. However, the highest temperatures were measured by the sensor located just above the tailings. Phenomenon repeated after the deposition of the second layer.

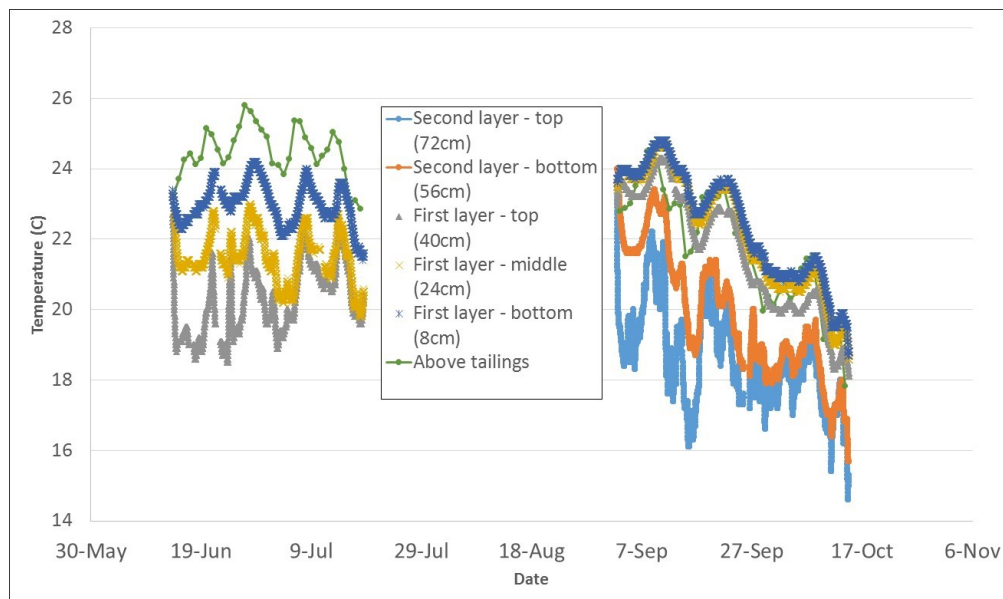


Figure 75: Overall temperature profile - Thick-lift test

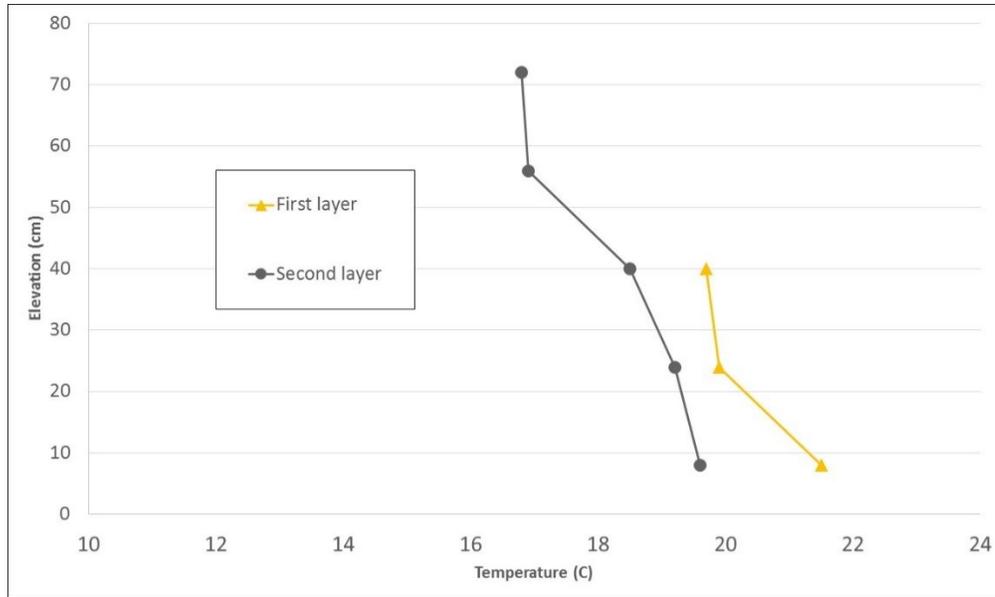
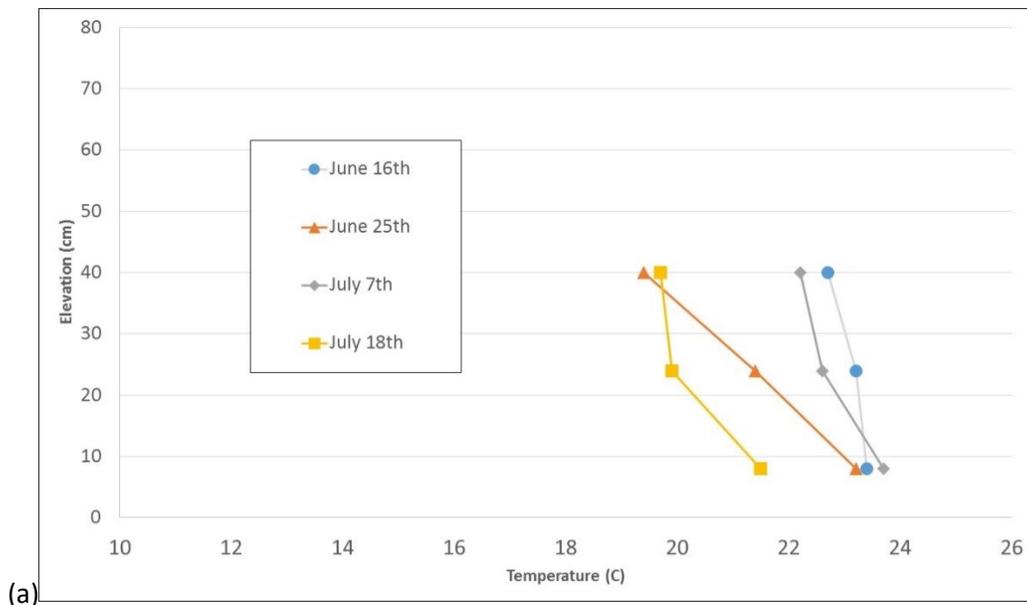


Figure 76: Temperature profiles upon completion of each layer - Thick-lift test

Upon completion of each layer, temperature profiles obtained from the VWC sensors along the height of the dry box were plotted in Figure 76. Here, temperatures revealed a decreasing pattern with elevation, in agreement with observations in Figure 75. Conclusions further backed by the tailings temperature profile progression shown in Figure 77, where the highest temperatures remained always at the bottom of the tailings, even as the overall tailings temperature decreased over time.



(a)

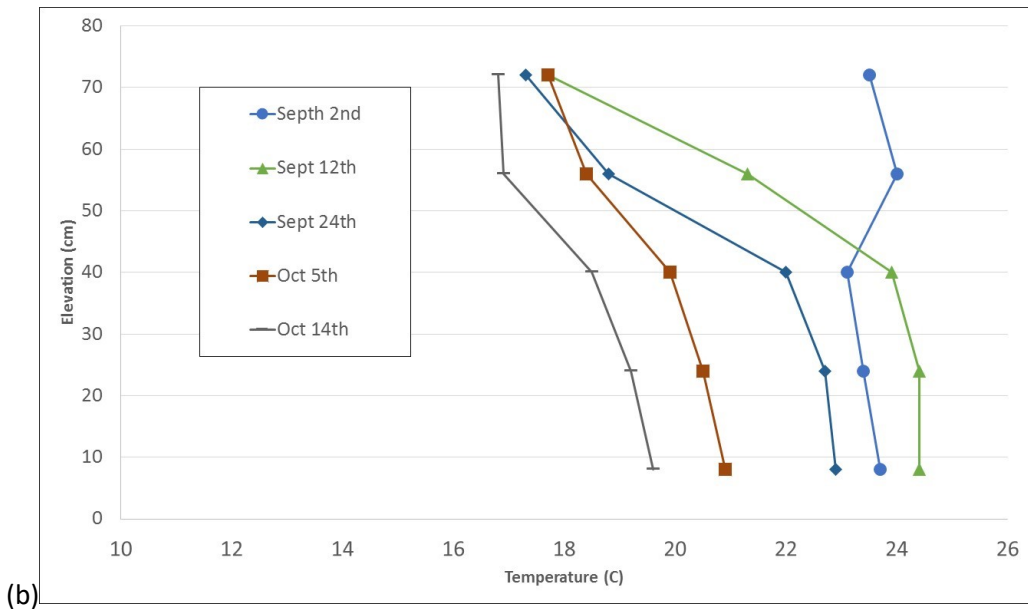
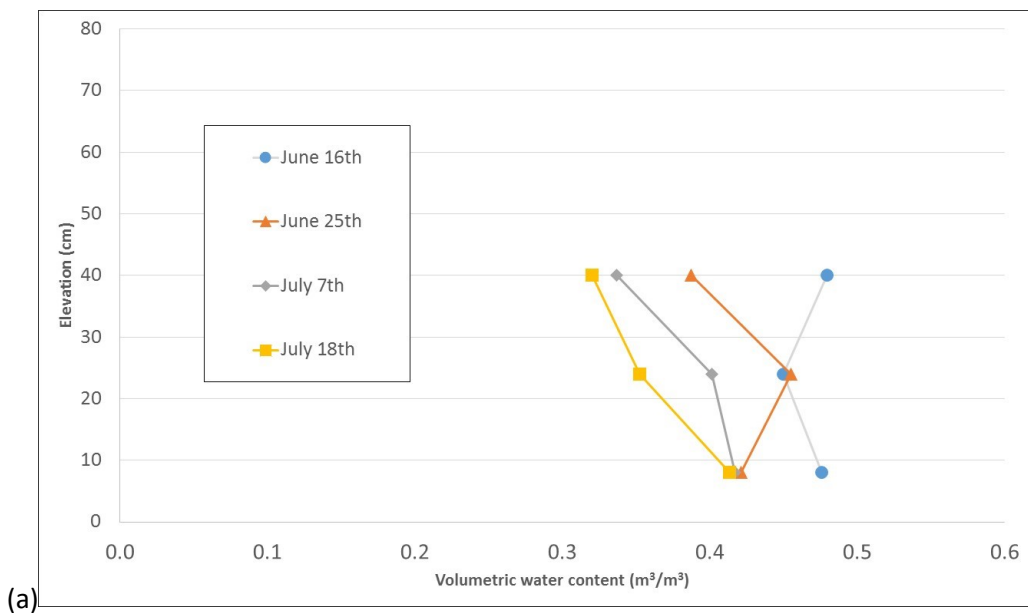


Figure 77: Temperature profiles progression of (a) first layer deposition, and (b) second layer deposition - Thick-lift test

Similarly, Figure 78 shows measurements from the VWC sensors located along the height of the dry box. After the first layer deposition, VWC initially decreased on top and at the bottom of the tailings due to both evaporation and drainage. However, as time progressed, evaporation became the main water removal mechanism. On the other hand, after the second layer was added, most of the water lost was driven by evaporation of the top later, while VWC remained steady at the bottom.



(a)

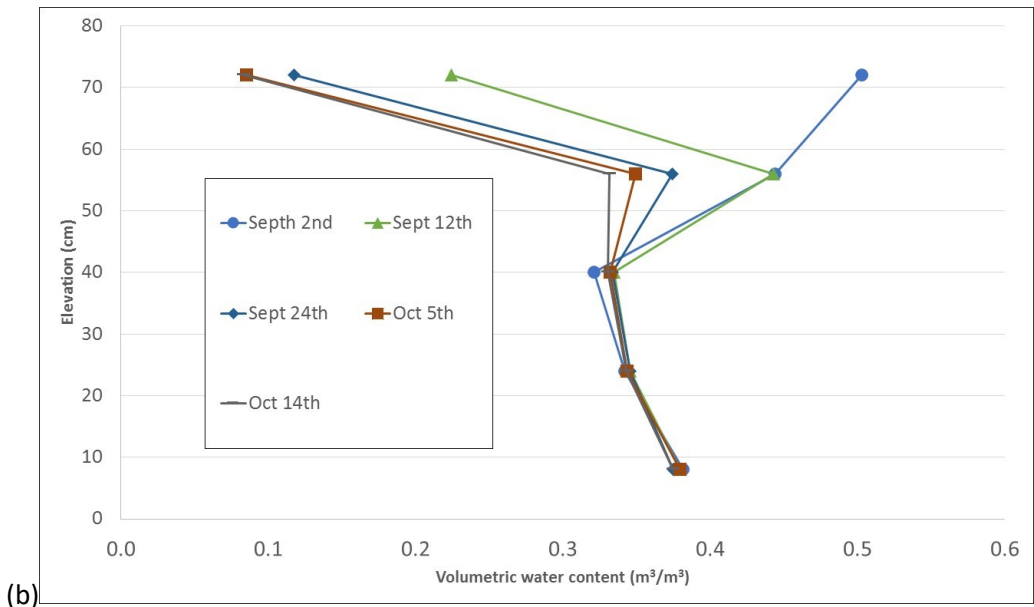


Figure 78: Volumetric water content profiles progression of (a) first layer deposition, and (b) second layer deposition

The temperature, RH and dewpoint values registered by the Easy Log USB sensors above the tailings described reversed patterns of progression between both depositions, in accordance with the seasonal changes in the environment (Figure 79).

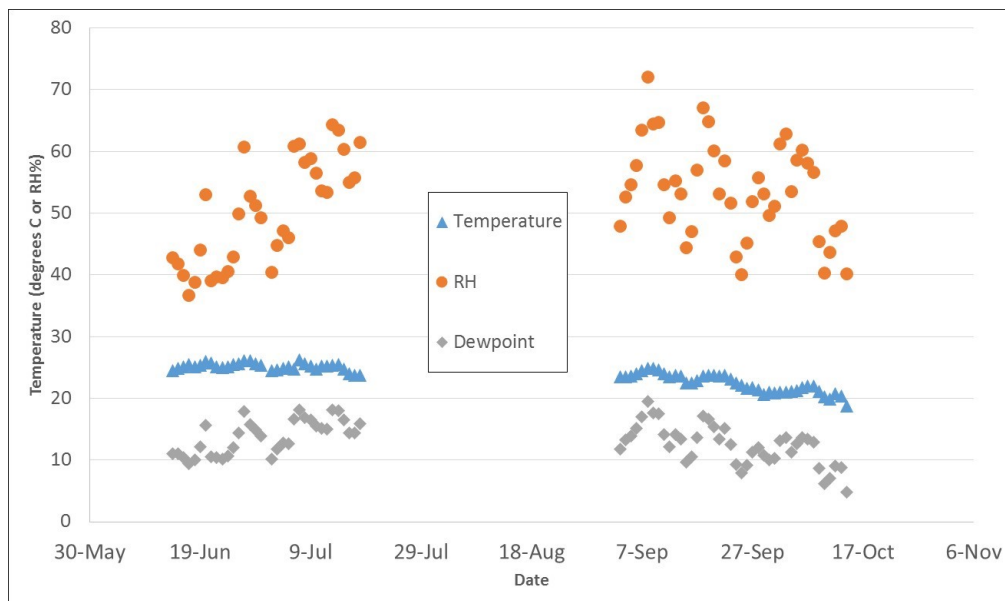


Figure 79: Temperature, RH and dewpoint profiles above the tailings - Thick-lift test

As can be seen in Figure 80,  $A_E$  approximately matched the  $P_E$  for both depositions, eventually falling below it by the end of each desiccation period. These results suggest that the pattern of evaporation for this type of tailings is largely unaffected by crack development, unlike similar oil sands tailings streams where crack development significantly influenced the tailings evaporation behavior (Innocent-Bernard, 2013; Rozina et al., 2015). In addition, this final stage of evaporation coincided with the sharp decrease in suction measurements in the surface of the tailings (Figure 81).

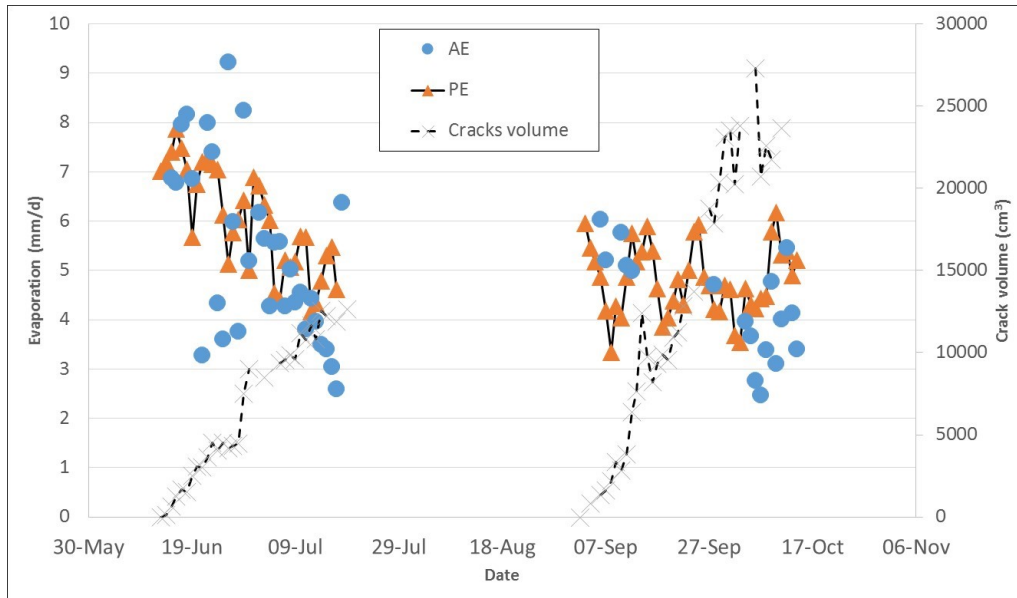


Figure 80: Actual and potential evaporation - Thick-lift test

As observed from Figure 81, the average GWC linearly decreased with time for both layers. However, surface measurements within the top 1cm were observed to converge to around 12%, coincidentally as the  $A_E$  dropped below the  $P_E$  for both layers (Figure 80). In addition, from the figure, it is evident that the rate of evaporation is much higher for the first layer, possibly influencing crack development (Figure 82) and suction in the surface (Figure 88).

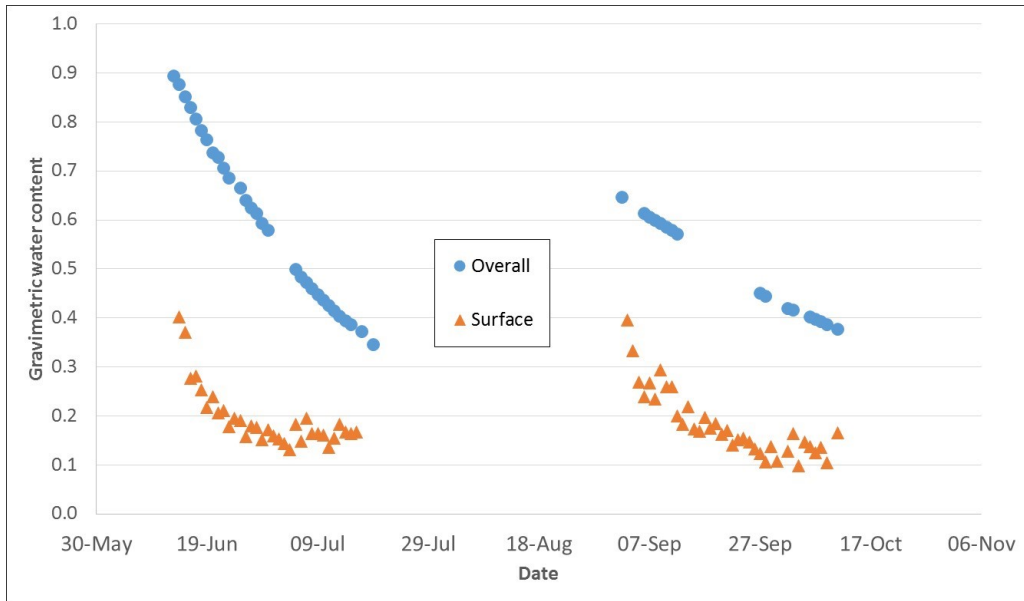


Figure 81: Gravimetric water content - Thick-lift test

Figure 82 shows a linear progression in crack development of both layers starting as soon as deposition occurred. However, the crack volumes measured for the second layer were higher than in the first layer, and developed quicker. Crack volumes have been shown to depend on the aspect ratio of the experiment, and related factors such as rate of overall dewatering (Simms et al. 2017, Djalal 2014).

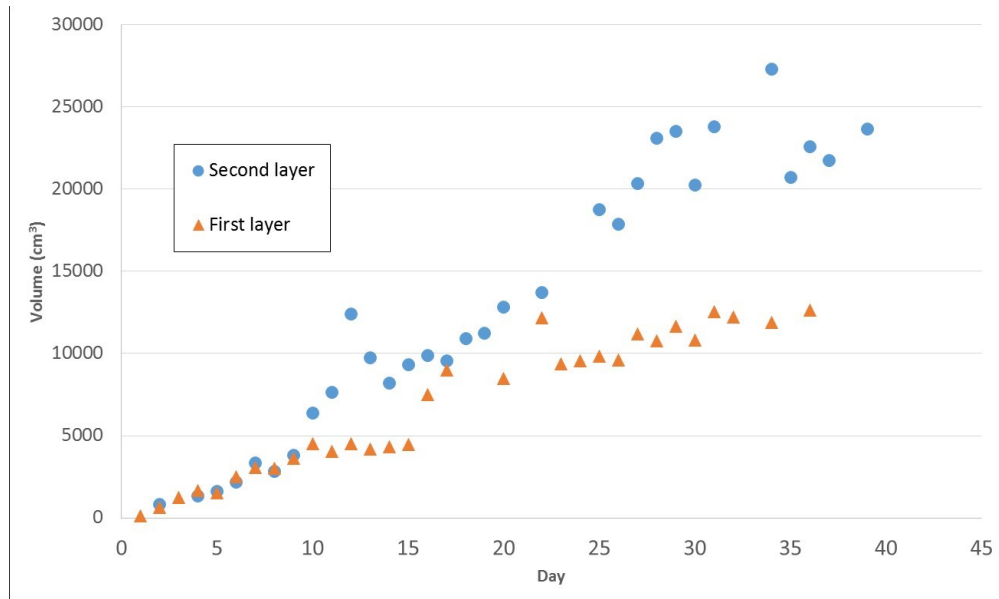


Figure 82: Crack development - Thick-lift test

Samples were taken daily at the surface, and as soon as cracks started to develop, around the cracks geometry for both desiccation periods. As a result of the solid content analysis, seen in Figure 83, it is possible to conclude that, generally the lowest solid content values were obtained from measuring the newly exposed material at the bottom of the cracks, as it would be expected. In contrast, the highest solid content values occurred at the surface as well as the edge of cracks.

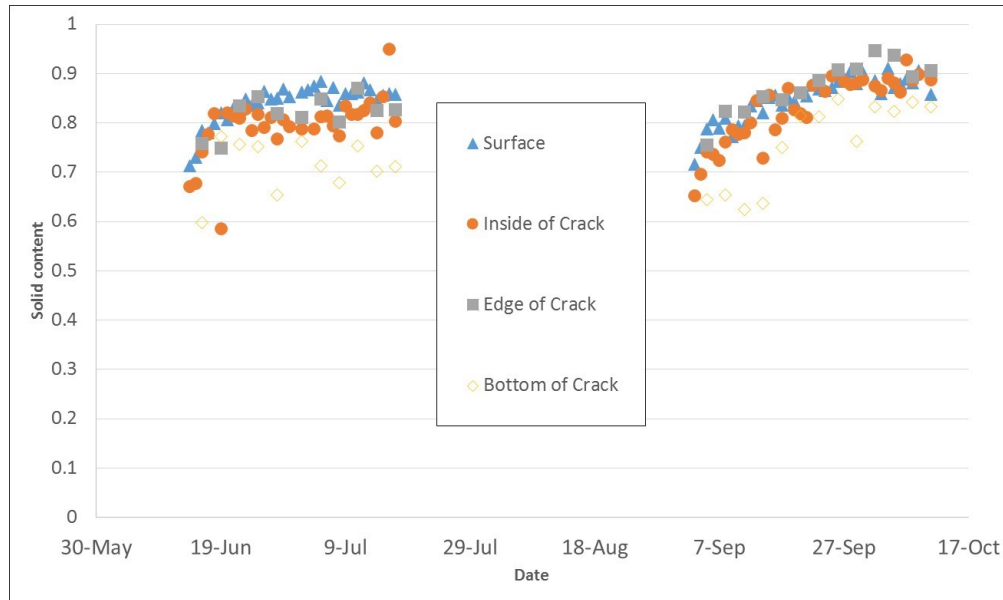


Figure 83: Surface sample solid contents - Thick-lift test

Similarly, daily suction measurements of the surface samples were taken for both deposition tests, and can be found in Figure 84. Generally, suction was the highest at the surface and the crack edges for both tests. However, the significantly larger suction values observed after the second deposition may be explained by the combination effects of evaporation and filtration of liquid into the bottom layer.

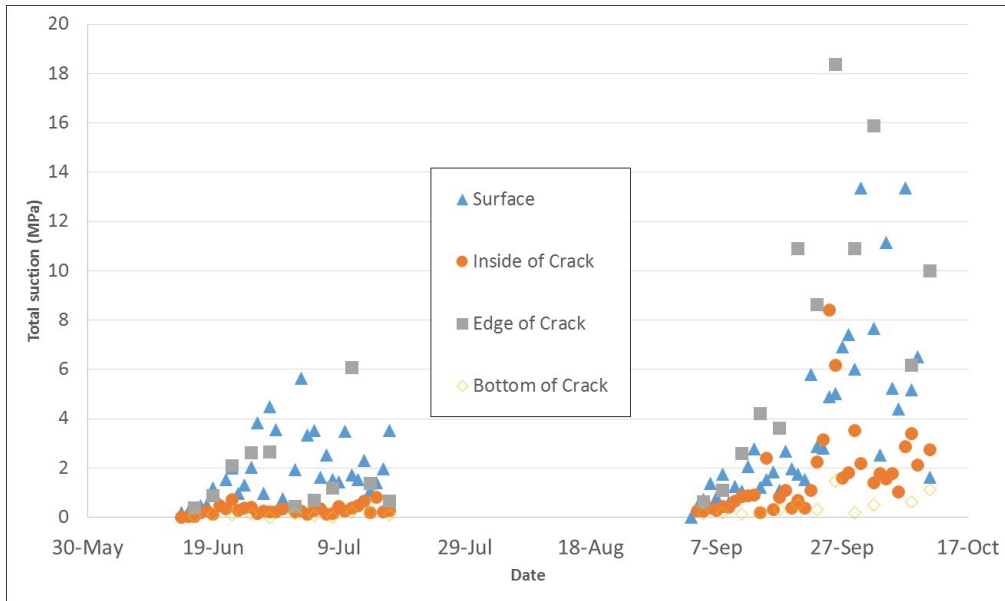


Figure 84: Surface cracks total suction - Thick-lift test

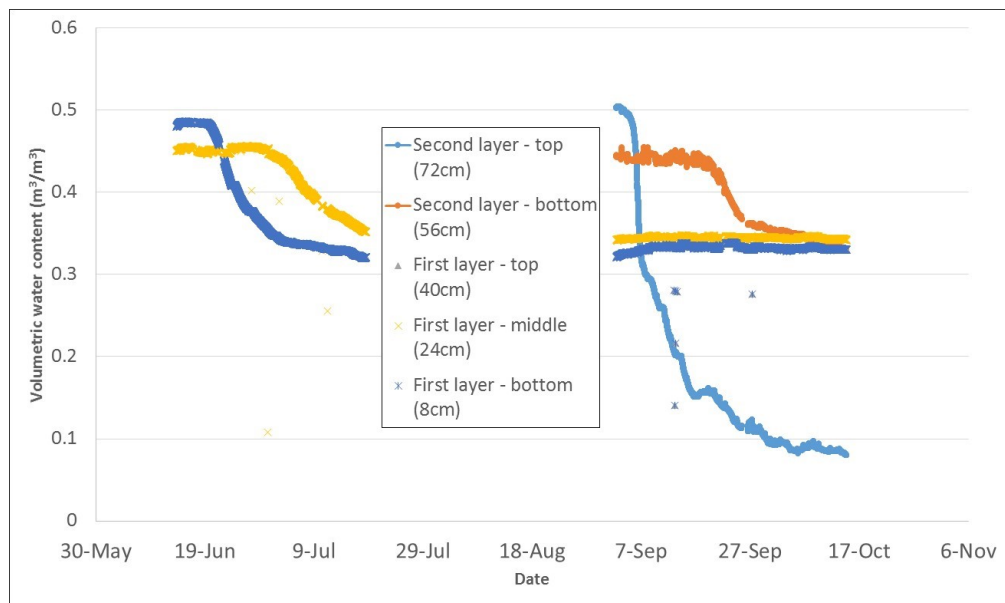


Figure 85: Volumetric water content at various heights - Thick-lift test



Figure 87 shows the matric suction measured along the height of the dry box, which further illustrates the dramatic dewatering of the tailings surface after the second layer deposition.

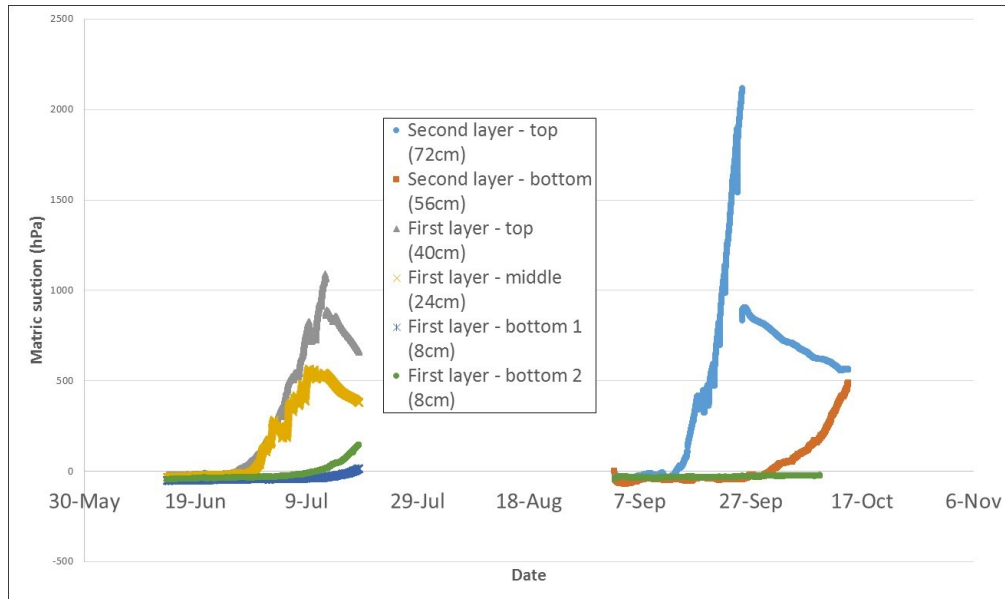


Figure 87: Matric suction at various heights - Thick-lift test

Figure 88 shows osmotic and total suction values measured from surface grab samples describing similar growth patterns for both deposition tests. However, values recorded after the second layer deposition clearly suggest higher rates of dewatering at this level, possibly aided by both evaporation and infiltration. In addition, for both tests, osmotic suction represents a large fraction of total suction, illustrating the precipitation of mass in the surface. This, in turn, may explain the limited effects of crack development on evaporation.

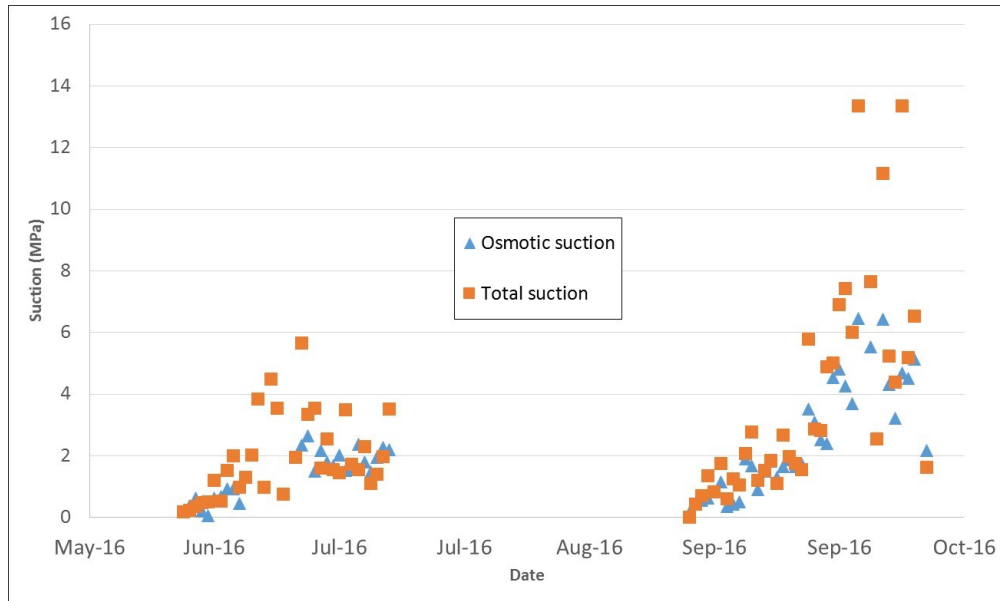


Figure 88: Surface sample total and osmotic suction - Thick-lift test

In order to compare desiccation performance between the experiments, the overall dry box weight variation was divided by the original thickness of the tailings resulting in Figure 89. As observed, water lost occurred more rapidly for the first layer, probably due to the influence of drainage (Figure 46). As a result, it is possible to conclude that desiccation is more effective for the first layer of the experiment.

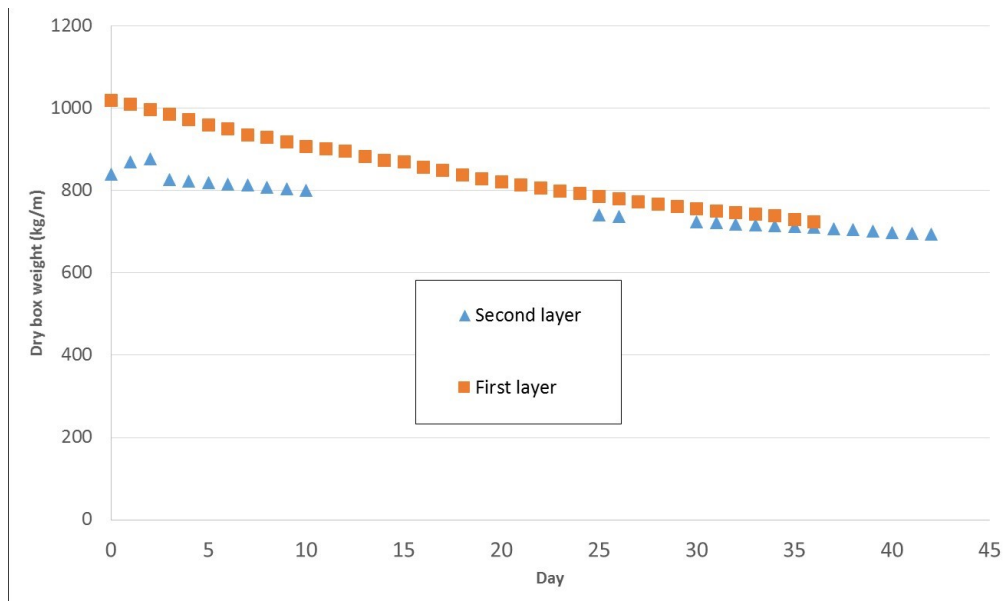


Figure 89: Dry box weight variation - Thick-lift test

Figure 90 shows the solid content progression of the overall dry box for both layer depositions. From the figure it can be observed that for both tests, the material takes 28 days to reach a solid content of 70%.

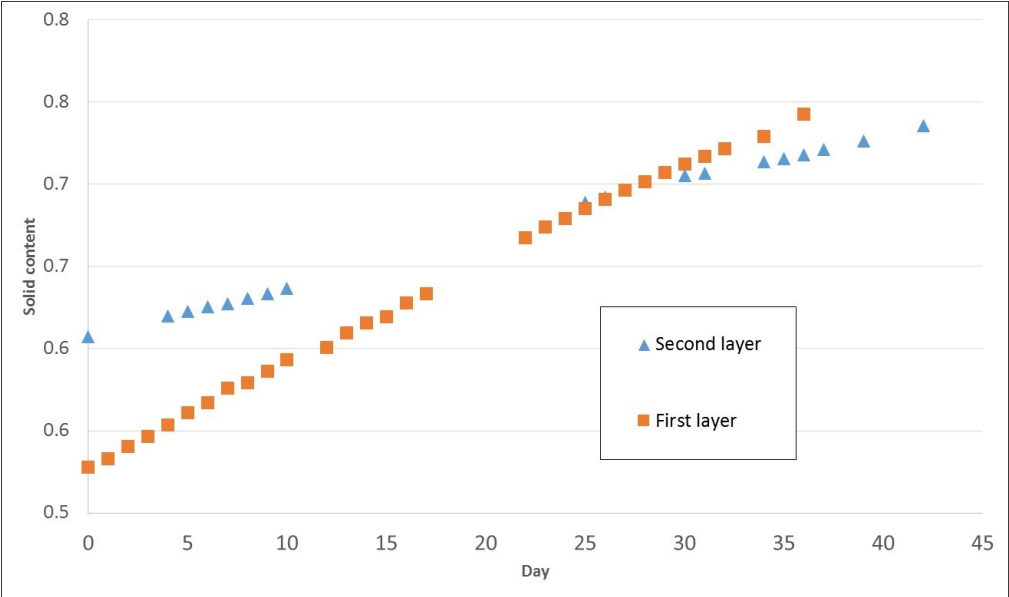


Figure 90: Solid content comparison - Thick-lift test

### 4.3 Thin-lift dry box test

Approximately one year later, a thin-lift dry box test was performed. In a similar fashion as the thick-lift test, three 35cm layers were deposited into the dry box using plastic buckets after the re-mixing process, each having ~7kg of material, while a solid content test was performed every 10 buckets for quality control purposes. The first layer, deposited the 15<sup>th</sup> of May, achieved 35cm at an initial average GWC of 92% (52% solids), the second layer, deposited the 23<sup>th</sup> of July, at an average GWC of 61% (62% solids), and the third layer, deposited the 18<sup>th</sup> of October, at an average GWC of 51% (66% solids). The first deposition lasted two hours and the second and third deposition lasted two and a half hours. A time lapse of one of the deposition processes is provided at the following link: "<https://paulsimms0.wixsite.com/tailings-carleton>". Additional details concerning the deposition can be found in Appendix D, E, and F.

#### 4.3.1 First layer deposition

Mass lost due to evaporation was observed to range between 2 and 6mm/d, following the potential evaporation pattern for most of the experiment, but significantly oscillating as early as just a few days after deposition. This behavior remained steady until around June 15<sup>th</sup>, at which point it fell below the  $P_E$  (Figure 37).

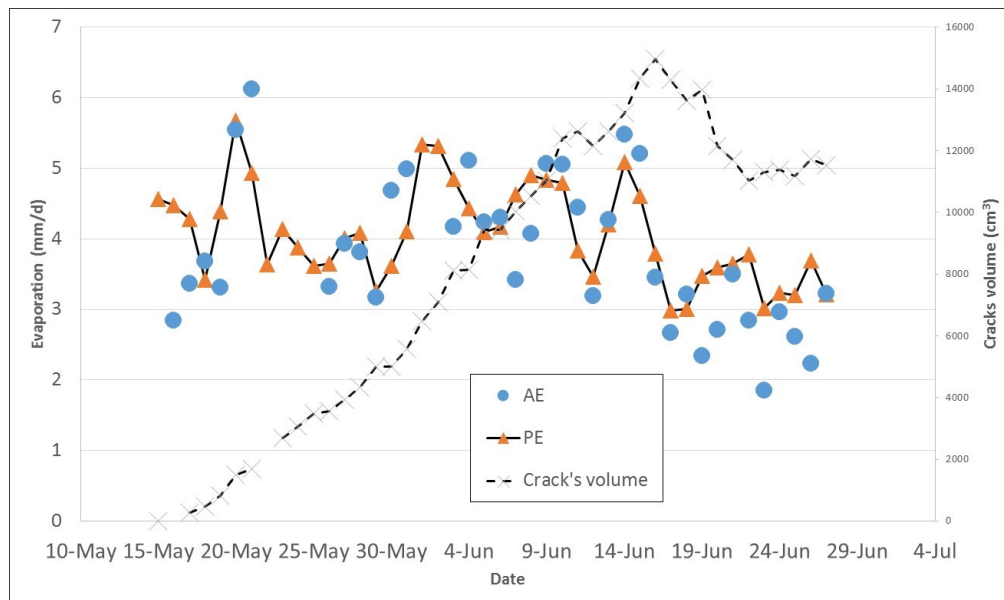


Figure 91: Actual and potential evaporation - First layer

As shown in Figure 92, the average GWC of the dry box decreased steadily through the experiment. In contrast, the GWC observed from the surface grab samples, initially drops rapidly, leveling off at around 12% by the middle of June.

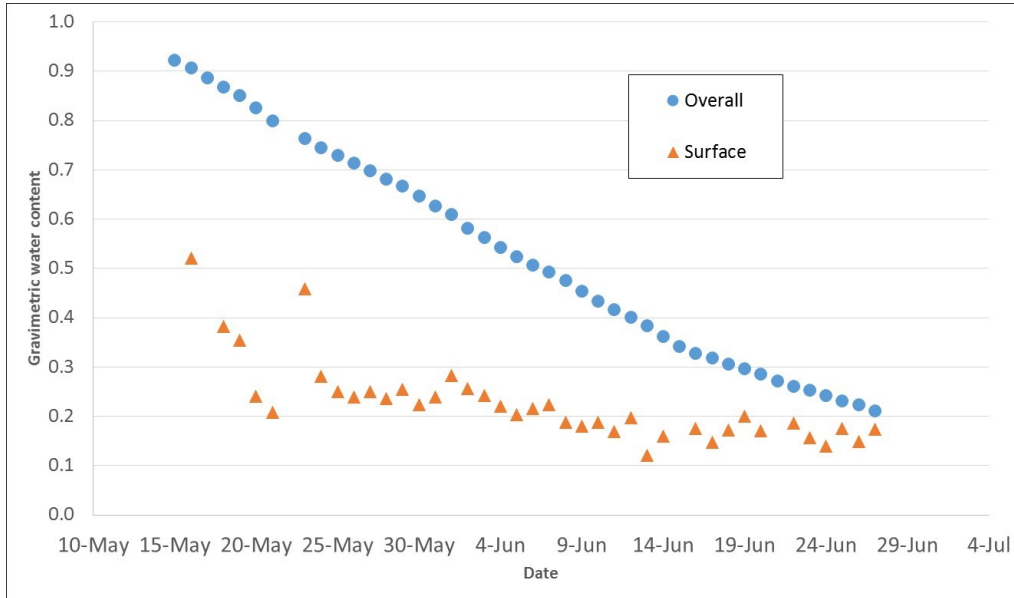


Figure 92: Gravimetric water content - First layer

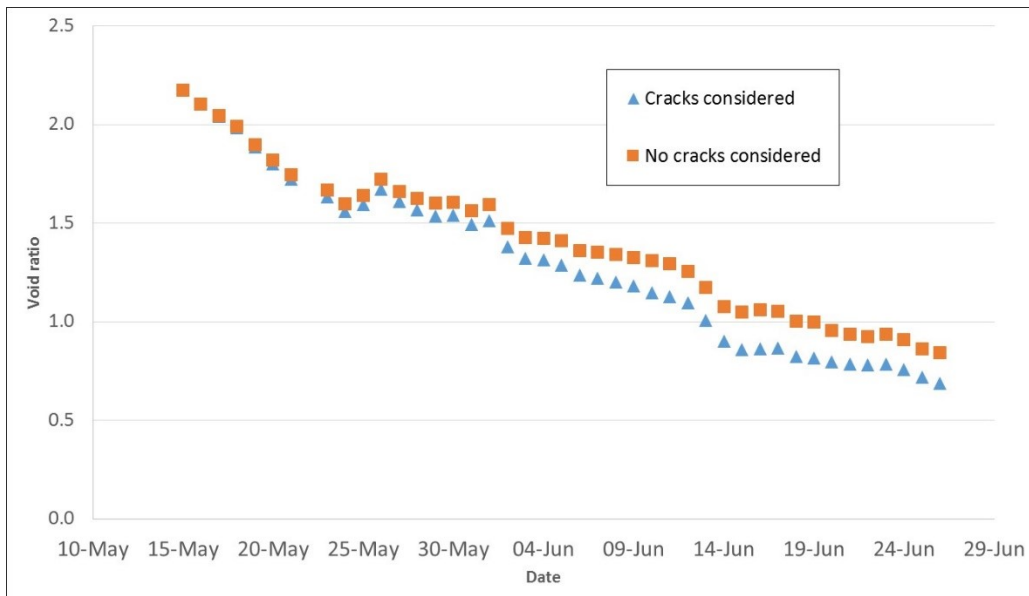


Figure 93: Average void ratio - First layer

Figure 93 shows the void ratio measurements, with and without considering cracks. In general, results agree with the thick-lift test observations, showing an ever increasing difference between the measurements, as cracks develop further. Unlike the thick layer test, the void ratio appears to more clearly approach the shrinkage limit.

Figure 94 show the degree of saturation after the first layer deposition. Results from this figure, however, indicate issues with the sensors data measurements, which may require further consideration.

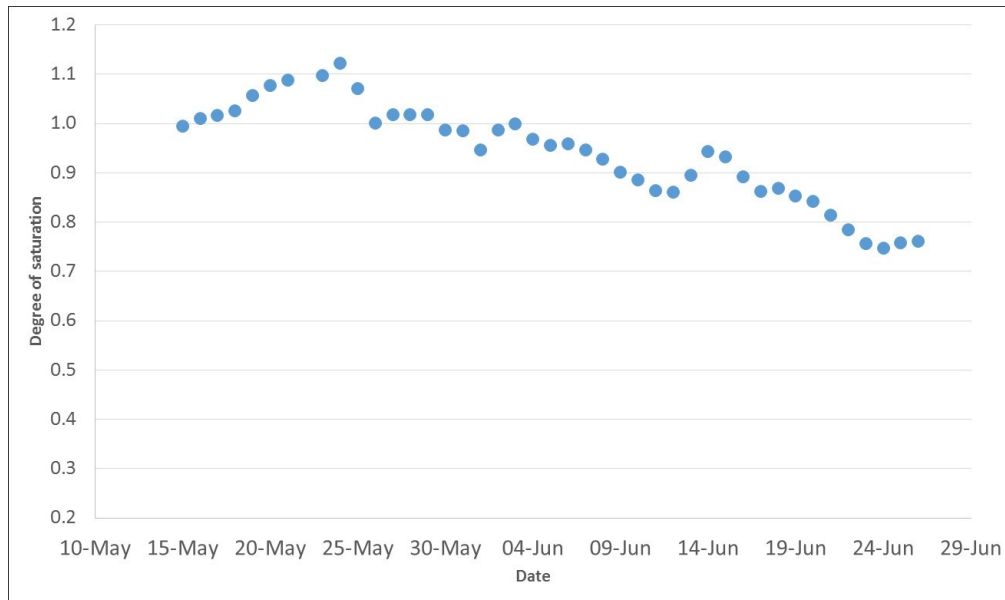


Figure 94: Average degree of saturation - First layer

Based on the tailings vertical displacement, crack volume measurements, and average GWC, an apparent shrinkage curve was constructed, as shown in Figure 95. Some consolidation, though less than in the thick-lift, reduces the final void ratio to less than the expected value (~0.7).

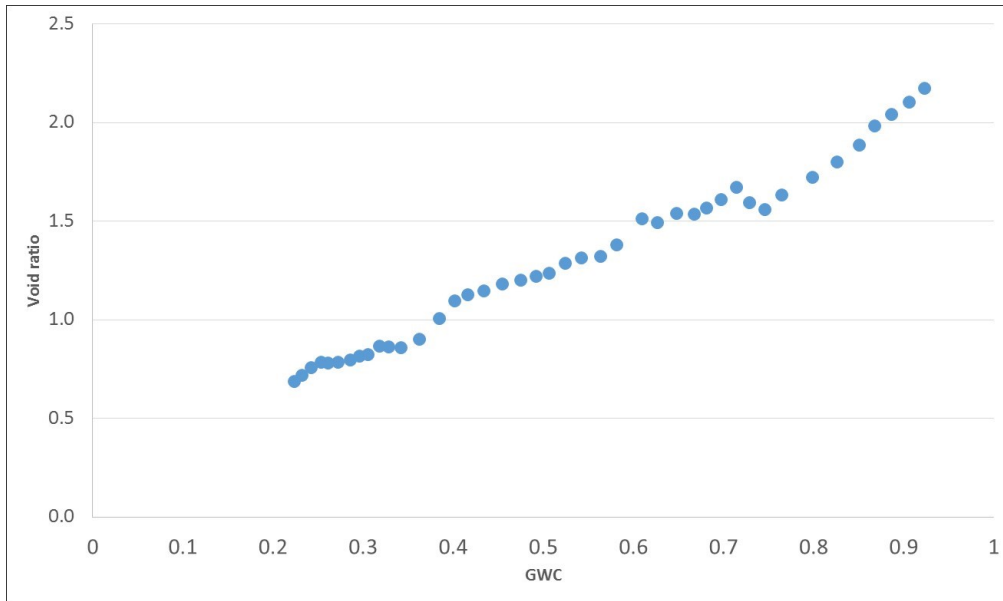


Figure 95: Shrinkage curve - First layer

Crack volume, as shown in Figure 96, peaked on June 16<sup>th</sup>, after which point it leveled off by the end of the month to around 11 400cm<sup>3</sup>. This gives a clear indication that the shrinkage limit was actually reached, unlike in the thick-lift where crack development is continuous.

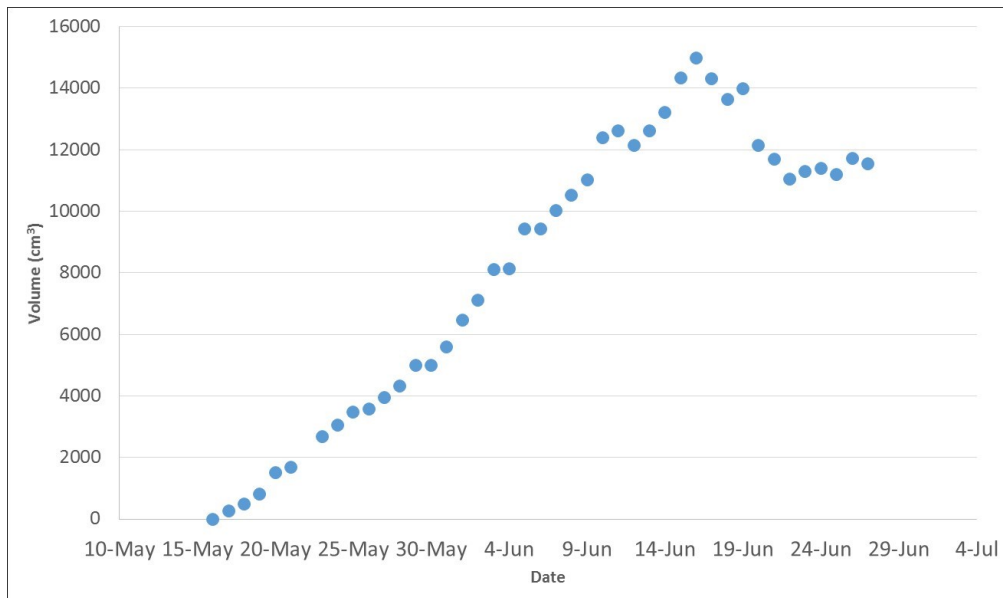


Figure 96: Crack development - First Layer

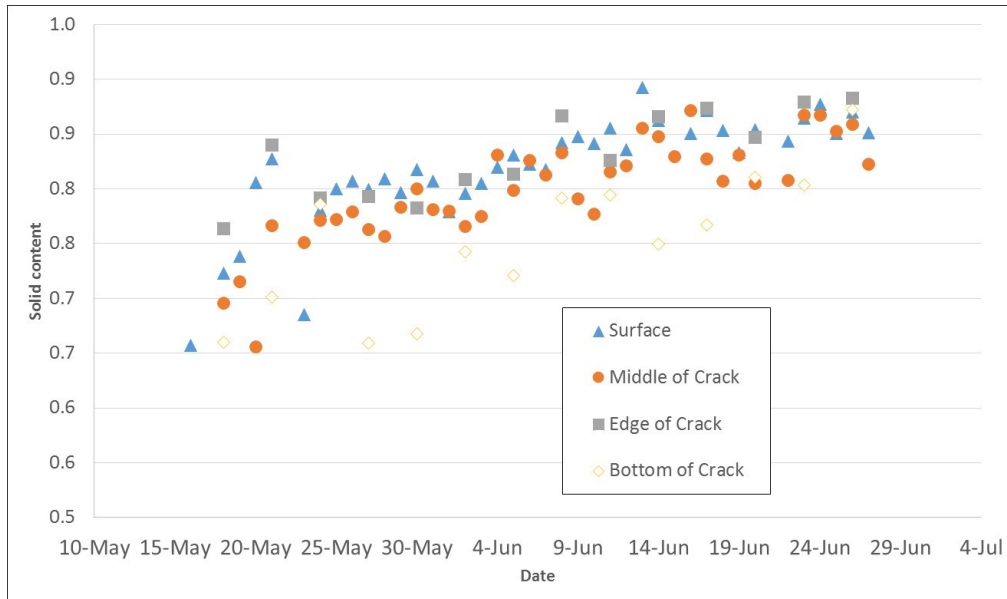


Figure 97: Surface cracks solid content - First Layer

Surface samples taken at various locations around the surface, described solid content data initially increasing at the same rate for all measurements, eventually leveling off around June 10th (Figure 97). In agreement with the thick-lift test as well, the samples taken at the surface and the edge of cracks showed the largest solid content values throughout the experiment, as compared to the samples taken deeper into the cracks.

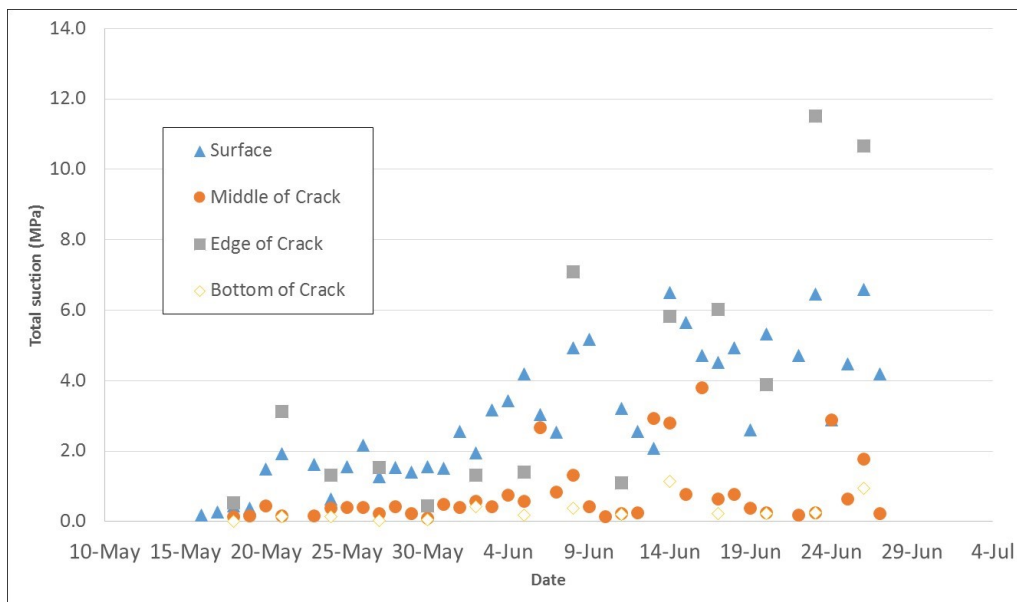


Figure 98: Surface cracks total suction - First layer

Total suction measured inside the cracks showed relatively small changes compared to the surface (Figure 98).

As observed from Figure 99, initially after deposition, the volumetric water content readings along the height of the tailings did not show much variations. Likely, consolidation occurred mainly near the bottom of the layer, which may have not been detected by the sensors, though a small decrease in the VWC in the lower sensor is measured during the first 10 days. Consolidation is suggested both by the trend in average void ratio, and by some drainage being reported (Figure 100) during this period. However, a week and a half later, an initial decrease in VWC was observed at the top of the layer, eventually matched by the VWC readings at bottom of the tailings, suggesting evaporation as the main water removal mechanism.

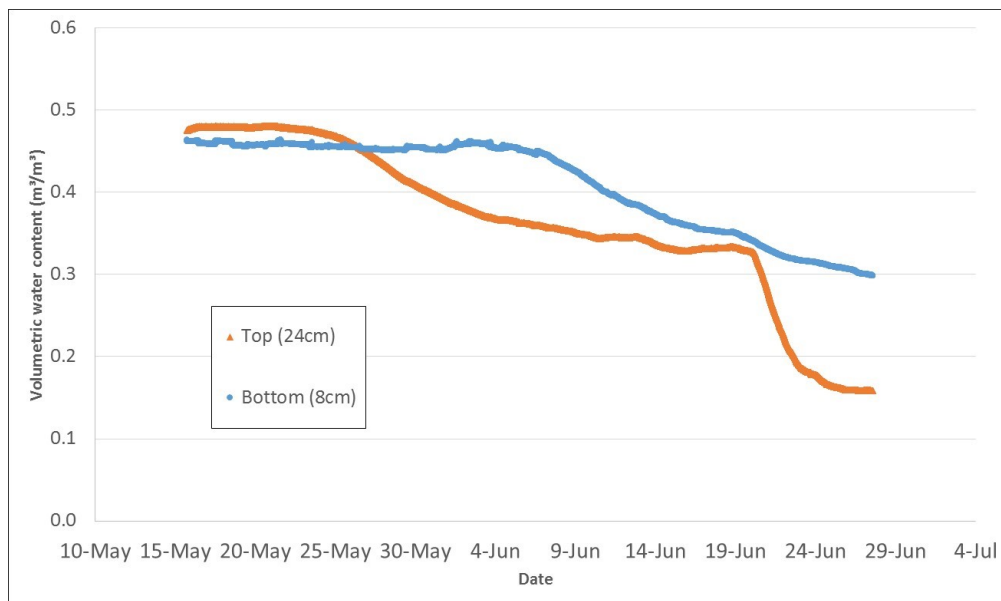


Figure 99: Volumetric water content at various heights - First layer

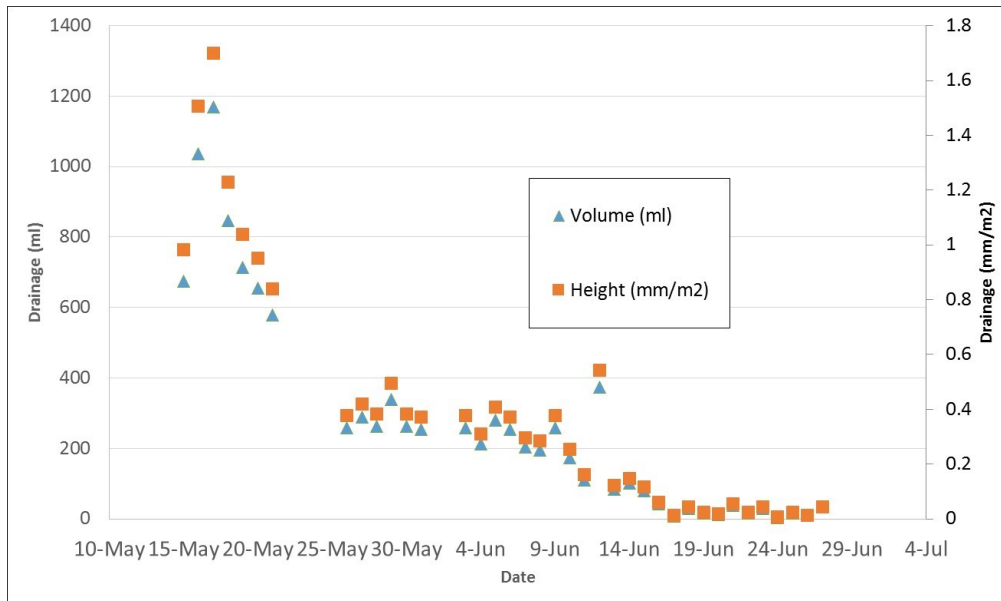


Figure 100: Drainage - First layer

Two tensiometers were placed at the bottom of the tailings at the same height, while another one was placed close to the top. From this set up (Figure 101), matric suction measurements at the top as well as at the bottom of the tailings remained steady for two weeks and a half, until matric suction levels started to rise around June 5th. In this case, the slow rise of matric suction recorded by the second tensiometer at the bottom seemed to be localized. As a result, the constant overall suction increment of the tailings was consistent with the slow decline in VWC along the tailings height (Figure 99), further supporting the previous interpretation of the sharp decrease in VWC at the top.

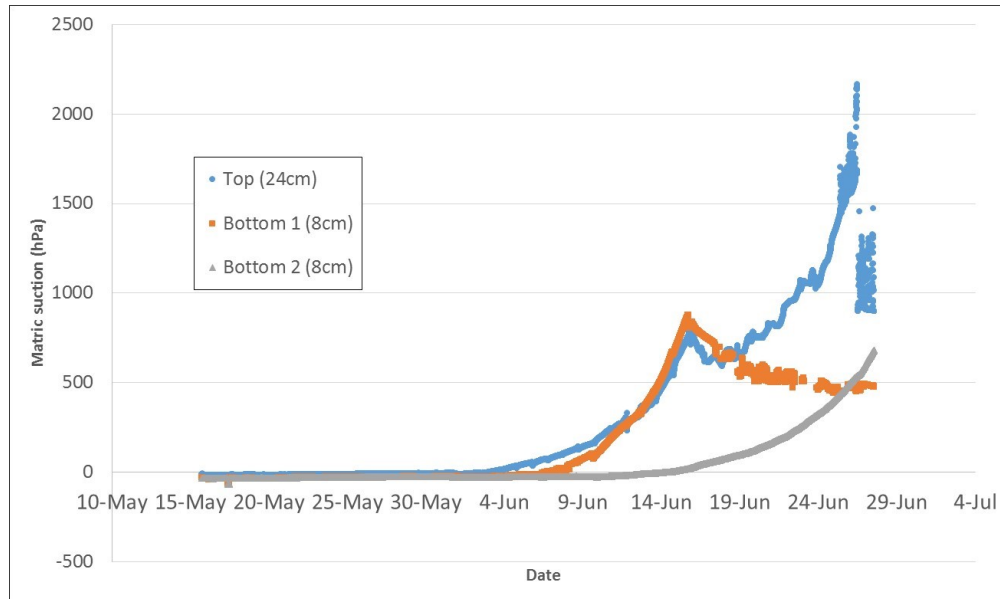


Figure 101: Matric suction at various heights - First layer

#### 4.3.1.1 Surface samples

As shown by Figure 102, the osmotic suction measurements taken from the top 1cm of the tailings surface constitutes the biggest component of total suction for most of the experiment, signaling salt precipitation deposition at the surface. In addition, by analysing the suction increment patterns, it is possible to observe both suction components reaching a maximum value at around June 14th, development coincidentally occurring around the same time as the drop in  $A_E$  of the overall dry box (Figure 91), and the leveling off of the surface GWC (Figure 92), after which point they seemed to converge to a lower suction value. Similar behaviors were observed in the thick-lift dry box test.

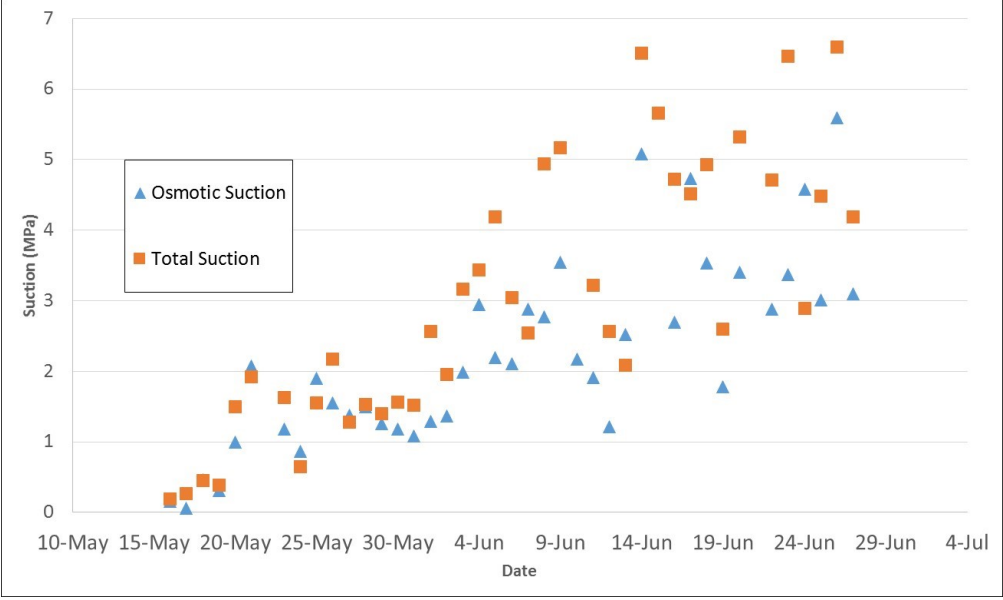


Figure 102: Surface sample total and osmotic suction - First layer

Close examination of the crack progression in this layer (Figure 103) revealed evidence of salt precipitation at the surface from the beginning of June, which correlates with the high relative levels of osmotic suction observed in Figure 102.



Figure 103: Crack progression - First layer

#### 4.3.1.2 Core sample analysis

Once the layer reached an average GWC of 21% (83% solids), a core sample was extracted. The location of the sample within the dry box is shown in Figure 104. During extraction, the sample broke into two pieces, as shown in Figure 105. Numbered from the top down, the sample was used to further study the desiccation history of the layer.



Figure 104: Tailings top view after extraction- First layer

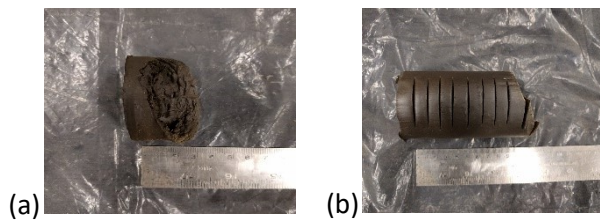


Figure 105: (a) Core sample bottom section and (b) core sample top section, both: top (right hand-side) to bottom (left hand-side) - First layer

Based on observations from Figure 106, the GWC was found to be significantly lower at the top of the layer, explaining the variation in density between the very top of the core and the rest of the sample, observed in Figure 105.

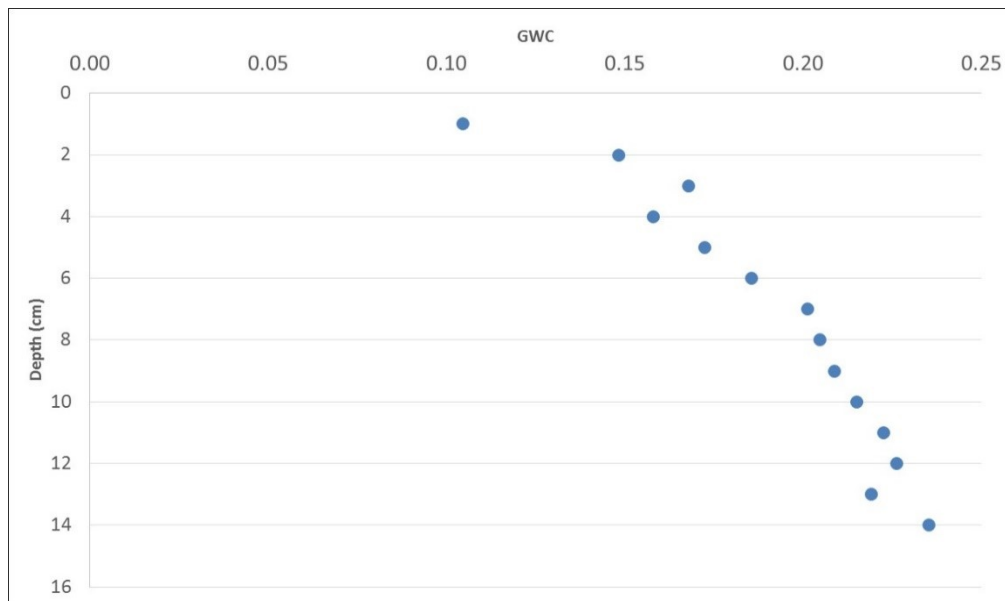


Figure 106: Core sample gravimetric water content profile - First Layer

Suction levels along the height of the tailings were also reported to decrease with depth, as shown in Figure 107. It is also possible to discern consisting high measurements of osmotic suction in relation to salt precipitation observed in Figure 103.

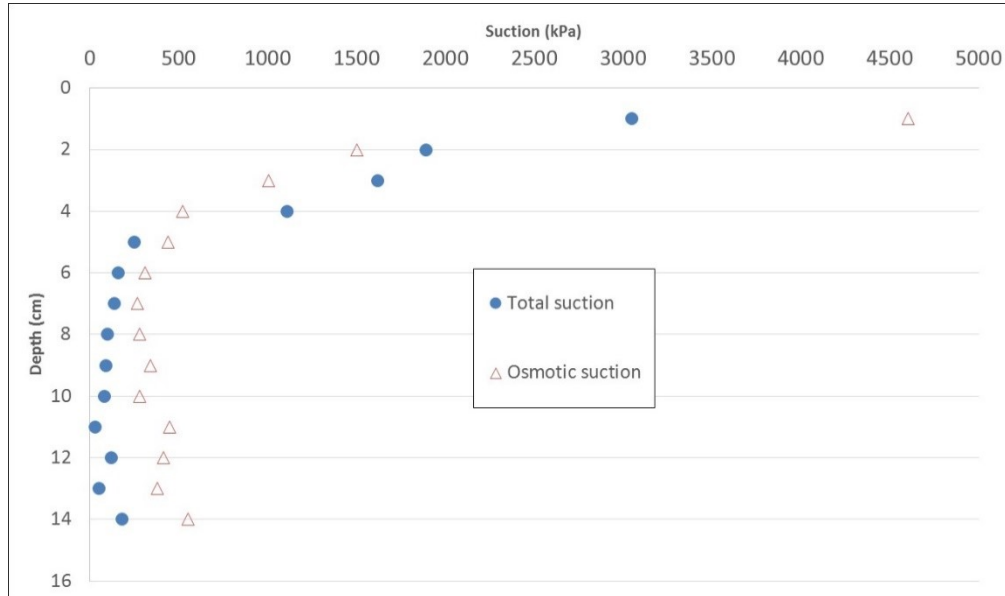


Figure 107: Core sample suction profile - First layer

#### 4.3.2 Second layer deposition

Soon after the core sample was extracted, the second layer (48% solids, 35cm height) was added on top, leading to an initial average GWC of 61% (62% solids), and a total tailings height of 53.5cm. Height achieved after all cracks were filled with new material and some consolidation occurred.

Figure 108 shows  $A_E$  varying between 2.5 to 5mm/d, which is generally in agreement with the first layer. In the same fashion as well, the  $A_E$  was found to generally follow the  $P_E$  pattern up until the end of the experiment. However, very low evaporation values were observed just after deposition, inconsistent with the previous layer. As a result, further observations of this phenomenon may be necessary.

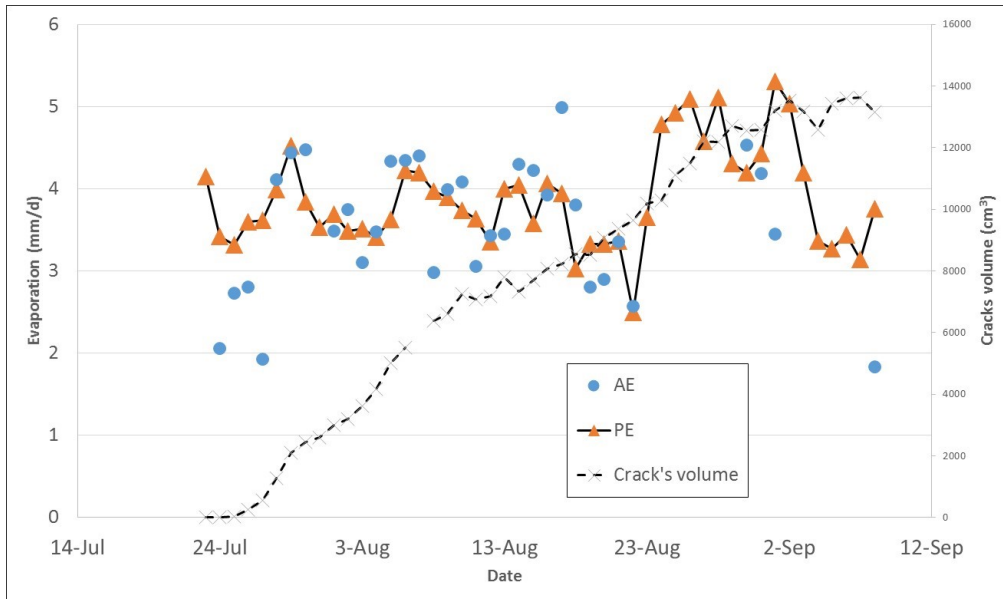


Figure 108: Actual and potential evaporation - Second layer

Figure 109 shows a slow steady decline in the average GWC in the dry box, as expected. In addition, the surface grab samples, consistent with the last layer, also showed a general steady decline in GWC measurements. However, contrary to the first layer, their convergence to a specific value was not clear.

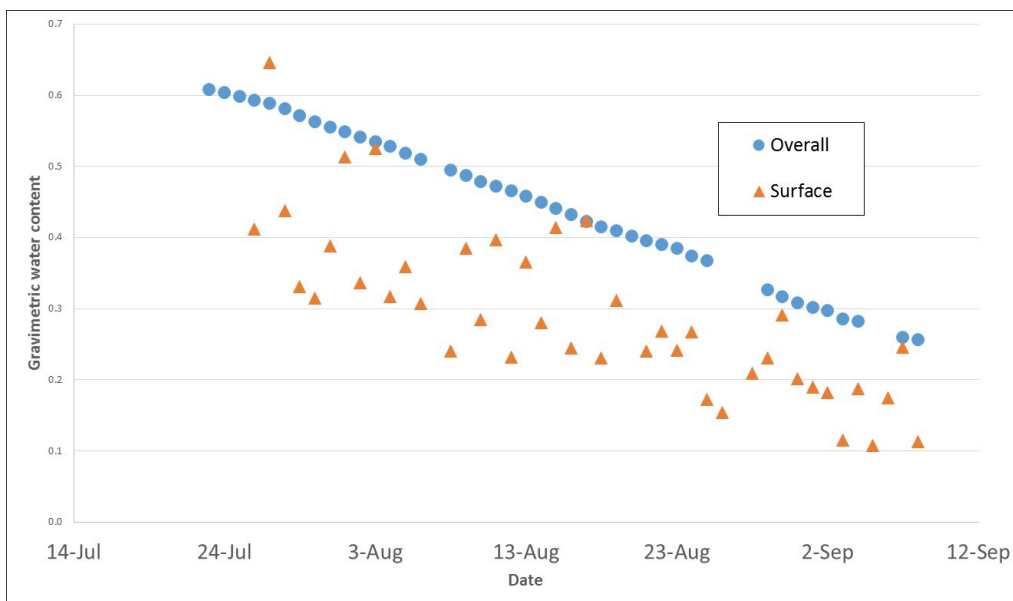


Figure 109: Gravimetric water content - Second layer

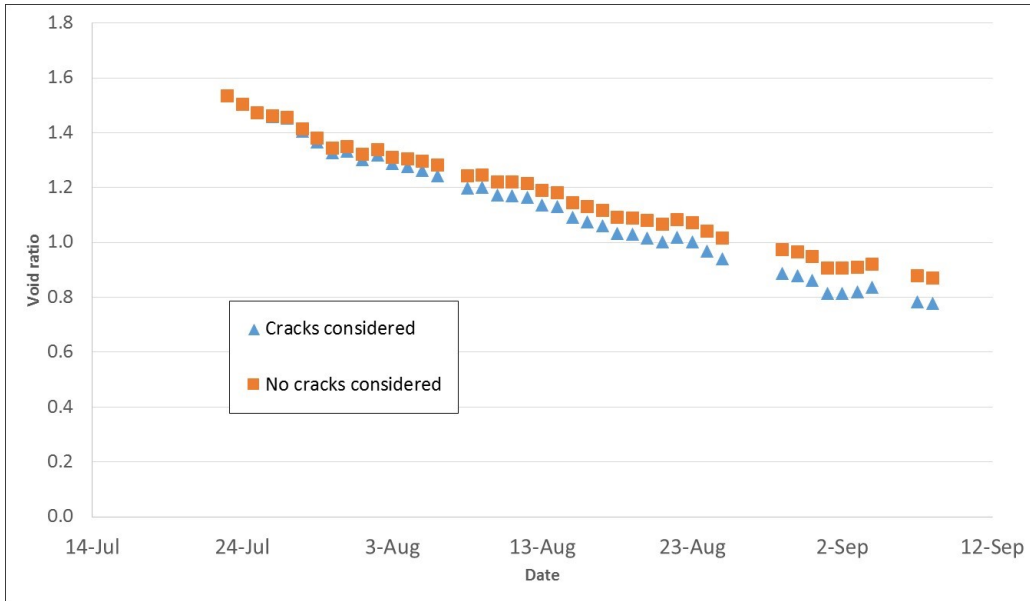


Figure 110: Average void ratio - Second layer

In agreement with the previous layer, Figure 110 and Figure 111 show the influence of crack development in the average void ratio measurements and the steady decline in degree of saturation with desiccation, respectively.

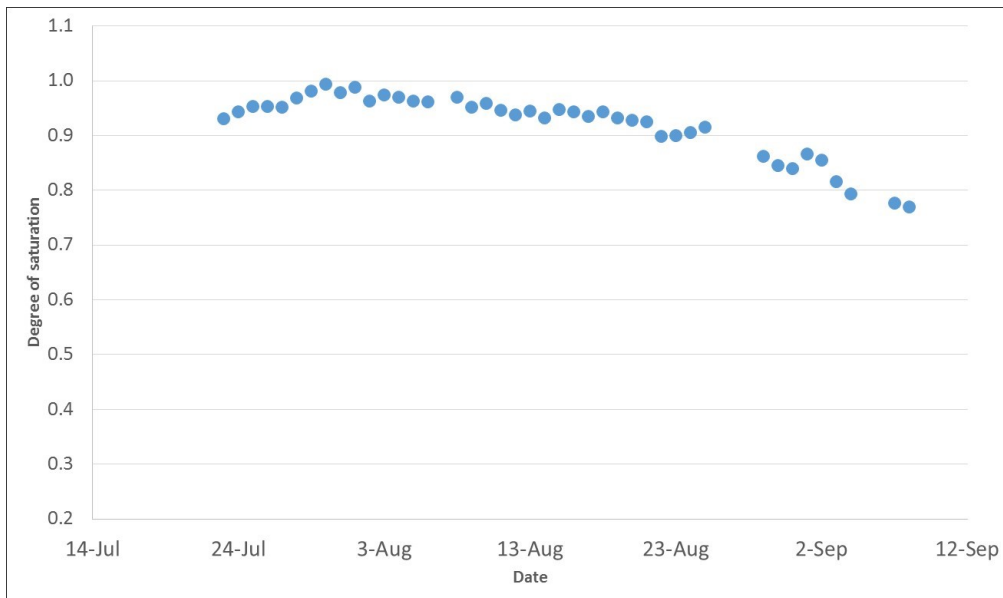


Figure 111: Average degree of saturation - Second layer

Based on the data obtained from the experiment, a shrinkage curve was constructed (Figure 112) from where is possible to discern the shrinking limit being close to 31%, corresponding to a void ratio close to 0.81.

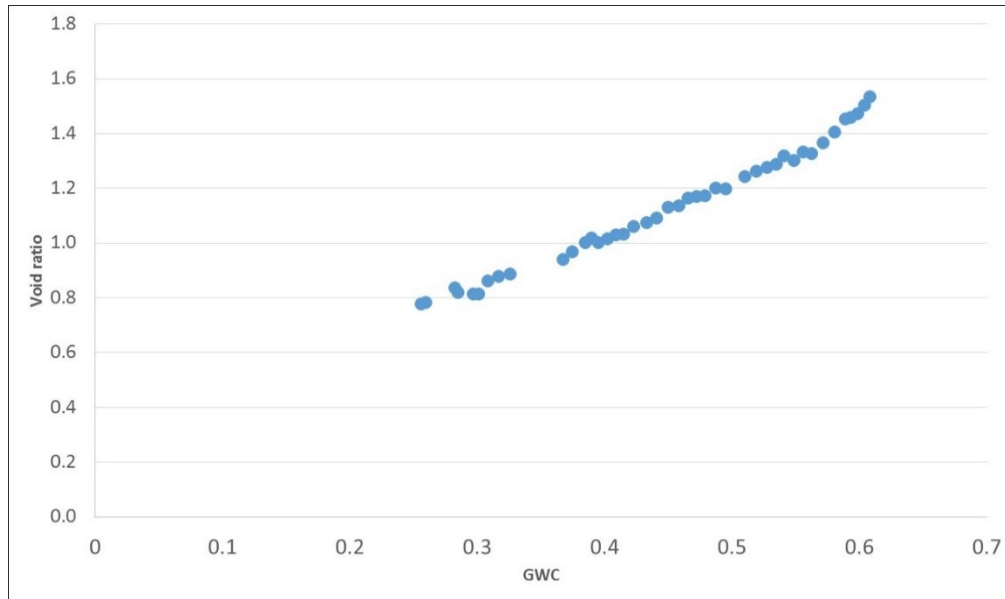


Figure 112: Shrinkage curve - Second layer

Unlike the thick-lift test, the crack volumes developed during this experiment were smaller than the ones of the first layer. In addition, the development occurred more slowly, eventually leveling off to a slightly higher final volume. This inconsistency in crack volumes may be related to the overall rate of evaporation.

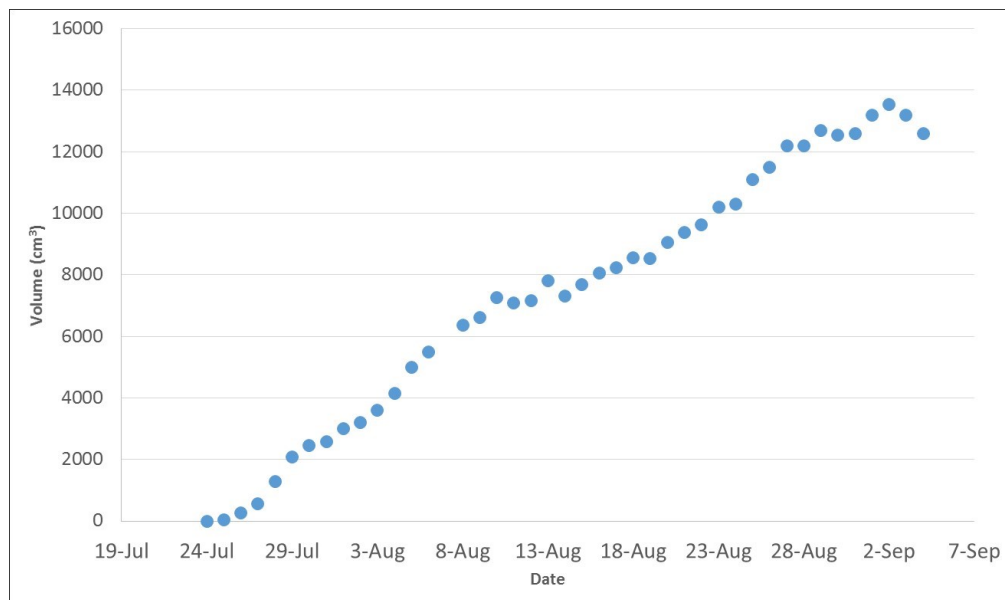


Figure 113: Crack development- Second layer

Figure 114 provides a breakdown of the daily solid content measurements at the surface and within the cracks for this experiment, results similar to the ones obtained in the previous layer.

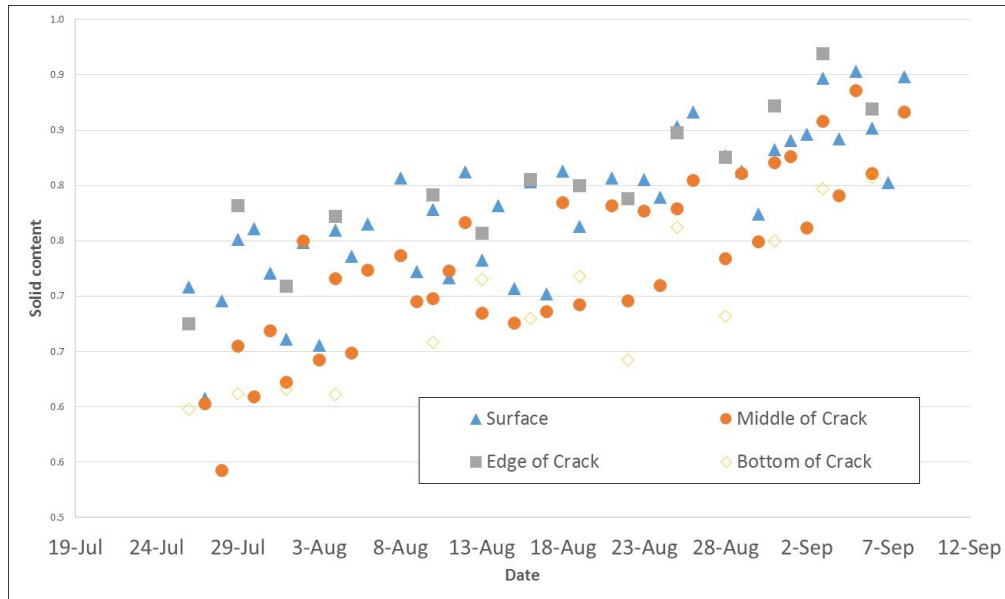


Figure 114: Surface cracks solid content - Second layer

Overall, samples taken from the top 1cm of the surface of the tailings, middle of crack, edge of crack, and bottom of crack analyzed for total suction using the WP4-T dewpoint hydrometer followed a very similar pattern as in the previous layer (Figure 115). However, suction values taken at the edge of cracks reached much greater values as those obtained from the first layer, results that may be attributed to the rate of dewatering of this layer.

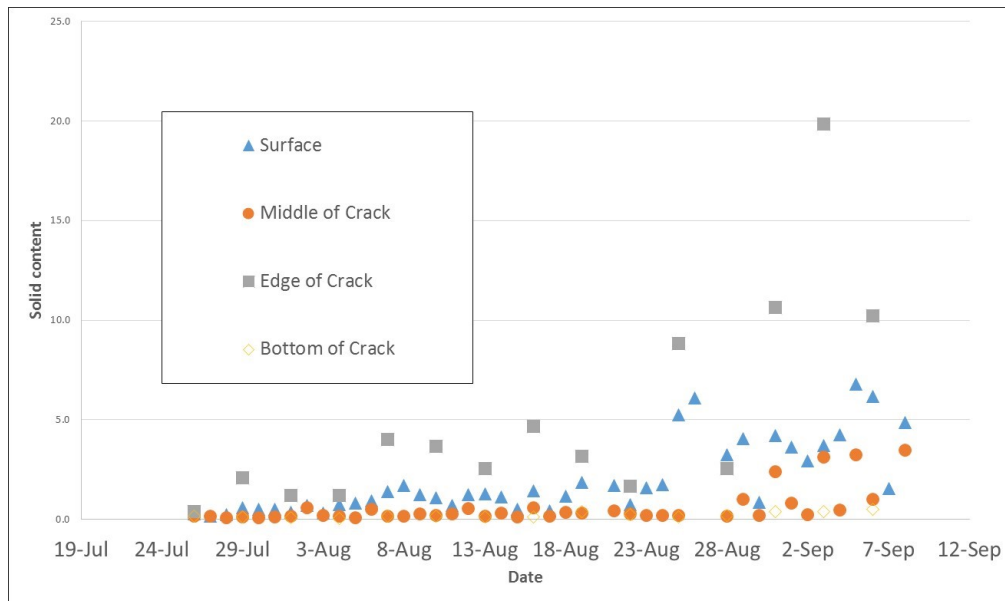


Figure 115: Surface cracks total suction - Second layer

Upon deposition of the second layer, the VWC sensor located on the top layer recorded a steady decrease in VWC through the experiment, as seen in Figure 116, phenomenon correlated to the decrease in VWC measurements recorded by the sensor located at the top of the bottom layer, in Figure 117. As a result, it can be inferred that some infiltration of liquid from the top layer to the bottom layer of the tailings took place, phenomenon also observed during the thick-lift test.

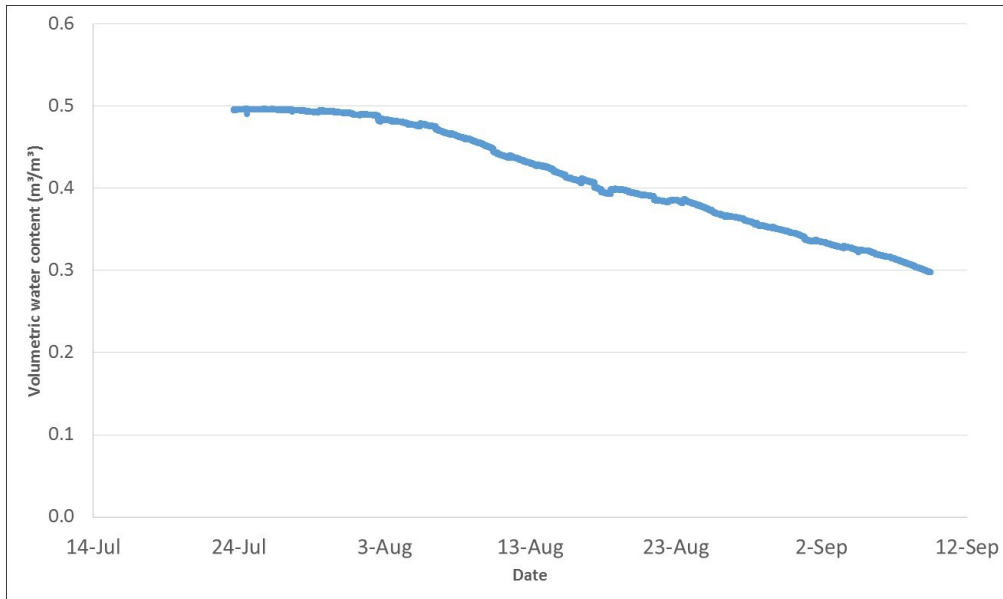


Figure 116: Volumetric water content top layer–Second layer

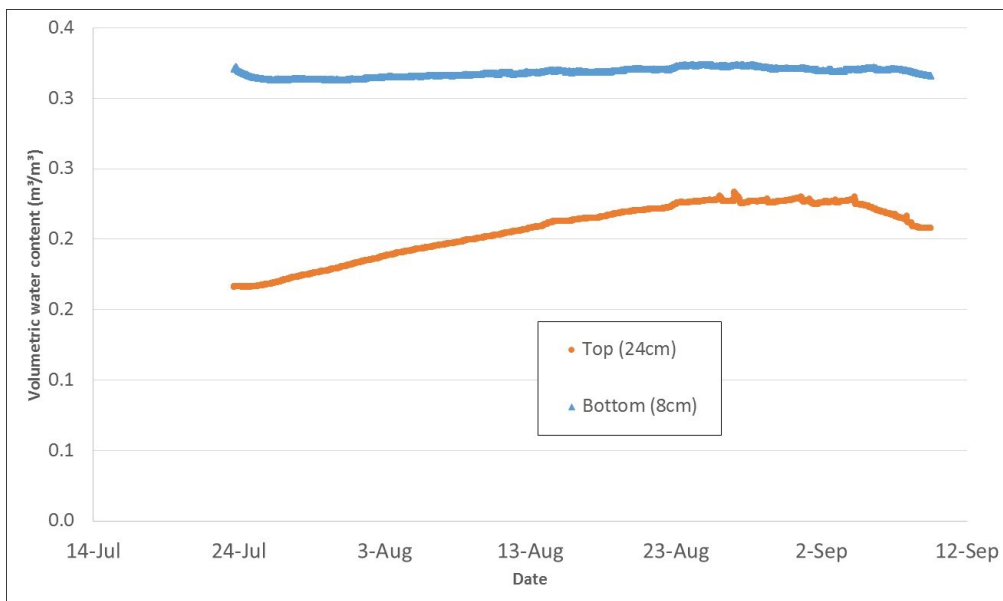


Figure 117: Volumetric water content bottom layer - First layer

Figure 118 shows the cumulative drainage obtained after deposition. As observed, somewhat of an increment was recorded by August 20<sup>th</sup>.

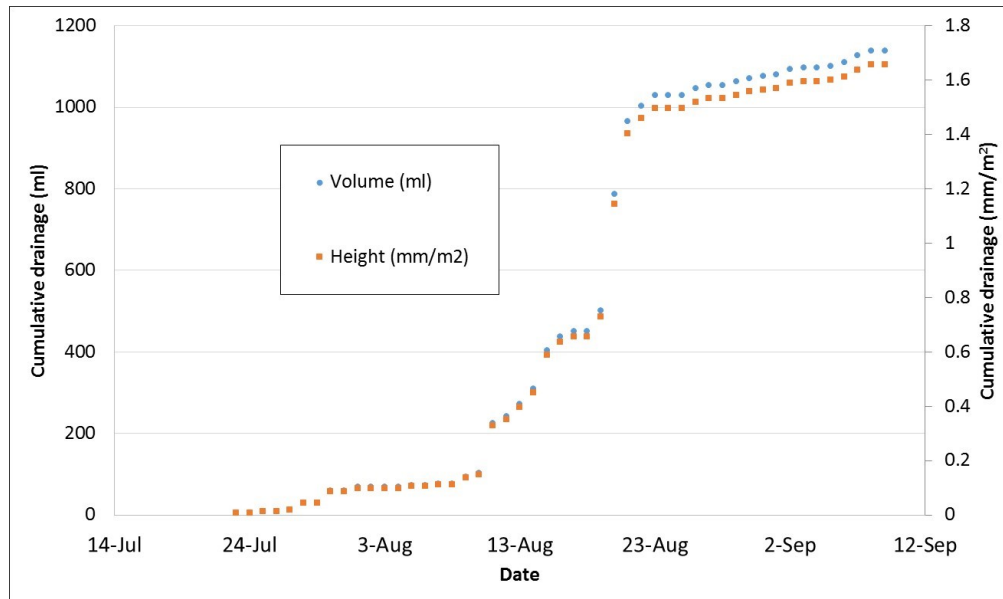


Figure 118: Cumulative drainage - Second layer

Prior to deposition, two tensiometers were inserted to the top layer at the same height (Figure 119), both recording much sharper increments in matric suction in comparison to the first layer, around August 10<sup>th</sup>. However, in the bottom layer (Figure 120), no discernable decrease in matric suction is observed at the top, indicating just limited infiltration from the top layer. On the other hand, a rapid decrease in the matric suction at the bottom of the layer could have contributed to further consolidation just after deposition.

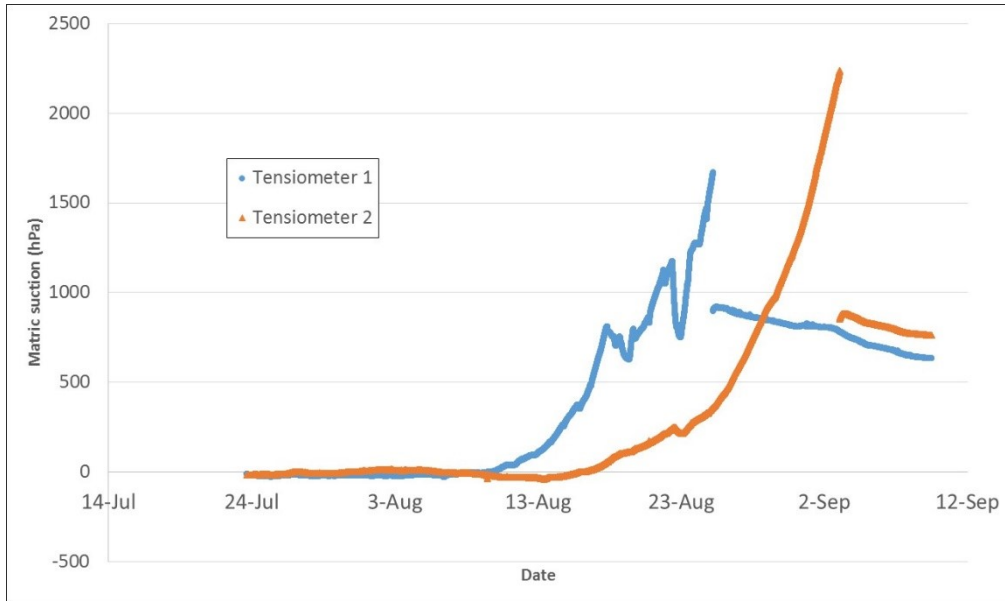


Figure 119: Matric suction top layer - Second layer

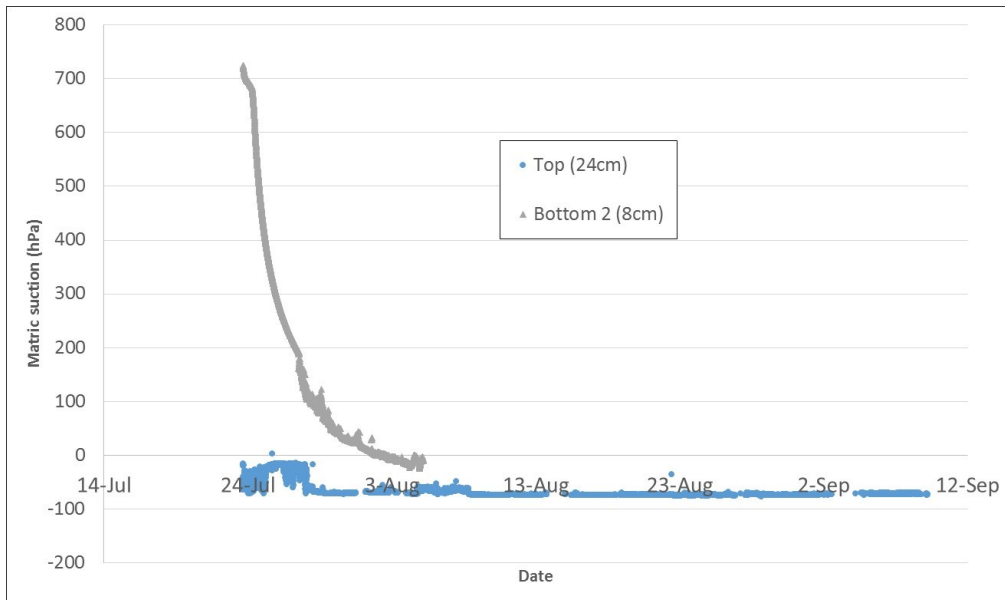


Figure 120: Matric suction bottom layer - Second layer

#### 4.3.2.1 Surface samples

Figure 121 shows somewhat of a incremental pattern, including a high increment in the suction measurements by the end of August. In addition, in agreement with previous experiments, the osmotic suction is relatively large in comparison to total suction, implying some evidence of mass transport along the tailings height, as can be observed in Figure 122.

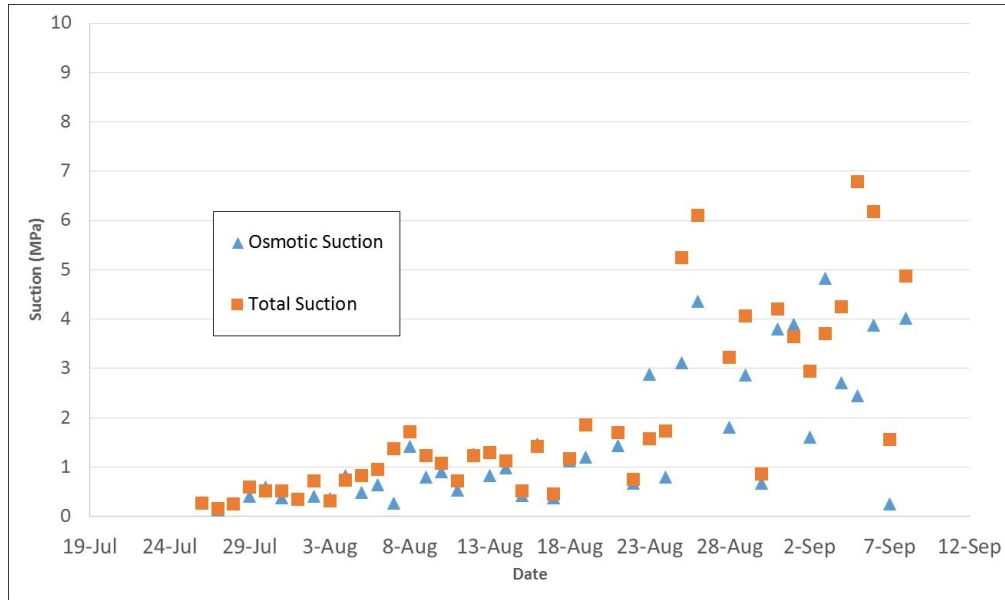


Figure 121: Surface sample total and osmotic suction - Second layer

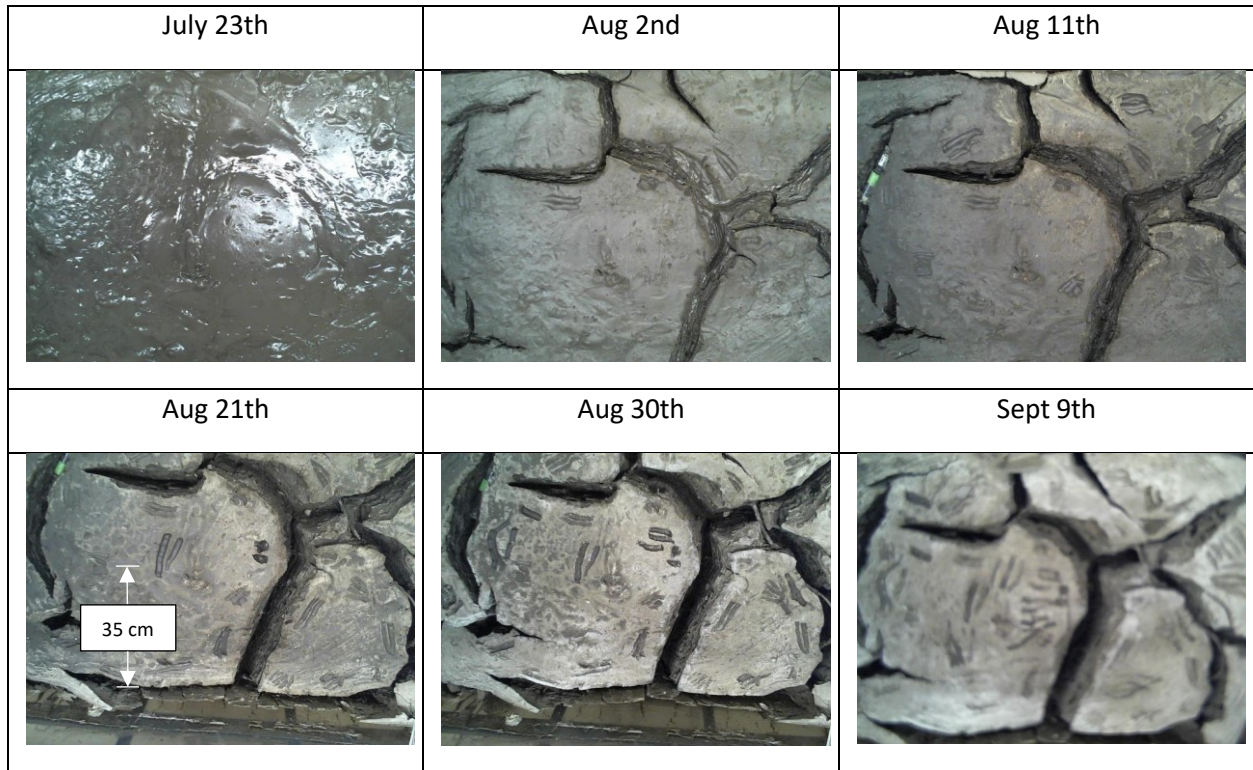


Figure 122: Crack progression - Second layer

#### 4.3.2.2 Core sample analysis

A core sample was extracted once the dry box reached an average GWC of 26% (80% solids). Obtained from the right-side of the tailings (Figure 123), the sample was extracted in three separate sections, as can be seen in Figure 124. Numbered from top to bottom:



Figure 123: Tailings top view after extraction- Second layer



Figure 124: Core sample from top (right hand-side) to bottom (left hand-side) - Second layer

As can be seen from Figure 125, in this sample, the GWC does not vary as much as previous cases, suggesting uniform drying with depth.

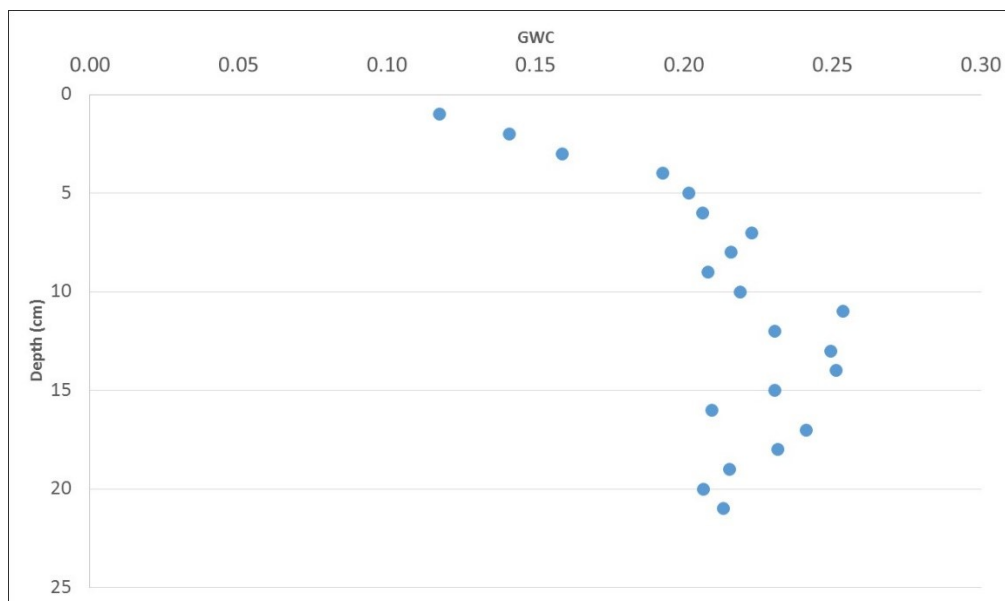


Figure 125: Core sample gravimetric water content profile - Second layer

In the case of suction, the resulting suction measurements do imply some dissolved mass transport, although limited in comparison to previous cases (Figure 107).

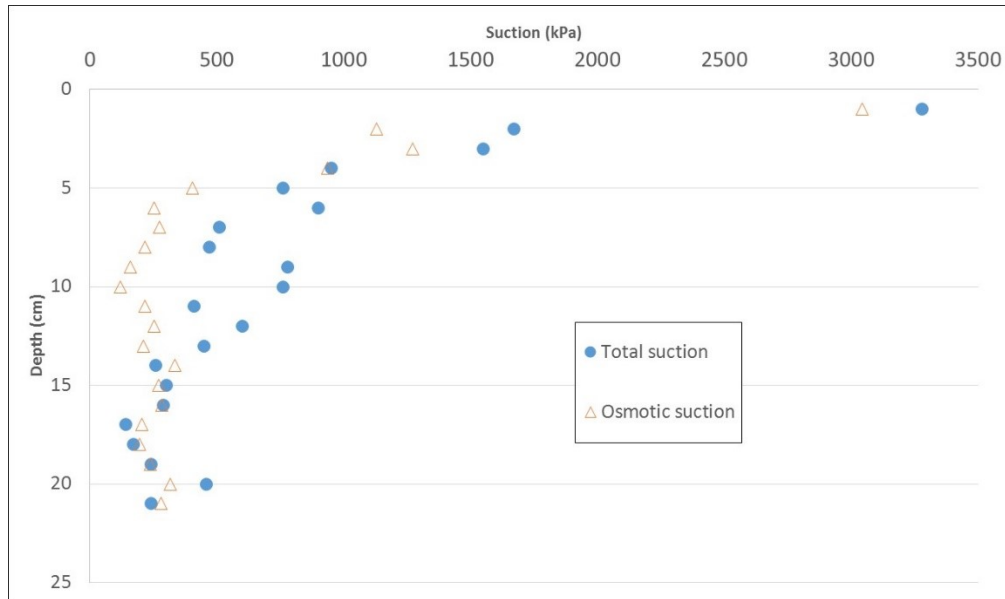


Figure 126: Core sample suction profile - Second layer

#### 4.3.3 Third layer deposition

The final layer (48% solids, 35cm height) was added to the dry box once the average GWC reached a value of 26% (80% solids), leading to an initial average GWC of 51% (66% solids) and a total tailings height of 71.5cm after consolidation.

As observed in Figure 127,  $A_E$  varied between 3 to 7mm/d. In this case,  $A_E$  followed an ambiguous oscillation pattern until the end of the experiment, at which point it fell below the  $P_E$ . These results agree with the observations of previous layers.

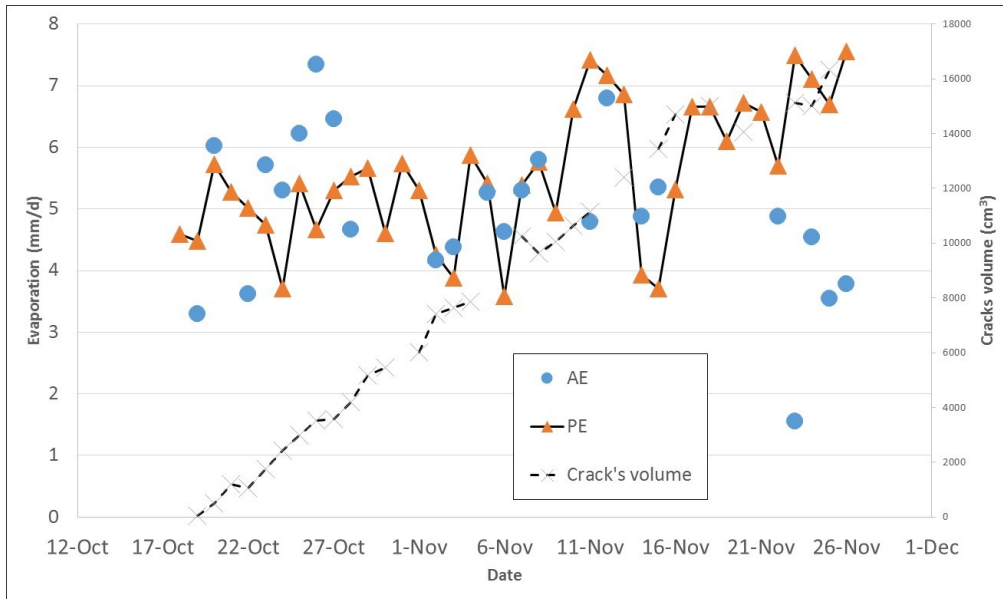


Figure 127: Actual and potential evaporation - Third layer

As expected, the dry box average GWC uniformly decreased over time (Figure 128). However, as in the previous layer, the GWC measurements obtained from the surface grab samples decreased in value indefinitely in a similar way.

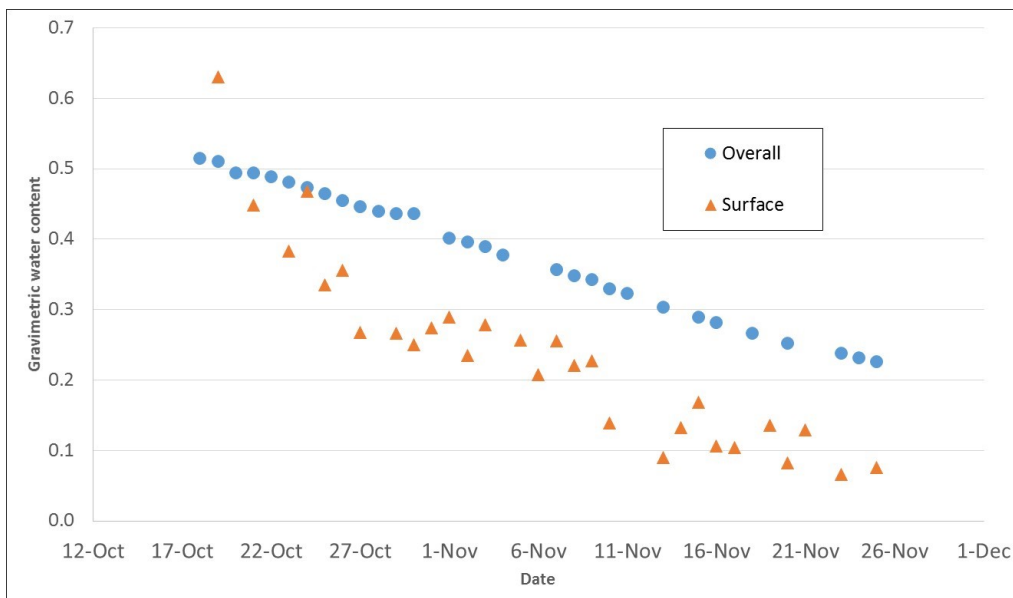


Figure 128: Gravimetric water content - Third layer

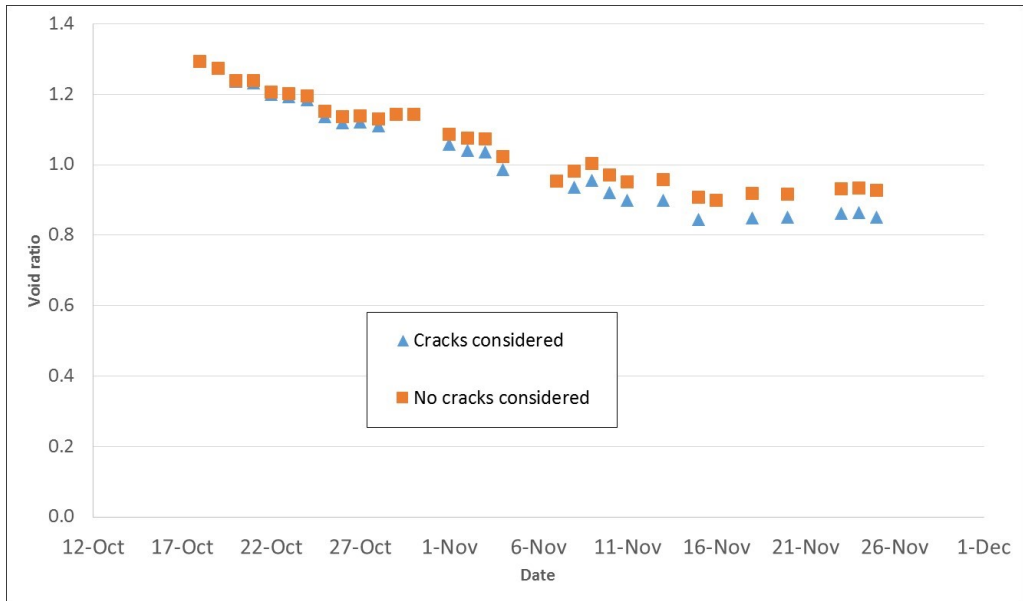


Figure 129: Average void ratio - Third layer

Data obtained from the senix sensors and load cells yielded a void ratio variation as observed in Figure 129. Cracks considered, the void ratio was observed to decrease more rapidly than without considering them, as previous cases.

Figure 130 shows the change in degree of saturation after the deposition of the third layer.

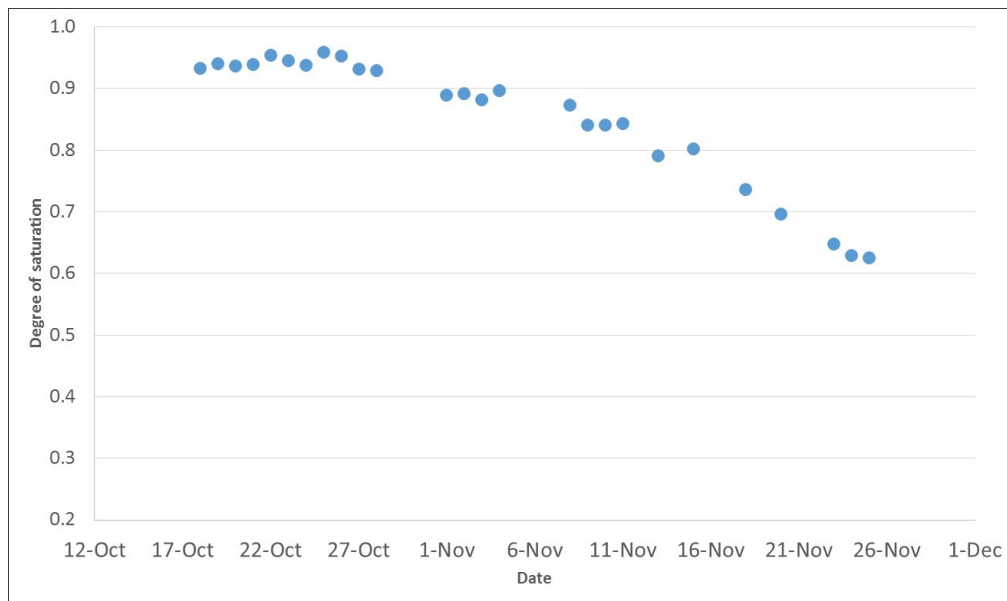


Figure 130: Average degree of saturation - Third layer

In this case, the shrinkage curve derived from the overall volume and mass variations of the dry box clearly identifies the shrink limit of the material around a GWC of 31%, corresponding to a void ratio of 0.81, shown in Figure 131, in agreement with the previous layer.

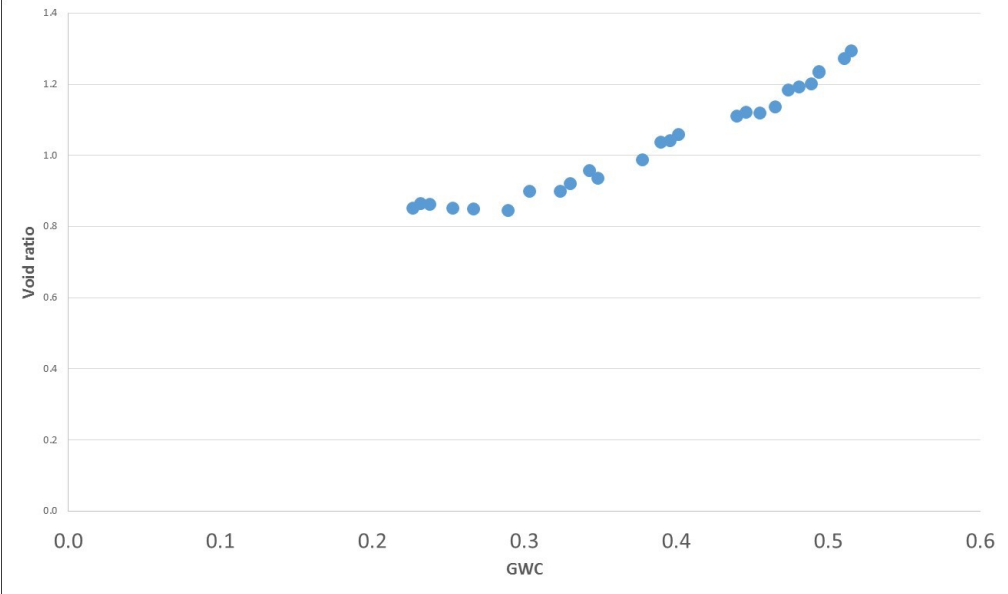


Figure 131: Shrinkage curve - Third layer

Interestingly, crack development for this layer mimicked the first layer pattern, both peaking around the 30th day of evaporation (Figure 132).

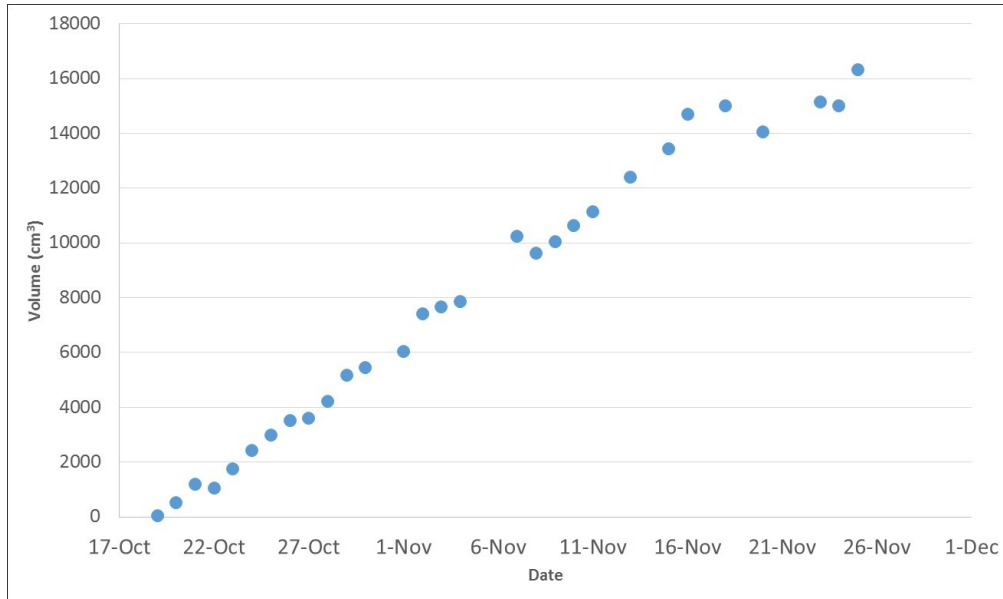


Figure 132: Crack development- Third Layer

Figure 133 describes a similar pattern of dewatering for samples taken at the surface at various locations to the ones obtained in previous layers.

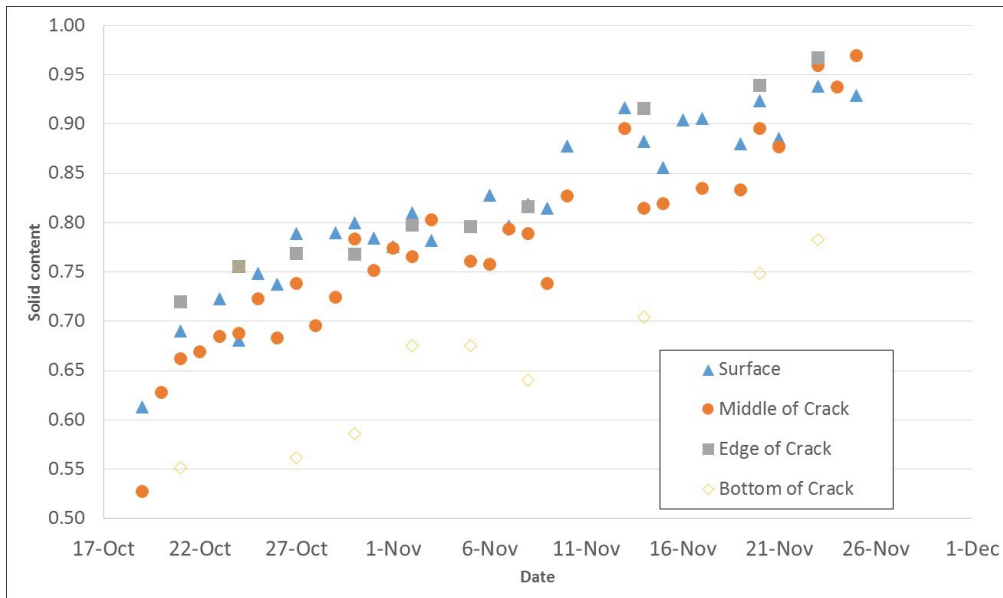


Figure 133: Surface cracks solid content - Third layer

Daily suction measurements, shown in Figure 134, greatly surpassed the measurements obtained by the previous layers, suggesting a faster rate of dewatering at the surface level of the tailings. This phenomenon can be contributed to the combined effects of infiltration by both underlying layers as well as evaporation.

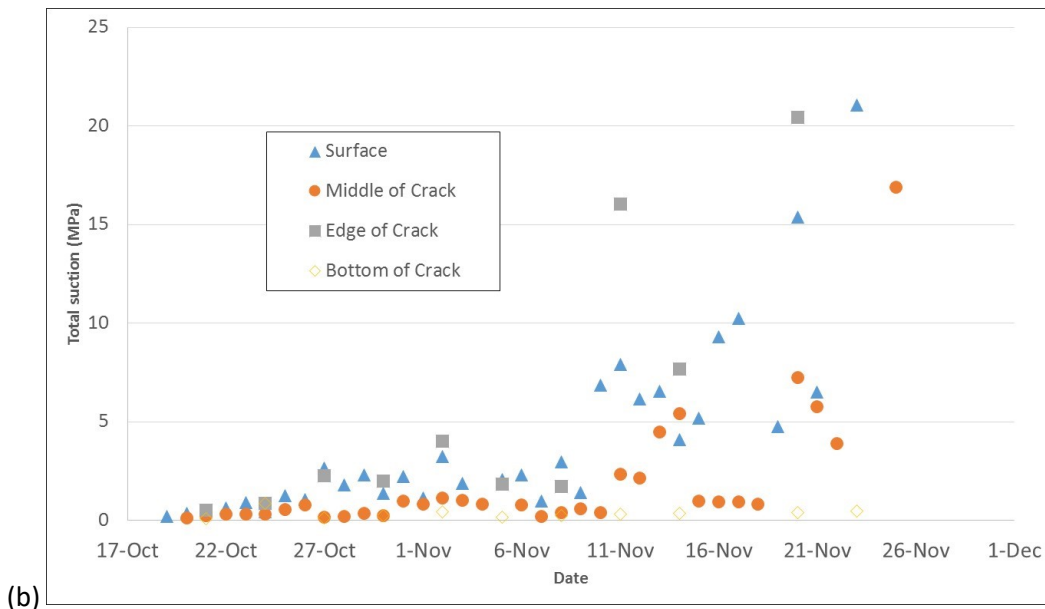
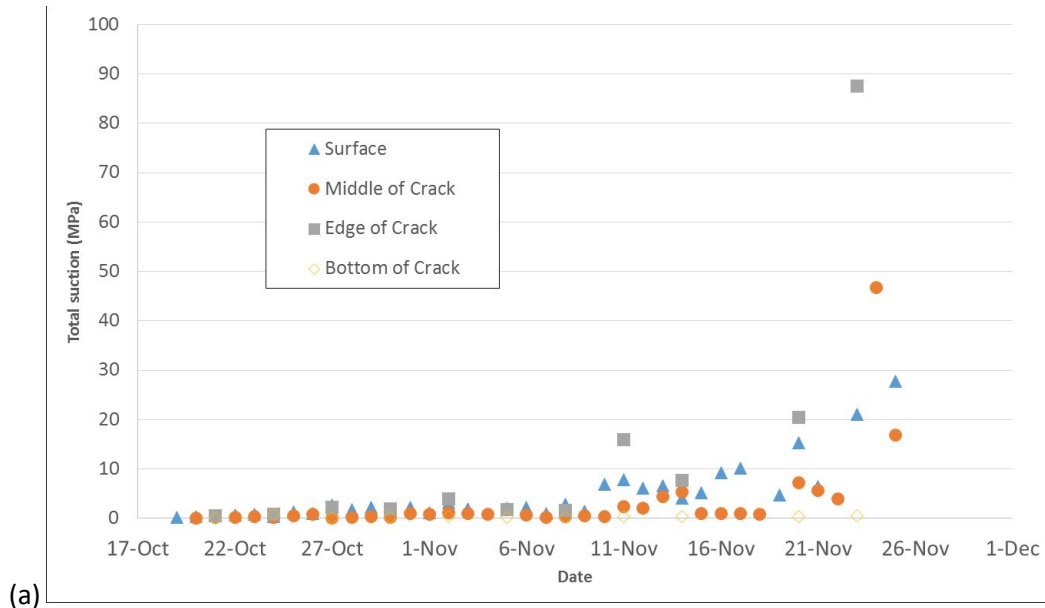


Figure 134: Surface cracks total suction (a) regular figure and (b) low suction range detail - Third layer

The volumetric water content readings for this layer suggested a great influence of evaporation at the top of the tailings, evident by the initial sharp decline in VWC at the surface, later followed by a subsequent decrease at the bottom of that layer (Figure 135). This is also evident by the sudden increment and later decrease in VWC in the middle layer, suggesting some initial liquid infiltration from the top layer and eventual removal by evaporation (Figure 136). Finally, no apparent change in VWC in the bottom layer (Figure 137), nor large increment in drainage (Figure 138), imply little influence of evaporation or consolidation at this level.

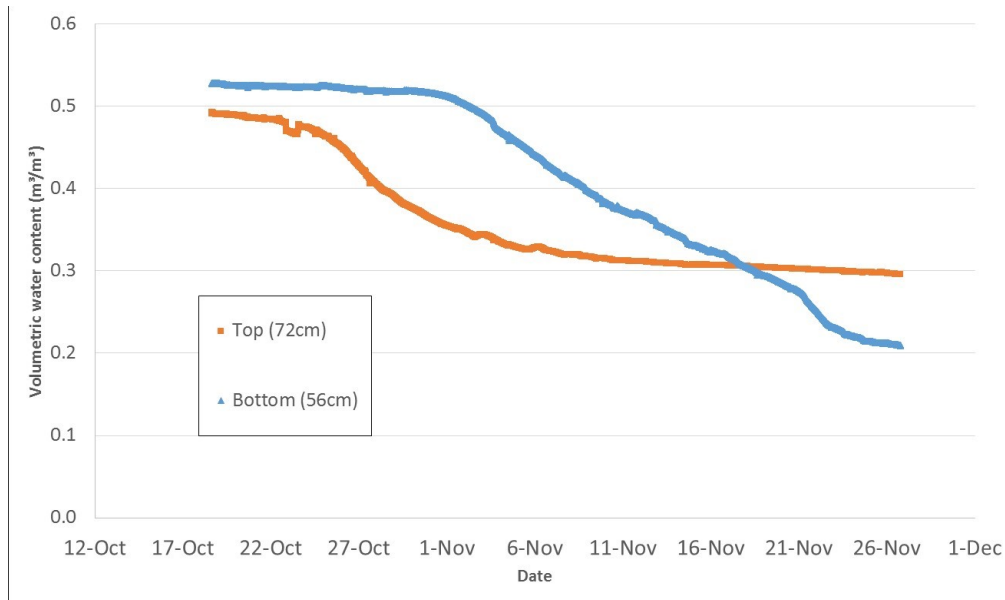


Figure 135: Volumetric water content at various heights top layer –Third layer

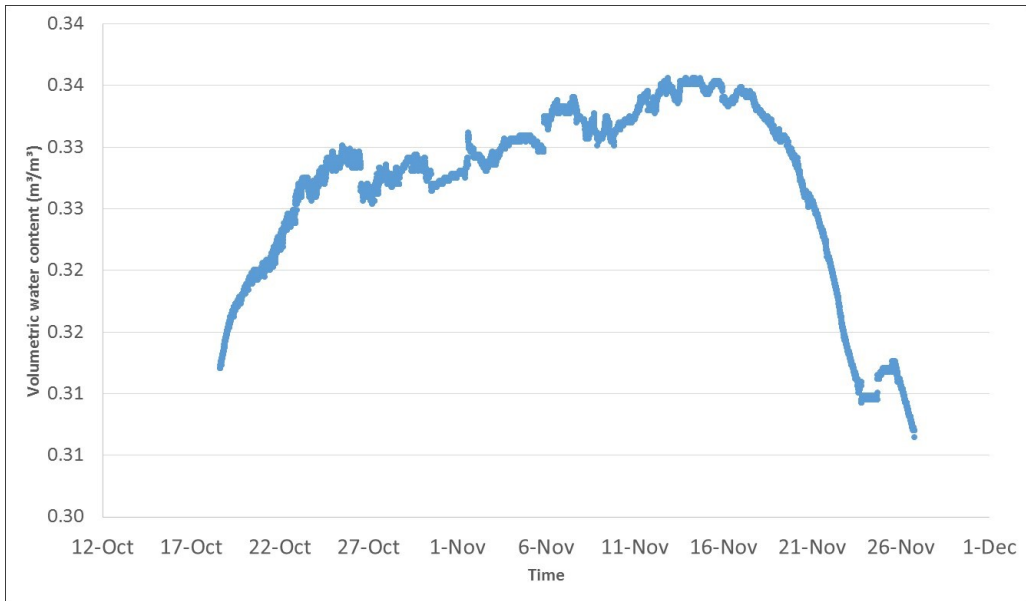


Figure 136: Volumetric water content middle layer –Third layer

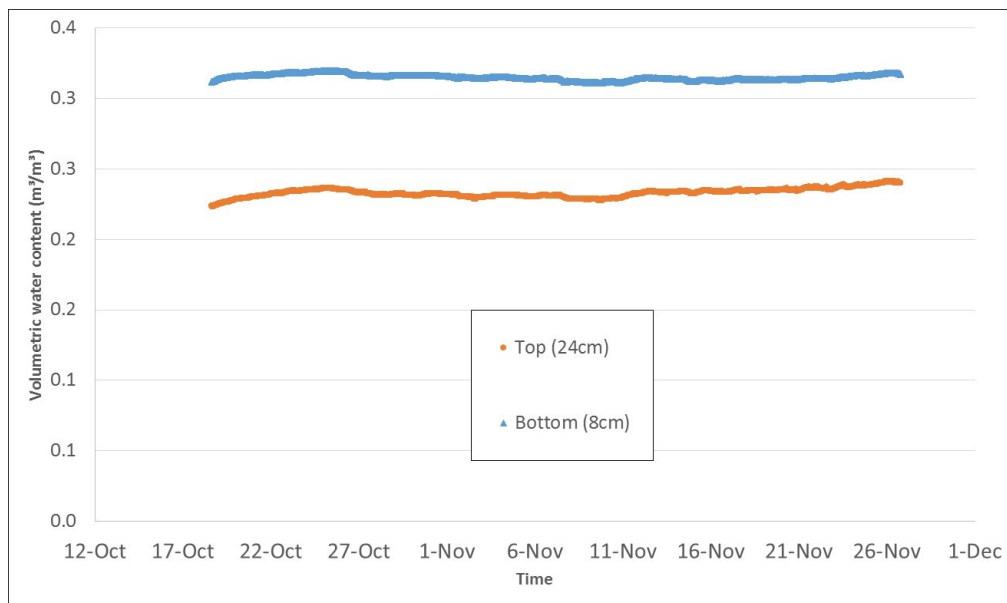


Figure 137: Volumetric water content at various heights bottom layer - Third layer



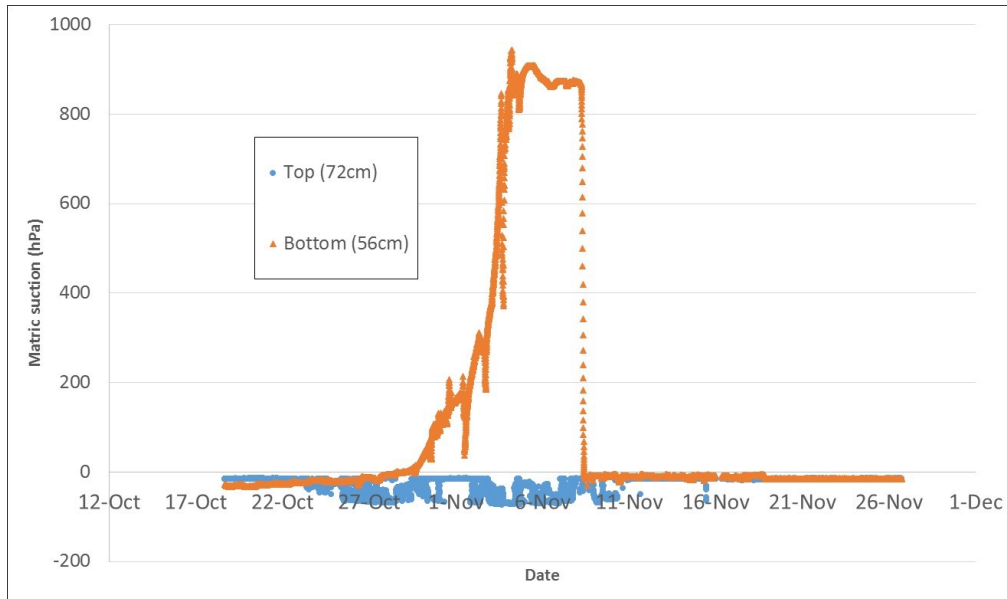


Figure 139: Matric suction at various heights top layer - Third layer

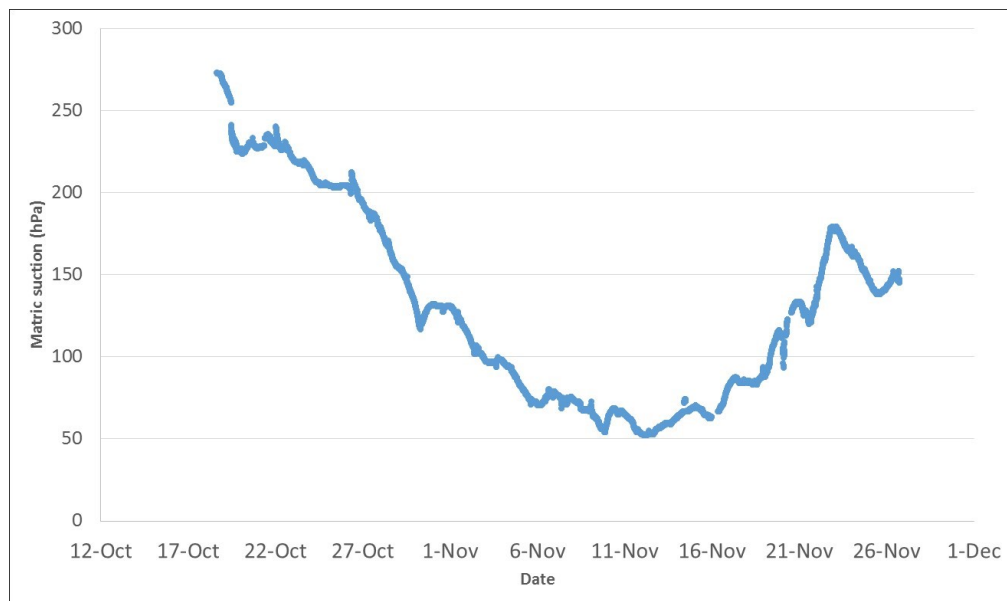


Figure 140: Matric suction middle layer - Third layer

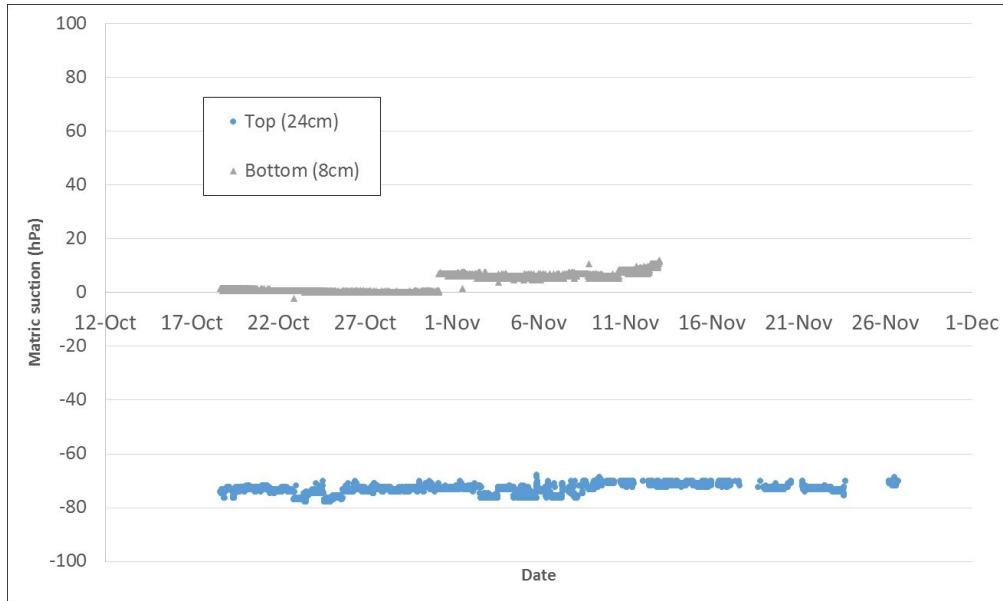


Figure 141: Matric suction at various heights bottom layer - Third layer

#### 4.3.3.1 Surface samples

Similar to previous layers, the ratio between osmotic and total suction throughout the experiment suggested some degree of mass precipitation into the surface of the tailings, as shown in Figure 142. In addition, as the experiment progressed, suction measurements were found to reach a maximum value about November 11<sup>th</sup>, as in previous cases.

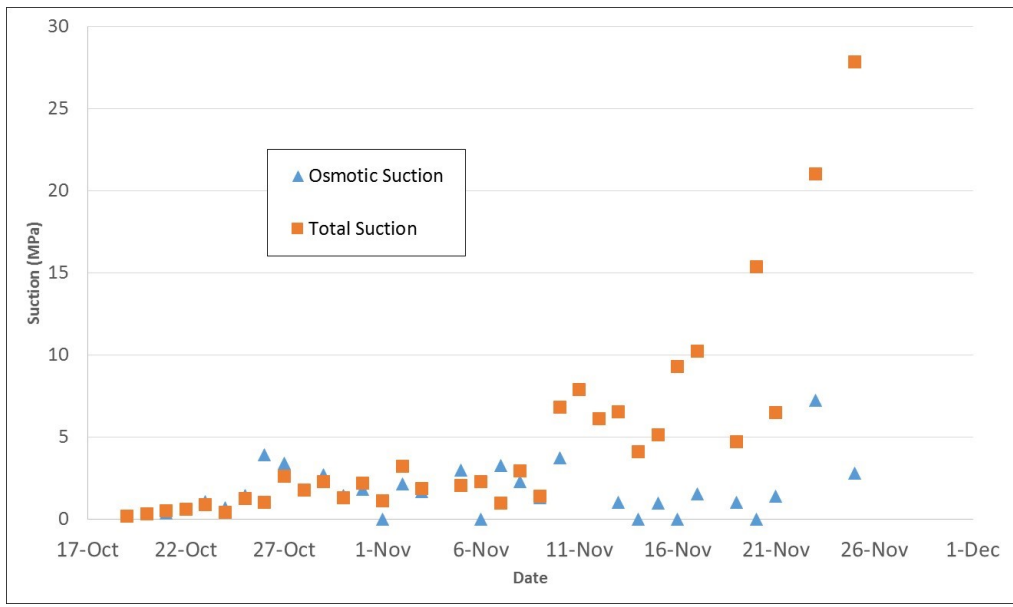


Figure 142: Surface sample total and osmotic suction - Third layer

Figure 143 reveals limited mass precipitation on the surface of the tailings relative to other layers examined in this study.

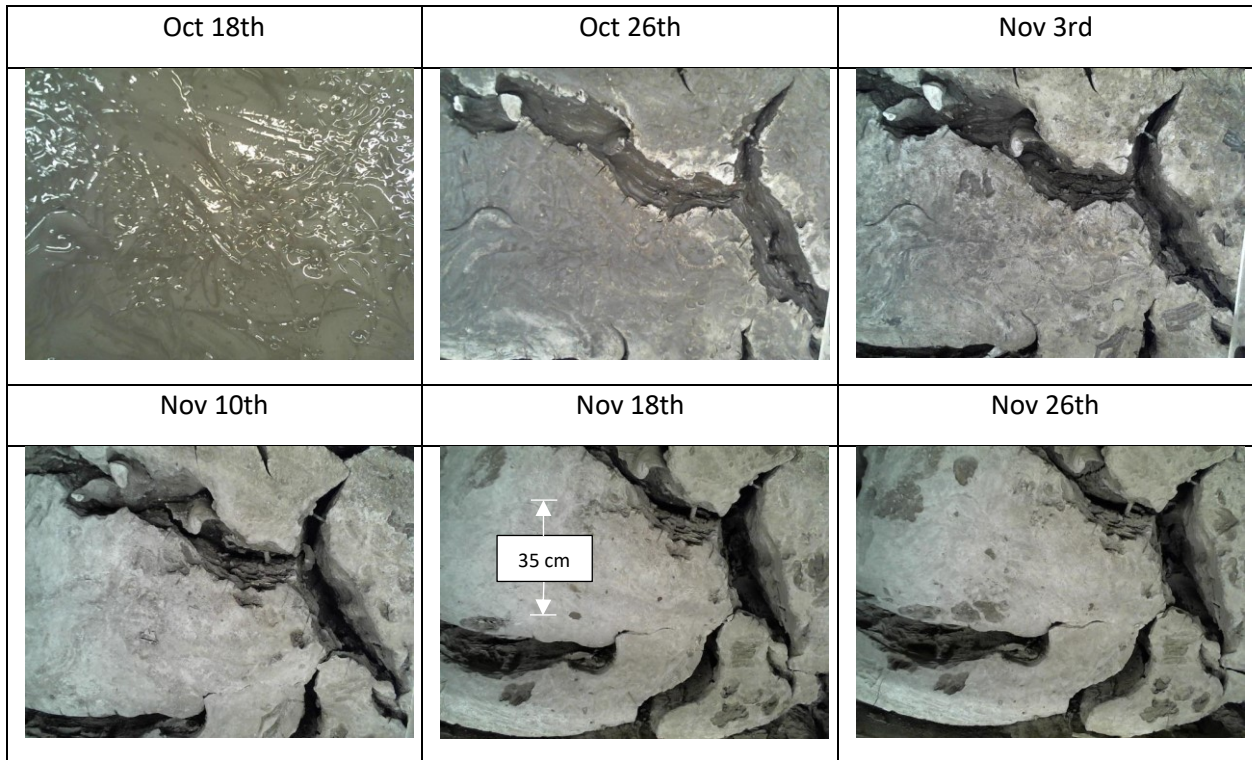


Figure 143. Crack progression -Third layer

#### 4.3.3.2 Core sample analysis

Once the second layer was completed (23% GWC, 82% solids), a core sample was extracted from the right-hand side of the dry box (Figure 144). Due to the strength of the tailings in the surface, however, the sample had to be drilled out of the dry box, resulting in its sectioning, as shown in Figure 145:



Figure 144: Tailings top view after extraction- Third layer



Figure 145: Core sample from top (right hand-side) to bottom (left hand-side) - Third layer

As observed from Figure 145, the bottom section of the tailings mostly corresponded to the bottom layer which did not experience much desiccation after deposition, conclusion backed by the results in Figure 146, where the highest GWC values corresponds to the lowest height intervals. Similarly, GWC was found to be the lowest at the top of the tailings, which is also evident from Figure 145.

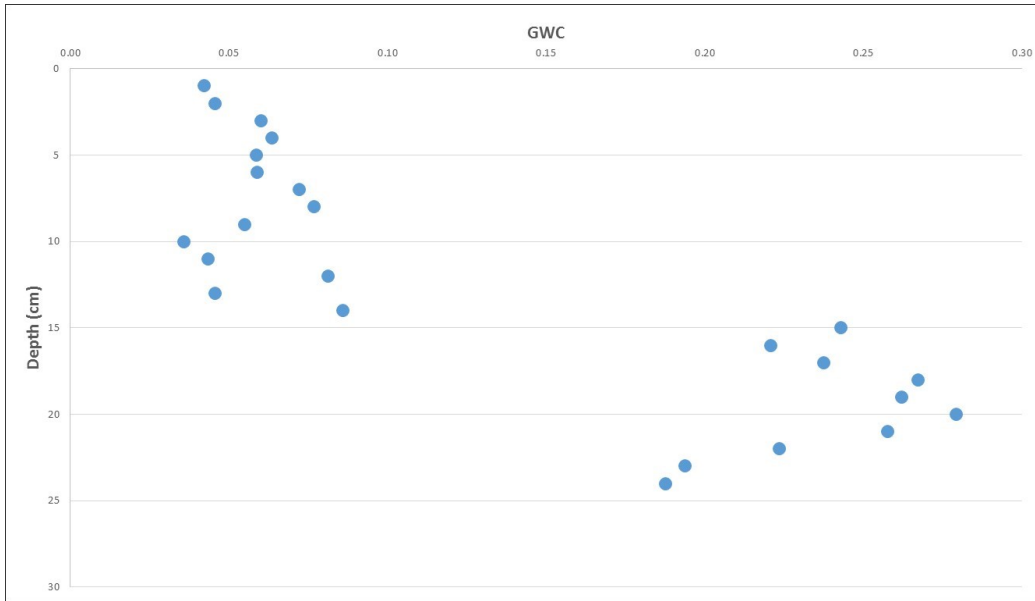


Figure 146: Core sample gravimetric water content profile - Third Layer

Figure 147 depicts the strong influence of osmotic suction relative to total suction along the tailing's depth. This indicates the influence of mass precipitation throughout the tailings.

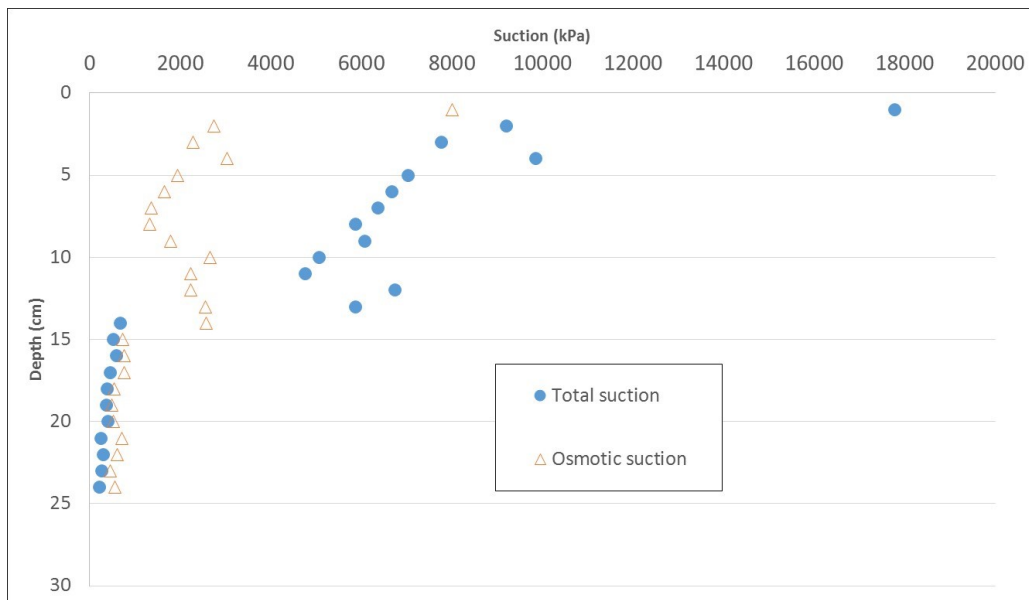


Figure 147: Core sample suction profile - Third layer

#### 4.4 Thin-lift overall results

This section analyses the overall results of the thin-lift dry box test.

Figure 148 shows the overall temperature profile of the dry box, constructed from the temperature measurements associated to the VWC sensors located along the height of the dry box, as well as the temperature measurements from an Easy Log USB sensor situated above the tailings. In a similar fashion as the thick-left test, temperature values remained the highest at the bottom, decreasing with elevation. Here, as well, the highest temperatures were recorded above the tailings.

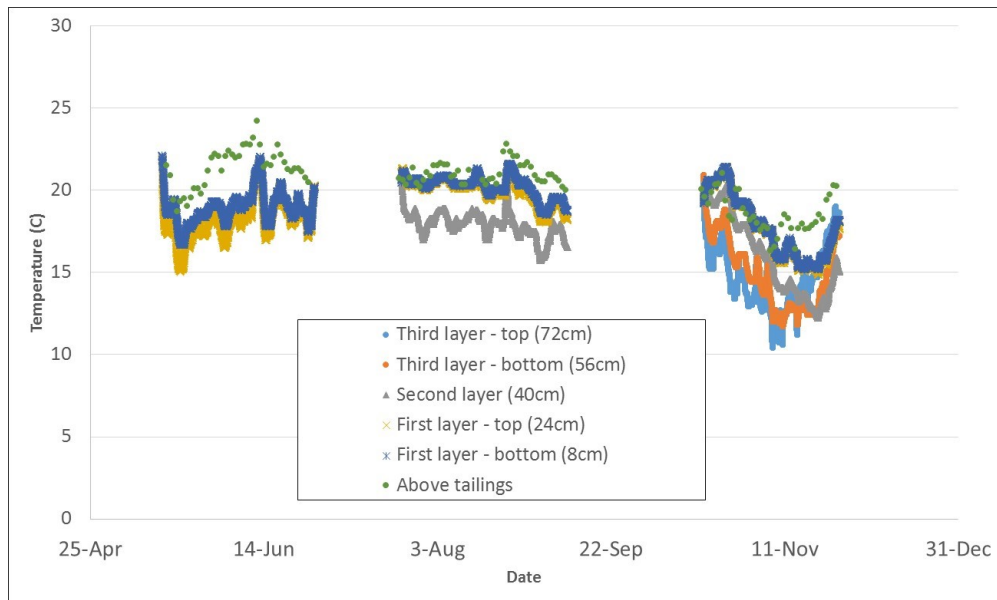


Figure 148: Overall temperature profile - Thin-lift test

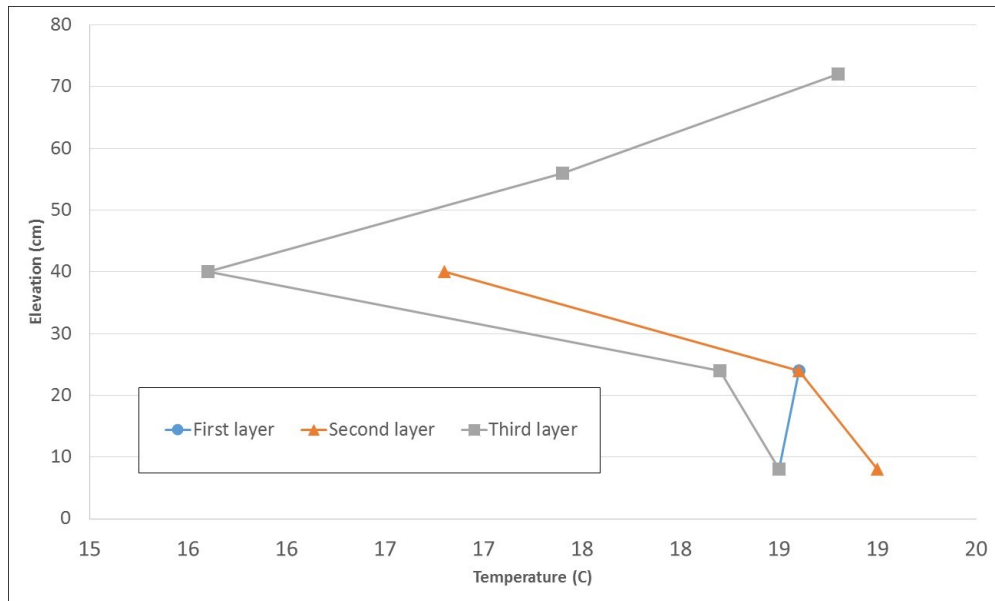
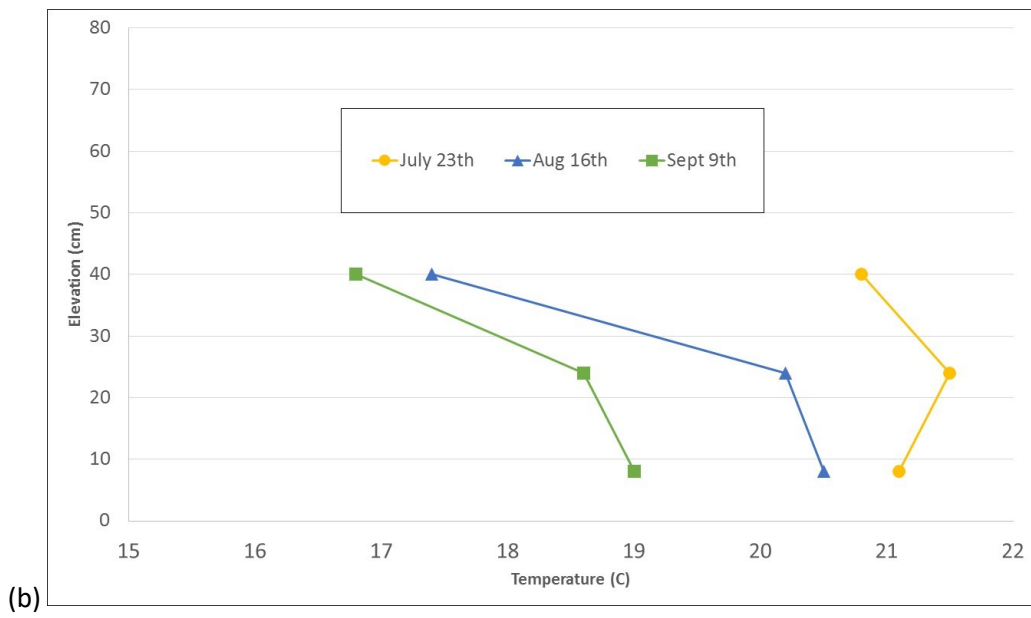
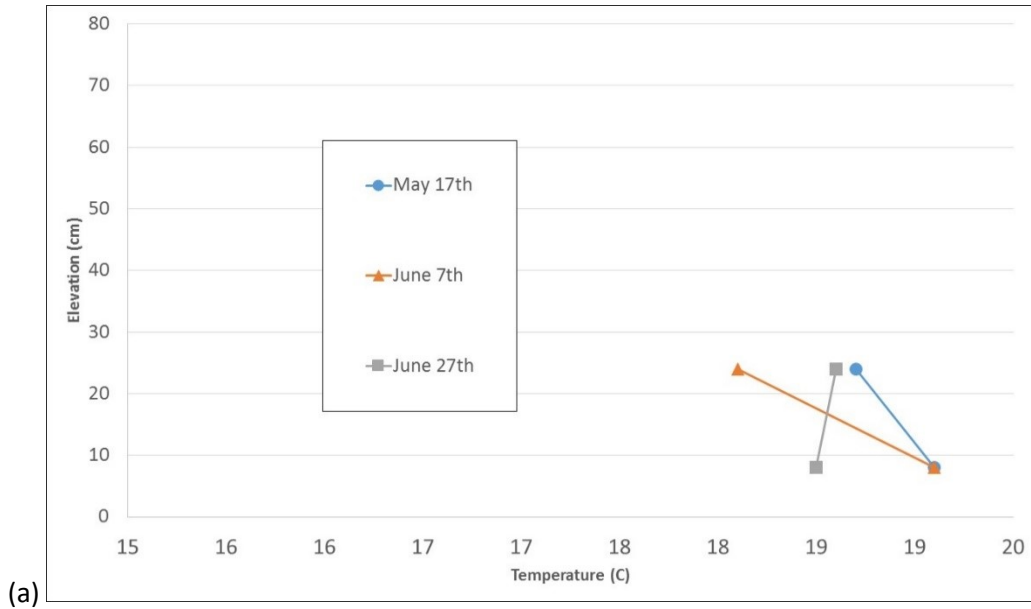


Figure 149: Temperature profiles upon completion of each layer - Thin-lift test

Using the VWC sensor data, temperature profiles were plotted for each layer just as the desiccation process was getting to an end (Figure 149). Interestingly, temperatures were found to increase with depth, while the bottom remained more or less constant. Observations further supported by analyzing the temperature profiles evolution over time (Figure 150). Indeed, for most of the desiccation process, the lowest temperatures remained at the top of the tailings. As per the high temperature observed at the top of the tailings upon completion of the third layer (Figure 149), this value may be caused by the particular large drop in  $A_E$  relative to  $P_E$  which occurred on this layer. This outcome, in turn, possibly reduced the amount of evaporative cooling caused by evaporation, and therefore, increased the surface temperature.



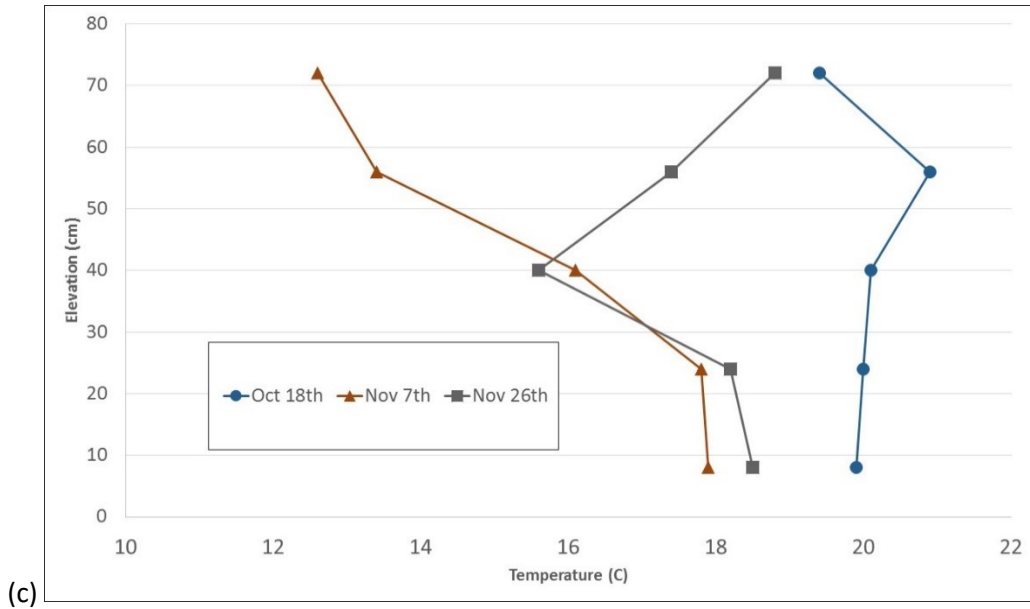
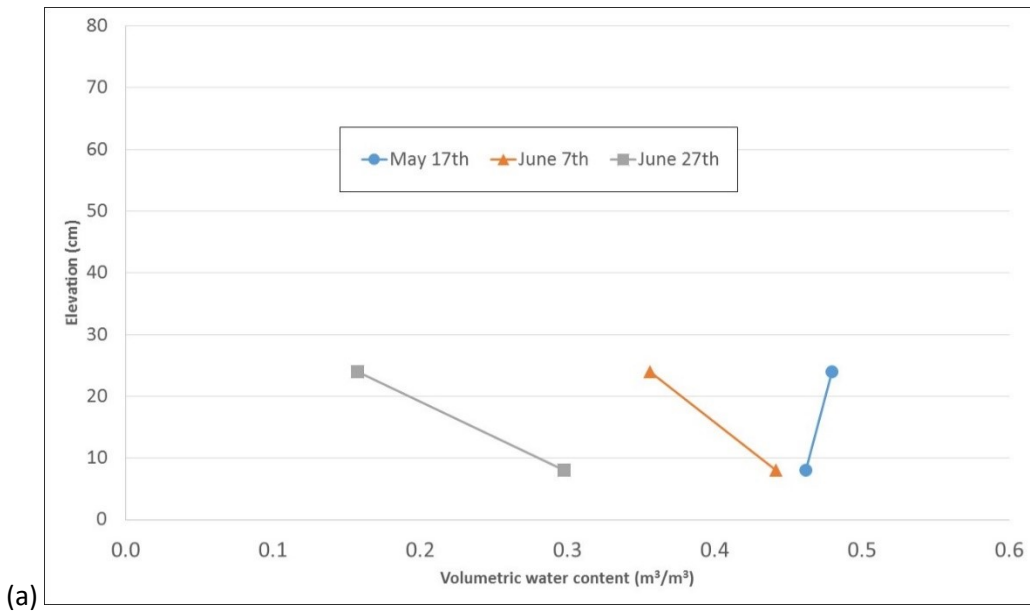


Figure 150: Temperature profiles progression of (a) first layer deposition, (b) second layer deposition, and (c) third layer deposition - Thin-lift test



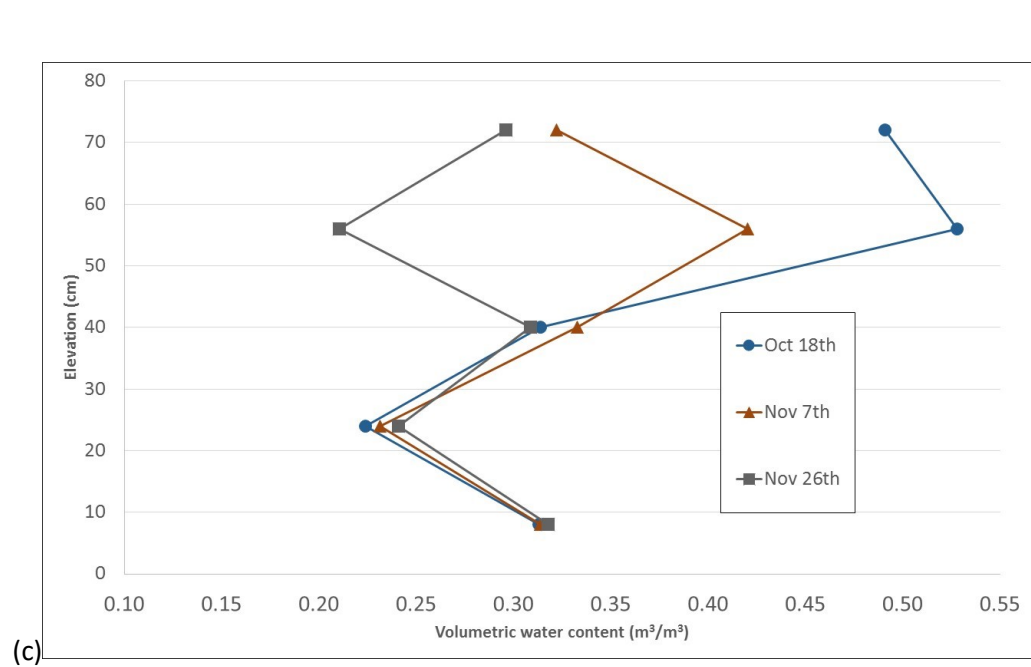
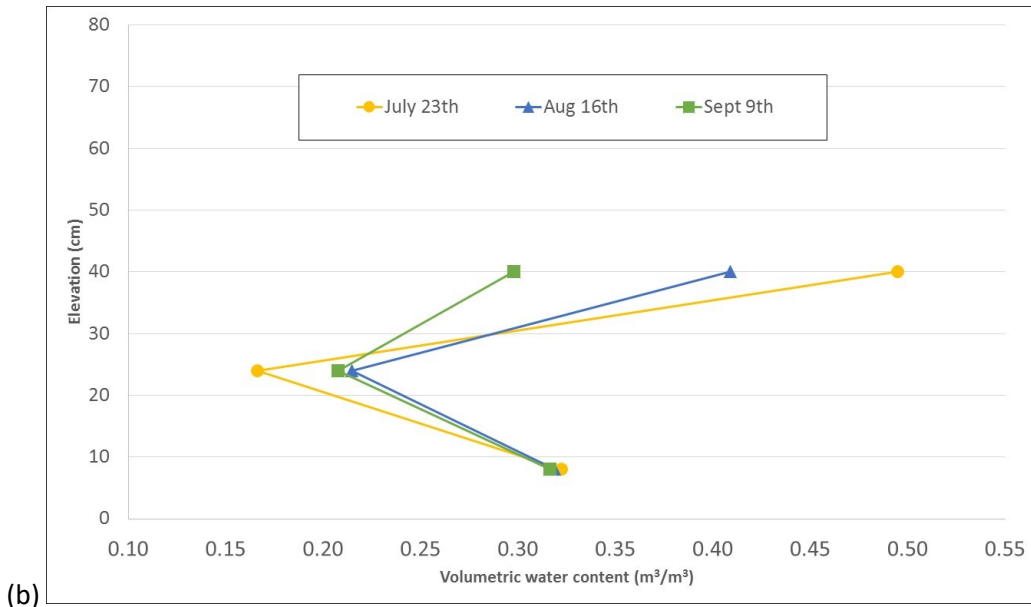


Figure 151: Volumetric water content profiles progression of (a) first layer deposition, (b) second layer deposition, and (c) third layer deposition - Thin-lift test

Figure 151 shows the moisture content readings obtained from the VWC sensors located along the height of the dry box. In agreement with the thick-lift test, the combined effects of evaporation and drainage drive tailings dewatering after the first layer deposition, while after the second layer is added, some water infiltrates into the underlying layer, accelerating the top layer dewatering. Similarly, after the third layer deposition, the top layer loses mass through both evaporation and infiltration into the layer underneath.

Greatly influenced by the weather seasons, conditions surrounding the dry box somewhat mirror the environmental conditions outdoors, as seen Figure 152. Temperature more or less stays steady for all three layers, as opposed to RH and dewpoint values, which substantial oscillate throughout, dipping below the values recorded during the thick-lift test by the end of the third layer desiccation.

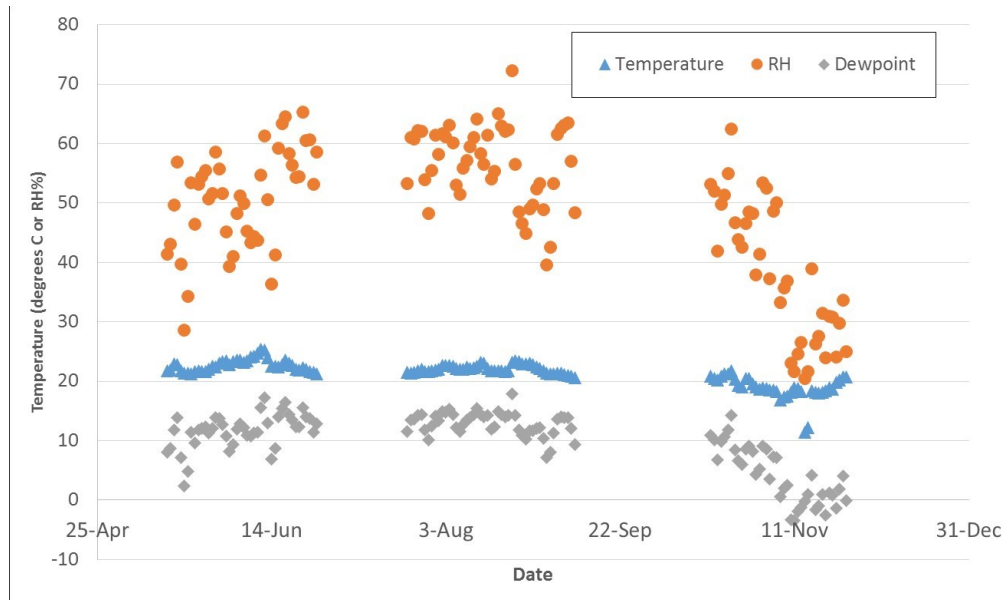


Figure 152: Temperature, RH and dewpoint profiles above the tailings - Thin-lift test

Similar to the previous thick-lift test, the tailings on this test showed  $A_E$  values being equal or higher than  $P_E$  for all layers (Figure 153). In a similar fashion as well, towards the end of each test, these values dipped below the  $P_E$ . In addition, in all cases, crack development did not discernibly influenced the overall evaporation behavior, neither by suddenly peaking towards the end of the test (first layer), or by linearly progressing until the end of the desiccation period (third layer).

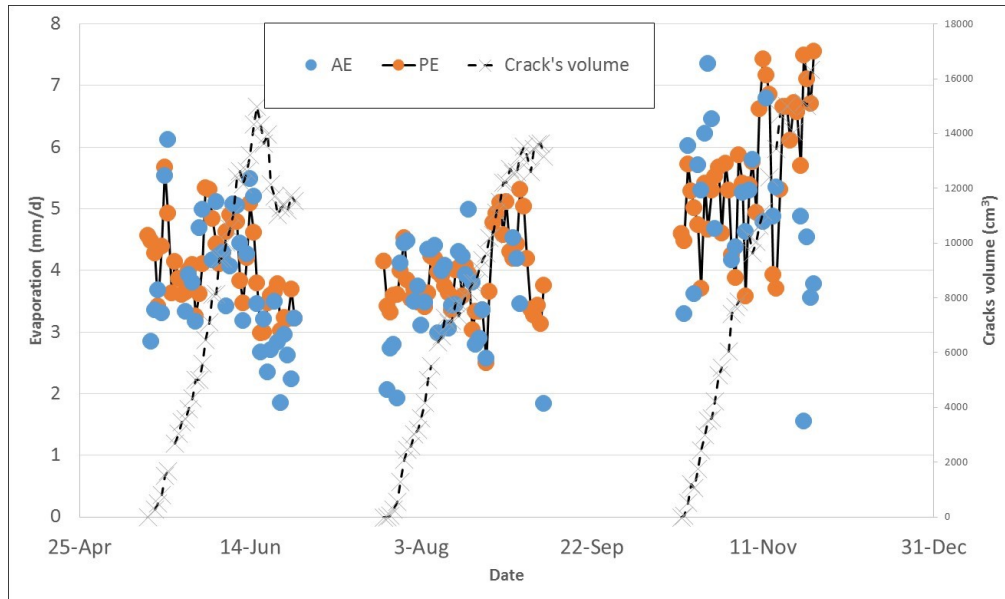


Figure 153: Actual and potential evaporation - Thin-lift test

The average GWC calculated from the dry box weight variations for all three layers as well as the surface measurements within the top 1cm were plotted in Figure 154. In all cases, the GWC variation in the surface tended to converge, in agreement with the thick-lift test results.

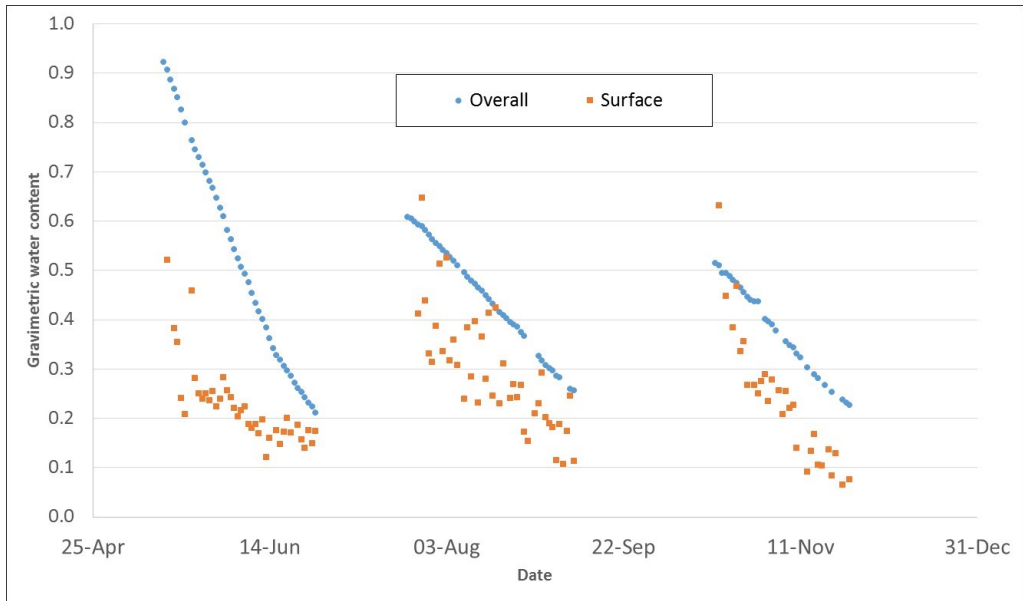


Figure 154: Gravimetric water content - Thin-lift test

Crack development initially followed a linear trend, as in the thin-lift test. However, over time, crack growth patterns diverged upon completion of each layer, as observed in Figure 155. Interestingly, unlike the thick-lift test, crack development was slower after the second layer deposition.

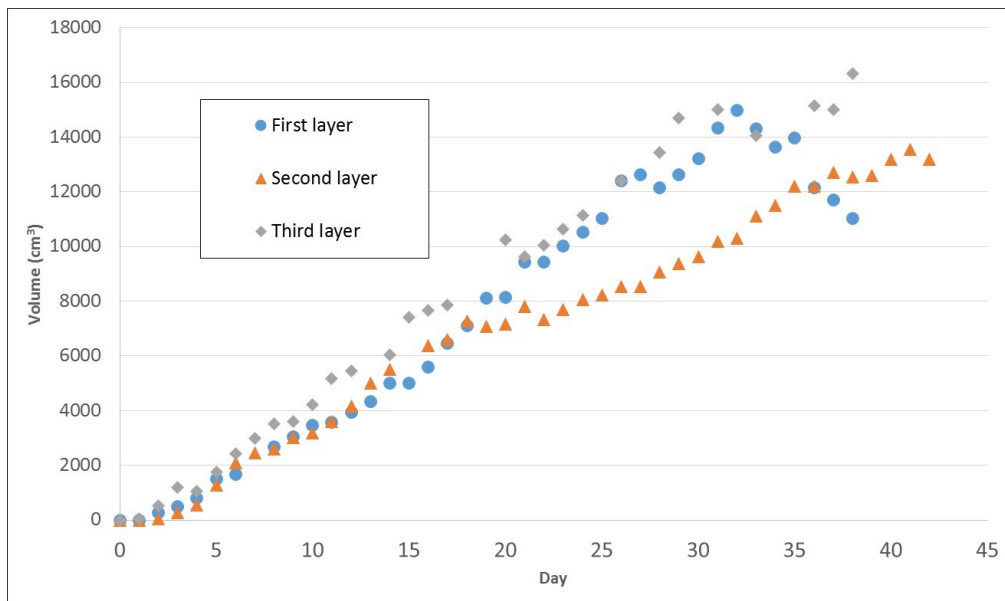


Figure 155: Crack development - Thin-lift test

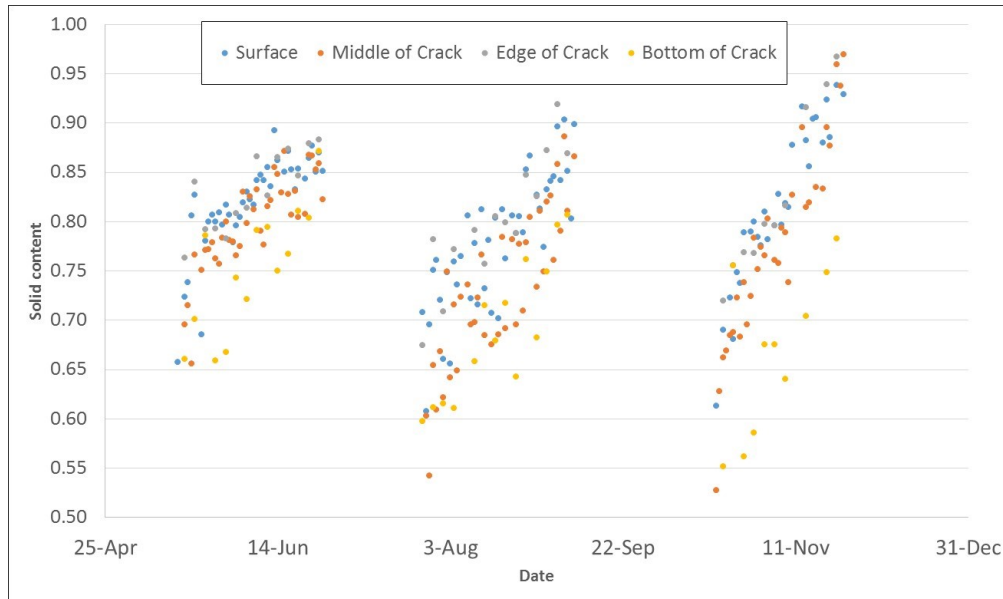


Figure 156: Surface sample solid contents - Thin-lift test

Figure 156 shows the solid content analysis performed on surface samples taken daily at various locations including the surface of the tailings, and the edge, middle, and bottom within cracks. Similarly to the thick-lift test, the highest solid contents were recorded at the surface and at the edges of cracks. This is also reflected in the suction measurements recorded from the surface samples shown in Figure 157. Here, it is clear that initially, the crack edges were wetter than those at the surface; however, as time progressed, the suction values measured from them increased considerably, often surpassing the surface values. In addition, consistent with the thick-lift test, suction tended to increase as more layers were added to the test.

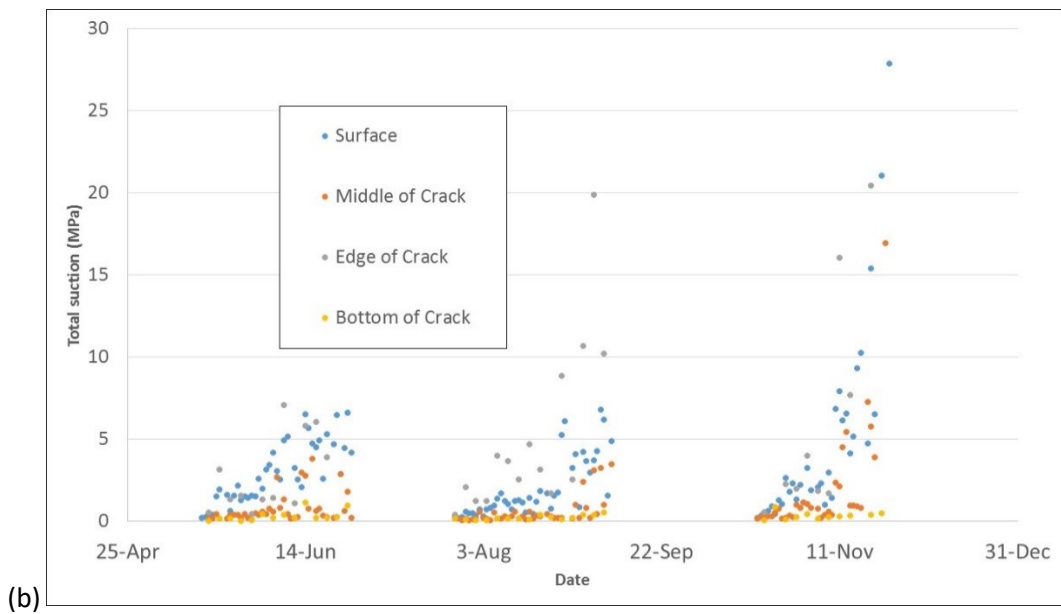
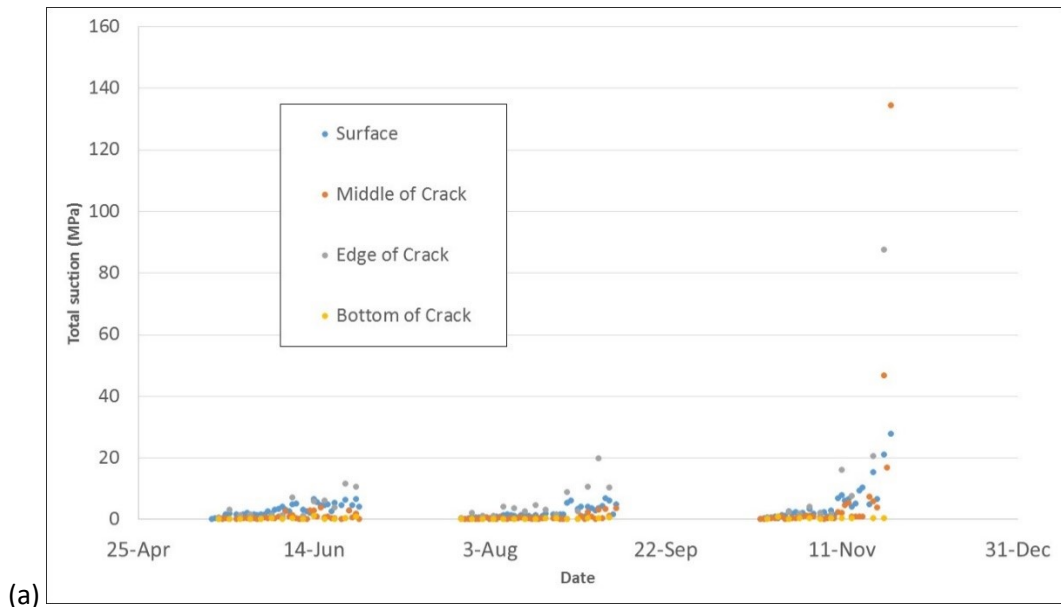


Figure 157: Surface cracks total suction (a) regular figure and (b) low suction range detail - Thin-lift test

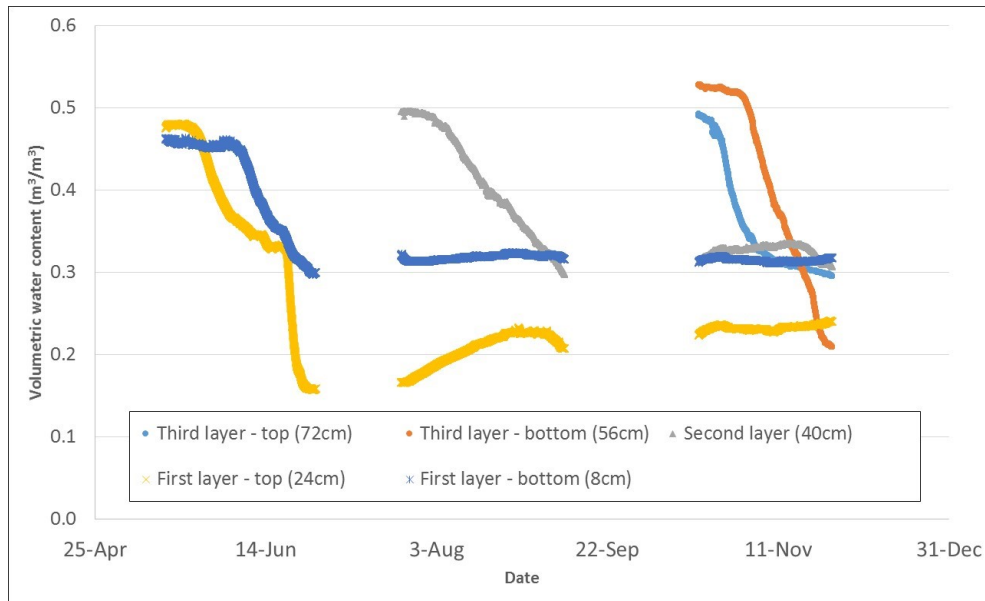


Figure 158: Volumetric water content at various heights - Thin-lift test

Figure 158 describes the VWC measurements along the height of the tailings which depict an initial sharp decline in VWC at the top just after the first layer deposition. This can be attributed to the evaporation effects working in conjunction with drainage, as seen in Figure 159, followed by a similar decrease in VWC at the bottom of the dry box. After the second layer is added, however, the VWC at the top of the bottom layer increased again, signaling infiltration from the layer on top, which also explains the rapid decline in VWC at the surface of the tailings. Finally, after the third layer deposition, VWC values registered from the recently added material decreased in a similar fashion, with the sharpest decline recorded at the surface. Interestingly, except for the top and bottom of the dry box, all VWC measurements tend to converge to 0.3, results consistent with what was found in the thick-lift test.

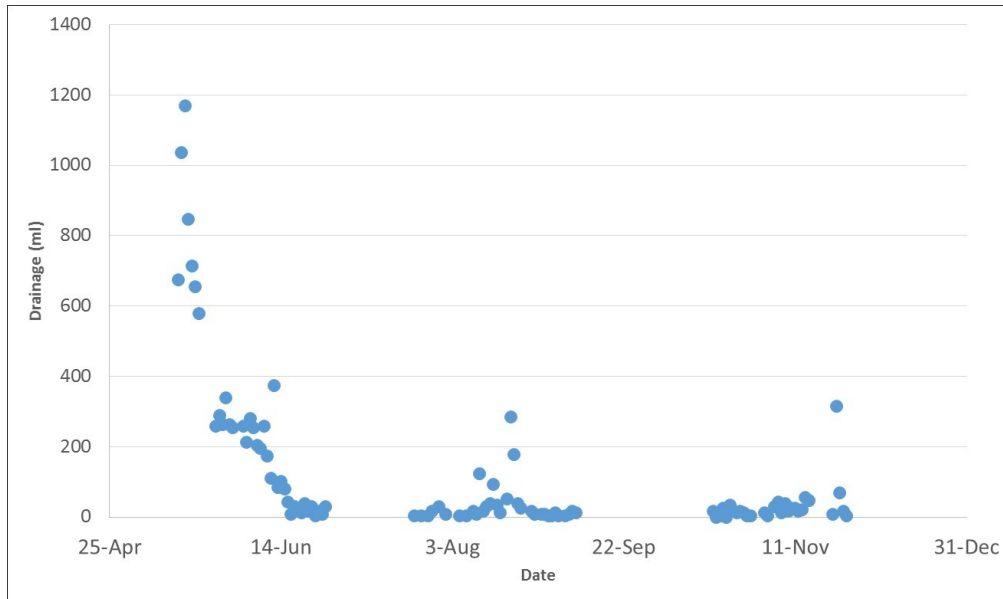


Figure 159: Drainage - Thin-lift test

Figure 160 shows the matric suction measured along the height of the dry box, which mirrors the tailings dewatering behavior observed in Figure 158.

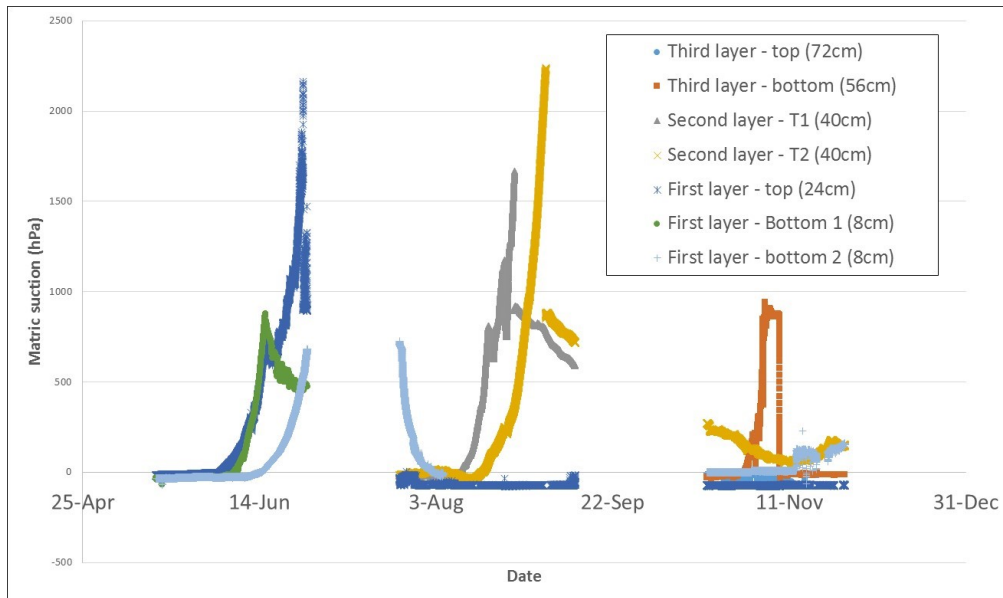
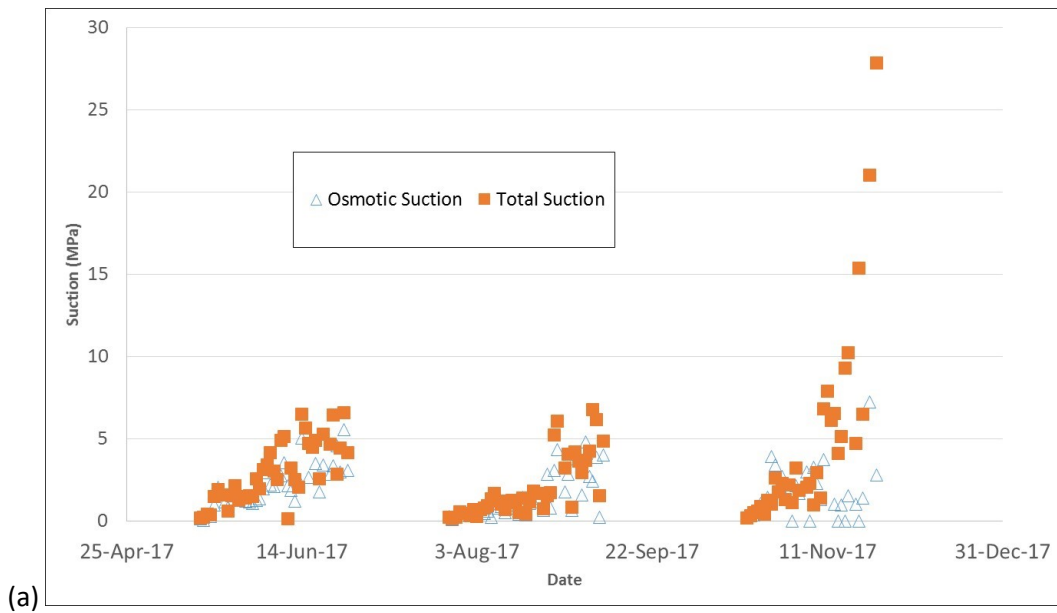


Figure 160: Matric suction at various heights - Thin-lift test

By examining osmotic and total suction values measured from the surface grab samples, as seen in Figure 161, three observations are worth mentioning: i) osmotic suction formed the largest component of total suction for all deposition experiments, ii) suction measurements tended to increase with each deposition, consistent with crack suction measurements in Figure 157, and iii) after reaching a maximum value, both suction values presented substantial oscillation by the end of the desiccation period, correlating with the decrease in  $A_E$  and the leveling off of the surface GWC. Both phenomena are especially obvious during the first desiccation period.



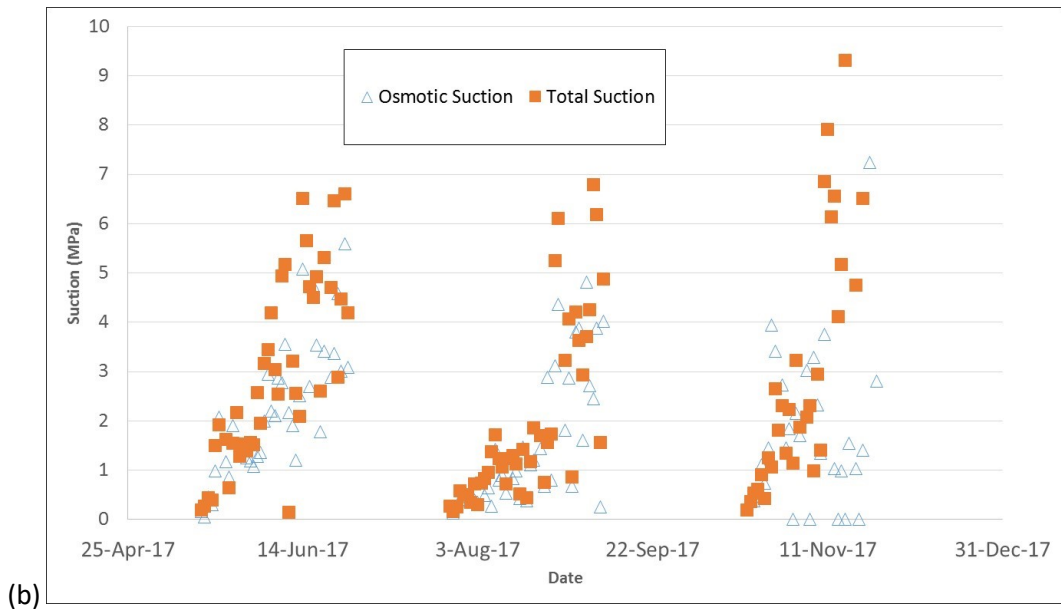


Figure 161: Surface sample total and osmotic suction (a) regular figure and (b) low suction range detail (b) - Thin-lift test

As done in the thick-lift performance analysis, the overall dry box weight variation of each layer was divided by the original thickness of the tailings, as shown in Figure 162. Consistent with the thick-lift test analysis as well, desiccation was found to be more effective during the first stage of the experiment, while the second and third layer depositions showed smaller weight variations.

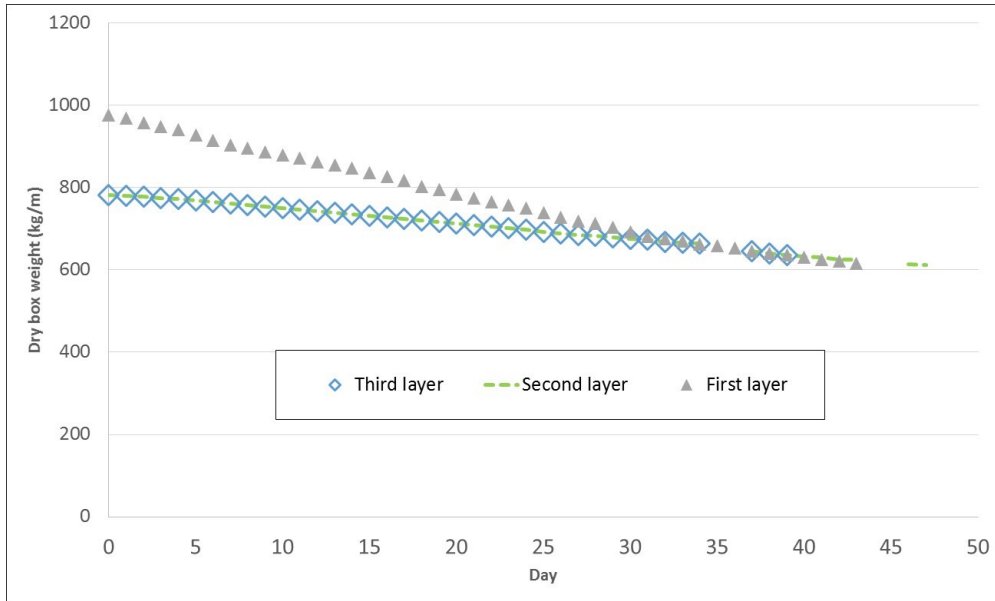


Figure 162: Dry box weight variation - Thin-lift test

Finally, the solid content progression of the overall dry box for all layer depositions, shown in Figure 163, described a 70% solid content value reached after 27 days, only one day less than in the thick-lift test.

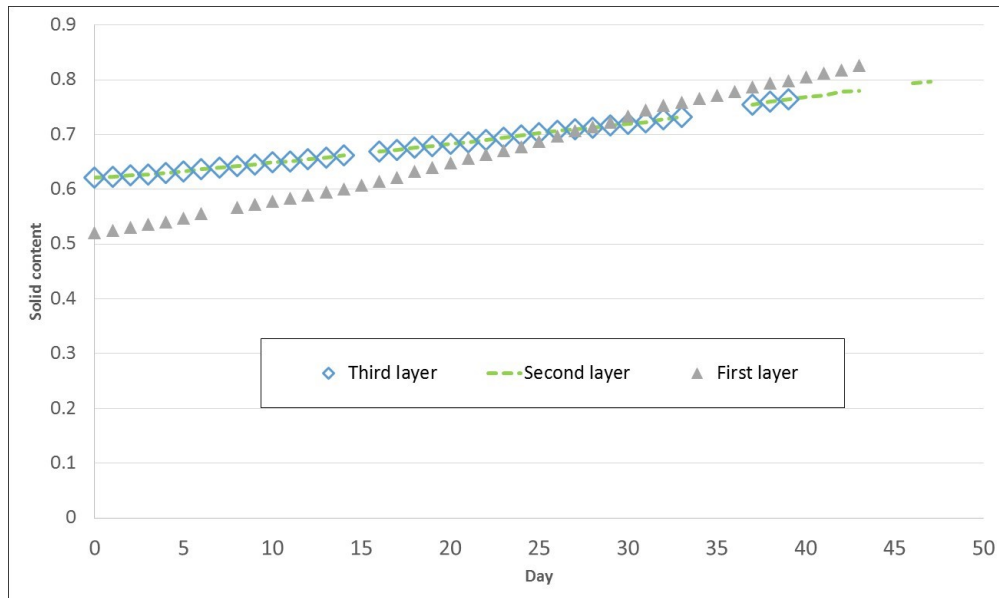


Figure 163: Solid content comparison - Thin-lift test

## 5 Discussion of results

### 5.1 Thin vs. Thick-lift tests

In this section, the results obtained from the thick and thin-lift tests are compared.

In Figure 164, the weight loss comparison between tests is calculated by dividing the overall dry box weight variation of the first layer depositions with the original thickness of the tailings. These observations lead to the conclusion that the rate of desiccation was slightly superior for the thin-lift test.

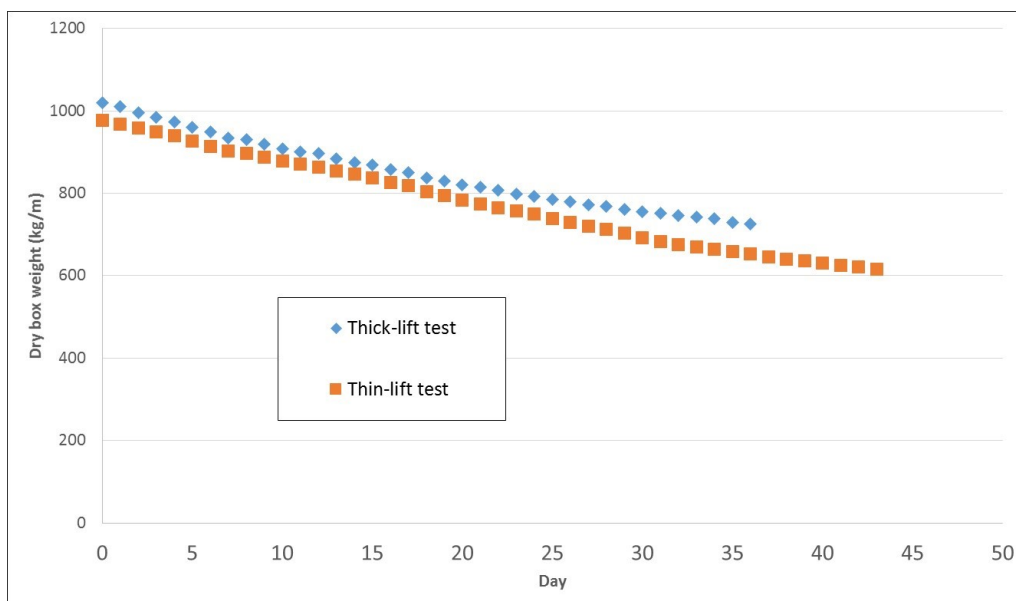


Figure 164: Comparison weight variation in thick and thin-lift tests

Subsequently, evaporation performance was compared by calculating the cumulative  $P_E$  of both tests, shown in Figure 165, and estimating the dry box weight variation in relation to the cumulative  $P_E$  normalized over the thickness of each experiment, as shown in Figure 166.

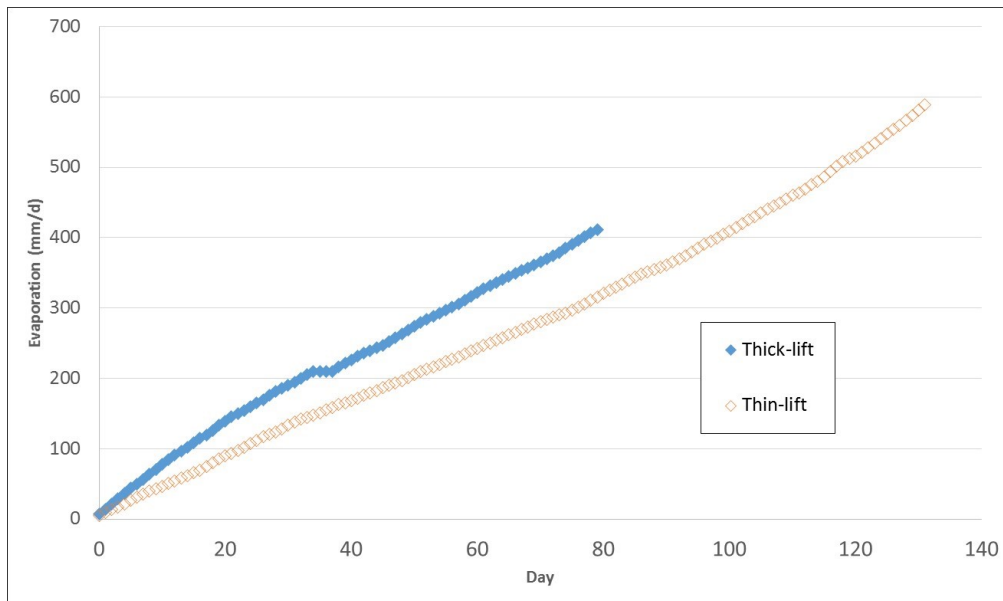


Figure 165: Cumulative potential evaporation for thick and thin-lift dry box experiments

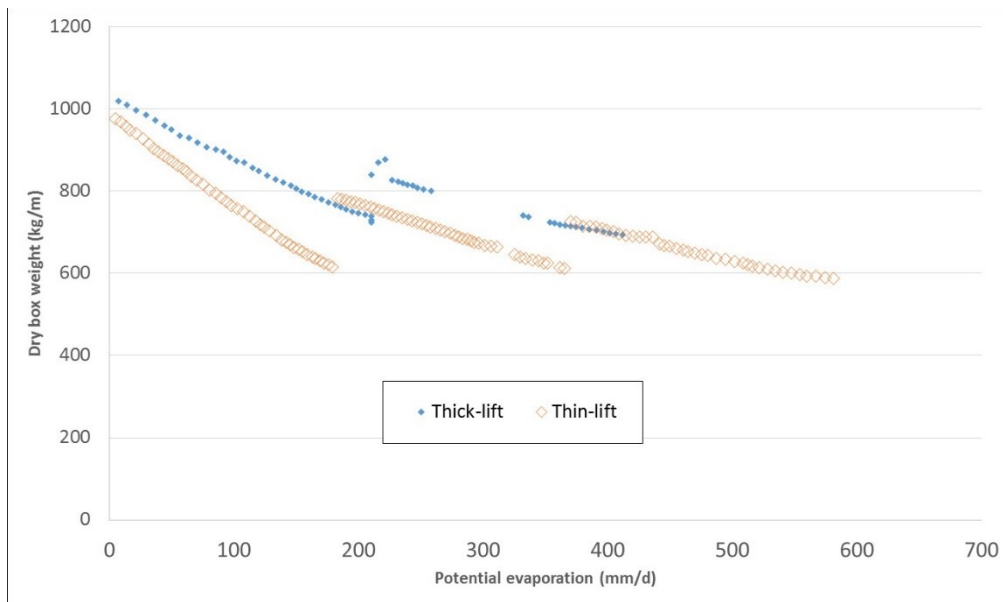
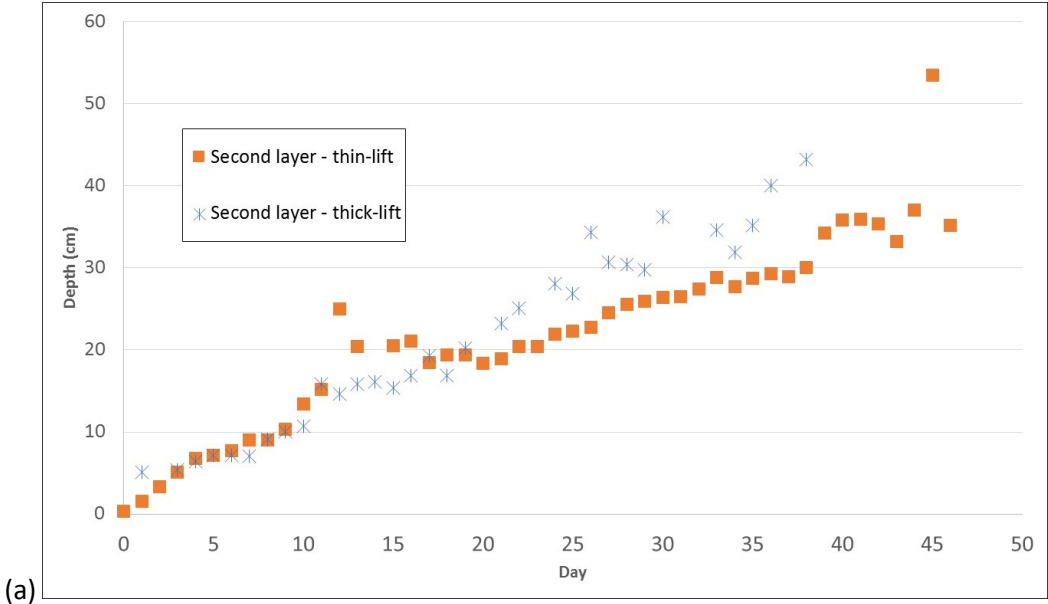


Figure 166: Comparison weight variation in relation to the cumulative potential evaporation for thick and thin-lift dry box experiments

These results lead to the conclusion that, initially, evaporation from the thin-lift test greatly outperforms the thick-lift dewatering rate by virtue of its smaller size. However, as the number of layers added increased, larger dewatering contributions due to consolidation improved the thick-lift dewatering performance, reducing the gap. Extrapolation of these results using modelling could provide more concrete recommendations.

In order to extrapolate these results in the field, the need of a numerical model which is able to combine the effects of consolidation and evaporation is required.

In terms of cracks geometry, shown in Figure 167, in general, cracks stayed consistent across all layers.



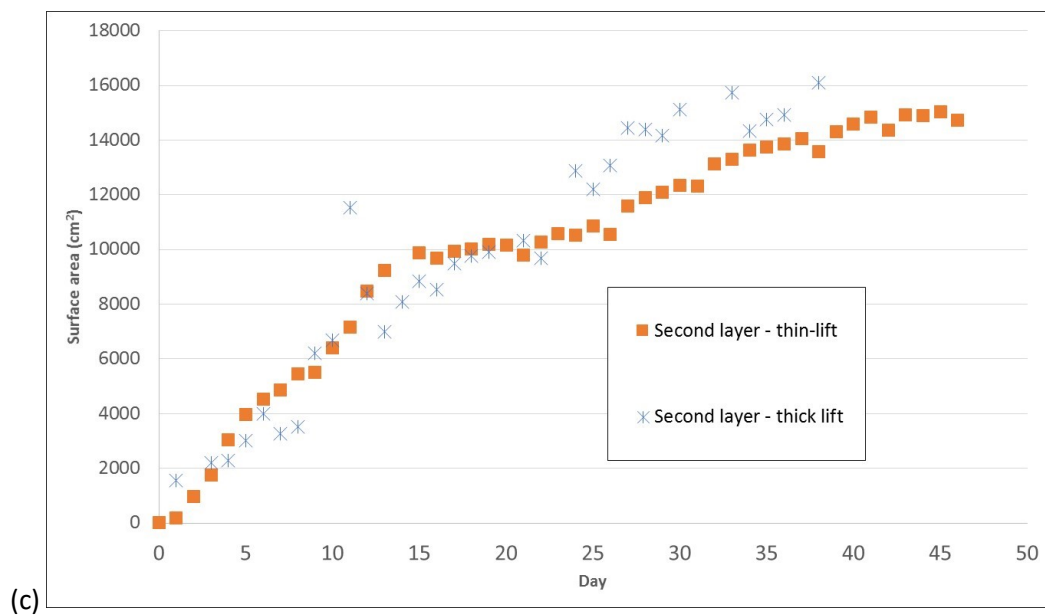
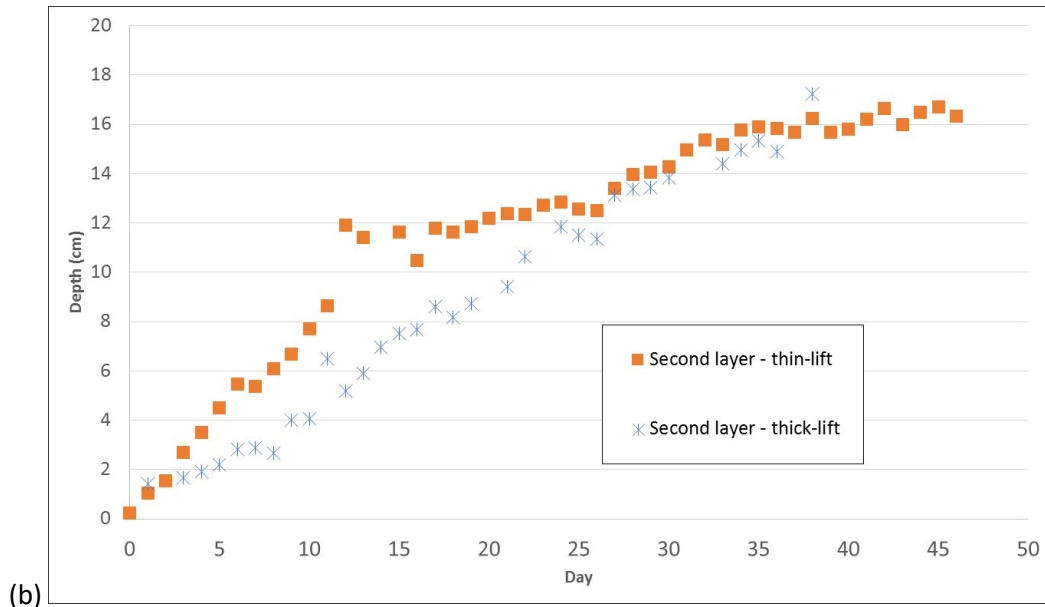


Figure 167: Comparison between (a) average, (b) maximum crack depth, and (c) exposed surface area in the second layer of both thick and thin-lift tests

A strength test was supposed to be performed upon completion of each layer of the thin-lift test; however, surface tailings strength was found to be too high for the vane shear test device to be used.

## 5.2 SWCC and shrinkage curves inferred from the dry box experiments

A shrinkage curve was constructed from the GWC and void ratio data obtained from the first layer depositions of both tests and the SWCC test (Figure 168). From this comparison, it is apparent that the shrinkage limit of the material is 31%, corresponding to a void ratio of 0.81.

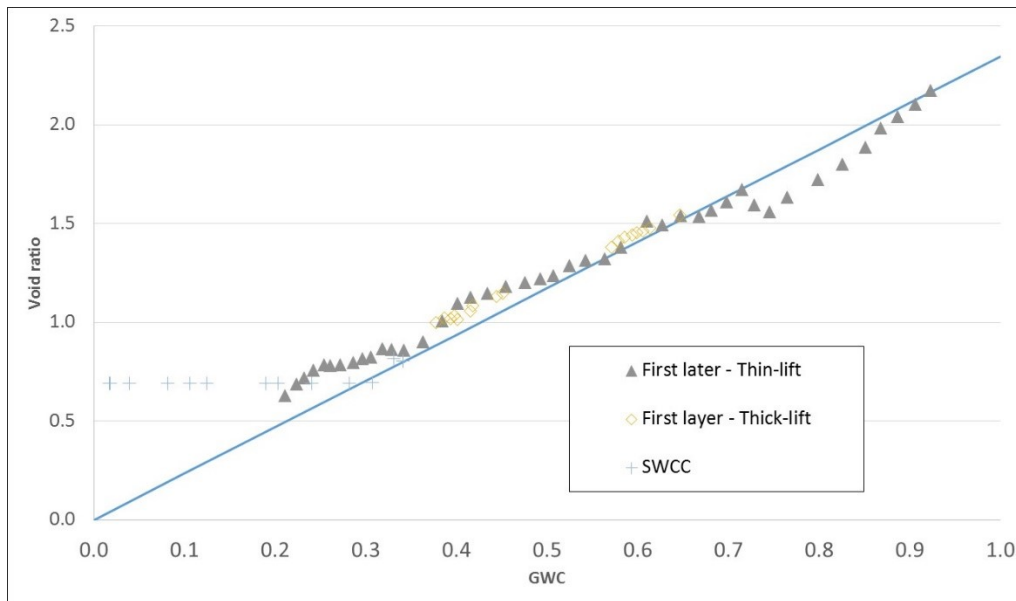


Figure 168: Shrinkage curve all tests

The SWCC of the tailings was constructed using the axis translation technique accounting volume change for low suction values, and using a WP4-T dewpoint hydrometer to measure total suction for higher suction values, as can be seen in Figure 169. Based on this figure, the air-entry value was found to be between 20 and 30kPa. In addition, the air-entry value obtained from the shrinkage curve (Figure 168) corresponds to a void ratio of approximately 0.87.

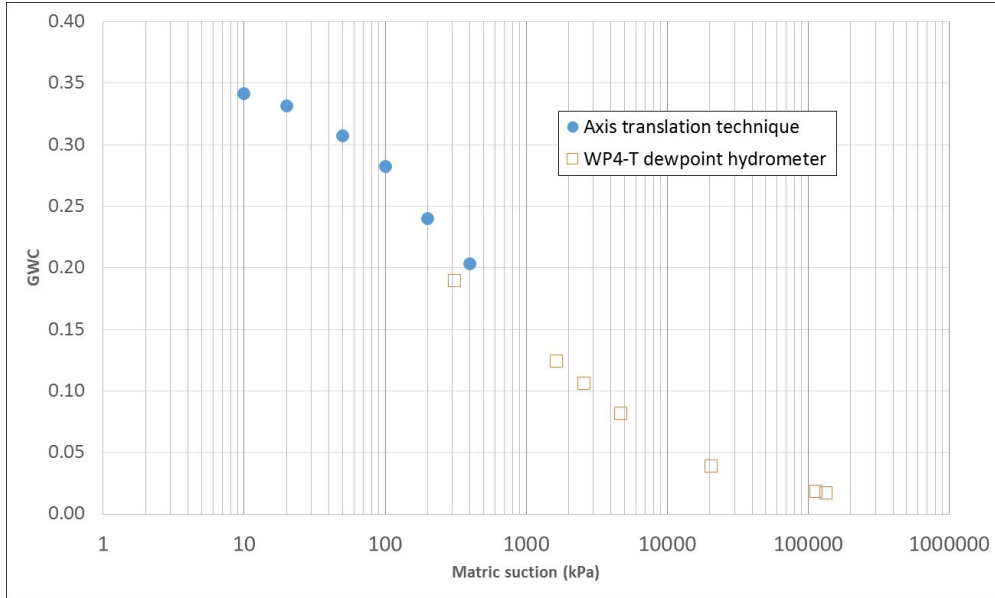


Figure 169: SWCC for centrifuge oil sands tailings in terms of GWC

The SWCC for the material can also be found in terms of degree of saturation in Figure 170 and in terms of void ratio in Figure 171.

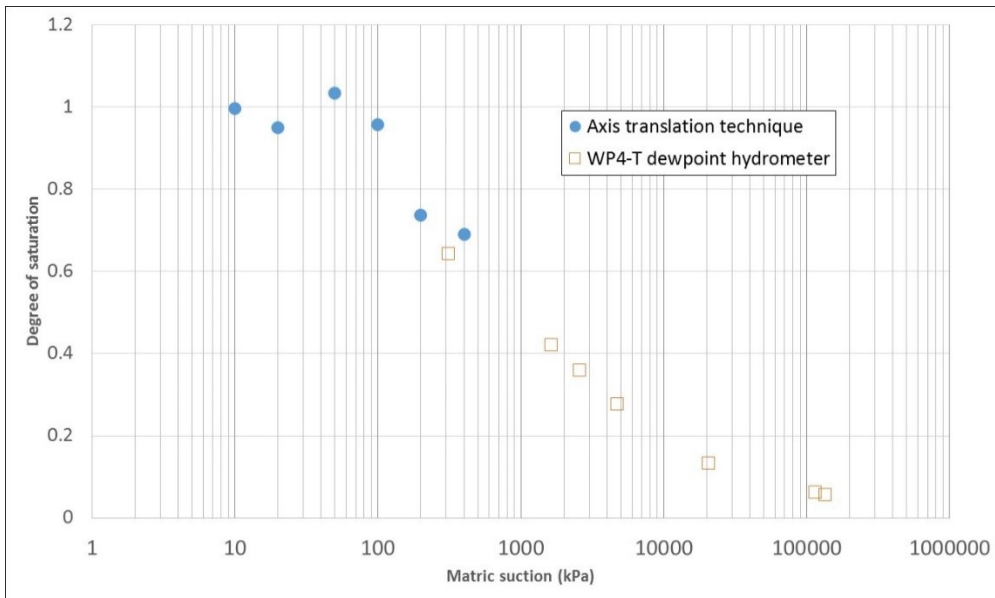


Figure 170: SWCC for centrifuge oil sands tailings in terms of degree of saturation

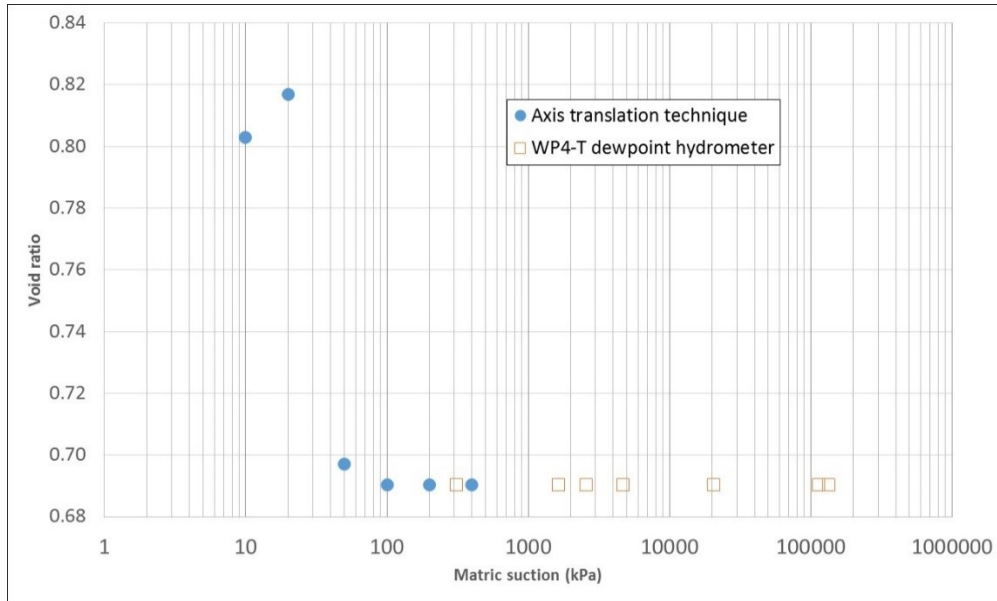


Figure 171: SWCC for centrifuge oil sands tailings in terms of void ratio

In addition, a number of SWCCs were derived from total suction measurements obtained from the surface samples taken during the first layer deposition of the thick-lift test (Figure 172). Here, the high suction values observed in the figure, relative to the measured SWCC, may hint to the contribution of crack development to the overall rate of evaporation. However, as no apparent contribution is appreciated during the experiment (Figure 178), it is possible to conclude that high concentrations of dissolved mass, as evidenced in Figure 172, suppressed evaporation from cracks, therefore neutralizing their effects.

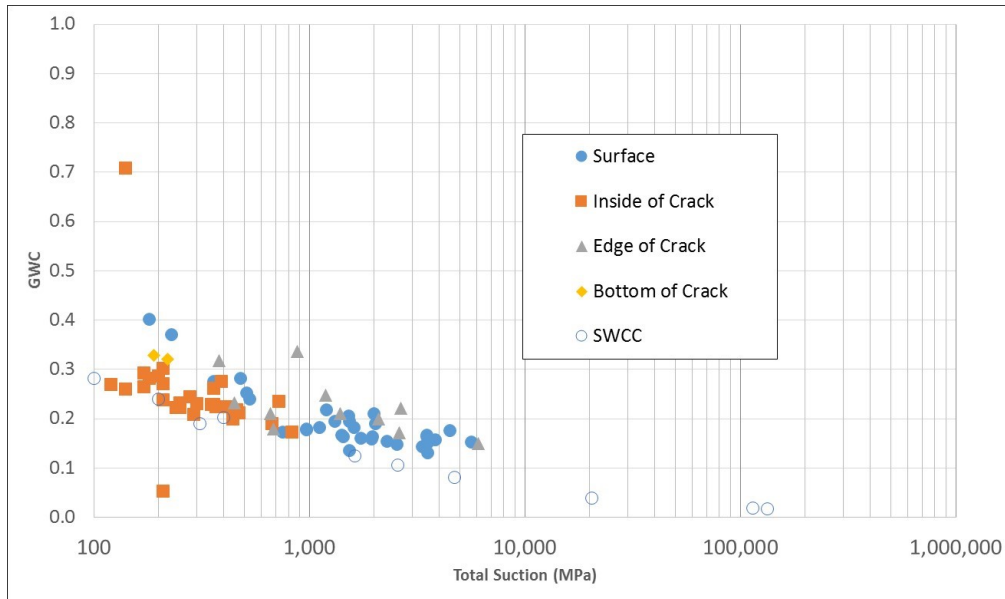


Figure 172: SWCC in terms of GWC and total suction from surface samples from the first layer of the thick-lift test, compared with those of the SWCC

Figure 173 shows an SWCC derived from the matric suction measurements taken by a tensiometer located close to the surface, during the first layer deposition of the thick-lift test. In addition, total suction measurements obtained from surface samples above the tailings were also plotted. In general, tensiometer data seem to agree with the measured SWCC, also plotted in the figure, while the relative high suction values taken from the surface samples evidenced the influence of the osmotic suction at the surface.

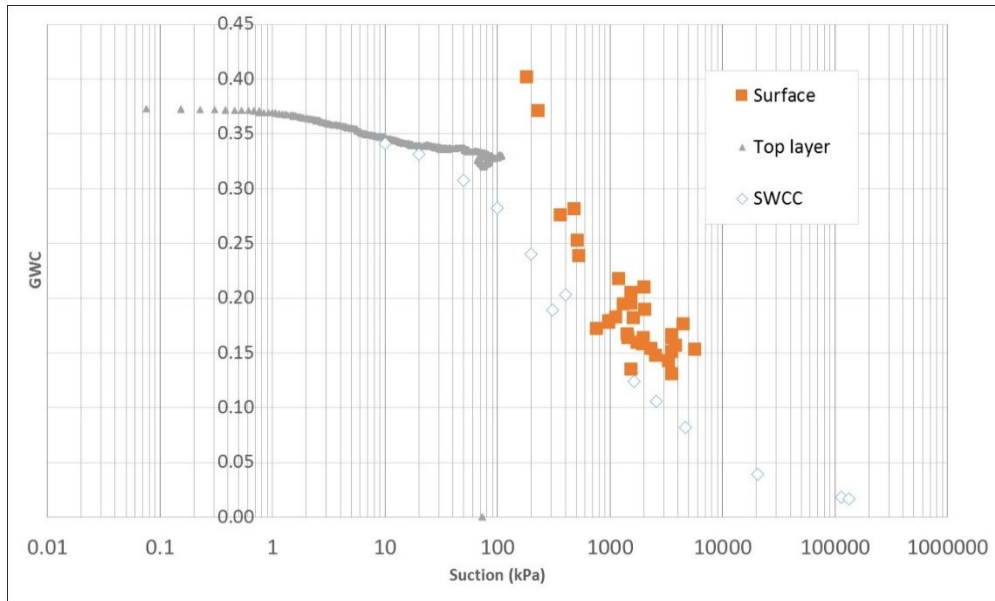


Figure 173: Water content and total suction measurements of surface samples and matric suction tensiometer data from the thick-lift test, compared with those of the SWCC

Alternatively to Figure 173, the relationship between total suction and GWC taken from all surface samples from both tests was plotted in Figure 174 and from all core samples in Figure 175.

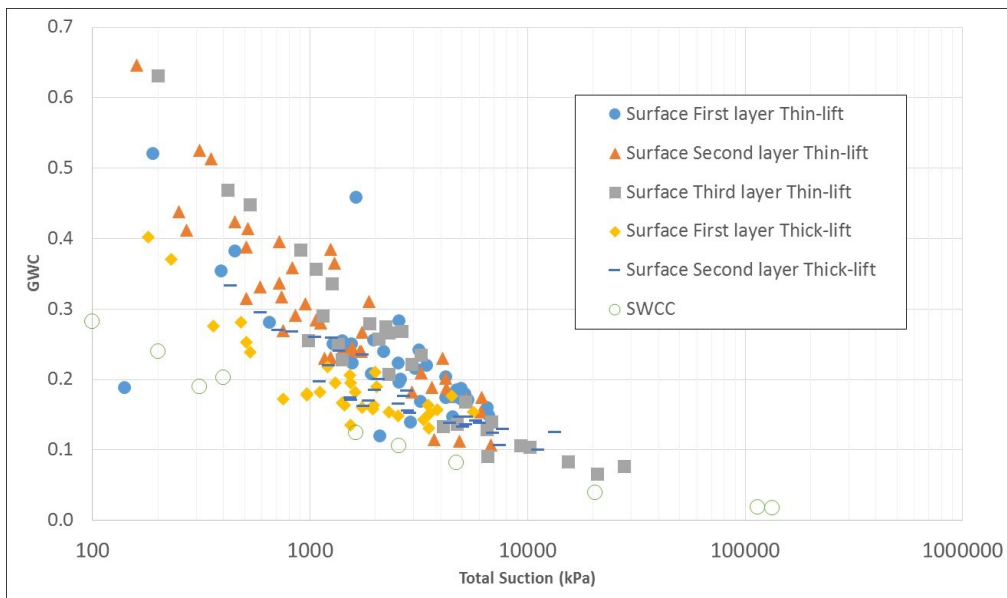


Figure 174: SWCC in terms of GWC and total suction from surface samples

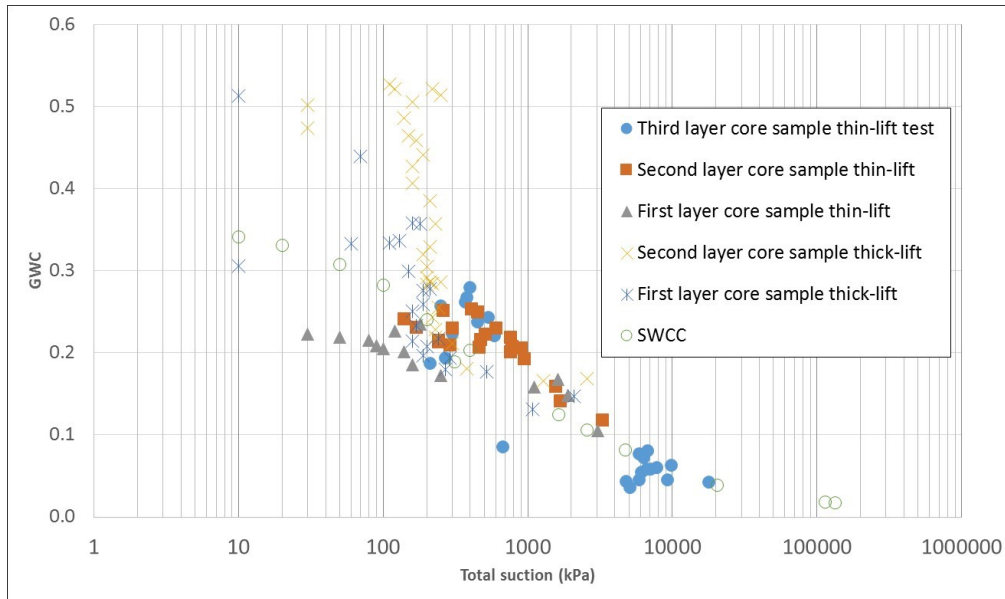


Figure 175: SWCC in terms of GWC and total suction from all core samples

Overall, both figures seem to agree; however, more reliable values would be associated to higher suction measurements, as the accuracy of the WP4-T dewpoint hydrometer increases on the higher range. As a result, values obtained from the core samples observed in Figure 175 corresponding to suctions below 500kPa are not very reliable.

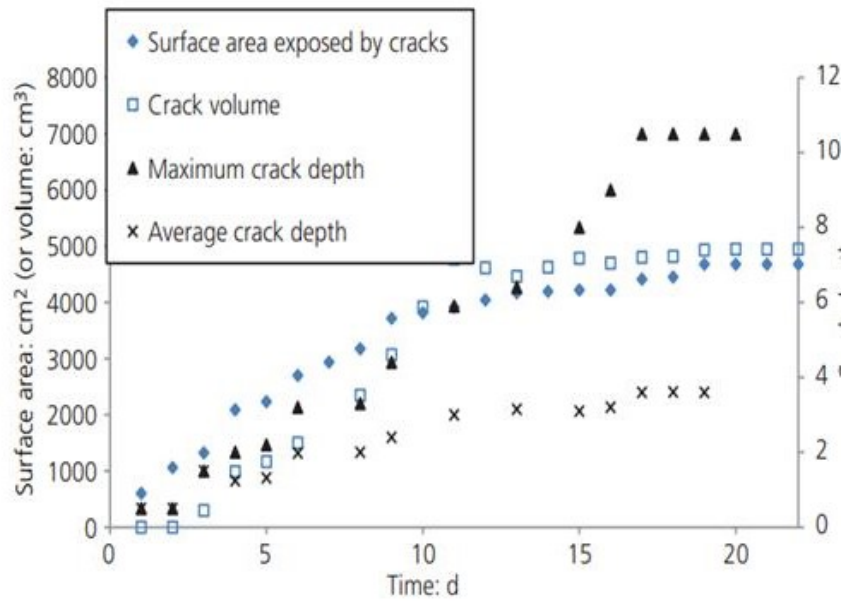
### 5.3 Centrifuge tailings vs. different type of tailings

The lack of influence of crack development in the dry box was unexpected, as similar experiments with other types of tailings did reported some kind of influence in evaporation (Daliri, 2013; Innocent-Bernard, 2013; Rozina 2013).

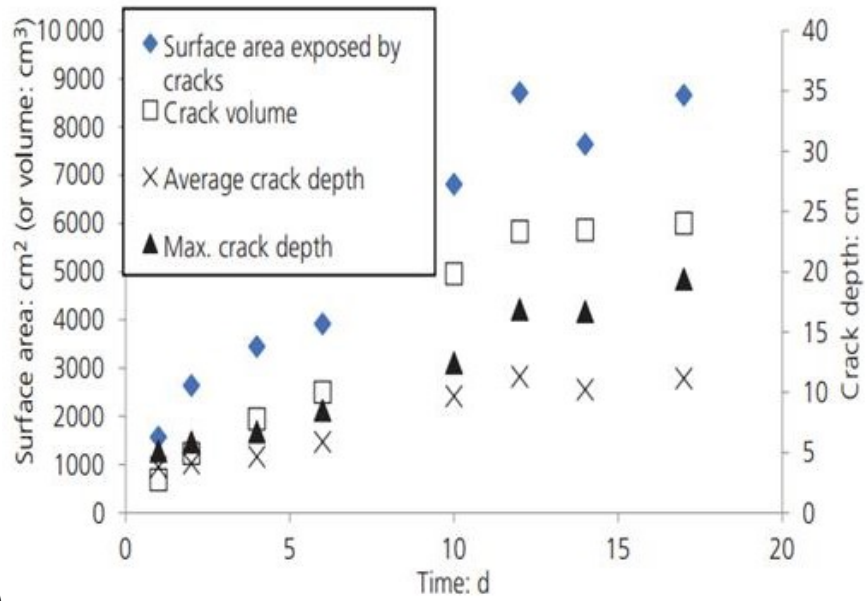
Centrifuge tailings		Polymer-amended MFT	
Sept 2nd	Sept 12th	June 13th	June 23th
			
Sept 24th	Oct 5th	June 28th	July 8th
			

Figure 176: Crack progression comparison between the second layer of centrifuge oil sands tailings and polymer-amended MFT

This difference in crack influence may be at least partially explained by the differences in crack geometry, as observed in Figure 176. From the figure, noticeable distinctions between crack propagation patterns as well as crack volumes (Figure 177) can be observed. Cracks from centrifuge oil sands tailings seem to greatly diverge in measurements from their counterparts (both generated from polymer-amended MFT and thickened oil sands tailings), leading to variations in their wind dynamics, and in turn, influence in evaporation behavior.



(a)



(b)

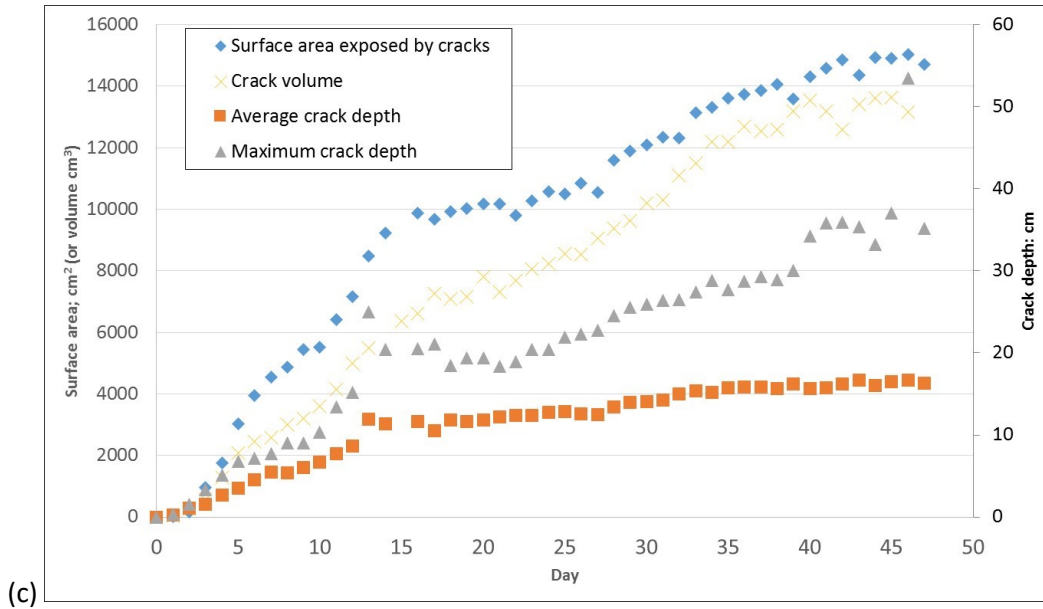


Figure 177: Crack volumes comparison between (a) thickened oil sands tailings, (b) polymer-amended MFT, and (c) centrifuge oil sands tailings

Overall, however, caution should be exercised when applying these results on a larger scale, as crack geometry, frequency, and their associated wind dynamics observed in the dry box may not necessarily translate in the field.

In terms of evaporation behavior patterns, it was observed that suction, greatly influenced by osmotic suction, seemed to correlate with the decrease of actual evaporation below the potential evaporation for all layers, after it reached a maximum value. This phenomenon, observed consistently in all layers, is attributed to mass transport and salt precipitation on the surface (Figure 178).

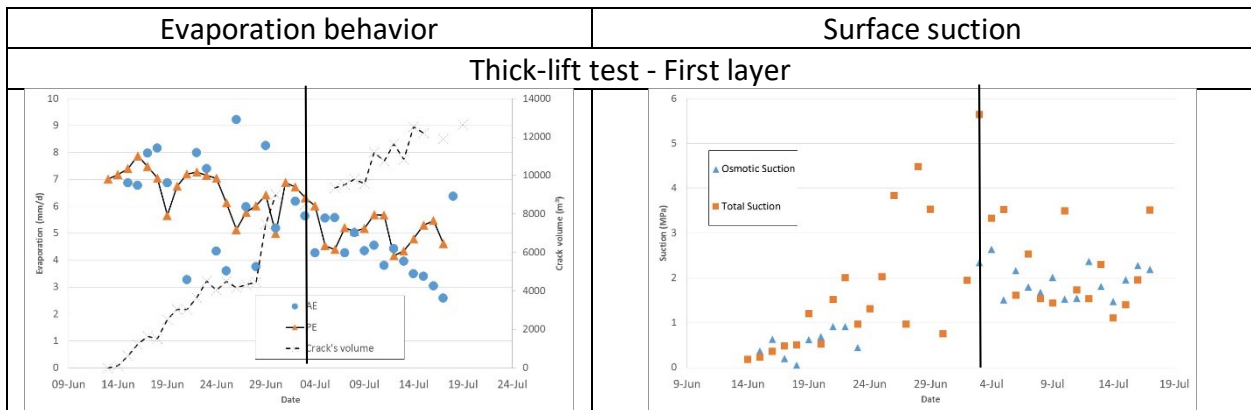




Figure 178: Comparison between evaporation behavior and surface suction development of the tailings surface, for all layers

## 6 Conclusions

In order to study the dewatering history of centrifuge tailings in the field, two dry box tests were performed. GWC, evaporation rate, drainage, total suction, and osmotic suction was recorded, taking into account their crack development history and solute concentration along each layer.

In terms of evaporation rate, actual evaporation proceeded near the potential rate for most of the experiments. Towards the end of the drying phase for each layer, however, salt precipitation, which formed a salt crust on the tailing's surface, eventually suppressed evaporation somewhat.

Crack formation did not influence evaporation. Cracks were found to be larger in volume than the ones observed from other types of tailings, possibly changing the surface wind dynamics on top of the tailings, and the evaporation rate.

Dewatering occurred more rapidly after a new layer was added, for both tests, due to the combined evaporation and absorption of water by the underlying layer. Buried layers, in turn, appeared to re-saturate up to their shrinkage limit (a void ratio of 0.81).

Initially, thinner layers greatly outperformed thicker ones, in terms of dewatering. However, as the number of layers was increased, consolidation effects reduced the gap between the tests somewhat.

Modeling of the dewatering behavior of the thick-lift test was satisfactory. Predictions approximated the experimental data profile shape, confirming the influence of consolidation at the bottom of the first layer.

Future extrapolation of the results of this thesis will require consideration of the evaporation and consolidation effects encountered during the experiments. This data, in turn, will be used to test desiccation-models used in deposition planning for centrifuge and other tailings types in oil sands operations.

## 7 Recommendations

In order to assess the transferability of the results in the field, it would be beneficial to compare observations between this experiment and other similar experiments of different scales in order to quantify the crack's influence on evaporation. This may be able to expose some unseen crack influence on dewatering or the possibility of the aspect ratio affecting evaporation.

Consolidation characteristics, specifically the hydraulic conductivity-void ratio function and the compressibility function, should be measured to refine the model predictions.

The influence of the underlying layers in terms of dewatering performance should be studied, as they influence the rate of dewatering of the top layers.

The characterization of the chemical composition of the salts should be studied and linked to the original pore water chemistry of the tailings.

## References

- Adams, J. E., & Hanks, R. J. (1964). Evaporation from Soil Shrinkage Cracks1. *Soil Science Society of America Journal*, 28(2), 281-284.
- Adams, J. E., & Ritchie, J. T. (1974). Field Measurement of Evaporation from Soil Shrinkage Cracks. *Soil Science Society of America Journal*, 38(1), 131-134.
- Aitchison, G. D., & Richards, B. G. (1965). Broad-scale study of moisture conditions in pavement subgrades throughout Australia., (pp. 184-232). Sydney.
- Alberta Energy Regulator. (2016).
- Alberta Energy Regulator. (2017). *Directive 085*. Retrieved 2018, from <https://www.aer.ca/rules-and-regulations/bulletins/bulletin-2017-17>
- Allen, R. G. (1996). Assessing integrity of weather data for reference evapotranspiration estimation. *Journal of Irrigation and Drainage Engineering*, 122(2), 97-106.
- Audet, P., Pinno, B. D., & Thiffault, E. (2014). Reclamation of boreal forest after oil sands mining: anticipating novel challenges in novel environments. *Canadian Journal of Forest Research*, 45(3), 364-371.
- Barron, R. (1948). The influence of drain wells on the consolidation of fine-grained soils. *US Eng. Office*.
- Bartholomeeusen, G., Sills, G., Znidarcic, D., Van Kesteren, W., Merckelbach, L., Pyke, R., . . . Masala, S. (2002). Sidere: numerical prediction of large-strain consolidation. *Géotechnique*, 52(9), 639–648.
- Been, K. (1980). Stress strain behaviour of cohesive soil deposited under water. *Oxford University*, Ph.D. thesis.
- Beier, N., & Segó, D. (2008). The oil sands tailings research facility. *Geotechnical news*, 26(2), 72-7.
- Beier, N., Wilson, W., Dunmola, A., & Segó, D. (2013). Impact of flocculation-based dewatering on the shear strength of oil sands fine tailings. *Canadian Geotechnical Journal*, 50(9), 1001-1007.
- BGC Engineering. (2010). *Oil sands tailings technology review*. Edmonton: University of Alberta - Oil Sands Research and Information Network.
- Birn, K., & Khanna, P. (2010). A discussion paper on the oil sands: challenges and opportunities. *Natural Resources Canada*.
- Bittelli, M., Ventura, F., Campbell, G. S., Snyder, R. L., Gallegati, F., & Pisa, P. R. (2008). Coupling of heat, water vapor, and liquid water fluxes to compute evaporation in bare soils. *Journal of Hydrology*, 362(3-4), 191-205.
- Boratynec, D. J. (2003). Fundamentals of rapid dewatering of composite tailings. *University of Alberta - M.Sc Thesis*.
- Boratynec, D. J., Chalaturnyk, R. J., & Scott, J. D. (1998). Experimental and fundamental factors affecting the water release rates of CT. *51st Canadian Geotechnical Conference*, (pp. 4-7). Edmonton.
- Bromwell, L. (1984). Consolidation of mining wastes. In *Sedimentation Consolidation Models—Predictions and Validation*. ASCE, 275-295.

- Brooks, R. H., & Corey, A. T. (1966). Properties of porous media affecting fluid flow. *Journal of the Irrigation and Drainage Division*, 92(2), 61-90.
- Bürger, R., Damasceno, J., & Karlsen, K. (2004). A mathematical model for batch and continuous thickening of flocculated suspensions in vessels with varying cross-section. *International Journal of Mineral Processing*, 183-208.
- Caldwell, J., Revington, A., McPhail, G., & Charlebois, L. (2014). Optimised seasonal deposition for successful management of treated mature fine tailings. *17th International Seminar on Paste and Thickened Tailings*, (pp. 8-12). Vancouver, BC.
- Cargill, K. W., & Schiffman, R. L. (1980). Fscn1-I, V.I. Level, A. Dimensionless one-dimensional finite strain consolidation: void ratio for a thick, normally consolidated homogeneous layer. *University of Colorado*.
- Carillo, N. (1942). Differential equation of a sliding surface in an ideal saturated soil. *Journal of Mathematics and Physics*, 1-5.
- Carrier III, D., Bromwell, L., & Frank, S. (1983). Design capacity of slurried mineral waste ponds. *Journal of Geotechnical Engineering*, 109(5):699-716.
- Carrier III, W. D., & Beckman, J. F. (1984). Correlations between index tests and the properties of remoulded clays. *Géotechnique*, 34(2), 211-228.
- Carrier, D., Bromwell, L., & Somogyi, F. (1983). Design Capacity of Slurried Mineral Waste Ponds. *Journal of Geotechnical Engineering*, 109(5), 699-716.
- Chalaturnyk, R. J., Don Scott, J., & Özüm, B. (2002). Management of oil sands tailings. *Petroleum Science and Technology*, 20(9-10), 1025-1046.
- Chalaturnyk, R. J., Scott, J. D., & Ozum, B. (2004). Environmentally Acceptable Deposition of Oil Sands Tailings, SWEMP 2004. *8 International Symposium on Environmental Issues and Waste Management in Energy and Mineral Production May*, (pp. 17-20).
- Childs, E. C., & Collis-George, N. (1950). The permeability of porous materials. *Proc. R. Soc. Lond. A*, 201(1066), 392-405.
- Coffin, J. (2010). A 3D model for slurry storage facilities. *University of Colorado*.
- COSIA. (2015). *Tailings Projects*. Retrieved March 2018, from Canada's Oil Sands Innovation Alliance : <http://www.cosia.ca/initiatives/tailings/tailings-projects>
- Daliri, F. (2013). The influence of desiccation and overconsolidation on monotonic and cyclic shear response of thickened gold tailings. *Carleton University - Doctoral dissertation*.
- Daliri, F., Simms, P., & Sivathayalan, S. (2016). Shear and dewatering behaviour of densified gold tailings in a laboratory simulation of multi-layer deposition. *Canadian Geotechnical Journal*, 53(8), 1246-1257.
- Decagon. (2009). *User Manual: T5/T5x pressure transducer tensiometer*. Retrieved January 2018, from [http://manuals.decagon.com/Manuals/UMS/T5\\_Manual.pdf](http://manuals.decagon.com/Manuals/UMS/T5_Manual.pdf)
- Decagon. (2016). *5TE Water Content, EC and Temperature Sensor*. Retrieved 2018, from ICT International: [http://manuals.decagon.com/Manuals/13509\\_5TE\\_Web.pdf](http://manuals.decagon.com/Manuals/13509_5TE_Web.pdf)
- Delage, P., Romero, E., & Tarantino, A. (2008). Recent developments in the techniques of controlling and measuring suction in unsaturated soils. *1st Eur. Conf. on Unsaturated Soils*, (pp. 33-52).
- Devenny, D. W. (2010). *A screening study of oil sand tailings technologies and practices*. Prepared for Alberta Energy Research Institute.

- Ding, Y., Wang, B., & McLeod, H. (2010). Characterizing tailings to. *CDA 2010 Annual Conference*, (p. Vol. 75). Niagara.
- Djalal, K. (2014). The effect of cracking and geomorphology on evaporation from clay soils. *Carleton University - M.A.Sc. Thesis*.
- Dunmola, A., Cote, C., Freeman, G., Kolstad, D., Song, J., & Masala, S. (2013). Dewatering and shear strength performance of in-line flocculated mature fine tailings under different depositional schemes. *Tailings and Mine Waste*.
- Ebrahimi-Birang, N., Gitirana Jr, G. F., Fredlund, D. G., Fredlund, M. D., & Samarasekera, L. (2004). A lower limit for the water permeability coefficient. *57th Canadian Geotechnical Conference*, (pp. Vol. 1, pp. 12-19). Quebec City.
- Escario, V. (1986). The shear strength of partly saturated soils. *Geotech*, 36(3), pp.453-456.
- Fisseha, B., Bryan, R., & Simms, P. (2010). Evaporation, unsaturated flow, and salt accumulation in multilayer deposits of "paste" gold tailings. *Journal of geotechnical and geoenvironmental engineering*, 136(12), 1703-1712.
- Fox, P. J., & Baxter, C. D. (1997). Consolidation properties of soil slurries from hydraulic consolidation test. *Journal of Geotechnical and Geoenvironmental Engineering*, 123, (8), 770-776.
- Fox, P., & Berles, J. (1997). CS2: A piecewise-linear model for large strain consolidation. *International Journal for Numerical and Analytical Methods in Geomechanics*, 21(7), 453 - 475.
- Fredlund, D. G. (1967). *Comparison of soil suction and one-dimensional consolidation characteristics of a highly plastic clay*. National Research Council Canada, Division of Building Research.
- Fredlund, D. G. (1997). From theory to the practice of unsaturated soil mechanics. *Proc. 3rd Brazilian Symp. on Unsaturated Soils*.
- Fredlund, D. G. (2006). Unsaturated soil mechanics in engineering practice. *Journal of geotechnical and geoenvironmental engineering*, 132(3), 286-321.
- Fredlund, D. G., & Rahardjo, H. (1993). *Soil mechanics for unsaturated soils*. John Wiley & Sons.
- Fredlund, D. G., & Xing, A. (1994). Equations for the soil-water characteristic curve. *Canadian geotechnical journal*, 31(4), 521-532.
- Fredlund, D. G., Houston, S. L., & Caicedo, B. (2013). *Interpretation of soil-water characteristic curves when volume change occurs as soil suction is changed*.
- Fredlund, D. G., Rahardjo, H., & Fredlund, M. D. (2012). *Unsaturated Soil Mechanics in Engineering Practice*. John Wiley & Sons.
- Fredlund, D. G., Stone, J., Stianson, J., & Sedgwick, A. (2011). Determination of water storage and permeability functions for oil sands tailings. *Tailings and Mine Waste Conference*. Vancouver.
- Fredlund, D. G., Xing, A., & Huang, S. (1994). Predicting the permeability function for unsaturated soils using the soil-water characteristic curve. *Canadian Geotechnical Journal*, 31(4), 533-546.
- Fredlund, M. D. (2000). The role of unsaturated soil property functions in the practice of unsaturated soil mechanics.

- Fredlund, M. D., Wilson, G. W., & Fredlund, D. G. (2002). Representation and estimation of the shrinkage curve. *3rd International Conference on Unsaturated Soils, UNSAT*, (pp. 145-150).
- Fujimaki, H., Shimano, T., Inoue, M., & Nakane, K. (2006). Effect of a salt crust on evaporation from a bare saline soil. *Vadose Zone Journal*, 5(4), 1246-1256.
- Fujiyasu, Y., & Fahey, M. (2000). Experimental study of evaporation from saline tailings. *Journal of geotechnical and geoenvironmental engineering*, 126(1), 18-27.
- Fujiyasu, Y., Fahey, M., & Newson, T. (2000). Field investigation of evaporation from freshwater tailings. *Journal of Geotechnical and Geoenvironmental Engineering*, 126(6), 556-567.
- Gardner, W. R. (1958). Some steady-state solutions of the unsaturated moisture flow equation with application to evaporation from a water table. *Soil science*, 85(4), 228-232.
- Gee, G. W., Campbell, M. D., Campbell, G. S., & Campbell, J. H. (1992). Rapid measurement of low soil water potentials using a water activity meter. *Soil Science Society of America Journal*, 56(4), 1068-1070.
- Gibson, England, & Hussey. (1967). The Theory of One-Dimensional Consolidation of Saturated Clays. *Géotechnique*, 17(3), 261-273.
- Government of Alberta. (2016). *About the industry*. Retrieved February 2018, from Alberta Canada: <http://www.albertacanada.com/business/industries/og-about-the-industry.aspx>
- Griend, A. A., & Owe, M. (1994). Bare soil surface resistance to evaporation by vapor diffusion under semiarid conditions. *Water Resources Research*, 30(2), 181-188.
- Hilf, J. W. (1956). An investigation of pore water pressure in compacted cohesive soils.
- Hillel, D. (1980). *Applications of soil physics*. New York: Academic Press.
- Houlihan, R., & Haneef, M. (2008). Oil sands tailings: regulatory perspective. *International Oil Sands Tailing Conference*. Edmonton.
- Huerta, A., & Rodríguez Ferran, A. (1992). Numerical analysis of nonlinear large-strain consolidation and filling. *Computers and structures*, 357-365.
- Imai, G. (1981). Experimental studies on sedimentation mechanism and sediment formation of clay materials. *Soils and Foundations*, 21(1), 7-20.
- Innocent-Bernard, T. (2013). Evaporation, cracking, and salinity in a thickened oil sands tailings. *Carleton University - Doctoral dissertation*.
- Innocent-Bernard, T., Simms, P., Xiaoli, Y., & Sedgwick, A. (2014). Multilayer deposition of two batches of thickened oil sands tailings: experiments and modeling. *International Oil Sands Tailings Conference*, (pp. 7-10). Lake Louise.
- Jakubick, A. T., McKenna, G., & Robertson, A. (2003). Stabilization of tailings deposits: international experience. *Mining and the Environment Conference*. Sudbury.
- Jeeravipoolvarn, S. (2010). Geotechnical Behavior of In-Line Thickened Oil Sands Tailings. *University of Alberta*.
- Kasperski, K. L. (1992). A review of properties and treatment of oil sands tailings. *AOSTRA Journal of Research*, 8, 11-11.
- Kolstad, D., Dunmola, A., Dhadli, N., O'Kane, M., Song, J., & Masala, S. (2012). Towards the improvement in geotechnical performance of atmospheric fines drying (AFD) deposits at Shell's Muskeg River Mine. *3rd International Oil Sands Tailings Conference*, (pp. 411-420). Edmonton.

- Koppula, S. (1970). The consolidation of soil in two dimensions and with moving boundaries. *University of Alberta*.
- Krahn, J., & Fredlund, D. G. (1972). On total, matric and osmotic suction. *The Emergence of Unsaturated Soil Mechanics*, 35.
- Kynch, G. J. (1952). A theory of sedimentation. *Transactions of Faraday Society*, 48, 166-176.
- Lal, R., & Shukla, M. K. (2004). *Principles of soil physics*. CRC Press.
- Lee, K. (1979). An analytical and experimental study of large strain soil consolidation. *University of Oxford*.
- Lehmann, P., Assouline, S., & Or, D. (2008). Characteristic lengths affecting evaporative drying of porous media. *Physical Review E*, 77(5), 056309.
- Leong, E. C., & Rahardjo, H. (1997). Review of soil-water characteristic curve equations. *Journal of geotechnical and geoenvironmental engineering*, 123(12), 1106-1117.
- Leong, E. C., Tripathy, S., & Rahardjo, H. (2003). Total suction measurement of unsaturated soils with a device using the chilled-mirror dew-point technique. *Geotechnique*, 53(2), 173-182.
- Marinho, F. A. (2005). Nature of soil–water characteristic curve for plastic soils. *Journal of Geotechnical and Geoenvironmental Engineering*, 131(5), 654-661.
- Marinho, F., Take, W., & Tarantino, A. (2008). Measurement of matric suction using tensiometric and axis translation techniques. *Geotechnical and Geological Engineering*, 26, 615-631.
- Matthews, J. G., Dhadli, N., House, P., & Simms, P. (2011). Field trials of thin-lift deposition of amended mature fine tailings at the Muskeg River Mine in Northern Alberta. *Paste*, (pp. 271-280).
- McKenna, G. (2017). Soft Tailings Landform Design. *Tailings and Mine Waste Conference 2017*. Banff.
- McLaws, I. J. (1980). *Silica sands in the Fort McMurray area, Alberta*. Alberta Research Council.
- Mizani, S. (2016). Experimental Study and Surface Deposition Modelling of Amended Oil Sands Tailings Products. *Carleton University - Doctoral dissertation*.
- Morris, P., Lockington, D., & Apelt, C. (2000). Correlations for mine tailings consolidation parameters. *International Journal of Surface Mining, Reclamation and Environment*, 14(3), 171–182.
- Moussavi, R. (2013). Application of Dewatering Technologies in Production of Robust Non-Segregating Tailings. *University of Alberta*.
- Mualem, Y. (1976). A new model for predicting the hydraulic conductivity of unsaturated porous media. *Water resources research*, 12(3), 513-522.
- Mualem, Y. (1986). Hydraulic conductivity of unsaturated soils: prediction and formulas. *Methods of Soil Analysis: Part 1. Physical and Mineralogical Methods*, (methodsofsoilan1), 799-823.
- Nagaraj, B. K., Olson, T. L., & Chaudhry, U. (1994). Reduced stress plastic package. *U.S. Patent No. 5,278,446*.
- Newson, T. A., & Fahey, M. (2003). Measurement of evaporation from saline tailings storages. *Engineering geology*, 70(3-4), 217-233.
- NRCan, N. R. (2013). *Natural Resources Canada*. Retrieved February 2018, from Oil Sands Processes: <http://www.nrcan.gc.ca/energy/oil-sands/5853>

- Oil Sands Discovery Centre. (2009). *Government of Alberta*. Retrieved February 2018, from Facts about Alberta's oil sands and its industry: [http://history.alberta.ca/oilsands/docs/facts\\_sheets09.pdf](http://history.alberta.ca/oilsands/docs/facts_sheets09.pdf)
- Olson, R. E., & Langfelder, L. J. (1965). Pore water pressures in unsaturated soils. *Journal of Soil Mechanics & Foundations Div*, 97(SM1).
- OMEGA. (2018). *Temperature, Humidity and Dew Point Data Logger with LCD Display*. Retrieved April 2018, from Omega Environmental: [https://www.omega.ca/pptst\\_eng/OM-EL-USB-2-LCD.html](https://www.omega.ca/pptst_eng/OM-EL-USB-2-LCD.html)
- Pan, H., Qing, Y., & Pei-yong, L. (2010). Direct and indirect measurement of soil suction in the laboratory. *Electronic Journal of Geotechnical Engineering*, 15(3), 1-14.
- Philip, J. R., & De Vries, D. A. (1957). Moisture movement in porous materials under temperature gradients. *Eos, Transactions American Geophysical Union*, 38(2), 222-232.
- Power, K. (2005). Suction and compressibility characteristics of an unsaturated till. *University of Ottawa - M.Sc. thesis*, 229.
- Qi, S., Simms, P., & Vanapalli, S. (2017). Piecewise-Linear Formulation of Coupled Large-Strain Consolidation and Unsaturated Flow. I: Model Development and Implementation. *Journal of Geotechnical and Geoenvironmental Engineering*, 143(7), 04017018.
- Qiu, Y. (2000). Optimum deposition for sub-aerial tailings disposal. *University of Alberta - Doctoral dissertation*.
- Rahardjo, H., & Leong, E. (2006). Suction measurement. *Proc. Int'l Conference on Unsaturated Soils*, (pp. 81-104). Arizona.
- Rahimi, A., Rahardjo, H., & Leong, E. C. (2015). Effects of soil-water characteristic curve and relative permeability equations on estimation of unsaturated permeability function. *Soils and Foundations*, 55(6), 1400-1411.
- Richards, B. G. (1965). Richards, B. G. Measurement of free energy of soil moisture by the psychrometric technique, using thermistors. 39-46.
- Richards, L. A. (1931). Capillary conduction of liquids through porous medium. *Physics*, 1, 318-333.
- Rima, U. S. (2013). Characterization and centrifuge dewatering of oil sands fine tailings. *University of Regina - Doctoral dissertation*.
- Robinski, E. I. (1999). *Thickened tailings disposal in the mining industry*. Toronto: E.I. Robinsky Associates.
- Rozina, E. (2015). Bearing Capacity of Multilayer-deposited In-line Flocculated Oil Sand Tailings. *Carleton University - M.A.Sc. Thesis*.
- Rozina, E., Mizani, S., Malek, M., Sanchez, M., & Simms, P. (2015). Desiccation and consolidation in a laboratory simulation of multilayer deposition of oil sands fine tailings. *Paste*.
- Schiffman, R., Pane, V., & Gibson, R. E. (1984). The theory of onedimensional consolidation of saturated clays: Iv. An overview of nonlinear finite strain sedimentation and consolidation. *ASCE*, 1-29.
- Scott, J. D., Jeeravipoolvarn, S., Kabwe, L., Wilson, G. W., & Sorta, A. (2013). Properties which affect the consolidation behaviour of mature fine tailings. *International conference on tailings and mine waste*. Banff.

- Senix. (2017). Retrieved April 2018, from <https://senix.com/tspc-30s1-232-ultrasonic-sensor-is-now-the-toughsonic-14/>
- Shahraeeni, E., Lehmann, P., & Or, D. (2012). Coupling of evaporative fluxes from drying porous surfaces with air boundary layer: Characteristics of evaporation from discrete pores. *Water Resources Research*, 48(9).
- Shimajima, E., Yoshioka, R., & Tamagawa, I. (1996). Salinization owing to evaporation from bare-soil surfaces and its influences on the evaporation. *Journal of Hydrology*, 178(1-4), 109-136.
- Siddiqua, S., & Ahmed, I. (2014). A review on consolidation behavior of tailings. *International Journal of Geotechnical Engineering*, 102-111.
- Simms, P., Dunmola, A., & Fisseha, B. (2009). Generic Productions of Drying Time in Surface Deposited Thickened Tailings in a "Wet" Climate". *Thirteenth International Conference on Tailings and Mine Waste '09*, (pp. 2009: 749-758). Banff.
- Simms, P., Grabinsky, M., & Zhan, G. (2007). Modelling evaporation of paste tailings from the Bulyanhulu mine. *Canadian Geotechnical Journal*, 44(12), 1417-1432.
- Simms, P., Soleimani, S., Mizani, S., Daliri, F., Dunmola, A., Rozina, E., & Innocent-Bernard, T. (2017). Cracking, salinity and evaporation in mesoscale experiments on three types of tailings. *Environmental Geotechnics*, 1-15.
- Simms, P., Soleimani, S., Mizani, S., Daliri, F., Dunmola, A., Rozina, E., & Innocent-Bernard, T. (2017). Cracking, salinity and evaporation in mesoscale experiments on three types of tailings. *Environmental Geotechnics*, 1-15.
- Smith, G., & Smith, I. (1998). *Elements de soils mechanics*. Blackwell Science.
- Somogyi, F. (1980). Large Strain Consolidation of Fine Grained Slurries. *Canadian Society for Civil Engineering*. Winnipeg.
- Somogyi, F., Carrier III, W., Lawver, J., & Beckman, J. (1984). Waste phosphatoc clay disposal in mine cuts, in Sedimentation consolidation models: predictions and validation. *ASCE*, 545-580.
- Tarantino, A., & Romero, E. (2009). *Laboratory and Field Testing of Unsaturated Soils*. Springer.
- UMS. (2009). *T5/T5X Pressure Transducer Tensiometer User Manual*. Retrieved July 2015, from [http://www.umsmuc.de/fileadmin/produkt\\_downloads/Tensiometer/T5\\_Manual.pdf](http://www.umsmuc.de/fileadmin/produkt_downloads/Tensiometer/T5_Manual.pdf)
- United States Department of Agriculture, U. (1954, February). *Saline and Alkali Soils*. Retrieved January 2018, from Agriculture Handbook No. 60: [http://www.ars.usda.gov/sp2UserFiles/Place/20360500/hb60\\_pdf/hb60complete.pdf](http://www.ars.usda.gov/sp2UserFiles/Place/20360500/hb60_pdf/hb60complete.pdf)
- Van Genuchten, M. T. (1980). A closed-form equation for predicting the hydraulic conductivity of unsaturated soils 1. *Soil science society of America journal*, 44(5), 892-898.
- Vanapalli, S. K., Fredlund, D. G., Pufahl, D. E., & Clifton, A. W. (1996). Model for the prediction of shear strength with respect to soil suction. *Canadian Geotechnical Journal*, 33(3), 379-392.
- Vanapalli, S. K., Fredlund, D. G., Pufahl, D. E., & Clifton, A. W. (1996). Vanapalli, S. K., Fredlund, D. G., Pufahl, D. E., & Clifton, A. W. (1996). Model for the prediction of shear strength with respect to soil suction. *Canadian Geotechnical Journal*, 33(3), 379-392.
- Vogel, H. J., Hoffmann, H., Leopold, A., & Roth, K. (2005). Studies of crack dynamics in clay soil: II. A physically based model for crack formation. *Geoderma*, 125(3-4), 213-223.

- Weisbrod, N., Nachshon, U., & Dragila, M. (2011). Fracture ventilation by surface winds. *AGU Fall Meeting Abstracts*, 1: 1167.
- Weisbrod, N., Pillersdorf, M., Dragila, M., Graham, C., Cassidy, J., & Cooper, C. A. (2005). Evaporation from fractures exposed at the land surface: Impact of gas-phase convection on salt accumulation. *Dynamics of fluids and transport in fractured rock*, 151-164.
- Wells, P. S., Revington, A., & Omotoso, O. (2011). Mature fine tailings drying—technology update. *Paste*, (pp. 155-166).
- Wilson, G. W., Fredlund, D. G., & Barbour, S. L. (1994). Coupled soil-atmosphere modelling for soil evaporation. *Canadian Geotechnical Journal*, 31(2), 151-161.
- Wilson, G. W., Fredlund, D. G., & Barbour, S. L. (1997). The effect of soil suction on evaporative fluxes from soil surfaces. *Canadian Geotechnical Journal*, 34(1), 145-155.
- Witteman, M. (2013). Unsaturated flow in hydrating porous media with application to cemented mine backfill. *Carleton University - Masters thesis*.
- Xu, Y., Dabros, T., & Kan., J. (2008). Filterability of oil sands tailings. *Process Safety and Environmental Protection*, 86(4), 268-276.
- Yao, D., & Znidarcic, D. (1997). Crust formation and desiccation characteristics for phosphatic clays-users' manual for computer program condese0. *Florida Institute of Phosphate Research*.
- Zhang, F., Wilson, G. W., & Fredlund, D. G. (2017). Permeability function for oil sands tailings undergoing volume change during drying. *Canadian Geotechnical Journal*, (999), 1-17.
- Zhu, Q. (2013). Understanding the role of caustic addition in oil sands processing. *University of Alberta - M.S.c. thesis*.

## Appendices

### Appendix A: Thick-lift – First layer

The following tables summarized the measurements taken during the deposition of the first layer in the thick-lift test.

Date: June 13<sup>th</sup> 2016

Table 7: Quality control and initial solids content from first layer (thick-lift test)

Bucket #	Slump (cm)	Dish Weight (g)	Dish + Wet Sample (g)	Dish + Dry Sample (g)	Moisture Content	Solids Concentration
1	13.2	1.7	9.54	5.71	0.95	0.51
10	12.9	1.68	18.15	10.20	0.93	0.52
20	12.5	1.67	12.57	7.38	0.91	0.52
30	13.5	1.64	15.51	8.98	0.89	0.53
40	13.3	1.69	13.76	8.03	0.90	0.53
50	13.7	1.68	16.33	9.44	0.89	0.53
60	13	1.63	15.03	8.90	0.84	0.54
70	12.2	1.65	21.85	12.68	0.83	0.55
						0.528

Table 8: Data from barrels used in deposition of the first layer (thick-lift test)

Barrel	Solids Concentration	Percentage of the Layer
Barrel 2	0.52	0.33
Barrel 3	0.55	0.17
Barrel 4	0.53	0.5
		0.53

## Appendix B: Thick-lift – Second layer

The following information summarizes the measurements obtained from the tailings added to the dry box the day of the deposition.

Table 9: Data from tailings added to the first layer (thick-lift test)

Total Weight (kg)	Mass Solids (kg)	Mass Water (kg)	Solid Content
484.6047	240.9177	243.6869	0.50

The following information summarizes the measurements obtained from the dry box just before the deposition.

Table 10: Mass lost between the end of the drying process of the first layer and the deposition of the second layer (thick-lift test)

Date	Weight (kg)	Weight Loss (kg)
2016-07-20	507.5626	2.222749
2016-09-02	505.3399	

Table 11: Data from the first layer just before the deposition of the second layer (thick-lift test)

Dry Box Weight (kg)	Weight (kg)	Total Weight (kg)	Mass Solids (kg)	Mass Water (kg)	Solid Content
150	505.3399	355.3399	269.1418	86.19813	0.757421

The following tables summarized the measurements taken during the deposition of the second layer in the thick-lift test.

Date: Sept 2<sup>nd</sup> 2016

Table 12: Quality control and initial solids content from second layer (thick-lift test)

Bucket #	Slump (cm)	Dish Weight (g)	Dish + Wet Sample (g)	Dish + Dry Sample (g)	Moisture Content	Solids Concentration
1	14	1.90	86.00	40.79	1.16	0.46
10	14	1.89	80.20	41.36	0.98	0.50
20	14	1.90	84.80	43.26	1.00	0.50
30	11.5	1.87	104.00	44.44	1.40	0.42
40	14	1.87	85.30	57.64	0.50	0.67
50	14	1.88	90.36	44.42	1.08	0.48
60	14	1.87	89.00	46.35	0.96	0.51
70	14	1.88	101.70	49.40	1.10	0.48
						0.50

Table 13: Data from barrels used in deposition of the second layer (thick-lift test)

Barrels before deposition	Solids Concentration	Percentage of the Layer
Barrel 1	0.49	0.43
Barrel 2	0.50	0.43
Barrel 3	0.51	0.14
		0.50

## Appendix C: Thick-lift – UNSATCON simulation

The following information summarizes the UNSATCON software input information used to model the thick-lift test.

Two sets of parameters were considered:

Case I:

Table 14: Parameters used in Case I (thick-lift test)

Volume change behavior								
Parameters	$a$	$b$	$c$	$d$	$f$	$g$	$\alpha$	$\alpha_s$
Value	2.4	0.33	0.015	0.03	6000	5000	0.005	0.001
Water retention behavior								
Parameters	$C_{drying}$	$C_{wetting}$	$\alpha_{se}$	$\alpha_{sr}$	$\alpha_{ss}$			
Value	3.0	1.35	0.15	0.17	0.04			
Permeability								
Parameters	$H_1$		$H_2$		$M$			
Value	17.5E-11		8		0.75			

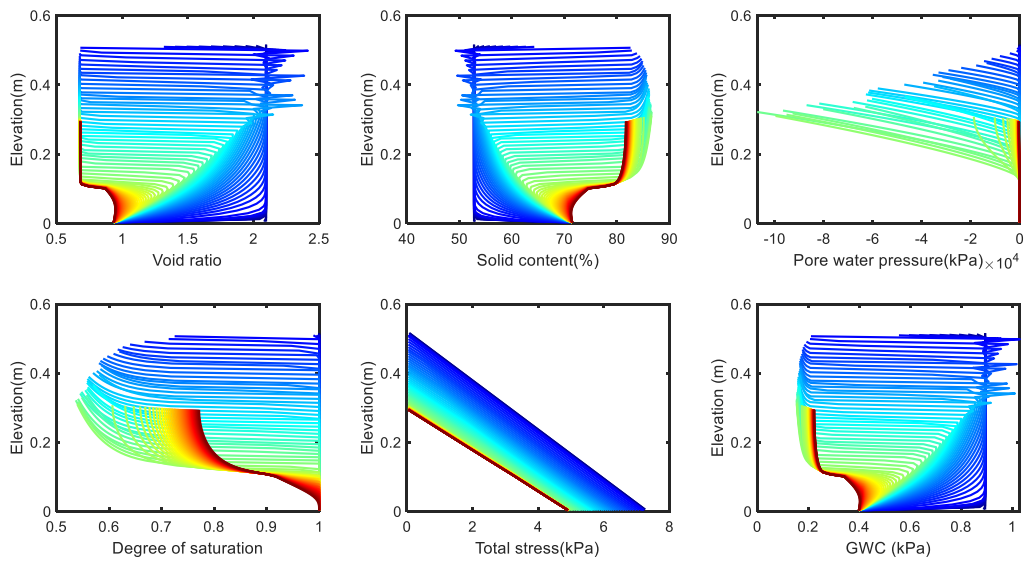


Figure 179: Overall results obtained from UNSATCON for the first layer deposition using CASE I parameters (thick-lift test)

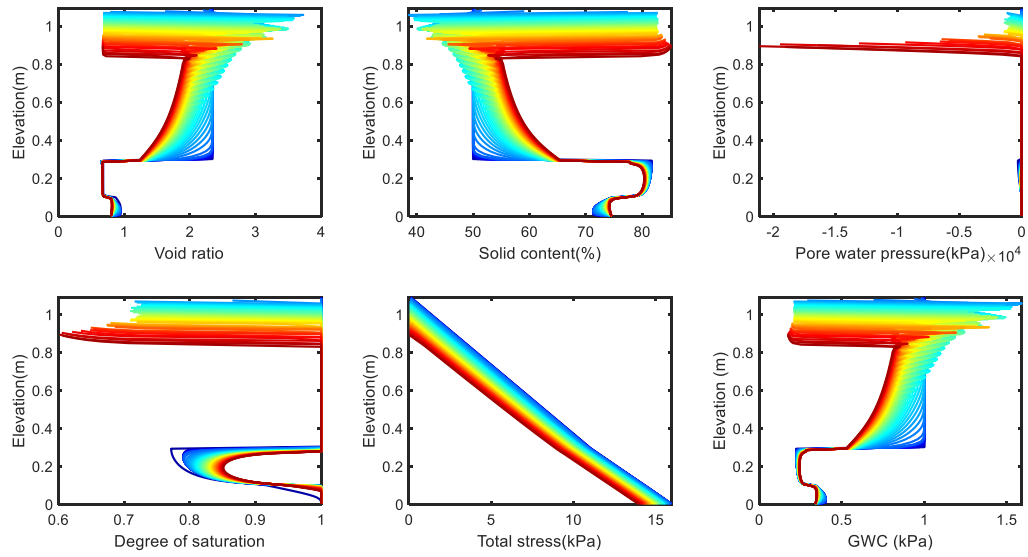


Figure 180: Overall results obtained from UNSATCON for the second layer deposition using CASE I parameters (thick-lift test)

Case II:

Table 15: Parameters used in Case II (thick-lift test)

Volume change behavior								
Parameters	$a$	$b$	$c$	$d$	$f$	$g$	$\beta$	$\beta_s$
Value	2.4	0.33	0.015	0.03	6000	5000	0.005	0.001
Water retention behavior								
Parameters	$C_{drying}$	$C_{wetting}$	$\beta_{se}$	$\beta_{sr}$	$\beta_{ss}$			
Value	3.0	1.35	0.15	0.17	0.04			
Permeability								
Parameters	$H_1$		$H_2$		$M$			
Value	5E-11		7		0.75			

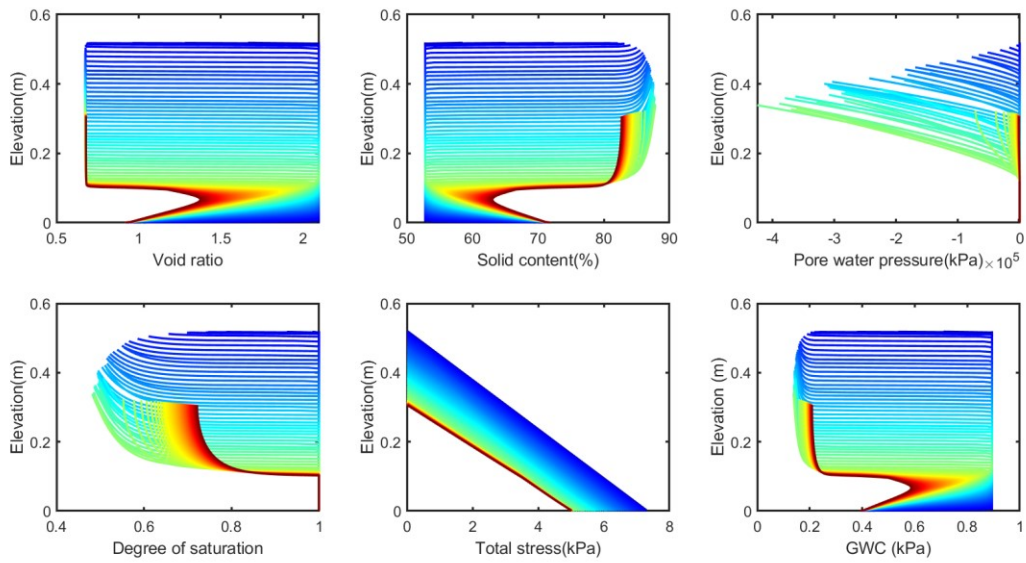


Figure 181: Overall results obtained from UNSATCON for the first layer deposition using CASE II parameters (thick-lift test)

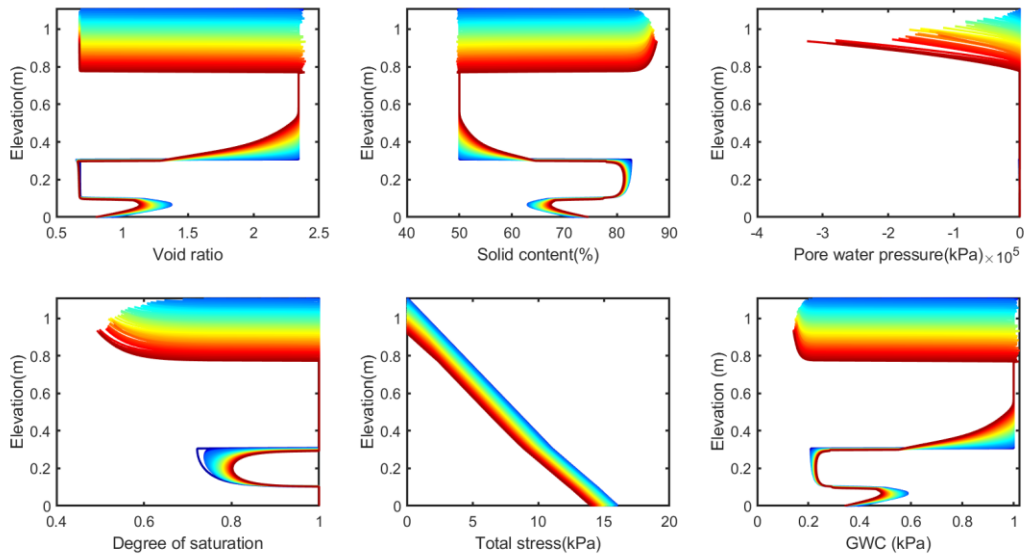


Figure 182: Overall results obtained from UNSATCON for the second layer deposition using CASE II parameters (thick-lift test)

## Appendix D: Thin-lift – First layer

The following tables summarized the measurements taken during the deposition of the first layer in the thin-lift test.

Date: May 15<sup>th</sup> 2017

Table 16: Quality control and initial solids content from first layer (thin-lift test)

Bucket #	Slump (cm)	Dish Weight (g)	Dish + Wet Sample (g)	Dish + Dry Sample (g)	Moisture Content	Solids Concentration
1	10.5	1.88	35.9	19.84	0.89	0.53
10	10	1.90	37.8	20.64	0.92	0.52
20	10.5	1.91	25.4	14.26	0.90	0.53
30	10.8	1.89	42.9	23.37	0.91	0.52
40	10.8	1.89	38.2	20.91	0.91	0.52
50	10.8	1.85	48	26.27	0.89	0.53
						0.53

Table 17: Data from barrels used in deposition of the first layer (thin-lift test)

Barrels before deposition	Solids Concentration	Percentage of the Layer
Barrel 1	0.52	0.63
Barrel 3	0.52	0.37
	0.52	

## Appendix E: Thin-lift – Second layer

The following information summarizes the measurements obtained from the tailings added to the dry box the day of the deposition.

Table 18: Data from tailings added to the first layer (thin-lift test)

Total Weight (kg)	Mass Solids (kg)	Mass Water (kg)	Solid Content
336.2585	162.842	173.4165	0.484276

The following information summarizes the measurements obtained from the dry box just before the deposition.

Table 19: Mass lost between the end of the drying process of the first layer and the deposition of the second layer (thin-lift test)

Date	Weight (kg)	Weight Loss (kg)
2017-06-27	365.21	3.612485
2017-07-23	361.60	

Table 20: Data from the first layer just before the deposition of the second layer (thin-lift test)

Dry Box Weight (kg)	Weight (kg)	Total Weight (kg)	Mass Solids (kg)	Mass Water (kg)	Solid Content
150	361.60	211.60	177.78	33.82	0.84

The following tables summarized the measurements taken during the deposition of the second layer in the thin-lift test.

Date: July 23<sup>th</sup> 2017

Table 21: Quality control and initial solids content from second layer (thin-lift test)

Bucket #	Slump (cm)	Dish Weight (g)	Dish + Wet Sample (g)	Dish + Dry Sample (g)	Moisture Content	Solids Concentration
1	10.8	1.63	31.65	15.95	1.10	0.48
10	9.8	1.63	24.98	12.80	1.09	0.48
20	9.5	1.58	33.26	16.57	1.11	0.47
30	8.2	1.59	63.38	31.19	1.09	0.48
40	9.7	1.62	34.77	18.75	0.94	0.52
47		1.66	30.12	15.70	1.03	0.49
50	9.6	1.67	33.75	15.70	1.29	0.44
						0.48

Table 22: Data from barrels used in deposition of the second layer (thin-lift test)

Barrels before deposition	Solids Concentration	Percentage of the Layer
Barrel 5	0.47	0.67
Barrel 3	0.52	0.29
Barrel 6	0.44	0.04
		0.48

## Appendix F: Thin-lift – Third layer

The following information summarizes the measurements obtained from the tailings added to the dry box the day of the deposition.

Table 23: Data from tailings added to the second layer (thin-lift test)

Total Weight (kg)	Mass Solids (kg)	Mass Water (kg)	Solid Content
336.80	162.23	174.58	0.48

The following information summarizes the measurements obtained from the dry box just before the deposition. As there was a problem with the data logger associated with the load cells measuring the weight of the dry box during this time, the final weight of the dry box just before the deposition was assumed to have been reduced 2.5kg from the last available measurements

Table 24: Mass lost between the end of the drying process of the second layer and the deposition of the third layer (thin-lift test)

Date	Weight (kg)	Weight Loss (kg)
2017-09-09	577.4809	?
2017-10-18	574.9809	<-Assumed

Table 25: Data from the dry box just before the deposition of the third layer (thin-lift test)

Dry Box Weight (kg)	Weight (kg)	Total Weight (kg)	Mass Solids (kg)	Mass Water (kg)	Solid Content
150	574.98	424.98	340.62	84.36	0.80

The following tables summarized the measurements taken during the deposition of the third layer in the thin-lift test.

Date: Oct 18<sup>th</sup> 2017

Table 26: Quality control and initial solids content from third layer (thin-lift test)

Bucket #	Slump (cm)	Dish Weight (g)	Dish + Wet Sample (g)	Dish + Dry Sample (g)	Moisture Content	Solids Concentration
1	11	1.60	35.61	18.04	1.07	0.48
10	11.5	1.60	33.83	17.26	1.06	0.49
20	11.2	1.61	43.29	21.81	1.06	0.48
30	11.5	1.59	39.86	20.01	1.08	0.48
40	12	1.61	38.73	19.34	1.09	0.48
50	12	1.61	47.98	23.72	1.10	0.48
						0.48

Table 27: Data from barrels used in deposition of the third layer (thin-lift test)

Barrels before deposition	Solids Concentration	Percentage of the Layer
Barrel 6	0.48	0.5
Barrel 6+7	0.48	0.02
Barrel 7	0.48	0.48
		0.48

## Appendix G: Tailings characterization analysis

Table 28: Water chemistry of bleed water

Sample Description			Sample #1	Sample #2	Sample #3
Date Sampled			04/16/2018	04/16/2018	04/16/2018
Parameter	Unit	RDL	9187232	9187233	9187234
Electrical Conductivity	µS/cm	2	2200	2190	2220
pH	pH Units	NA	7.81	7.85	7.85
Total Hardness (as CaCO <sub>3</sub> )	mg/L	0.5	378	393	377
Total Dissolved Solids	mg/L	20	1710	1740	1710
Total Suspended Solids	mg/L	10	334	875	371
Alkalinity (as CaCO <sub>3</sub> )	mg/L	5	399	395	388
Fluoride	mg/L	0.25	1.2	1.2	1.2
Chloride	mg/L	0.50	159	155	156
Nitrate as N	mg/L	0.25	<0.5	<0.5	<0.5
Sulphate	mg/L	0.50	674	650	667
Calcium	mg/L	0.10	91.9	96.7	90.7
Magnesium	mg/L	0.10	36.1	36.9	36.5
Sodium	mg/L	0.10	358	377	352
Potassium	mg/L	0.10	21.4	22.5	21.0
Total Iron	mg/L	0.05	16.3	22.0	13.8
Total Manganese	mg/L	0.020	1.05	1.28	0.950
Iron (Fe <sup>++</sup> )	mg/L	0.05	<0.05	<0.05	<0.05
Iron (Fe <sup>+++</sup> )	mg/L	0.05	16.3	22.0	13.8
% Difference/ Ion Balance	%	NA	5.75	2.05	5.53

9187232-9187234: Samples were received and analyzed past hold time for Iron (Fe<sup>++</sup>) analysis. Elevated RDL indicates the degree of sample dilution prior to the analysis in order to keep analytes within the calibration range of the instrument and to reduce matrix interference.

Table 29: Mineralogical composition: X-Ray diffraction analysis

TYPE OF ANALYSIS	WEIGHT %										
		Qtz	Plag	K-Feld	Cal	Dol	Anhy	Pyr	Musc	Bar	Sider
BULK FRACTION:	84.47	33	1	2	0	TR	0	1	1	0	2
CLAY FRACTION:	15.53	4	0	0	0	0	0	0	0	0	0
BULK & CLAY	100	28	1	2	0	TR	0	1	1	0	2

Table 30: Mineralogical composition: X-Ray diffraction analysis - Clay fraction

TYPE OF ANALYSIS	WEIGHT %	CLAYS					Total Clay
		Kaol	Chl	Ill	ML*	Smec	
BULK FRACTION:	84.47	50	0	10	0	0	60
CLAY FRACTION:	15.53	72	0	24	0	0	96
BULK & CLAY	100	53	0	12	0	0	65